

pH-Responsive Magnetism of Iron(II) Complexes
in Solution and Under Small Confinement
as Basis for Smart Contrast Agents

Dissertation

Zur Erlangung des akademischen Grades doctor rerum naturalium
(Dr. rer. nat.)

eingereicht an der Fakultät für Biologie, Chemie und Geowissenschaften der
Universität Bayreuth

von M. Sc. René Nowak
geboren am 28.04.1987
in Neustadt an der Waldnaab

Bayreuth, 2017

Die vorliegende Arbeit wurde in der Zeit von September 2014 bis April 2017 an der Universität Bayreuth am Lehrstuhl für Anorganische Chemie II unter Betreuung von Frau Prof. Dr. Birgit Weber angefertigt.

Vollständiger Abdruck der von der Fakultät für Biologie, Chemie und Geowissenschaften der Universität Bayreuth genehmigten Dissertation zur Erlangung des akademischen Grades eines Doktors der Naturwissenschaften (Dr. rer. nat.).

Dissertation eingereicht am: 09.06.2017

Zulassung durch die Promotionskommission: 05.07.2017

Wissenschaftliches Kolloquium: 17.11.2017

Amtierender Dekan: Prof. Dr. Stefan Peiffer

Prüfungsausschuss:

Prof. Dr. Birgit Weber	(Erstgutachter)
Prof. Dr. Stephan Förster	(Zweitgutachter)
Prof. Dr. Hans-Werner Schmidt	(Vorsitz)
Prof. Dr. Ernst Rössler	

René Nowak

pH-Responsive Magnetism of Iron(II) Complexes in Solution and Under Small Confinement
as Basis for Smart Contrast Agents

pH-Responsive Magnetism of Iron(II) Complexes
in Solution and Under Small Confinement
as Basis for Smart Contrast Agents

Dissertation

Zur Erlangung des akademischen Grades doctor rerum naturalium
(Dr. rer. nat.)

eingereicht an der Fakultät für Biologie, Chemie und Geowissenschaften der
Universität Bayreuth

von M. Sc. René Nowak
geboren am 28.04.1987
in Neustadt an der Waldnaab

Bayreuth, 2017

*Es war, als hätt' der Himmel
Die Erde still geküßt,
Daß sie im Blütenschimmer
Von ihm nun träumen müßt'.*

*Die Luft ging durch die Felder,
Die Ähren wogten sacht,
Es rauschten leis die Wälder,
So sternklar war die Nacht.*

*Und meine Seele spannte
Weit ihre Flügel aus,
Flog durch die stillen Lande,
Als flöge sie nach Haus.*

– *Joseph von Eichendorff, Schlesien*

Acknowledgement

First of all, I would like to thank Prof. Dr. Birgit Weber for giving me the opportunity to pursue this Ph.D. under her supervision and for her cheerful, supportive and optimistic personality. Furthermore, I would like to thank her for allowing me to follow my own ideas, create and conduct my own research as well as for encouraging me to apply for independent funding and for the nice time we had at international conferences.

I would also like to extend my gratitude to my colleague Johannes Weihermüller for being a wonderful friend and joyful lab companion, Dr. Charles Lochenie for his excellent and helpful knowledge in organic synthesis and the whole research group for the good working atmosphere. Especially I would like to thank Sophie Schönfeld for always gluing together the pieces of my shattered mind and heart during this work. Without you this thesis would not have been written.

I would like to thank Prof. Dr. Ernst Rößler and Max Flämig for the important opportunity to measure field-cycling ^1H -NMR relaxometry and making me familiar with the theoretical concepts as well as with the apparatus itself. For analytical work I am obligated to thank Dr. Christine Denner (SEM/EDX), Beate Bojer (MAS NMR and inversion-recovery measurements), Sonja Lutschinger (AAS) and Florian Puchtler (powder diffraction). For preparative work I would like to thank all of my practical students and especially Alper Aksit, Andreas Dürrmann and Jan Kuliga who proved to be extraordinarily skillful. Additionally, I would like to thank Nathalie Daro, Cédric Desplanches and Guillaume Chastanet for measurements of the total reflectivity in Bordeaux.

For giving me a fabulous work-life-balance I would like to thank *The Raccoonboys*: Christoph Aberle, Fabian Beranovsky, Christoph Häckner, Benjamin Horn, Martin Kelz, André Rauch and Manuel Zetlmeisl who made me realize that real friends can be found anywhere.

Finally I would like to give special thanks to my beloved parents and my significant other Dimitrios for their incessant support, help, encouragement and corroborative advice throughout the years.

For generous financial support I would like to thank the *Fond der Chemischen Industrie*, the *Elite Network of Bavaria* and the *ERASMUS scholarship program*.

Für meinen Großvater

Rudi Nowak

** 13.02.1932 in Breslau, Schlesien*

† 01.03.2016 in Trabitze, Bayern

1. Table of Contents

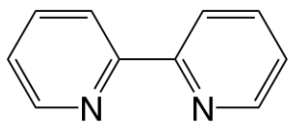
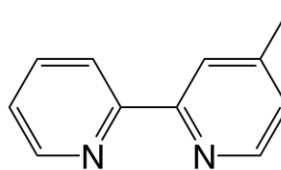
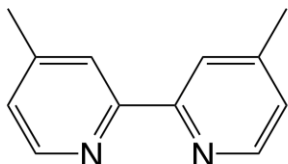
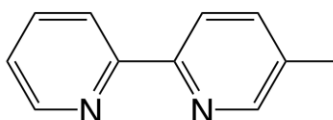
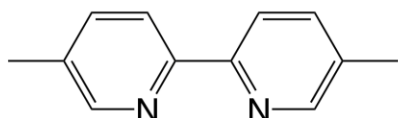
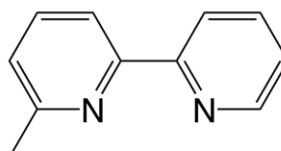
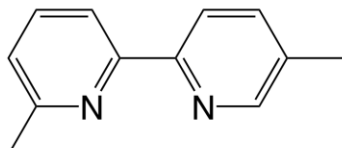
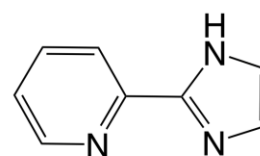
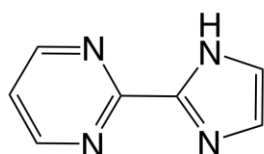
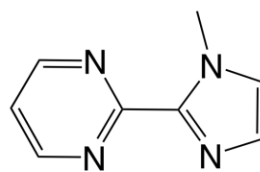
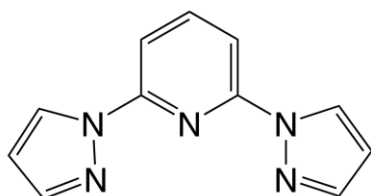
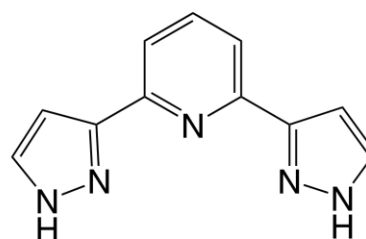
I. Table of Contents	I
II. Ligand Structures	IV
III. Primarily Discussed Complexes	V
IV. Zeolite Structures	VI
V. Abbreviations	VII

1. Introduction	1
1.1 Spin-crossover and coordination-induced spin state switches	1
1.2 Transition metal complexes as smart contrast agents	3
1.3 Zeolite structures and properties	10
1.4 Zeolites as smart contrast agents	16
1.5 Field-cycling ^1H -NMR relaxometry	18
1.6 Properties and numbering of the used ligand systems	21
1.7 Instrumental methods	23
1.8 Motivation	29
1.9 Aims of this work	30
2. Results and Discussion	32
2.1 Homoleptic iron(II) complexes	32
2.1.1 General information and characterization	32
2.1.2 Behavior in aqueous solution: ^1H -NMR spectroscopy	42

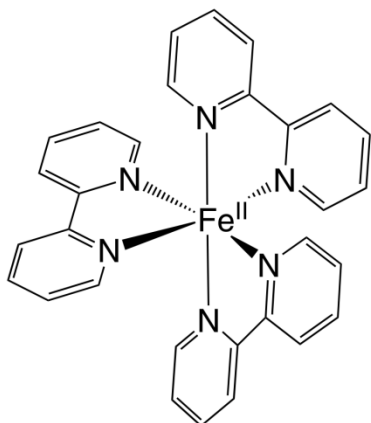
Table of Contents

2.1.3 Behavior in aqueous solution: UV-Visible experiments	62
2.1.4 Behavior in aqueous solution: Magnetic susceptibility studies	68
2.1.5 Behavior in aqueous solution: Field-cycling ^1H -NMR relaxometry	74
2.2 Proton-driven coordination-induced spin state switch	80
2.2.1 Observations and systematic trends	80
2.2.2 Consequences and predictions	84
2.3 Iron(II) complexes under small confinement	89
2.3.1 General information and characterization	89
2.3.2 Optical characterization and chromaticity	95
2.3.3 Magnetism of zeolite hybrid materials	99
2.4 pH-Responsive magnetism in zeolites	105
2.4.1 Observations and systematic trends	105
2.4.2 Consequences and predictions	107
2.5 Iron(II) complexes encapsulated in nanozeolites	108
2.5.1 Iron exchange experiments	108
2.5.2 General characterization of impregnated nanozeolites	112
2.5.3 Solid state investigations	116
2.5.4 Investigations in solution	127
2.6 PD-CISSS of iron(II) complexes in nanozeolites	133
2.6.1 Observations and systematic trends	133
2.6.2 Consequences and predictions	134

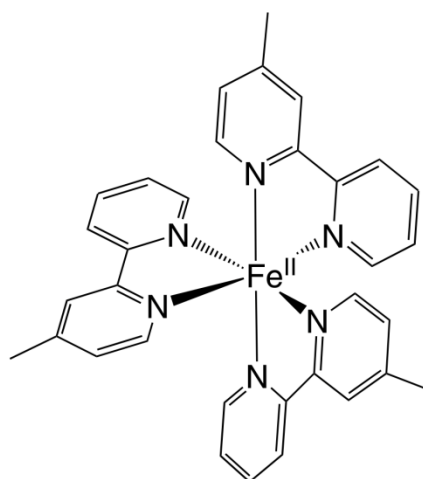
3. Summary	135
3.1 Summary (in English)	135
3.2 Summary (in German)	140
4. Experimental Section	145
4.1 General procedures and instrumentation	145
4.2 Synthesis	150
4.2.1 Synthesis of the iron(II) starting salts	152
4.2.2 Synthesis of mono- and dimethylated 2,2'-bipyridines	152
4.2.3 Alternative synthesis of 5-methyl-2,2'-bipyridine	155
4.2.4 Synthesis of pyrazolyl and imidazolyl ligands	156
4.2.5 Synthesis of the iron(II) chloride complexes	158
4.2.6 Preparation of cation exchanged zeolites	161
4.2.7 Preparation of iron exchanged nanosized zeolites	162
4.2.8 Impregnation of zeolites with iron(II) complexes	163
4.2.9 Impregnation of nanosized zeolites with iron(II) complexes	164
5. References	166
6. Publications and Conference Contributions	174
7. Declaration of Independence	175
A. Appendix	176

II. Ligand Structures**2,2'-bipyridine****4-methyl-2,2'-bipyridine****4,4'-dimethyl-2,2'-bipyridine****5-methyl-2,2'-bipyridine****5,5'-dimethyl-2,2'-bipyridine****6-methyl-2,2'-bipyridine****5,6'-dimethyl-2,2'-bipyridine****2-(1*H*-imidazol-2-yl)pyridine****2-(1*H*-imidazol-2-yl)pyrimidine****2-(1-methyl-1*H*-imidazol-2-yl)pyrimidine****2,6-di(1*H*-pyrazol-1-yl)pyridine****2,6-di(1*H*-pyrazol-3-yl)pyridine**

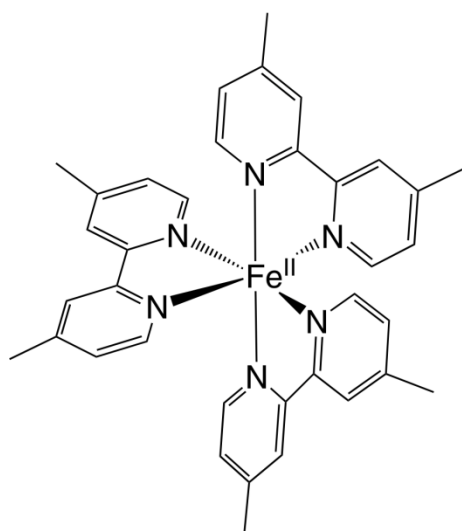
III. Primarily Discussed Complexes



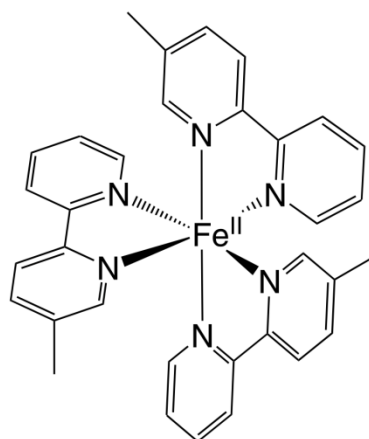
$[\text{Fe}(\text{Bpy})_3]^{2+}$



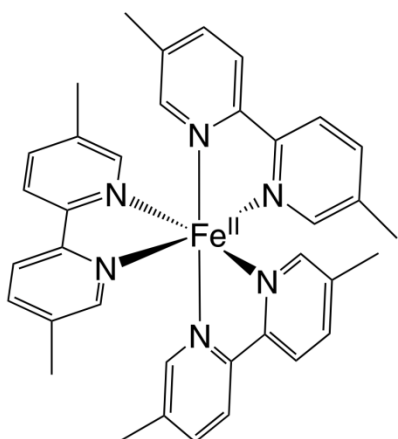
$[\text{Fe}(4\text{mBpy})_3]^{2+}$



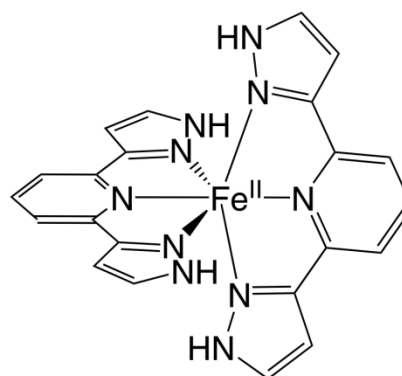
$[\text{Fe}(44\text{mBpy})_3]^{2+}$



$[\text{Fe}(5\text{mBpy})_3]^{2+}$

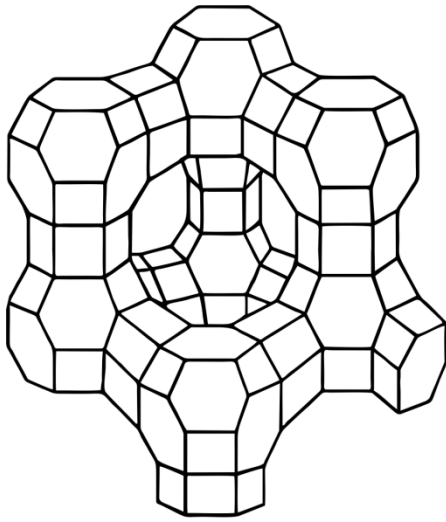


$[\text{Fe}(55\text{mBpy})_3]^{2+}$

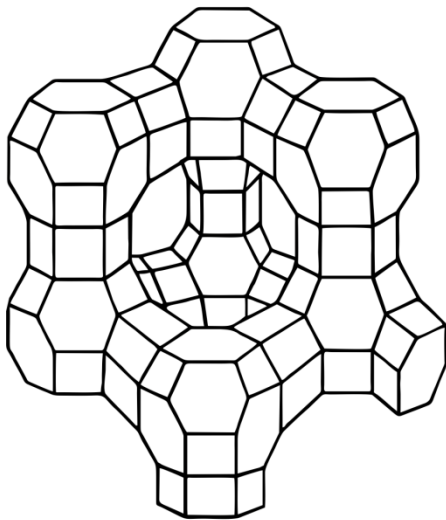


$[\text{Fe}(\text{Bpp})_2]^{2+}$

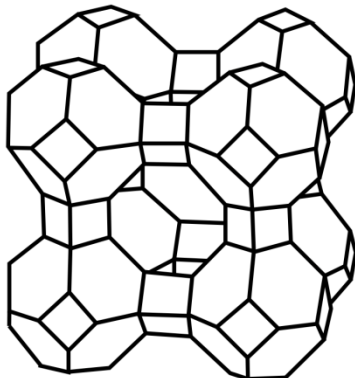
IV. Zeolite Structures



Zeolite NaX
Si/Al-ratio: ~ 1
Supercage: ~ 1.2 nm



Zeolite NaY
Si/Al-ratio: 3-5
Supercage: ~ 1.2 nm



Zeolite NaA
Si/Al-ratio: ~ 1
Supercage: < 1.2 nm

V. Abbreviations

4mBpy	4-Methyl-2,2'-bipyridine
44mBpy	4,4'-Dimethyl-2,2'-bipyridine
5mBpy	5-Methyl-2,2'-bipyridine
55mBpy	5,5'-Dimethyl-2,2'-bipyridine
@	Incorporated into following host material
AAS	Atomic absorption spectroscopy
Abs.	Absorption
B_0	External magnetic field
Bpy	2,2'-Bipyridine
Bpp	2,6-Bis(1 <i>H</i> -pyrazol-3-yl)pyridine
c	Concentration
CHN	Elementary analysis
CISSS	Coordination-induced spin state switch
CT	Charge transfer
d	Doublet
δ	Isomeric shift
ΔE_Q	Quadrupole splitting
Δr_1	Molar relaxivity
$\Delta\chi_{\text{Mass}}$	Mass susceptibility difference
EDX	Energy dispersive X-ray spectroscopy
<i>fac</i>	Facial
FC	Field-cycling
<i>f</i> MRI	Functional magnetic resonance imaging
G	Unit of the magnetic flux density (Gauß)
$\Gamma/2$	Full width at half maximum
γ	Gyromagnetic ratio
γ_{HS}	High-spin fraction

Abbreviations

γH^+	Fraction of the protonated complex
g	Acceleration of gravity
h	Hours
HS	High-spin
ID	Inner doublet (small ΔE_Q)
IR	Infra-red
IS	Isomeric shift
K	Kelvin
L	Ligand
LS	Low-spin
LTA	Linde-type zeolite (zeolite A)
m	Multiplet
MAS	Magic angle spinning
Max	Maximum
mCi	Millicurie
Me	Methyl
MeOH	Methanol
<i>mer</i>	Meridional
min	Minute
MLCT	Metal-to-ligand-charge-transfer
MRI	Magnetic resonance imaging
ν	Larmor frequency
NaA	Sodium exchanged Linde-type zeolite (zeolite LTA)
NaX	Sodium exchanged Faujasite-type zeolite (zeolite X)
NaY	Sodium exchanged Faujasite-type zeolite (zeolite Y)
OD	Outer doublet (large ΔE_Q)
Oe	Oersted
PD-CISSS	Proton-driven coordination-induced spin state switch
ppm	Parts per million

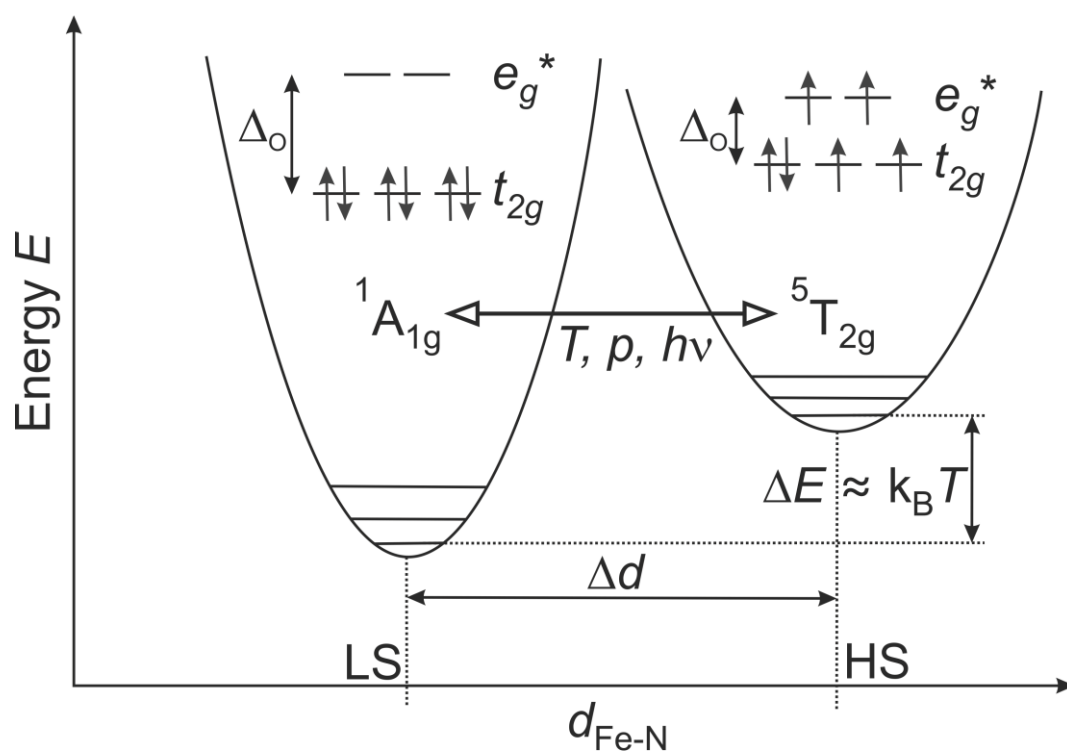
Abbreviations

py	Pyridine
QS	Quadrupole splitting
R	Organic rest
R_1	Longitudinal relaxation rate
R_1^{LM}	Longitudinal relaxation rate of the solvent
$r_{1\text{Obs}}$	Observed longitudinal relaxation rate
Rel.	Relative
RT	Room temperature
S	Total spin of an atom or molecule
SCO	Spin-crossover
SEM	Scanning electron microscope
SQUID	Superconducting quantum interference device
t	Triplet
T	Temperature
T_1	Longitudinal relaxation time
TG	Thermogravimetry
UV-Vis	Ultraviolet-Visible
v	Velocity
wt%	Weight percent
χ_{Dia}	Molar diamagnetic susceptibility
χ_{mol}	Molar magnetic susceptibility
χ_{Mass}	Mass susceptibility
χ_{MT}	Temperature dependent molar susceptibility
X	Faujasite-type zeolite (zeolite X)
XRD	X-ray powder diffraction
Y	Faujasite-type zeolite (zeolite Y)

1. Introduction

1.1 Spin-crossover and coordination-induced spin state switches

Besides redox activity, catalysis, striking chromaticity or their pivotal role as hemoglobin in the erythrocytes, iron complexes are known for their manifold magnetic properties.^[1,2] The most prominent magnetic phenomenon is known as spin-crossover (SCO) and was described for the first time by Cambi *et al.* in the year 1931 while observing abnormal behavior of iron(III)-tris(dithiocarbamate) isomers.^[3] Those complexes displayed differences in their total spin S in relation to the temperature. This could be explained by the ligand field theory and provided a consistent description in accordance with Werner's perception of coordination chemistry.^[4,5]

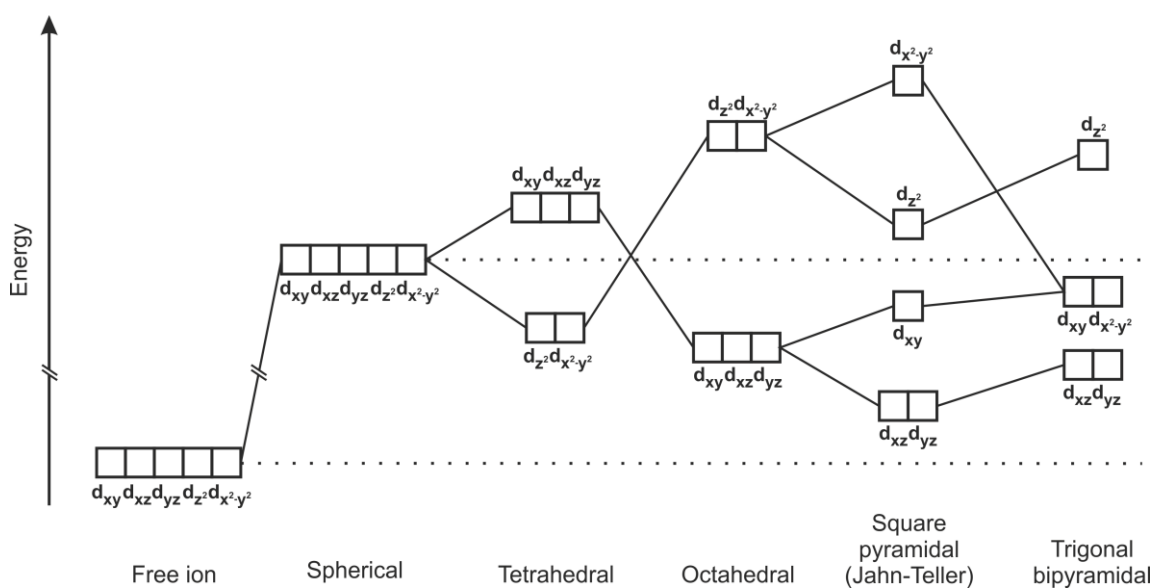


Scheme 1. Jablonski diagram of the spin-crossover process with the corresponding orbital splitting in an octahedral field and term symbols for an iron(II) compound. The energy E is plotted against the interatomic distance between the iron core and the adjacent nitrogen atom.

The ligand field theory was inferred from the electrostatic interaction between the central atom and the surrounding ligands which are considered as point charges. The ligand field perturbs the d-orbitals and leads to their degeneration.^[6] In relation to the geometry of the surrounding ligands different degeneration types can be observed. In an octahedral field with Δ_O the five degenerated d-orbitals (d_{xy} , d_{xz} , d_{yz} , d_{z^2} and $d_{y^2-z^2}$) are split into three energetically lowered t_{2g} and two energetically higher e_g^* orbitals.^[7] In such a system the central atom might display two different spin states when the electron configuration is between d^4 and d^7 like for Fe(II) with a d^6 population.^[8] If the ligand field splitting energy Δ_O is lower than the energy P required for spin pairing, the spins arrange in the high-spin state ($^5T_{2g}$).^[9] If it is higher, the low-spin state is realized ($^1A_{1g}$). In a special intermediary case, the states can be switched by external perturbations like pressure or temperature what is then called SCO.^[10] For the switching of S with light the phenomenon was given the name LIEEST what means light-induced excited spin state trapping.^[11] Additionally, also HAXIESST, SOXIESST and NIESST (hard-X-rays-induced, soft-X-rays-induced and Nuclear-decay-induced excited spin state trapping) are known.^[12,13] The Jablonski diagram for the SCO process is displayed in Scheme 1.^[10] Since antibonding e_g^* orbitals are populated in the HS state, a longer bond length is observed.

We have seen that changes of S during a SCO don't go alongside with changes of the coordination itself. Nevertheless, one can imagine easily that configurational change around a metal center can also induce magnetic alterations since the ligand field changes in an even more drastic way than during a normal SCO. Such a change is called coordination-induced spin state switch (CISSS).^[14,15] Possible ligand field splittings are depicted in the following Scheme 2.^[16] For a d^6 ion in a spherical field we can only observe $S = 2$ since all orbitals are degenerated. A tetrahedral coordination can have $S = 1$ in a LS state or $S = 2$ in a HS state although usually the later will be observed since Δ_T is rather small.^[17] As discussed, Δ_O can lead either to $S = 0$ or $S = 2$.^[16,17] A square pyramidal or Jahn-Teller distorted system can exhibit $S = 0$ in a LS, $S = 2$ in a HS and $S = 1$ in between when d_{xy} and d_{z^2} are in a similar energy range what is called intermediate spin state.^[18,19] $S = 1$ and $S = 2$ are observable for a trigonal bipyramidal fashion. Since spherical ligand fields as well as trigonal bipyramidal ones can hardly be realized synthetically, the biggest difference $\Delta S = 2$ can only be observed between an octahedral LS state and a square pyramidal or Jahn-Teller distorted HS state. Such a transition can be easily accomplished by removing or substituting one coordinating ligand from a diamagnetic iron center which is then becoming paramagnetic or vice versa. This

might alter the coordination but permits the use of external triggers and linking spin state changes to other physical or chemical properties than temperature, pressure or light.^[20,21] Such an amalgamation is in many cases difficult to accomplish for SCO compounds. Additionally, the mechanism is also applicable to other transition metal complexes like chrome, manganese, cobalt, nickel or copper.^[22] Therefore it is not surprising that a significant amount of research has been devoted to switch the magnetic state of transition metal complexes via coordination in a reversible or irreversible way with a number of possible applications like sensors, triggered release systems or responsive contrast agents.^[20-22]



Scheme 2. Possible ligand field splittings that can be observed for transition metal complexes in a spherical, tetrahedral, octahedral, square pyramidal (Jahn-Teller distorted) or trigonal bipyramidal ligand field.

1.2 Transition metal complexes as smart contrast agents

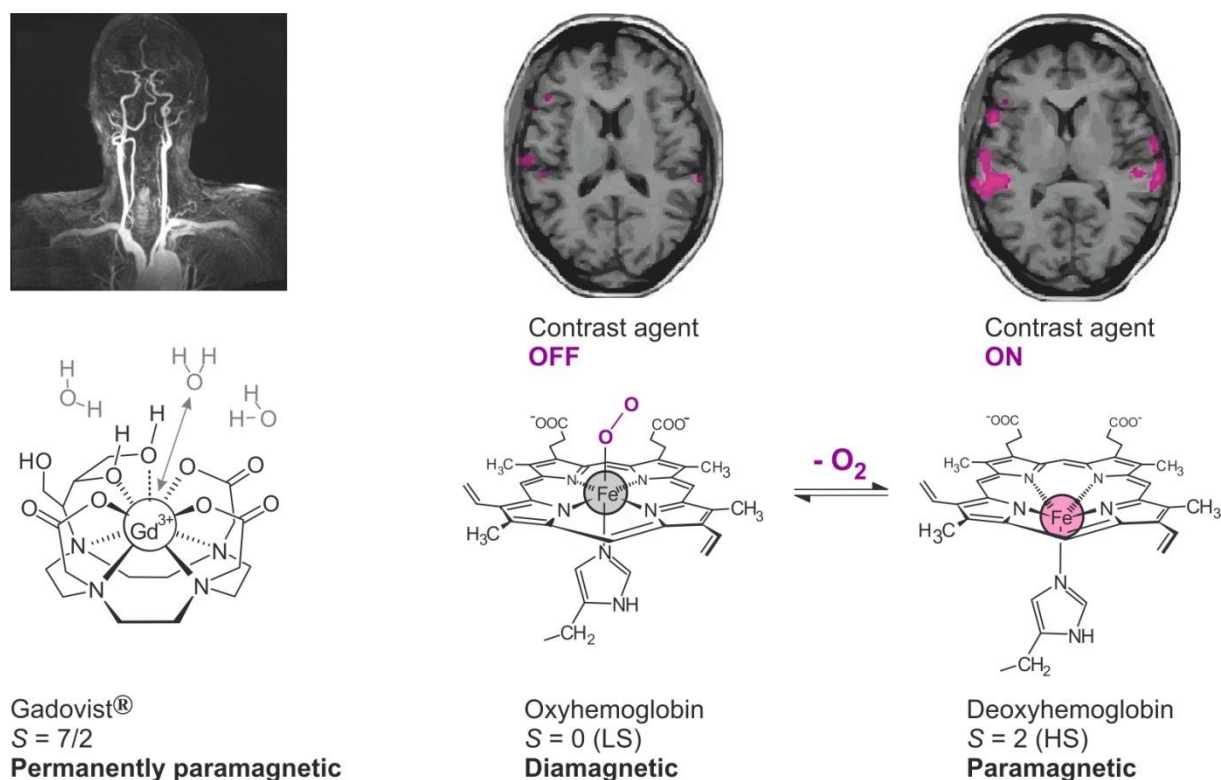
Today, magnetic resonance imaging is one of the most powerful tools in medical diagnostics due to several advantages like its general noninvasiveness and no need for ionizing radiation compared to computer tomography.^[23] It generates contrast images from physical properties of the most common substance in the human body – water.^[24] An amount up to 60 wt% make

H₂O the ideal molecule to gain a deep insight into structure, constitution and physiology of the organism.^[25] Depending on the type of tissue the associated water protons have different relaxation times. Those consist of longitudinal and transverse components T_1 and T_2 and are influenced by confinement, proteins, salt concentration or other tissue properties.^[26] Nevertheless, those natural differences are usually very small resulting in an insufficient contrast ratio (low signal-to-noise ratio).^[27] Therefore, contrast agents are used which reduce the relaxation times and consequently yield a more contrasted and detailed image.^[28] The paramagnetic enhancement of the relaxivity is caused by the electronic spin relaxation.^[29] Such contrast agents are usually Gd(III) chelate complexes like Gd(III)DTPA (Magnevist®), Gd(III)DTPA-BMA (ProHance®), Gd(III)DO3A-butrol (Gadovist®) or Gd(III)DOTA (Dotarem®) and are injected on a gram scale into the blood vessels (see Scheme 3).^[20,30] This does not only sum up to several tons of gadolinium waste per year but the toxic lanthanides are also known for accumulating in the brain and causing nephrogenic systemic fibrosis (NSF). NSF involves abnormal tissue growth of internal organs, skin or eyes.^[31] This leads to a search for nontoxic alternatives like Fe(II). Additionally, the Gd(III) ions are permanently paramagnetic which usually doesn't allow the implementation of a functional magnetism which responds to and contrasts selectively a desired biological property.^[32]

A contrast agent with a specific response is called *smart* contrast agent or *intelligent* contrast agent.^[33] Similarly to gadolinium chelate complexes it enhances the relaxivity of surrounding tissue water but is in contrast not permanently paramagnetic. Triggered by an external stimulus it transitions from a diamagnetic to a paramagnetic state.^[20,21] The first one can be referred to as MRI-*silent* since it doesn't affect T_1 properties while the later can be referred to as MRI-*active* because of paramagnetic relaxation enhancement.^[14,34,35] Therefore, contrast is always generated by the trigger respectively the tissue property that is associated with the trigger.^[14,20,21,34]

A striking example for such a smart contrast agent was not created in the laboratory but by nature itself – hemoglobin. The iron(II) ion at the porphyrin center of the heme is oxygenated in the pulmonary capillaries.^[36] The end-on coordination of oxygen appears in a concerted mechanism causing the iron to move in plane with the porphyrin guided by an additionally coordinated proteinogenic amino acid.^[37] The perfect octahedral ligand assembly causes oxyhemoglobin to be diamagnetic (d^6 , LS, $S = 0$) as long as it's just transported. When oxygen is consumed iron faces a square pyramidal coordination (see Scheme 2) making the

deoxyhemoglobin paramagnetic (d^6 , HS, $S = 2$).^[38] Cerebral neurons in the brain consume considerably more oxygen when they are active than the inactive neurons.^[23] This haemodynamic response leads to more deoxyhemoglobin near excited neurons respectively more paramagnetic iron(II) in areas with a high cerebral activity and therefore an enhanced paramagnetic relaxation of cerebrospinal fluid which is depicted in Scheme 3.^[20] Hence, blood-oxygenation-level dependent contrast imaging is suitable to visualize thinking processes.^[39] Due to the involvement of hemoglobin it is also referred to as *functional* MRI (*f*MRI). This outstanding process of biochemically altered spin states of one single molecule is the earliest and indeed practically exploited example of smart contrast agents.^[40] Thus, it is no surprise that hemoglobin inspired several other researchers to synthesize novel types of responsive 3d-transition-metal complexes for *f*MRI.



Scheme 3. Left: Structure of Gadovist® (Gd(III)DO3A-butrol) and coordinative exchange of water molecules; Right: Molecular principles of blood-oxygenation-level-dependent contrast imaging with hemoglobin.^[20]

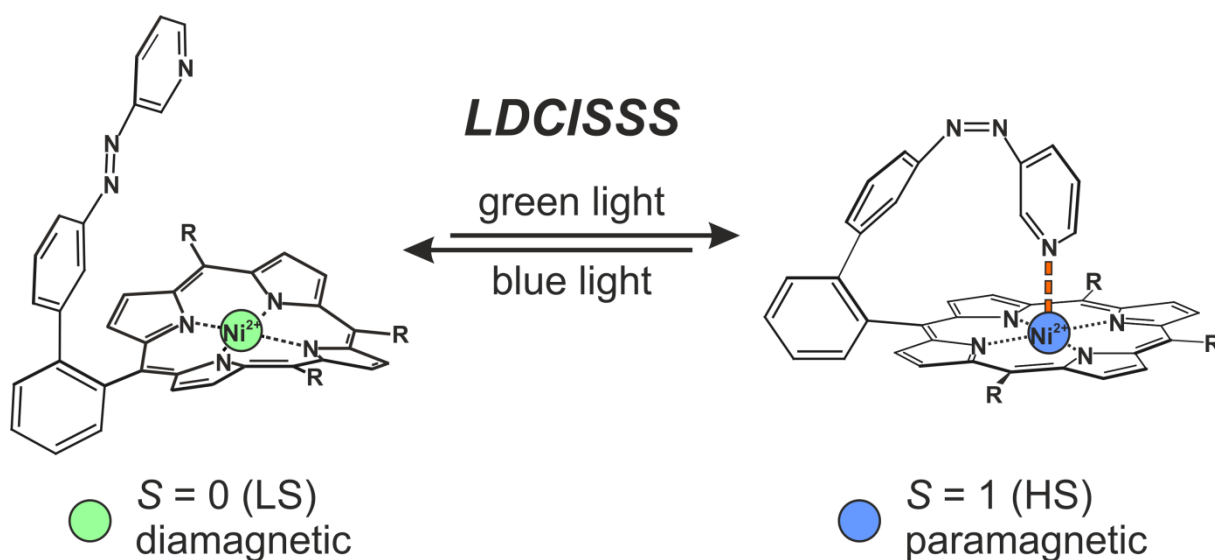
The earliest attempts to decrease T_1 used the T -dependent magnetism of SCO compounds. In 1998, Janiak *et al.* prepared bis[hydro-tris(1,2,4-triazolyl)borate]iron(II) with an abrupt SCO around 330 K in the solid state.^[41] The magnetism of this compound is like all other SCO compounds Boltzmann-distributed in solution. They showed that T_1 in a 99.7% D₂O mixture is reduced linearly as a result of SCO between 20 °C and 80 °C for three concentrations of the compound.^[41] This served as proof of principle. Five years later Muller *et al.* presented polymeric triazole iron(II) particles changing the relaxation properties of cyclohexane in a hysteretic fashion between 395 K and 310 K. However, with no application in aqueous solution.^[42] 2008, Stavila *et al.* showed that coordination-induced spin state switches can generate a significant relaxivity gap between a LS and HS iron(II) complex by comparing the relaxation times T_1 of the structural similar [Fe(tptacn)](ClO₄)₂ ($S = 0$) and [Fe(dptacn)(Cl)](PF₆) ($S = 2$).^[43] The last one had a longitudinal relaxivity r_1 of 1.29 mM⁻¹s⁻¹ which is very close to Gd(III)DOTA with $r_1 = 2.44$ mM⁻¹s⁻¹ and thus raised the overall consideration of iron(II) complexes as contrast agent although the published systems are not switchable by an external trigger.^[43]

Que *et al.* prepared mixed Gd(III)-Cu(I/II) chelates with large changes of r_1 during coordinative alteration.^[44] The chelate rings are decorated with thioether-groups binding selectively Cu(I) and Cu(II) under exclusion of other transition metals at cellular concentrations. The entrapment of copper results in a simultaneous opening of a free coordination spot at the Gd(III) ion where H₂O molecules can be exchanged. This enhances the relaxivity r_1 from 1.2–2.2 mM⁻¹s⁻¹ to 2.3–6.9 mM⁻¹s⁻¹ with severe changes in T_1 -weighted phantom MRI under clinical conditions.^[44]

Subsequently Herges *et al.* demonstrated that Ni(II) porphyrins can modulate T_1 in a range far larger than it is possible between the inner- and outer-sphere-relaxation of Gd(III).^[14,15,20,45] This is quite outstanding since this first example of Ni(II) is only switched between $S = 0$ and $S = 1$ and not $S = 2$. These porphyrin complexes are constituted with a photoswitchable group changing the coordination sphere of Ni(II) between a diamagnetic, saddleshaped, square planar coordination and a paramagnetic, square pyramidal coordination (see Scheme 2).^[45] The mechanism is known as light-driven coordination-induced spin state switch (LD-CISSS) which is given in Scheme 4 and exhibits a remarkable long-term stability although the switching itself does not affect 100% of the molecules.^[14,15,20,45]

Also in 2014 Touti *et al.* highlighted the pH-responsive CISSS of a macrocyclic iron(II) complex in H₂O.^[46] The diamagnetic iron center is coordinated by six nitrogen atoms where one belongs to an amidine ring. The amidine is protonated irreversibly by dithionate leaving a paramagnetic complex and a free coordination spot for aqueous exchange. T_1 values are reduced drastically from 3.5 s to 0.4 s by the pH-responsive CISSS although the transition is limited to pH 4.5 and is completely irreversible.^[46] Nevertheless, it is the first time an explicit trigger has been introduced which corresponds to a cellular property – in this case, the extracellular pH.

The visualization of tissue pH via *f*MRI is important since it would be an excellent method to locate tumorous tissue in a precise and non-invasive way.^[20,47] Cancer cells are known to have a higher glycolytic activity compared to healthy cells.^[48] The glycolysis results in the production of lactic acid inside the cell what is called Warburg-effect.^[49] The intracellular pH is balanced by the metabolism causing the cancer cell to excrete L-(+)-lactic acid.^[47-49] This lactic acidosis is the major reason why tumorous tissue has a lowered extracellular pH compared to healthy tissue.^[47-50] One can understand easily that smart contrast agents based on a pH-responsive CISSS would be a huge benefit for medical diagnostics.

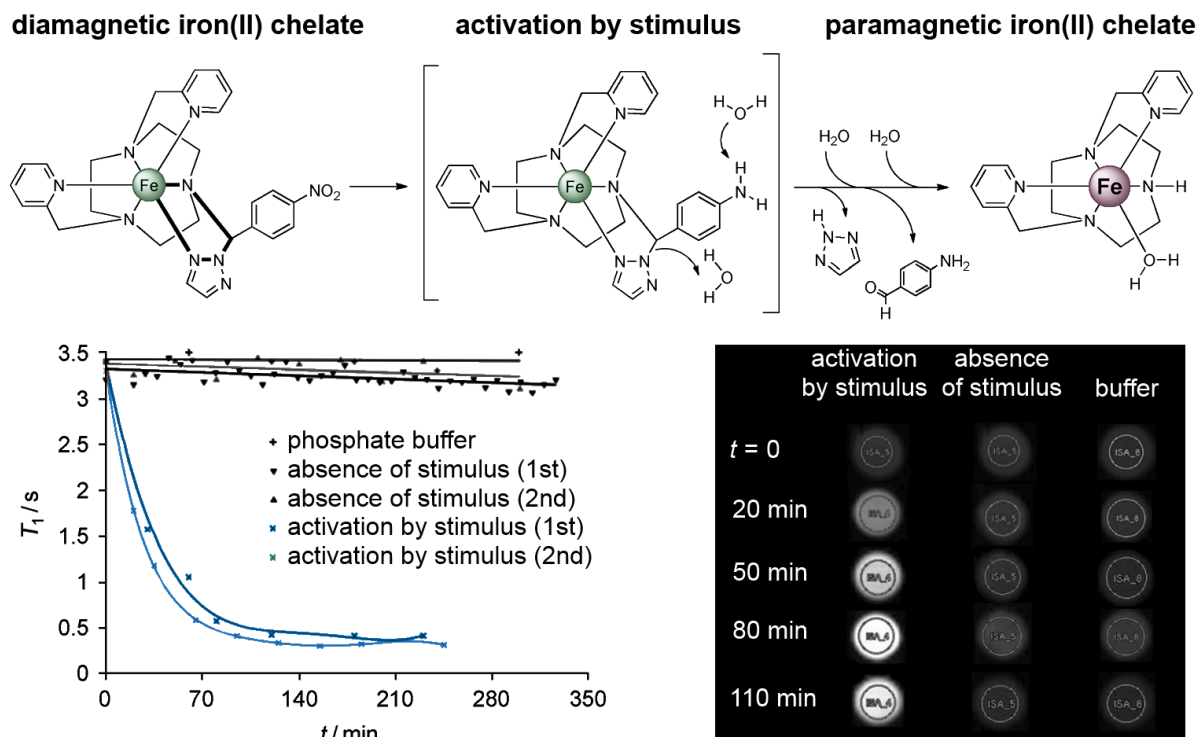


Scheme 4. Light-driven coordination-induced spin state switch (LD-CISSS) of Ni(II) porphyrin compounds with a photoswitchable azopyridine group.^[45]

Shortly after these findings the first SCO systems with 4'-(4''''-pyridyl)-1,2''':6'1''-bispyrazolylpyridine ligands were patented by Rajadurai *et al.* for their usability as *fMRI* contrast agent with temperature-response and B_0 -field-dependence.^[51] This intensified the research in this area and Jeon *et al.* presented the first two examples of SCO iron(II) systems using exchangeable protons to influence the relaxation of water protons.^[52] T -dependent SCO affects the relaxivity properties of ligand associated but exchangeable protons. Those transfer the paramagnetic enhanced relaxivity via paramagnetic cross-exchange saturation transfer (CEST) to the protons of the solvent.^[53] The corresponding Z -spectra of $[\text{Fe}(\text{Bpp})_2](\text{BF}_4)_2$ and $[\text{Fe}(\text{Me}_2\text{NPY5Me}_2)(\text{H}_2\text{O})](\text{BF}_4)_2$ show a linear dependence of the chemical proton shift with temperature.^[52] Extensive research was meanwhile conducted by Touti and Hasserodt who published an electroneutral, paramagnetic, macrocyclic iron(II) complex able to enhance MRI contrast *in vivo* by injecting 25 μL of a 25 mM aqueous solution into the legs of a mouse.^[54] Despite the fact that the chosen complex had neither SCO nor any CISSS properties the example highlights the biocompatibility and possible applicability of iron(II) systems as contrast agent.

Mn(II) was shown by Regueiro-Figueroa *et al.* to even promote higher relaxivities r_1 than Gd(III)DOTA.^[55] $\text{Mn}(\text{dpama})(\text{H}_2\text{O})_2$ and its dinuclear derivative interact with human serum albumin under coordination what changes the amount of free coordination spots. This resulted in an outstanding r_1 of $39.0 \text{ mM}^{-1}\text{s}^{-1}$ per Mn, at 20 MHz and 37 °C in nondeuterated water.^[55] The success of Mn(II) continued with the compound $[\text{Mn}(\text{PyC3A})(\text{H}_2\text{O})]^{-1}$. Gale *et al.* reduced the motion of this complex by binding it selectively to fibrin what led to r_1 values of $11 \text{ mM}^{-1}\text{s}^{-1}$ in blood plasma and under realistic clinical conditions.^[56] This is probably the most spectacular and fast-forward work considering 3d-transition-metals as smart alternative to gadolinium-based contrast agents.

A recent work of Hasserodt nicely illustrates the overall principle of CISSS in *fMRI*.^[21] A diamagnetic iron(II) macrocycle with a triazole group experiences bond cleavage upon interaction with the enzyme nitroreductase leaving a paramagnetic complex with exchangeable coordinated water. The time-dependence of this response is exponentially reducing T_1 values of phosphate buffer from 3.5 s to 0.5 s and could be also visualized by T_1 -weighted MRI monitoring of the probe as it can be seen in Scheme 5.^[21]



Scheme 5. Conversion of a diamagnetic iron(II) chelate into a paramagnetic one via a chemical stimulus. T_1 of the phosphate buffer is reduced drastically during CISSS.^[21]

A selection of the reported properties of smart contrast agents is given in Table 1. It should be stressed that the measurements are not always conducted under completely identical conditions like for example under the same field strength. Therefore, the table should be interpreted more qualitatively. It can be summarized that several transition metals are suitable and can even exceed the performance of Gd(III) systems, especially Mn(II). Furthermore it is noteworthy that a large variety of possible triggers has already been reported highlighting a broad applicability of smart contrast agents. Paramagnetic iron(II) systems do not have necessarily the highest r_1 values compared to other metals but perform best concerning the overall difference between r_{1A} and r_{1B} (see Table 1). Additionally, they are switched with the broadest variety of possible triggers and could under certain conditions perform as well as Gd(III)DOTA what shows that they should indeed be considered as smart contrast agents.^[14,15,20,41-46,51-56] Furthermore, unswitchable iron(II) complexes are already clinically applied like paramagnetic ferric ammonium citrate as Ferriseltz® from Otsuka America.^[57] It is usually given as orange-flavored oral suspension for bowel marking.^[57]

Table 1. Summary of smart CA's in literature with the r_1 values before (r_{1A}) and after (r_{1B}) the response; (a) CC = coordinative change without magnetic change; (b) PB = phosphate buffer, BP = blood plasma; (c) r_1 was calculated from c when only T_1 was given.

Metal	Trigger ^(a)	Solvent ^(b)	r_{1A} [$\text{mM}^{-1}\text{s}^{-1}$] ^(c)	r_{1B} [$\text{mM}^{-1}\text{s}^{-1}$] ^(c)	Factor	Lit.
Fe(II)	Nitroreductase (CISSS)	PB	0.01	0.05	5.0	[21]
Fe(II)	Related complexes	H ₂ O	0.18	0.57	3.2	[43]
Fe(II)	Temperature (SCO)	D ₂ O	0.041	0.082	2.0	[41]
Fe(II)	Dithionite (CISSS)	H ₂ O	0.074	0.625	8.4	[46]
Fe(II)	Related complexes	PB	0.17	1.29	7.6	[54]
Mn(II)	Fibrin binding (CC)	BP	8.5	13.5	1.6	[56]
Mn(II)	Albumin binding (CC)	H ₂ O	12.2	39.0	3.2	[55]
Mn(II)	Albumin binding (CC)	H ₂ O	8.9	12.2	1.4	[55]
Ni(II)	LD-CISSS	DMSO	0.045	0.159	3.5	[45]
Ni(II)	LD-CISSS	DMSO	0.029	0.155	5.3	[45]
Ni(II)	LD-CISSS	DMSO	0.018	0.121	6.7	[45]
Gd(III)	β -Glucuronidase (CC)	H ₂ O	3.90	4.75	1.2	[21]
Gd(III)	Cu(II) binding (CC)	PB	1.5	6.9	4.6	[44]
Gd(III)	Cu(II) binding (CC)	PB	2.2	3.8	1.7	[44]

1.3 Zeolite structures and properties

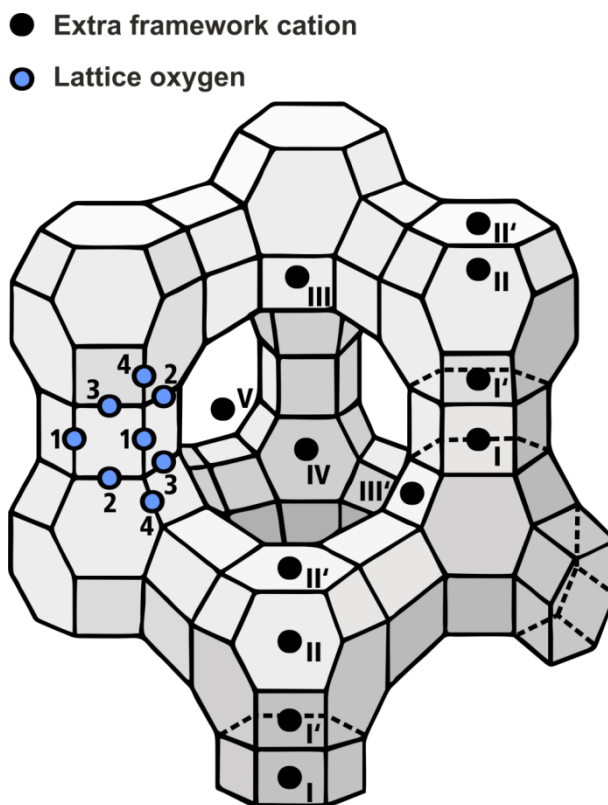
Zeolites are a special class of mesoporous materials which consist basically out of aluminum, silicon and oxygen.^[58] Additionally, hydrogen and different counter cations belong to the composition.^[58] These crystalline, hydrated aluminum silicates can be found in nature for example as chabazite or clinoptilite but are also produced synthetically.^[59] As a result of different compositions a variety of 232 structures is known which are always built up out of AlO_4^- and SiO_4 -tetrahedrons.^[60] The aluminum is consequently bridged via oxygen to the silicon according to Loewenstein's rule.^[61] Aluminum has a formal charge of three and is bonded to two oxygen atoms what gives the zeolite framework a negative charge.^[58] This negative charge is compensated by different alkali and alkaline earth counter cations which

can be e.g. Na^+ , K^+ , Ca^{2+} or Mg^{2+} . Those are normally solvated because zeolites are likely to incorporate water molecules.^[62] Therefore they are used primarily for water and gas purification, adsorption and catalysis.^[58]

An industrially very important zeolite with special applications is zeolite Y which is named NaY when Na^+ is present as a counter cation. It's the analogue to the faujasite found in nature and was first used in 1959 by *Union Carbide* as part of catalyst.^[63] Its general composition is $\text{Na}_{58}[(\text{AlO}_2)_{58}(\text{SiO}_2)_{134}] \cdot 240 \text{H}_2\text{O}$ and the H_2O content may vary.^[64] The lattice is formed by sodalite cages which are linked by hexagonal prisms creating a large void called supercage.^[58,64] Zeolite X has a similar architecture that ought not to be mixed up with the zeolite A whose sodalite cages are linked by cubes.^[65] Both of them belong to the aluminum-rich zeolites with a Si/Al-ratio ≈ 1 . Zeolite Y has a Si/Al-ratio between 3 and 5 and a mesoporous structure which consists out of cavities interconnected by smaller channels.^[66] The cavities have a diameter of 12 \AA while the small channels have a diameter of 7.4 \AA .^[67] Overall a cubic unit cell (8 supercages) with a length of 24.7 \AA is realized belonging to the space group $Fd3m$.^[67] The specific shape and the perpendicular arrangement of the pores permits an incorporation of other molecules or complexes inside the voids.^[68] Especially for complexes this is very interesting because the synthesis can be done in such a way that the product is formed inside and cannot leave the cage again.^[69] Such systems are called ship-in-a-bottle complexes in analogy to the toy ships inside of small bottles which catch attention because one is wondering how they got inside. This one-way street accessibility can be used also for shape-selective synthesis what means that the sterical configuration of a product is determined by the limiting space of the voids.^[70]

In Scheme 6 the traditional schematic view of a faujasite-type zeolite together with the usually described cation location and oxygen bridging is given.^[67,71] Sodium cations can occupy all of these sites.^[67,71] Site I indicates cations inside of the hexagonal prism while I' are facing position I from the inside of the sodalite cages. The sites II and II' are also located there but are in contrast not interconnecting. III and III' are cations at the inner walls of the supercage. Both of them are known to have a higher potential energy than all others.^[67,71] Consequently sites I, I' and II are occupied unexceptional at a silicon-aluminum-ratio below 2.^[67,71] Regarding the complete unit cell site I has a multiplicity of 16, I' and II have one of 32. Site III has with 48 the highest multiplicity. Position IV represents the center of the pseudo cell (one supercage and one sodalite cage) while position V is located inside of the 12-

membered ring. When the cations are solvated they can move nearly freely through the whole zeolite framework.^[71]



Scheme 6. Schematic representation of a dehydrated faujasite-type zeolite. The positions of oxygen framework atoms are indicated in blue while the different counter cation sites are illustrated as black dots. The center of the supercage is represented by position IV.

The nanovoids of faujasite-type zeolites can be accessed through channels which have a much smaller diameter. This fact enables it to incorporate other molecules or complexes inside the voids.^[68,69] Fundamental works about the effects of small confinement on transition metal complexes have been carried out by Lunsford *et al.*^[72] Based on the knowledge of cobalt, copper and ruthenium complexes entrapped in NaY he and his co-workers were also the first ones to study tris(2,2'-bipyridine)iron(II) inside the supercage. Their first work on this appeared 1981 where they discussed samples prepared by an iron exchange.^[72] A sample gained by a wet impregnation technique showed a powder diffraction pattern different from the bare zeolite but was not analyzed further although Lunsford has described in detail in

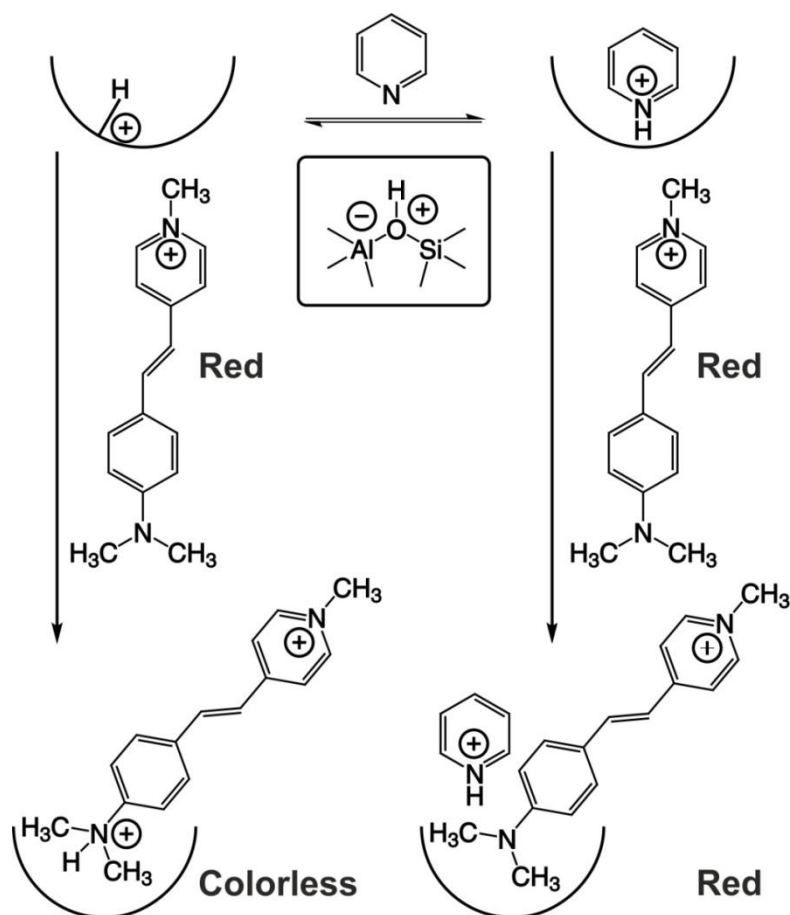
previous studies that wet impregnation can lead to ship-in-a-bottle systems with relatively high loadings.^[73,74] In the other samples complex formation was confirmed by X-ray diffraction, EPR, reflective UV-Vis and Mössbauer spectroscopy. Alongside the six-coordinated complex, uncoordinated iron was identified which was for some samples found to undergo strong π -bridging.^[72]

Petrera *et al.* conducted an extensive Mössbauer study of iron containing zeolites for which they used only a contact solution (wet impregnation technique).^[75] By this they synthesized samples with different loadings of phenantroline and bipyridine complexes and proved that not only iron exchange but also impregnation can incorporate complexes into zeolites. They recorded various spectra for evacuated or air-exposed samples and also for samples which were evacuated between 300 °C and 400 °C in order to characterize decomposition products. Incorporation of iron complexes results in basically two doublets. One with a large ΔE_Q belongs to paramagnetic iron(II) inside the sodalite cages while the one with a small ΔE_Q belongs to complexes in the supercages.^[75] In 1993 Umemura *et al.* claimed to have found evidence for the strong distortion of those complexes upon small confinement based on an uncommonly large quadrupole splitting.^[76] This paper was tackled harshly by Vankó *et al.* who attributed the findings to a false assignment of the Mössbauer doublets.^[77] Umemura prepared the samples by iron exchange and wanted to wash out uncomplexed iron with a saline solution but this could not be followed in the Mössbauer spectra.^[76] Vankó solves this problem with a lanthanum-blocking and claims that washing with saline solutions leads to a decomposition of the incorporated complexes.^[77] This highlights the differences between the used incorporation methods and that zeolite hybrids need to be analyzed precisely to rule out the presence of unwanted side products like paramagnetic iron in the sodalite cages or hexaquo iron(II) complexes in the supercage.

The most recent findings were published by Yamashita *et al.* who used also an iron exchange procedure to prepare a cation varied zeolite Y.^[62,78] In this sample several iron species must be present but interestingly a strong catalytic activity for the oxidation of α -methyl styrene upon photo-irradiation is found. In 2008, a noteworthy DFT-study appeared which calculated bond lengths and all Mössbauer parameters for the LS- and HS-state of tris(2,2'-bipyridine)iron(II) embedded in zeolite Y and predicts a destabilization of the HS state with regard to the LS state.^[79]

Although iron(II) complexes have been incorporated excessively into zeolites only a handful of publications can be found dealing with the effects of small confinement on the spin state of iron(II) complexes. The first was conducted by Mizuno and Lunsford in 1983 which observed a spin equilibrium for tris(2,2-bipyridine)cobalt(II) entrapped in potassium exchanged zeolite Y in an EPR study. Such a behavior was neither observed in the solid state nor in solution for this pure LS ($S = 0$) compound yet.^[80] The metal cores of the entrapped complex are completely in the LS state till 80 K and then undergo an abrupt transition. At 100 K more than 50% of the centers are in the HS state while at room temperature solely the HS state is found. The transition is very abrupt and both researchers argue with the sterical limitations inside the zeolite, stabilizing the more space-saving LS state. The study was repeated by Tiwary and Vasuvedan in 1997 who synthesized a similar compound and made the first SQUID measurements.^[81] The magnetic susceptibility shows an extremely gradual but truly T -dependent behavior. In contrast to Mizuno and Lunsford which argue with the sterical restrictions, Tiwary and Vasuvedan argue with the highly symmetrical void geometry. This is part of a second publication which followed the first shortly and adds a computational study.^[82] A completely intramolecular origin of the temperature-dependent magnetic susceptibility is claimed but it is highly interesting that also a color change upon humidity exposure is observed.^[81,82] This noteworthy feature is neglected and will be also part of the following study.

Umemura *et al.* showed a spin transition occurring for tris[(2-(aminomethyl)pyridine]iron(II).^[83] The latest study dealing with $[\text{Fe}(\text{pyim})_3]^{2+}$ encapsulated at NaY was published in 2003 by Vijayalakshmi and finds a dynamic spin equilibrium.^[84] Another exciting feature is shown by Sojka and Witkowski that noticed a reversible coordination-induced spin state switch caused by small coordinative changes of carbonmonoxide at cobalt exchanged ZSM-5.^[85] All of this examples show that the incorporation of iron(II) complexes into zeolites can lead to unexpected magnetic properties and that the spin state can be even modulated via CISSS under small confinement.



Scheme 7. Acid-base-reaction of trans-4-[4-(dimethylamino)styryl]-1-methylpyridinium iodide with intrazeolitic Brønsted acids during and without the presence of the stronger base pyridine.^[88]

Another chemical characteristic that is often determining the properties of a zeolite is their Brønsted acidity. From their bare formula $\text{Na}_{58}[(\text{AlO}_2)_{58}(\text{SiO}_2)_{134}] \cdot 240 \text{H}_2\text{O}$ one would not expect this but Brønsted acids are present in every zeolite.^[58,86] They originate from a proton attached to an oxygen bridge between aluminum and silicon.^[58,86] Those protons are known for their involvement in catalysis and can interact easily with bases inside of the cavities.^[87] An example of such interaction is given in Scheme 7.^[88] Trans-4-[4-(dimethylamino)-styryl]-1-methylpyridinium iodide is a red dye which can be used to titrate a zeolite.^[89] The intrazeolitic protons undergo an acid-base-reaction with the dye that becomes colorless upon proton attachment what can be followed by a bathochromic shift of the π - π^* -transition. When the zeolite is saturated priorly with pyridine that acts in this case as the stronger base the dye stays colored since the protons are now associated with the pyridine.^[88] In the study of

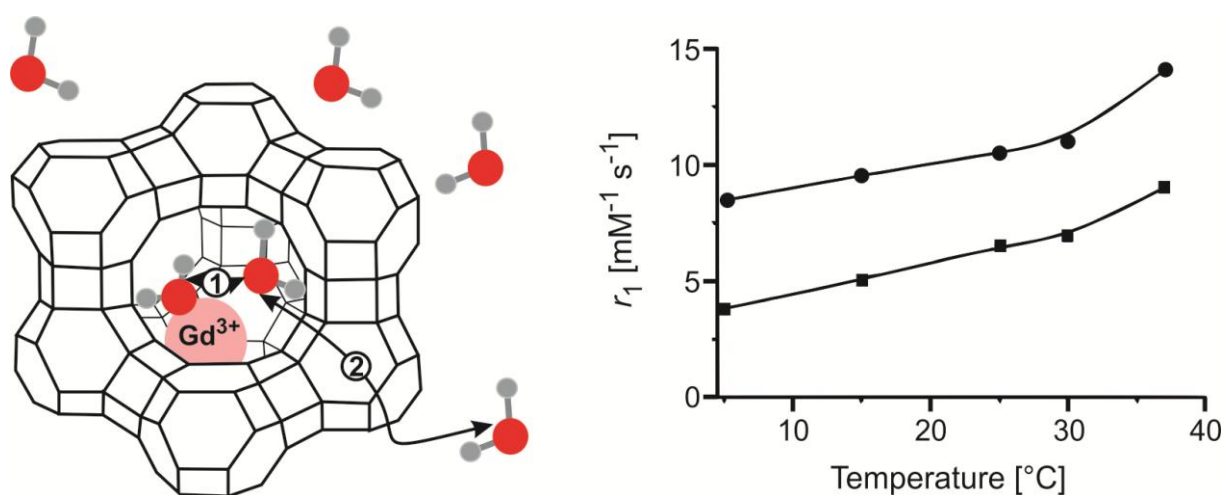
Thomas and Ramamurthy around one proton appears in 15 supercages. Brønsted acids should always be considered when discussing the properties of a zeolite hybrid material.

1.4 Zeolites as smart contrast agents

Gd(III) is not only used as chelate complex for MRI. Also contrast agents exist where zeolites are exchanged with Gd(III) and are indeed clinically used and approved by the Federal Drug Administration (FDA).^[90] Such an example is Gadolite® which is basically Gd(III) exchanged zeolite Y.^[91] It is applied as an oral suspension to map the gastrointestinal system with more precision. Usually traces of bowel fluid cause false signals associated with tumorous tissue what is significantly reduced when Gadolite® is given.^[92]

Therefore it is not surprising that several publications are dealing with zeolite immobilized contrast agents. Bresinska *et al.* characterized the effects of loading, concentration and pH of GdNaY on Δr_1 of water protons.^[93] A remarkable finding is that Δr_1 varies between $30 \text{ mM}^{-1}\text{s}^{-1}$ (1 wt% Gd) and $4 \text{ mM}^{-1}\text{s}^{-1}$ (8 wt% Gd) inversely to the Gd loading of the zeolite what can be traced back to the reduced water exchange at high Gd(III) loadings. The low loaded zeolites even exceed Δr_1 of free Gd(III) ($\Delta r_1 = 10 \text{ mM}^{-1}\text{s}^{-1}$) in aqueous solution by 300% what is a result of the macromolecular effect of the zeolite.^[93] Furthermore they demonstrate that the movement of Gd(III) from position V to II in the supercage leads to an increased water exchange. A similar study from Platas-Iglesias *et al.* describes stable suspensions of GdNaY nanoparticles which gained Δr_1 values up to $37.7 \text{ mM}^{-1}\text{s}^{-1}$ and explains the high values by simplifying GdNaY as concentrated aqueous solution of Gd(III).^[94] A very detailed publication from Csajbók *et al.* in 2015 deals with the effects of dealumination and calcinations on the relaxivity efficiency of GdNaY.^[95] A partial destruction of the zeolite framework by acid dealumination is found to raise Δr_1 as a result of higher water mobility. In contrast, calcinations lead to a lowered Δr_1 since Gd(III) moves to the sodalite cages (position II) where it is inaccessible for water molecules.^[95] A similar effect is observed when GdNaY is compared to GdNaA where diffusion is limited due to the smaller pore size. This diffusion could be enhanced by raising the temperature what is nicely illustrated via rise in Δr_1 what can be seen in Scheme 8 together with the two dominating water exchange mechanisms in zeolites.^[94,95]

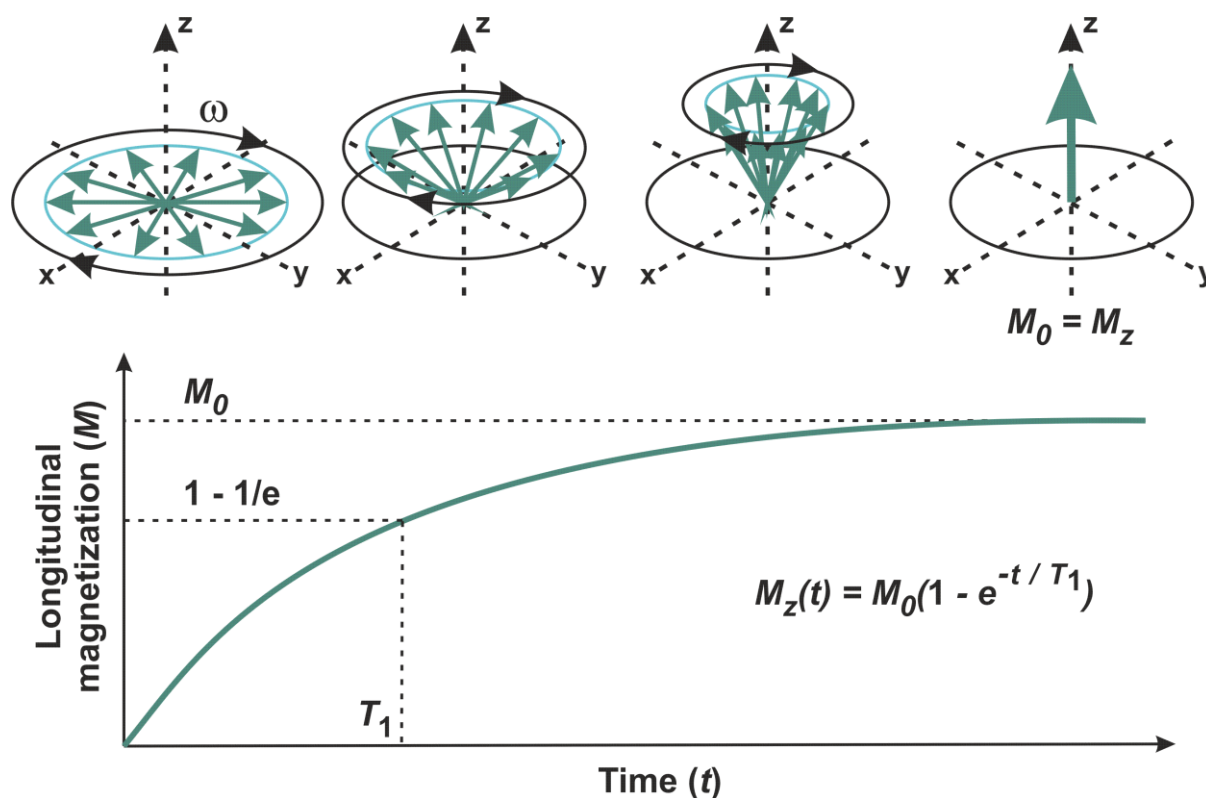
More advanced particles were prepared by Tsovalas *et al.* who used nanocontainers of zeolite L decorated with Gd(III)DOTA and a fluorescent label inside the porous structure.^[96] Since L-type zeolite features very large pores water diffusion is not limited and a significant temperature and thus pH-response of the relaxivity can be observed. Δr_1 could be raised up to $39 \text{ mM}^{-1}\text{s}^{-1}$ at $60 \text{ }^\circ\text{C}$ in aqueous solution.^[96] Calculated down to one particle a Δr_1 of $11000 \text{ mM}^{-1}\text{s}^{-1}$ is found.^[96] The pH-dependence of this system has been researched even more intensively by Zhang *et al.* who modeled the fast prototropic exchange and decrease Δr_1 from $32 \text{ mM}^{-1}\text{s}^{-1}$ to $7 \text{ mM}^{-1}\text{s}^{-1}$ when raising the pH from pH 4 to pH 9.^[97] Therefore we are justified to believe that zeolites belong to an exciting class of materials, which are well suited as biocompatible carriers for contrast agents.



Scheme 8: Two-step mechanism of water exchange in GdNaY. Temperature dependent relaxivity is observed for GdNaA as a result of diffusion control by the water exchange; Si/Al-ratio = 10 (squares), Si/Al-ratio = 1.5 (circles).^[94,95]

1.5 Field-cycling ^1H -NMR relaxometry

Field-cycling ^1H -NMR relaxometry is basically a time-resolved nuclear magnetic resonance spectroscopy experiment and is not only limited to ^1H nuclei but to all nuclei whose nuclear spin I is not zero in the ground state.^[98] A nuclear spin I unequal to zero always results in an angular momentum L which is described by the equation $|L| = \hbar\sqrt{I(I+1)}$.^[98,99] The component along the magnetic field B_0 is then $L_z = I_z \hbar = m \hbar$ with discrete values of $I_z = m = -I, -I+1, \dots, I-1, I$.^[98,99] Like all other rotations of an electrically charged object the gyration of the nucleus results likewise in a magnetic moment $\mu = \gamma L$ respectively $\mu_z = \gamma L_z$.^[101] The macroscopic magnetization M_0 can then be described as $M_0 = (\chi_0 B_0) / \mu_0$ which obeys the Curie-law $\chi_0 = C / T$.^[98,100]



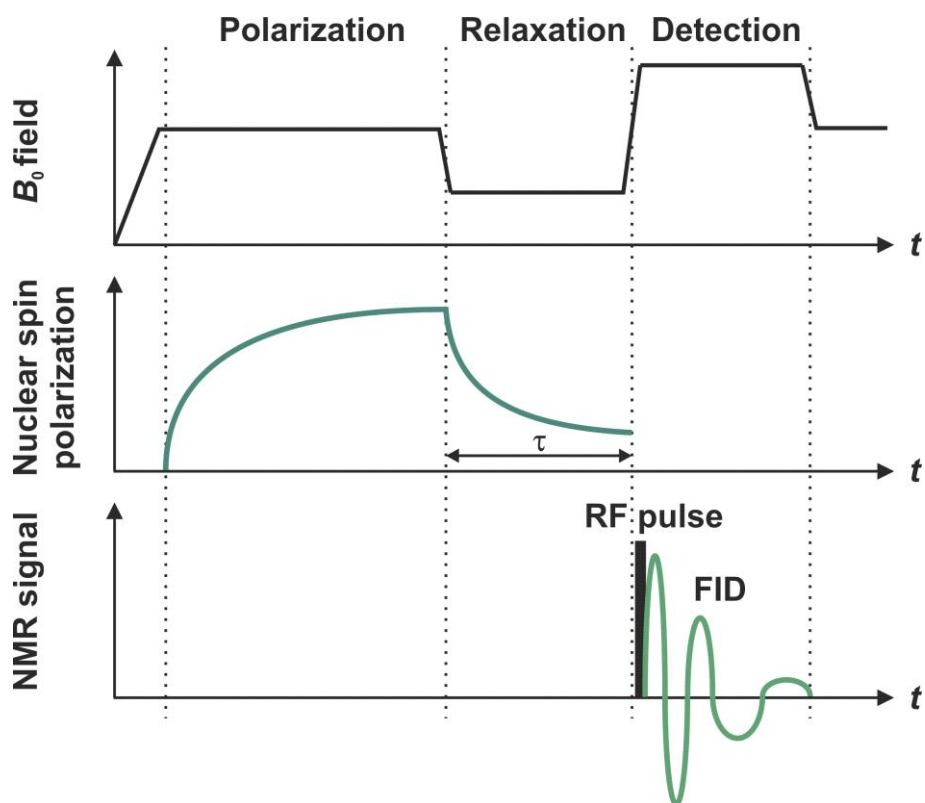
Scheme 9. Time evolution $M_z(t)$ of the macroscopic magnetization M_0 after a 90° pulse in an external magnetic field B_0 .^[101]

The equilibrium magnetization M_0 in an external magnetic field with B_0 follows a Boltzmann-distribution and is by convention given as the z -component of the magnetization.^[102] This means the magnetization in z -direction is described by $M_Z = |M| \cos \alpha$ and is therefore called the longitudinal magnetization.^[24,103] This equilibrium magnetization can be disturbed by several types of radio frequency pulses. A 90° pulse can switch M into the x - y -plane what will lead to $M_Z = 0$.^[103] The system will relax back into its equilibrium condition what can be seen in Scheme 9.^[101] The time the nucleus needs to relax back into its initial state where $M_0 = M_Z$ is called relaxation time.^[101] The relaxation proceeds exponentially with the equation given in Scheme 9.^[101] The time t when $1 - 1/e$ nuclei have relaxed back into their initial state is called longitudinal relaxation time T_1 .^[101]

T_1 is a characteristic property that provides information about all interactions with surrounding atoms. Therefore, it is also referred to as spin-lattice relaxation although the lattice can describe interactions with a liquid as well. T_1 values can be used to characterize porous systems or diffusion effects, analyze rotational dynamics, identify paramagnetic substances or determine crystalline or amorphous contributions.^[104]

Essentially, a FC ^1H -NMR experiment consists of three separated parts as depicted in Scheme 10.^[105] The initial step is a pre-polarization of the sample generating an equilibrated Curie magnetization in z -direction which is used to push the general signal intensity.^[105] After the pre-polarization the sample starts immediately to relax back into its initial state what is happening under an adjustable relaxation field that can be equal or unequal to zero.^[105] This field is maintained during the whole evolution time τ . The magnetization in the x - y -plane is then investigated by applying a radio-frequency-pulse of $\pi/2$ which generates a free induction decay (FID) that can be now analyzed via a detection field and converted by Fourier-transformation.^[105]

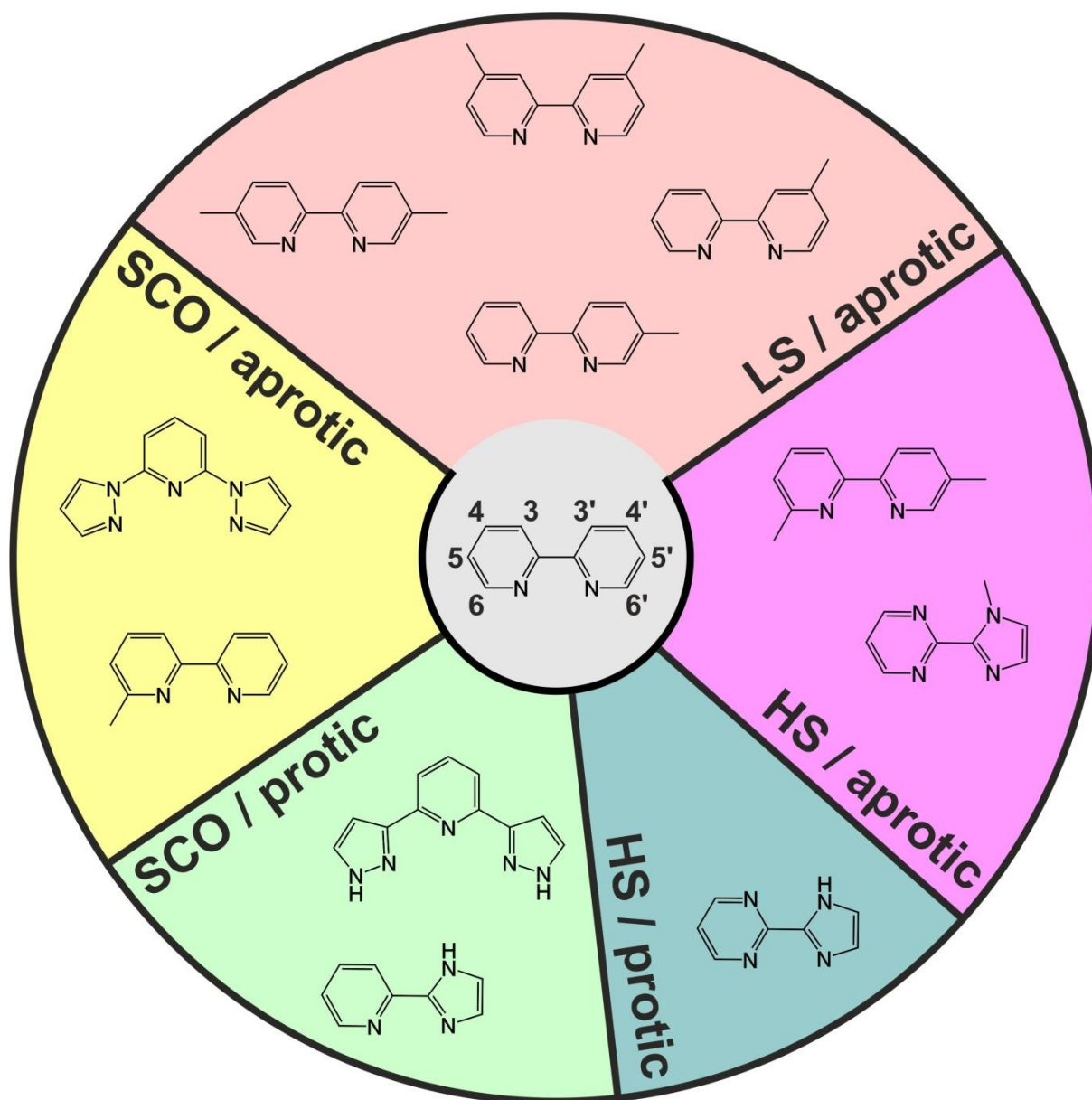
The electronic switching times between the fields are usually ultra-short and around $150 \mu\text{s}$.^[101,105] The whole sequence is then repeated what is called field-cycle but just after enough time t has passed to bring τ completely back to zero.^[101,105] In further cycles also the Larmor frequency ν can be varied. The corresponding data can be displayed as nuclear magnetic resonance dispersion (NMRD) profile providing further information about molecular dynamics and gyration.^[106]



Scheme 10. General three-step measurement mechanism during one field-cycle of a common FC ^1H -NMR relaxometer consisting out of pre-polarization, relaxation of the sample and detection of the FID.^[105]

Depending on the instrument, FC ^1H -NMR can be conducted between several kHz and up to 100 MHz.^[103] The T_1 value of a sample depends in general on the state of aggregation, concentration, viscosity, temperature, cofactor interactions, or paramagnetic impurities.^[104] FC ^1H -NMR is today used in various fields to analyze proteins, shelf-life, oil, gas, liquid crystals and to ensure their quality.^[104] In this work it plays an important role to analyze pH-responsive magnetism in solution and the corresponding molecular dynamics.

1.6 Properties and numbering of the used ligand systems



Scheme 11. Ligand systems used in this work which all can be derived from 2,2'-bipyridine due to a twistable bond connecting the aromatic ring systems with the nitrogen donor atoms. All ligands can coordinate iron(II) in an octahedral fashion and yield either LS, HS or SCO complexes. The spin state refers to the corresponding chloride salts of iron(II). Furthermore, the ligands are either aprotic or protic. The protic ligands exchange protons in aqueous solution.

The ligand systems used in this work can be derived from the 2,2'-bipyridine as it can be seen in Scheme 11. All of the ligands possess *N*-donor atoms able to coordinate iron since they are bridged via two other atoms that can either be carbon or also nitrogen. Furthermore, all *N*-donor atoms are part of an aromatic ring system and rotatable towards each other. The different types of substituents generate octahedral complexes of iron(II) chloride salts which can be either LS, HS or SCO complexes. The ligand system was chosen due to the rotatable backbone which should allow a controlled interaction with protic acids. Furthermore, additional nitrogen bases and exchangeable protons can influence the behavior in aqueous solution significantly. The aromatic rings are either pyridines, pyrimidines, imidazoles or methyl-imidazoles.

The general proton numbering of 2,2'-bipyridine will be consequently used throughout this work and is applied to the ligand as well as the complex and the substituted 2,2'-bipyridines and the derived complexes. 6, 5, 4 and 3 mark the protons on one, while 6', 5', 4' and 3' mark the protons on the other pyridyl ring. If a * is used (6*, 5*, 4*, 3*, 6'*, 5'*, 4'*, 3'*) it is indicative for the protonated form of the complex or the ligand and marks the corresponding proton.

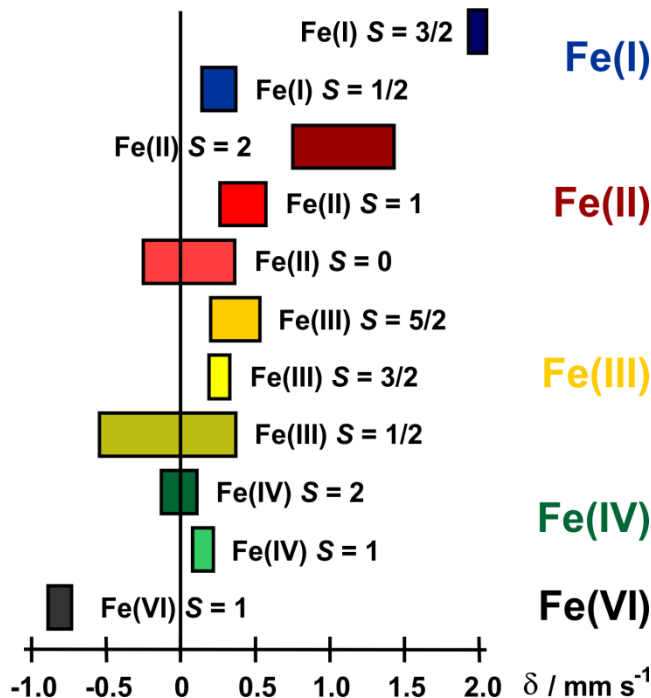
1.7 Instrumental methods

The basic principle discussed in this work is the exploitation of small coordination changes in order to generate differences in the ligand field splitting experienced by the iron(II) center leading to an alteration of the spin pairing. Therefore a number of methods are used, complementing each other since one method alone cannot generate an entire picture on the molecular level. For example, it is possible to observe magnetic changes via SQUID magnetometry but not the mechanism underneath. For this information $^1\text{H-NMR}$ or UV-Vis spectroscopy can be instrumentalized. Nevertheless, all three methods fail to describe physical effects of the complex coordination on solvent molecules like the longitudinal molar relaxivity for which FC $^1\text{H-NMR}$ relaxometry needs to be used. While the incorporation of complex molecules into the cages of zeolites can be analyzed via powder diffraction, SEM/EDX or IR spectroscopy, none of these methods is able to determine the selectivity or completeness of the incorporation. For this Mössbauer spectroscopy or magnetic measurements need to be used. Moreover, the physical condition plays a very important role. On the one hand electronic properties of complexes can be measured in solution with UV-Vis spectroscopy while the electronic transitions of the corresponding hybrid materials can only be analyzed with diffuse reflectance spectroscopy. Hence, all of the following methods were necessary to understand the true nature of the compounds on a molecular level:

pH-Determination is one of the most fundamental parts of this work and therefore significant importance was attached to its precise measurement. In this work solutions with a discrete pH-value were prepared, measured and then used consequently throughout the whole experimental phase. pH-dependent measurements in solution were done with respect to the magnetic behavior, the electronic and optical properties, the proton nuclear magnetic resonance, the relaxivity properties of the water molecules and the integrity of zeolite nanoparticles.

^{57}Fe Mössbauer spectroscopy is an effective method to determine the parameters of iron species in a sample like oxidation state, asymmetry, spin state and the general chemical environment of the metal core and is therefore complementing nicely SQUID magnetometry. The recoilless nuclear resonance absorption of X-rays by the respective core has three

characteristic parameters originating from three hyperfine interactions. Electric monopole interactions between protons of the nucleus and close s-electrons are reflected by the isomer shift δ . Site symmetry as well as the spin state determine the homogeneity of the electrical field recognized by the nuclear quadrupole moment. This electric quadrupole interaction is mirrored by the observable quadrupole splitting ΔE_Q . Magnetic dipole interactions provide information about the magnetic properties. In this work Mössbauer spectroscopy was used to characterize bulk complexes but was even more important to characterize zeolite hybrids. Due to the incorporation of the iron complexes they are invisible for several techniques making the composition often only inadequately describable. In the case of Mössbauer spectroscopy small confinement becomes an advantage since thermal motion and agility of the nuclei are reduced drastically inside the supercages. This allows determining the positions occupied by iron inside the zeolite (supercage or sodalite cages), completeness of complexation, presence of oxidized species or decomposition products and effects of small confinement on the complex symmetry even at very low complex loadings. Commonly observed isomer shift values are displayed in the following Scheme 12.^[107]



Scheme 12. Isomer shifts δ in mm/s of frequently observable oxidation and spin states in iron compounds. The isomer shift values are reported with respect to α -Fe as a reference at room temperature.^[107]

Magnetic susceptibility measurements are the most frequently conducted measurements in this work. It is the key method to gather magnetic data. The magnetism of iron(II) bulk complexes can be precisely determined in a temperature- or field-dependent fashion. This gives information about the oxidation and spin state. In the literature the main part of all described magnetometry is done in the solid state while measurements in solution are relatively scarce. This is probably due to the elaborate preparation, uncommon handling, endangerment of the magnetometer itself and a difficult evaluation. Here, several complexes are investigated in detail for the first time in solution and especially at different pH-values. This gives a unique insight into a so far undescribed mechanism of pH-responsive magnetism and how the total spin S can differ between the solid to the solubilized state. I hope this work will encourage others to determine more often magnetic properties also in solution and not only in the solid state.

^1H -NMR spectroscopy can deliver unique insights into possible coordination modes of a ligand around a metal center not only in solution but also at different pH-values. In this study it is used to locate complex protonation, small coordination changes caused by this protonation and induced alterations of the magnetic state indicated by line broadening and a paramagnetic shift of the signals especially analyzed via temperature dependent ^1H -NMR spectroscopy. Furthermore integral intensity is used to calculate the ratio of the protonated species against the original complex and to calculate the pK_A values of the complexes allowing a comparison of the protonation ability of different complexes.

MAS solid state NMR can be used to analyze compositions and conditions of insoluble samples. This is especially valuable for zeolites. ^1H -NMR locates Brønsted acids, Lewis acids and complex molecules inside the zeolite. In combination with inversion-recovery experiments longitudinal relaxation times of intrazeolitic water are measured at room and elevated temperatures. From this, conclusions about the magnetic state of incorporated complexes can be drawn. ^{23}Na , ^{27}Al and ^{29}Si MAS NMR are used to characterize the zeolite host, its site occupation, integrity and extraframework cations.

Field-cycling (FC) $^1\text{H-NMR}$ relaxometry of liquids is a method basically mirroring a MRI experiment. Its principals are based on spin relaxation and classical nuclear magnetic resonance spectroscopy. With this method molar relaxivities Δr_1 of aqueous complex solutions are measured at different pH. These values yield important information to evaluate the molecular dynamics involved during pH-induced coordination changes respectively the pH-responsive magnetism caused by unoccupied coordination spots at the metal center and to test if the respective complexes and underlying mechanism can serve as the basis for pH-responsive contrast agents. The molar relaxivity Δr_1 can be seen as indicative for how well a contrast agent performs.

Ultraviolet-Visible (UV-Vis) spectroscopy relates directly to the color of a compound, a property literally visible to everyone. Colors originate from the absorption of photons with specific energies respectively wavelengths by electrons. The reflected photons which are not absorbed result in the color we see. Especially transition metal complexes have several possible and intense transitions which are subjected to selection rules influenced by coordination geometry, spin state, oxidation number and the type of orbitals involved. Bipyridine-like iron(II) complexes undergo characteristic d-d-, π - π^* - and MLCT-transitions. Because of this, UV-Vis spectroscopy is a decent method to study those complexes and pH-related coordination changes in solution giving a direct glimpse into the electronic properties of the complex.

Diffuse Kubelka-Munk reflectance spectroscopy is an excellent and one of the only methods to study the electronic transitions of solids, wet powders and other samples which may not be solubilized, in the ultra-violet and visible region. Zeolites (and other hybrid materials) can be characterized with respect to effects of small confinement or solvation on electronic transitions of incorporated complexes, oxidation or decomposition products and the completeness of coordination inside the host.

Temperature dependent reflectivity measurements done in Bordeaux supplement the information gathered through diffuse reflectance spectra from the Cary 300 UV-Vis since it is not equipped with a temperature control. It allows studying temperature dependent changes of

the electronic properties by summarizing the whole light spectrum and should therefore be always done together with diffuse reflectance spectroscopy.

Infrared spectra recorded via attenuated total reflectance are based on evanescent waves and provide therefore mostly information about the surface of a sample. The zeolite host shields the complexes from the IR-waves and makes all spectra consequently only surface spectra. Nevertheless, the presence of bulk material on the surface and structural integrity of the host can be studied and is therefore complementing X-ray powder diffraction.

Elemental analysis is essential for validating the general composition of a synthesized compound. During this work it was found that also hybrid materials can be characterized with it to certain extent. Impregnated zeolites can be measured since most of the complexes are located in supercages near the particle surface and can be burned completely. Since nitrogen is only present in the ligand and not in the used solvent or host its percentage is characteristic for the prevailing coordination. In contrast it is not possible to analyze iron exchanged particles since the combustion proceeds incompletely.

Atomic absorption spectroscopy allows a qualitative and quantitative analysis of a samples elemental composition by evaluating the characteristic line spectrum of an element and is therefore complementing elemental analysis. It played a crucial role to determine the iron percentages and site occupation of the composites which is quantitatively merely possible with other methods.

X-Ray powder diffractograms are ideal to study the homogeneity of zeolite hybrids since crystalline bulk material inside or outside the cages will give characteristic reflexes. In contrast, incorporated complexes change only the intensities of the reflexes characteristic for the host material. Exchange or blocking modifications of the host can also be analyzed. Furthermore spin state changes of bulk complexes result often in structural changes altering the reflex fingerprint.

Mass spectroscopy is in our case only essential for analyzing the synthesized ligands since hybrid materials can't be measured and in the spectra of the homoleptic iron complexes itself solely the ligand can be seen.

Scanning electron microscopy does not only give micrographs on which the extent, shape, integrity or agglomeration of zeolite microparticles and nanoparticles can be evaluated. Furthermore surface depositions caused by calcinations, impregnations or ion exchanges can be detected.

Energy dispersive X-ray spectroscopy has a limited penetration depth and is therefore determining surface properties similar to the evanescent-wave IR which results it is extending. It is used to determine the composition of the zeolite surface with respect to purity, completeness of complex incorporation and decomposition as well as the iron percentages.

Thermogravimetric analysis was used to analyze the solvent loss at elevated temperatures for bulk complexes as well as hybrid materials. For the former the solvent loss can influence the spin state of the iron center while for the latter it changes the conditions inside of the intrazeolitic channels like the intrazeolitic pH significantly.

X-ray crystallography determines bond lengths and angles between atoms and was used to generally characterize ligands and bulk complexes.

Dynamic light scattering was essential to study zeolite nanoparticles in suspension and provided information about their stability at different pH values and possible agglomeration. Comparison with SEM makes the size determination very exact and reliable.

1.8 Motivation

The invention of MRI has altered the routine of medical diagnostics profoundly.^[22] Its anatomical resolution and non-invasiveness were honored with the Nobel Prize in physiology and medicine and helped to understand structure and function of organs and tissue.^[108] MRI relies on the principles of nuclear magnetic resonance and generates therefore images out of proton relaxation.^[22-26] The direct ambience of water molecules in the human body influences this relaxation and allows the exploitation for imaging purposes.^[23] Since the differences are rather small substances are used to enhance the contrast ratio.^[22] It was already explained that gadolinium CA's are complexed by chelate ligands due to their ultra-high toxicity. MRI alone is responsible for several tons of gadolinium waste per year and is known to accumulate in the brain and cause nephrogenic systemic fibrosis.^[20,31] This is one fact beside the global cancer epidemic which enlarges the demand for a new type of contrast agent. Cancer is already today one of the most common causes of mortality.^[109] Smart contrast agents are a considerably promising approach to detect cancer cells *in vivo*. Such a system should alter the proton relaxation significantly around tumorous tissue.^[20,22] This would allow the direct imaging of tumors at a very early stage but requires high selectivity. Therefore, specific properties of the affected tissue need to be exploited.^[110] Cancer cells have a higher glycolytic activity than healthy cells what lowers the pH as a result of a higher lactic acid concentration. This is known as Warburg Effect and can serve as basis for *fMRI*.^[111] A contrast agent able to display the pH by proton-triggered relaxation differences would be a huge benefit for medical diagnostics.^[112]

The most reasonable class for this type of application are iron(II) complexes which are well known for their manifold magnetic properties.^[1,8,9] They can be switched between the diamagnetic and the paramagnetic state via a CISSS triggered by pH when intelligent complex design is applied. Additionally, iron(II) is a cheap and nontoxic Gd(III) alternative and is already clinically used as contrast agent for example in Ferrisalz®.^[57] This is a crucial economic advantage since almost 80% of the increase of all cancer deaths will happen in less developed countries within the next 10 years. Expensive lanthanide-based systems are a doubtless barrier for proper cancer treatment.^[109] Efforts to use SCO iron(II) complexes as paramagnetic chemical exchange saturation transfer (PARACEST) contrast agent for temperature detection were already successful.^[52,113] Nevertheless, they exhibit an unneglectable disadvantage – the unpredictable instability of coordination compounds *in vivo*.

Iron is rather harmless but organic ligands – mostly with *N*-heterocycles – can be easily converted by the metabolism into toxic products when released inside the human body. Therefore it seems just logical to use hybrid systems for *f*MRI purposes which provide on the one hand triggered changes of magnetism and on the other hand total stability in aqueous media. Zeolites accomplish this last requirement easily and have been already used as imaging reporter, drug carrier, medical nanoprobe and are accepted by the FDA as contrast agent.^[90,96,114] Their extraordinary biocompatibility *in vivo* is one reason for the rapid evolution of medical nanotechnology.^[115] Especially faujasite is known for its unique architecture trapping transition metal complexes known as ship-in-a-bottle. The unique combination of small gates opening up slightly bigger cavities prevents the complexes from leaching once they are formed.^[65,67]

Consequently, the linkage between zeolites and iron(II) based CISSS systems does provide a valuable approach for the design of smart contrast agents. The synergy between the faujasites' nanocarrier properties and the imaging reporter function of iron(II) has not yet been explored and harbors great potential for providing new insights into the consideration of iron(II) composites for paramagnetic relaxation enhancement.

1.9 Aims of this work

The overall aim of this work is to investigate if homoleptic iron(II) complexes based on 2,2'-bipyridine-like ligands can serve as smart contrast agents in aqueous solution or aqueous nanocarrier suspensions by providing a means to change the molar relaxivity Δr_1 of surrounding solvent molecules in a pH-dependent style. The work can be subdivided into the following six key steps:

- ⊙ General investigation, if a pH-responsive magnetism of iron(II) complexes can be generated with the chosen ligand system and characterization of the diamagnetic and paramagnetic state with magnetometry, ¹H-NMR and UV-Vis spectroscopy in a multi-dependent fashion

- ⊙ Elucidation of the underlying mechanism responsible for the observed pH-responsive magnetism and considerations if and how this mechanism can be influenced by the selection or substitution of the ligand coordinating the metal center as well as the experimental verification by suitable measurements
- ⊙ Specific investigations with FC ^1H -NMR relaxometry to test if the observed proton-driven coordination-induced spin state switch allows a pH-dependent modification of the longitudinal molar relaxivity Δr_1 of surrounding H_2O molecules what would be the basis for a pH-responsive contrast agent
- ⊙ Attempts to incorporate selectively the iron(II) complexes into zeolites generating hybrid materials without unwanted paramagnetic side products and investigations if the observed pH-responsiveness can be preserved under small confinement and comparison with the complexes in solution
- ⊙ Incorporation of the iron(II) complexes into zeolite nanoparticles and investigations if the observed pH-responsiveness can be also preserved under small confinement in nanoparticles
- ⊙ Attempts to alter the longitudinal molar relaxivity Δr_1 of H_2O molecules in the near vicinity of the zeolite particles in a similar fashion as it was possible with the bare solubilized complexes

2. Results and Discussion

2.1 Homoleptic iron(II) complexes

The ligands that were used can all be derived from 2,2'-bipyridine which is known to form homoleptic complexes with iron(II) salts.^[8,116-120] Three ligands usually coordinate the iron center in an octahedral fashion with a very symmetric surrounding and a rather large ligand field splitting.^[8,121] Therefore mostly diamagnetic complexes are generated. Surprisingly, most of the chloride salts are unknown in the literature.^[116-120] The 2,2'-bipyridine ligand is basically the fusion of two aromatic pyridyl rings connected between two carbon atoms. This connection is completely rotatable in the uncoordinated mode but is also slightly twisted under coordination to a metal center.^[119] In general 2,2'-bipyridine based iron(II) salts are known for their intense MLCT-bands, their solubility in aqueous media, diamagnetism and stability under ambient conditions.^[122] Another feature is the possible interaction with H⁺ ions which is so far not understood. The earliest publications are dating back to 1960. A controversial discussion finds either dissociation of the ligands upon protonation, a steady-state condition or the formation of a so called half-bonded species.^[123,124] Nevertheless, none of the so far existing experiments could completely answer which species emerge under protonation. This is also related to the fact that most of the experiments have been conducted at severely different pH values, with different acids and varying counter cations.^[123,124]

2.1.1 General information and characterization

All used systems can be derived from Fe(Bpy)₃Cl₂ as the parent complex. The bulk material has been characterized completely with respect to its composition and magnetic state. This is essential to verify purity and to compare the bulk properties with solution experiments. Elemental analysis confirmed the general composition and revealed association with two water molecules (see Table 2). SQUID magnetometry between 50 K and 400 K was used to determine the magnetic properties as it can be seen in Figure 1. The compound was found to be completely diamagnetic between 50 K and 340 K. Above 340 K an abrupt and complete transition to the HS state is observed which is preserved upon subsequent cooling from 400 K to 50 K. All in all, the bulk material is in a LS state that should be also preserved in solution.

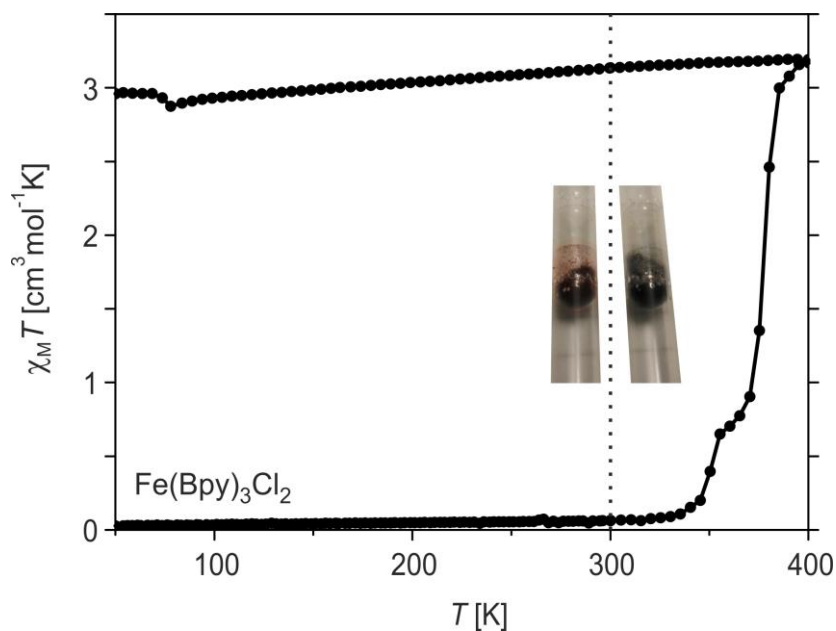


Figure 1. SQUID measurement between 50 K and 400 K in the settle mode of $\text{Fe}(\text{Bpy})_3\text{Cl}_2$.

Mössbauer spectroscopy before and after heating to 400 K is displayed in Figure 2. A very narrow doublet is observed in accordance with literature ($\delta = 0.32$ mm/s, $\Delta E_Q = 0.35$ mm/s) of $\text{Fe}(\text{Bpy})_3\text{Cl}_2$.^[116,125-127] The heated sample gives one broad doublet characteristic for a HS species ($\delta = 1.02$ mm/s, $\Delta E_Q = 2.90$ mm/s) and therefore almost coincides with the SQUID measurements (see Table 3). The broad doublet has the same parameters as the decomposition compound $\text{Fe}(\text{Bpy})_2\text{Cl}_2$ produced by heating in N_2 according to the literature.^[127]

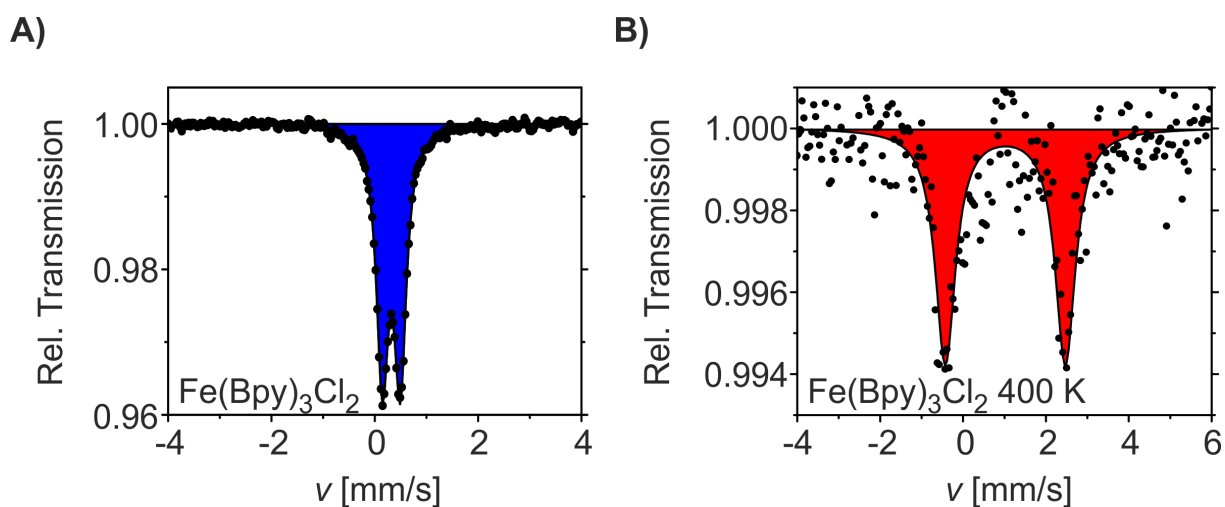


Figure 2. Mössbauer spectroscopy of $\text{Fe}(\text{Bpy})_3\text{Cl}_2$ at 300 K. **A:** Compound under ambient conditions. **B:** Compound after heating to 400 K in the vacuum.

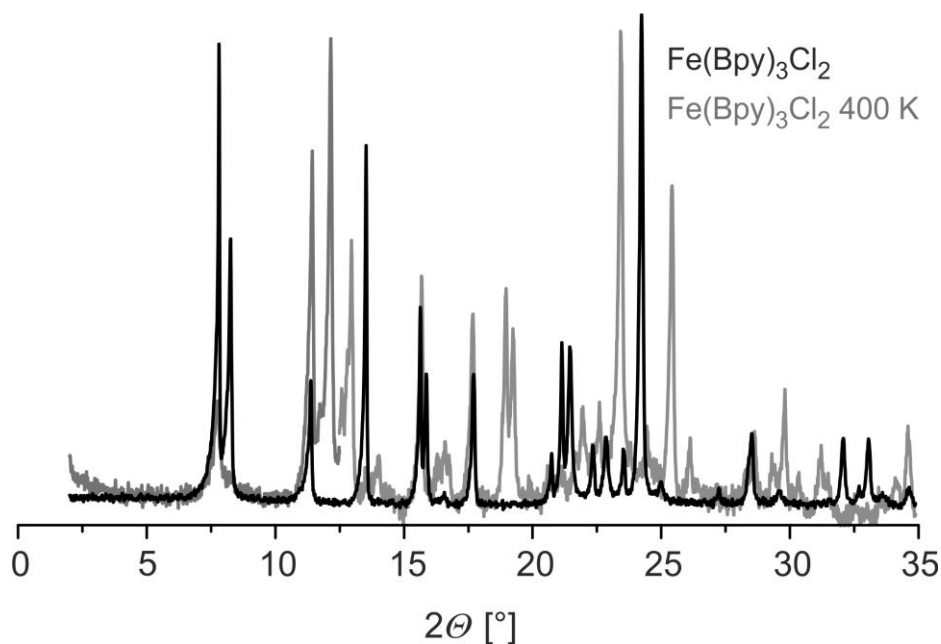


Figure 3. Powder diffraction patterns of $\text{Fe}(\text{Bpy})_3\text{Cl}_2$ under ambient conditions before (black) and after heating to 400 K (grey).

Powder diffraction patterns of both materials are fundamentally different which points towards drastic changes of the diffracting structures (see Figure 3). In summary, SQUID magnetometry, Mössbauer spectroscopy and powder diffraction are in very good agreement with each other and prove magnetic and structural changes upon heating above 340 K in the vacuum.

Mössbauer spectroscopy was also conducted to determine the spin state at RT of all other solid samples. The methylated derivatives $\text{Fe}(\text{44mBpy})_3\text{Cl}_2$, $\text{Fe}(\text{55mBpy})_3\text{Cl}_2$, $\text{Fe}(\text{4mBpy})_3\text{Cl}_2$ and $\text{Fe}(\text{5mBpy})_3\text{Cl}_2$ are also summarized in Table 2. Mössbauer properties are unknown for all those chloride salts.^[8,116-120] The spectra of the solid samples are presented in Figure 4 where the relative transmission is plotted against the velocity v of the source. Full parameters are given in Table 3. The overall data is in very good agreement with comparable salts known in the literature.^[116,125-127] One doublet is found for $\text{Fe}(\text{44mBpy})_3\text{Cl}_2$ which has a small isomer shift ($\delta = 0.32$ mm/s) and a narrow ΔE_Q with 0.25 mm/s; nearly a singlet. There is obviously a highly symmetric surrounding enforced by the methyl groups. $\text{Fe}(\text{55mBpy})_3\text{Cl}_2$ is very similar to $\text{Fe}(\text{44mBpy})_3\text{Cl}_2$ with one narrow doublet featuring $\delta = 0.31$ mm/s and $\Delta E_Q = 0.31$ mm/s. The complexes $\text{Fe}(\text{44mBpy})_3\text{Cl}_2$ and $\text{Fe}(\text{55mBpy})_3\text{Cl}_2$ are essentially diamagnetic in the solid state and consequently also in neutral aqueous media. $\text{Fe}(\text{4mBpy})_3\text{Cl}_2$ is also a LS complex

with $\delta = 0.30$ mm/s and $\Delta E_Q = 0.28$ mm/s as well as $\text{Fe}(\text{5mBpy})_3\text{Cl}_2$ with $\delta = 0.32$ mm/s and $\Delta E_Q = 0.31$ mm/s. The $\Gamma/2$ is for all samples in a common and expectable range.

Table 2. Summary of the compounds $\text{Fe}(\text{Bpy})_3\text{Cl}_2$, $\text{Fe}(\text{44mBpy})_3\text{Cl}_2$, $\text{Fe}(\text{55mBpy})_3\text{Cl}_2$, $\text{Fe}(\text{4mBpy})_3\text{Cl}_2$ and $\text{Fe}(\text{5mBpy})_3\text{Cl}_2$ discussed in this work, their abbreviations, their analytical composition as received from the synthesis and their magnetic properties.

Complex	Analysis	Ligand	Magnetism
Fe(Bpy)₃Cl₂	$\text{Fe}(\text{Bpy})_3\text{Cl}_2 \cdot 2 \text{H}_2\text{O}$	2,2'-bipyridine	LS
Fe(44mBpy)₃Cl₂	$\text{Fe}(\text{44mBpy})_3\text{Cl}_2 \cdot \text{H}_2\text{O} \cdot 2 \text{MeOH}$	4,4'-dimethyl-2,2'-bipyridine	LS
Fe(55mBpy)₃Cl₂	$\text{Fe}(\text{55mBpy})_3\text{Cl}_2 \cdot 2 \text{H}_2\text{O}$	5,5'-dimethyl-2,2'-bipyridine	LS
Fe(4mBpy)₃Cl₂	$\text{Fe}(\text{4mBpy})_3\text{Cl}_2 \cdot \text{H}_2\text{O} \cdot \text{MeOH}$	4-methyl-2,2'-bipyridine	LS
Fe(5mBpy)₃Cl₂	$\text{Fe}(\text{5mBpy})_3\text{Cl}_2 \cdot 2 \text{H}_2\text{O}$	5-methyl-2,2'-bipyridine	LS

SQUID measurements were also conducted for all chloride salts $\text{Fe}(\text{44mBpy})_3\text{Cl}_2$, $\text{Fe}(\text{55mBpy})_3\text{Cl}_2$, $\text{Fe}(\text{4mBpy})_3\text{Cl}_2$ and $\text{Fe}(\text{5mBpy})_3\text{Cl}_2$ since they are so far missing in the literature (see Figure 4). The methyl groups donate electron density into the pyridyl rings increasing the basicity at the nitrogen and should therefore favor protonation.^[128] For $\text{Fe}(\text{44mBpy})_3\text{Cl}_2$ we find a completely diamagnetic behavior up to 350 K in good agreement with the Mössbauer measurements (see Figure 4) and the literature.^[116] Above 350 K an abrupt transition to the HS state induced by solvent or ligand loss can be observed. $\text{Fe}(\text{55mBpy})_3\text{Cl}_2$ is also completely LS up to 350 K and then undergoes an abrupt transition to the HS state which is also irreversible. Exactly the same behavior in the solid state is observed for $\text{Fe}(\text{4mBpy})_3\text{Cl}_2$ and $\text{Fe}(\text{5mBpy})_3\text{Cl}_2$. This process was found to be reversible and is triggered either by the partial loss of ligands or solvent molecules as it could be inferred from TG analysis (see Appendix A1–5) and the elemental composition (Table 2).^[116]

The chloride salts have been chosen since all further experiments investigating pH-responsiveness were carried out using HCl in order to avoid interference of different anions.^[123] Aside from that, HCl was used to mimic gastric juices since iron(II) agents appear to be most suitable for gastrointestinal imaging.^[129] Included water molecules found by elemental analysis can be neglected for all measurements in aqueous media. Since all solutions are highly diluted any influence of MeOH molecules can also be neglected.

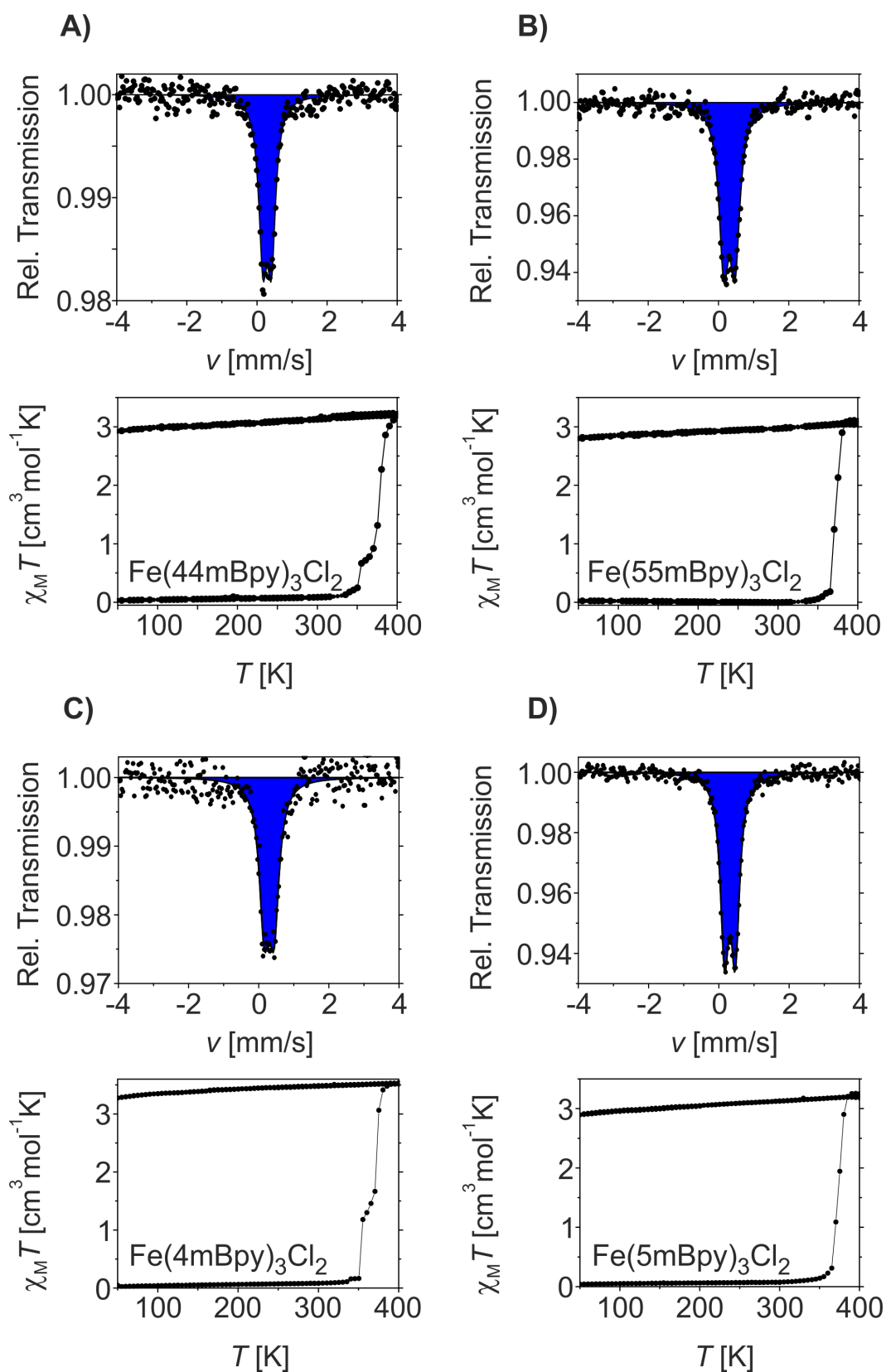


Figure 4. Mössbauer spectroscopy at 300 K of $\text{Fe}(44\text{mBpy})_3\text{Cl}_2$ (A), $\text{Fe}(55\text{mBpy})_3\text{Cl}_2$ (B), $\text{Fe}(4\text{mBpy})_3\text{Cl}_2$ (C) and $\text{Fe}(5\text{mBpy})_3\text{Cl}_2$ (D) is given in the upper row. Their magnetic measurements in the temperature range between 50 K and 400 K are shown below.

Table 3. Mössbauer parameters of $\text{Fe}(\text{Bpy})_3\text{Cl}_2$, $\text{Fe}(\text{44mBpy})_3\text{Cl}_2$, $\text{Fe}(\text{55mBpy})_3\text{Cl}_2$, $\text{Fe}(\text{4mBpy})_3\text{Cl}_2$ and $\text{Fe}(\text{5mBpy})_3\text{Cl}_2$. The characteristic isomer shift δ , quadrupole splitting ΔE_Q and full-width-at-half-maximum $\Gamma/2$ are given together with the population.

Complex	Spin state	δ [mm/s]	ΔE_Q [mm/s]	$\Gamma/2$ [mm/s]
$\text{Fe}(\text{Bpy})_3\text{Cl}_2$	LS	0.3204(19)	0.345(3)	0.139(3)
$\text{Fe}(\text{Bpy})_3\text{Cl}_2$ (400 K)	HS	1.02(3)	2.900(7)	0.30(5)
$\text{Fe}(\text{44mBpy})_3\text{Cl}_2$	LS	0.291(9)	0.245(17)	0.145(15)
$\text{Fe}(\text{55mBpy})_3\text{Cl}_2$	LS	0.310(7)	0.314(12)	0.166(11)
$\text{Fe}(\text{4mBpy})_3\text{Cl}_2$	LS	0.2970(16)	0.280(3)	0.17(3)
$\text{Fe}(\text{5mBpy})_3\text{Cl}_2$	LS	0.315(5)	0.303(7)	0.15(6)

Crystals suitable for X-ray structure analysis could be gained from $\text{Fe}(\text{4mBpy})_3\text{Cl}_2$ by slow diffusion of diethyl ether into a methanol solution of the complex and of the corresponding ligand 4-methyl-2,2'-bipyridine directly from the synthesis. The crystallographic data were collected at 133 K and are given in Table 6, as well as an ORTEP drawing of the ligand 4mBpy given in Figure 6. The ligand crystallizes in the orthorhombic space group $Pbca$, the asymmetric unit contains one molecule of the ligand. The complex $\text{Fe}(\text{4mBpy})_3\text{Cl}_2$ crystallizes in the trigonal space group $P321$. An ORTEP drawing of the complex and a picture of the packing of the molecule in the crystal along [001] is shown in Figure 5. The asymmetric unit contains two unequal Fe(II) centers; one Fe(II) is coordinated by half a molecule of 4,4'-dimethyl-2,2'-bipyridine (occupation 1/6 in the asymmetric unit), the second Fe(II) center is coordinated by one molecule of 4,4'-dimethyl-2,2'-bipyridine (occupation 1/3 in the asymmetric unit). The bond lengths of the coordination sphere and the octahedral distortion parameter Σ for both Fe(II) centers are given in Table 4. The intermolecular interactions are given in Table 5.

The bond lengths are with 1.955–1.968 Å in good agreement with an Fe(II) center in the LS state.^[116,119] During refinement, electron density of solvent molecules were present. However, those solvent molecules could not be refined due to partial occupancy. Therefore SQUEEZE from Platon was used to remove 197 electrons per unit cell. 4 intermolecular interactions between the pyridine rings of the ligands and the chloride ions are present. Details of those interactions are given in Table 5.

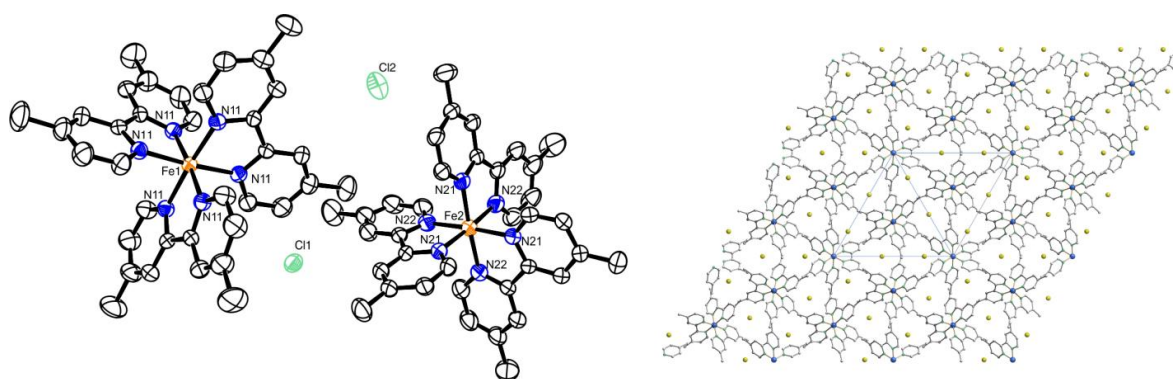


Figure 5. ORTEP drawing of $\text{Fe}(\text{4mBpy})_3\text{Cl}_2$ and molecule packing in the crystal along [001]. Ellipsoids were drawn at 50% probability level and hydrogen atoms omitted for clarity.

Table 4. Selected bond lengths and octahedral distortion parameter Σ for $\text{Fe}(\text{4mBpy})_3\text{Cl}_2$.

Fe1–N11 [Å]	1.968(3)	Σ [°]
Fe2–N21 [Å]	1.959(3)	Fe1
Fe2–N22 [Å]	1.955(4)	Fe2
		70.76
		60.27

Table 5. Overview of the intermolecular interactions of $\text{Fe}(\text{4mBpy})_3\text{Cl}_2$.

Donor	Acceptor	D–H [Å]	H\cdotsA [Å]	D\cdotsA [Å]	D–H\cdotsA [°]
C12–H12	Cl2	0.95	2.83	3.771(4)	173
C14–H14	Cl1	0.95	2.52	3.441(5)	163
C24–H24	Cl1	0.95	2.66	3.599(4)	168
C28–H28	Cl1	0.95	2.55	3.496(5)	177

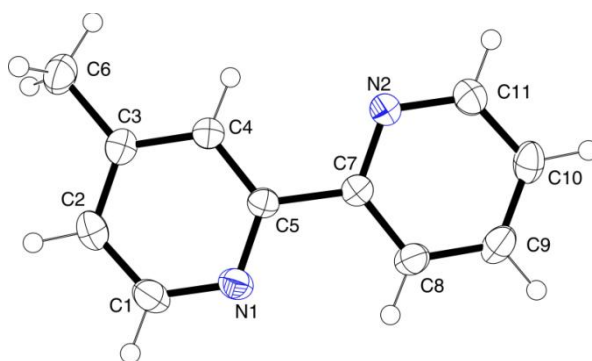


Figure 6. ORTEP drawing of the ligand 4-methyl-2,2'-bipyridine. Ellipsoids were drawn at 50% probability level.

Results and Discussion

Table 6. Crystallographic data of 4-methyl-2,2'-bipyridine and Fe(4mBpy)₃Cl₂.

	4-methyl-2,2'-bipyridine	Fe(4mBpy)₃Cl₂
formula	4mBpy	Fe(44mBpy) ₃ Cl ₂
sum formula	C ₁₁ H ₁₀ N ₂	C ₃₆ H ₃₆ Cl ₂ FeN ₆
<i>M</i>/ g mol⁻¹	170.21	679.46
crystal system	orthorhombic	trigonal
space group	<i>Pbca</i>	<i>P321</i>
crystal description	colourless block	dark red prism
<i>a</i>/ Å	7.3315(5)	18.1428(7)
<i>b</i>/ Å	11.3116(12)	18.1428(7)
<i>c</i>/ Å	21.5714(15)	11.3314(6)
α / °	90	90
β / °	90	90
γ / °	90	120
<i>V</i>/ Å³	1788.9(3)	3230.2(3)
<i>Z</i>	8	3
ρ_{calcd}/ g cm⁻³	1.264	1.048
μ/ mm⁻¹	0.077	0.502
crystal size	0.140×0.130×0.104	0.128×0.100×0.085
F(000)	720	1062
<i>T</i>/ K	133(2)	133(2)
λ/ Å	Mo-K α 0.71073	Mo-K α 0.71073
θ range/ °	2.61–27.85	1.3–28.6
Reflns. collected	3288	9279
Indep. reflns.(<i>R</i>_{int})	2128 (0.044)	5205 (0.090)
Parameters	118	205
<i>R</i>1 (all data)	0.0450	0.0425
<i>wR</i>2	0.1123	0.0914
GooF	0.88	0.85
Flack <i>x</i>	/	-0.01(2)

Apart from the 2,2'-bipyridine-like systems, $\text{Fe}(\text{Bpp})_2\text{Cl}_2$ was also characterized in the solid state. The bulk material of $\text{Fe}(\text{Bpp})_2\text{Cl}_2$ incorporates two water molecules and is a classical SCO complex.^[9,130] Two different iron sites are found for $\text{Fe}(\text{Bpp})_2\text{Cl}_2$ with an inner LS doublet ($\delta = 0.31$ mm/s and $\Delta E_Q = 0.71$ mm/s) occupying 77% and an outer HS doublet ($\delta = 0.99$ mm/s, $\Delta E_Q = 2.33$ mm/s) occupying 23% (see Figure 7). The data is also congruent with the literature.^[9,130] $\text{Fe}(\text{Bpp})_2\text{Cl}_2$ undergoes a gradual SCO comparable to other salts mentioned in the literature.^[9,130]

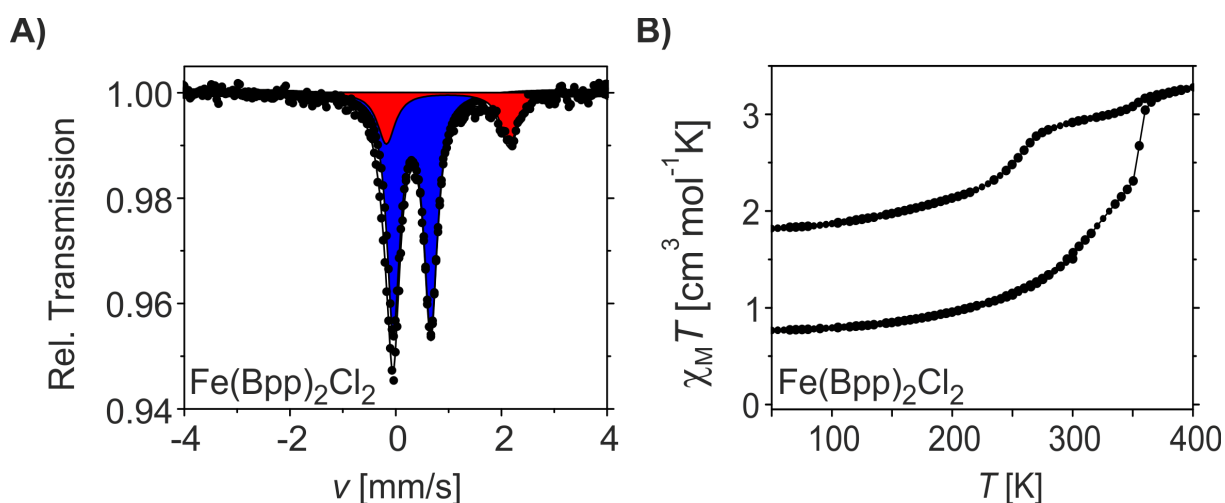
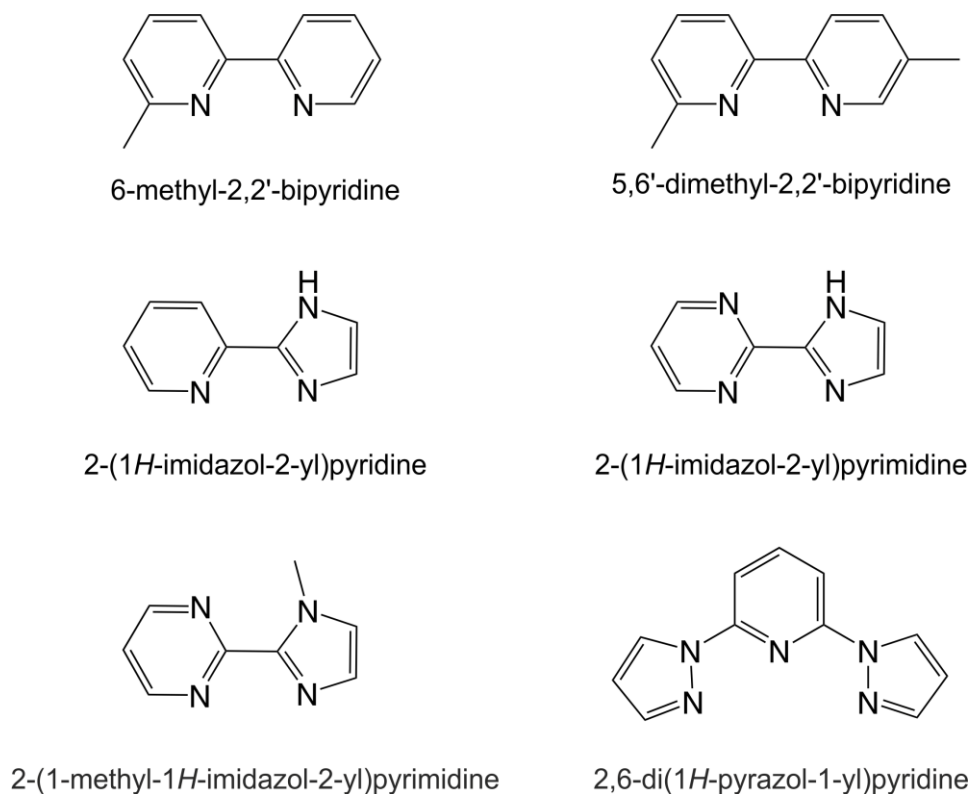


Figure 7. **A:** Mössbauer spectroscopy at 300 K of the homoleptic iron(II) complex $\text{Fe}(\text{Bpp})_2\text{Cl}_2$. **B:** Magnetic measurements in the temperature range between 50 K and 400 K.

Table 7. Analytical composition as received after synthesis and magnetism of $\text{Fe}(\text{Bpp})_2\text{Cl}_2$.

Complex	Analysis	Ligand	Magnetism
$\text{Fe}(\text{Bpp})_2\text{Cl}_2$	$\text{Fe}(\text{Bpp})_2\text{Cl}_2 \cdot 2 \text{H}_2\text{O}$	2,6-di(1 <i>H</i> -pyrazol-3-yl)pyridine	SCO

Apart from $\text{Fe}(\text{Bpy})_3\text{Cl}_2$, $\text{Fe}(\text{44mBpy})_3\text{Cl}_2$, $\text{Fe}(\text{55mBpy})_3\text{Cl}_2$, $\text{Fe}(\text{4mBpy})_3\text{Cl}_2$, $\text{Fe}(\text{5mBpy})_3\text{Cl}_2$ and $\text{Fe}(\text{Bpp})_2\text{Cl}_2$ several other iron(II)chloride complexes have been prepared from the ligands given in Scheme 13. Unfortunately, all of the resulting complexes were found to be unsuitable for any pH-responsive behavior in aqueous solution. They are either unstable in water, decompose in acidic media or oxidize. Nevertheless, synthesis and characterization are given in the Experimental Section. Further collected analysis is given in the Appendix A6–7.



Scheme 13. Ligands that were used for further iron(II) chloride complexes but were found to be unsuitable for any pH-responsive magnetism.

The iron(II) chloride complexes of 6-methyl-2,2'-bipyridine and 5,6'-dimethyl-2,2'-bipyridine are stable under ambient conditions and also in neutral aqueous media. Nevertheless, they start to oxidize rapidly when the pH of the solution is lowered, resulting in a brown μ -oxido species in solution and ligand dissociation. The situation is more sophisticated for complexes of 2-(1*H*-imidazol-2-yl)pyridine and 2-(1*H*-imidazol-2-yl)pyrimidine where indeed some pH-response could be observed via UV-VIS spectroscopy and FC $^1\text{H-NMR}$ relaxometry. Nevertheless, SQUID magnetometry did not yield corresponding results and pointed rather towards decomposition of the systems. The complex of 2-(1-methyl-1*H*-imidazol-2-yl)pyrimidine was found to be unstable under ambient conditions and starts to oxidize after several days at air. The yellow iron(II) chloride complex of 2,6-di(1*H*-pyrazol-1-yl)pyridine is stable under ambient conditions but decomposes immediately in neutral aqueous solution under complete ligand dissociation.

2.1.2 Behavior in aqueous solution: ^1H -NMR spectroscopy

The ^1H -NMR spectra of aqueous solutions ($\text{D}_2\text{O}/\text{H}_2\text{O}$) of $[\text{Fe}(\text{Bpy})_3]^{2+}$ ($c = 0.007 \text{ mol/L}$) at different pH are given in Figure 8A which show at pH 5.9 the typical four signals for the protons of the $[\text{Fe}(\text{Bpy})_3]^{2+}$ ion (3 (d), 4 (t), 5(t), 6(d)).^[131] Atom numbering is given in the Appendix A8. When lowering the pH new signals are emerging in the aromatic region that are associated with the appearance of a diamagnetic protonated species $[\text{Fe}(\text{Bpy})_3\text{H}]^{3+}$ (3^* (m), 4^* (m), 5^* (m), 6^* (d)). The relative integrals of those signals increase with H^+ concentration.

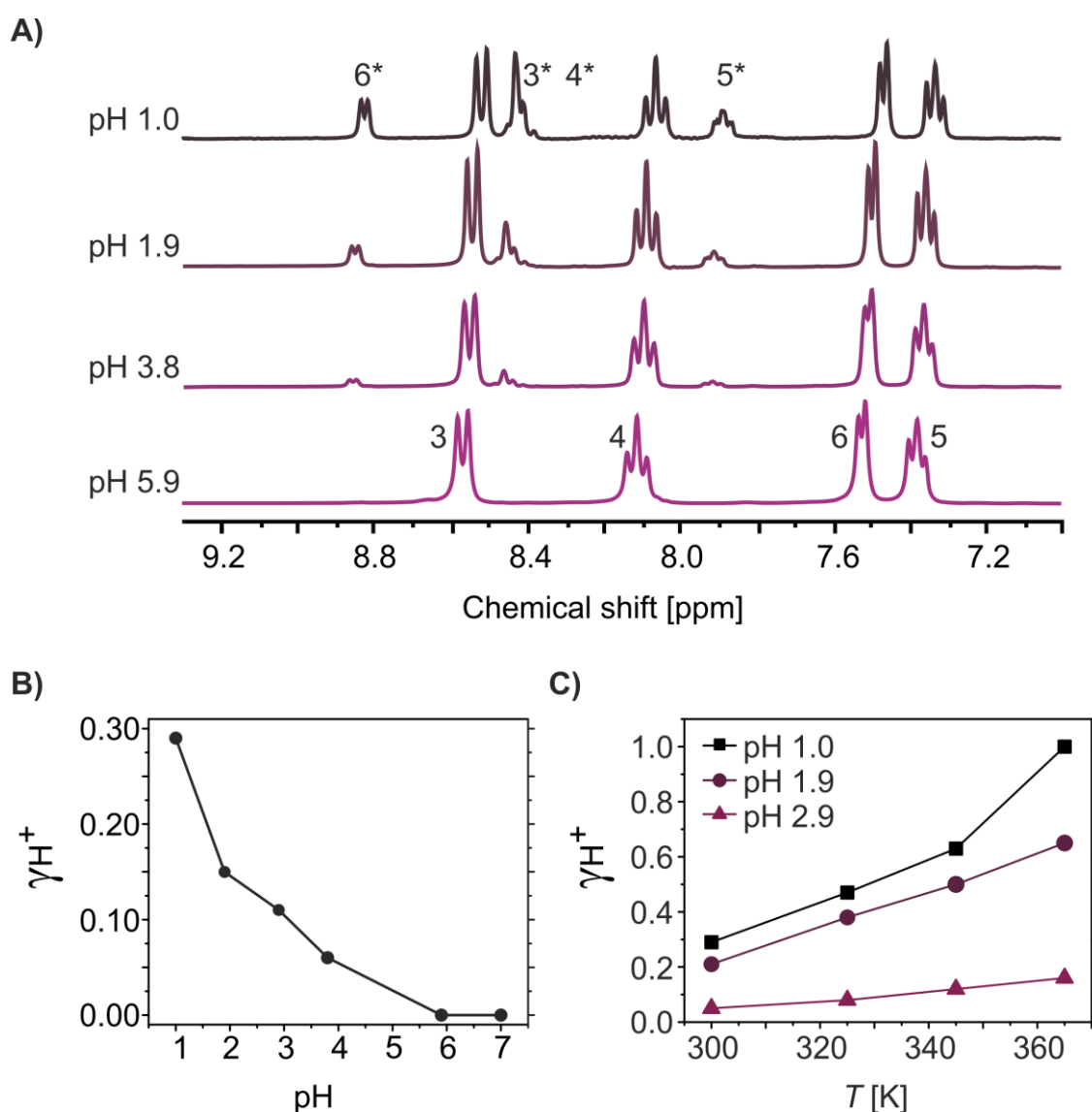


Figure 8. A: ^1H -NMR spectroscopy of $[\text{Fe}(\text{Bpy})_3]^{2+}$ in $\text{D}_2\text{O}/\text{H}_2\text{O}$ mixtures at different pH-values; **B:** plot of γ_{H^+} (calculated from A) against the pH giving an exponential relationship; **C:** plot of γ_{H^+} against the temperature for different pH-values giving linear functions.

Results and Discussion

In Figure 8B the fraction of the protonated species γH^+ is plotted against the pH (γH^+ was calculated dividing the integrals belonging to the new signals through the overall integral sum). γH^+ rises in an exponential fashion with the proton concentration from 0.00 at neutral pH to 0.29 at pH 1.0. Full ^1H -NMR data and corresponding calculations are given in Table 8.

Table 8. Peak positions and integrals for $[\text{Fe}(\text{Bpy})_3]^{2+}$ at 300 K and different pH-values.

$\text{Fe}[(\text{Bpy})_3]^{2+}$	Peak positions at different pH-values at 300 K				
	pH 5.9	pH 3.8	pH 2.9	pH 1.9	pH 1.0
3 (d)	8.558, 8.585	8.541, 8.568	8.532, 8.559	8.534, 8.560	8.508, 8.535
4 (t)	8.089 - 8.140	8.071 - 8.112	8.062 - 8.114	8.064 - 8.115	8.038 - 8.089
5 (t)	7.360 - 7.403	7.341 - 7.384	7.333 - 7.376	7.335 - 7.378	7.310 - 7.355
6 (d)	7.517, 7.534	7.500, 7.517	7.490, 7.509	7.489, 7.507	7.458, 7.478
3* (m)	-	8.414 - 8.487	8.408 - 8.481	8.410 - 8.480	8.283 - 8.450
4* (m)	-	8.414 - 8.487	8.408 - 8.481	8.410 - 8.480	8.283 - 8.450
5* (m)	-	7.897 - 7.937	7.894 - 7.934	7.890 - 7.934	7.865 - 7.908
6* (d)	-	8.868, 8.852	8.844, 8.862	8.846, 8.863	8.820, 8.838
$\text{Fe}[(\text{Bpy})_3]^{2+}$	Integrals at different pH-values at 300 K				
	pH 5.9	pH 3.8	pH 2.9	pH 1.9	pH 1.0
3 (d)	6.079	5.815	5.145	5.249	4.151
4 (t)	5.996	5.518	5.123	4.937	3.965
5 (t)	5.972	5.512	5.593	5.111	4.452
6 (d)	5.954	5.644	5.404	5.136	4.416
3*, 4* (m)	0.000	0.733	1.389	1.779	3.510
5* (m)	0.000	0.303	0.740	0.823	1.715
6* (d)	0.000	0.474	0.605	0.966	1.790
Full	24	24	24	24	24
$\text{Fe}[(\text{Bpy})_3]^{2+}$	1.00	0.94	0.89	0.85	0.71
$\text{Fe}[(\text{Bpy})_3\text{H}]^{3+}$	0.00	0.06	0.11	0.15	0.29

The temperature dependence of this phenomenon was additionally evaluated. In Figure 8C the γH^+ versus the temperature is given for pH 1.0, 1.9 and 2.9 at 300 K, 325 K, 345K and 365 K. It can be observed that γH^+ increases linearly with rising T . Interestingly, the altitude appears to be independent from the pH. A paramagnetic shift of the spectra coupled with a significant line broadening is observed upon heating for the solutions (pH 1.0, 1.9, 2.9) which are given

in the Figure 9. Such observation hints towards presence of paramagnetic species due to coordinative changes induced by protonation. This paramagnetic species is too broad to be detected directly by $^1\text{H-NMR}$ spectroscopy.^[132] The integral calculation is given in Table 9 and the peak positions for the T -dependence are given in the Appendix A9.

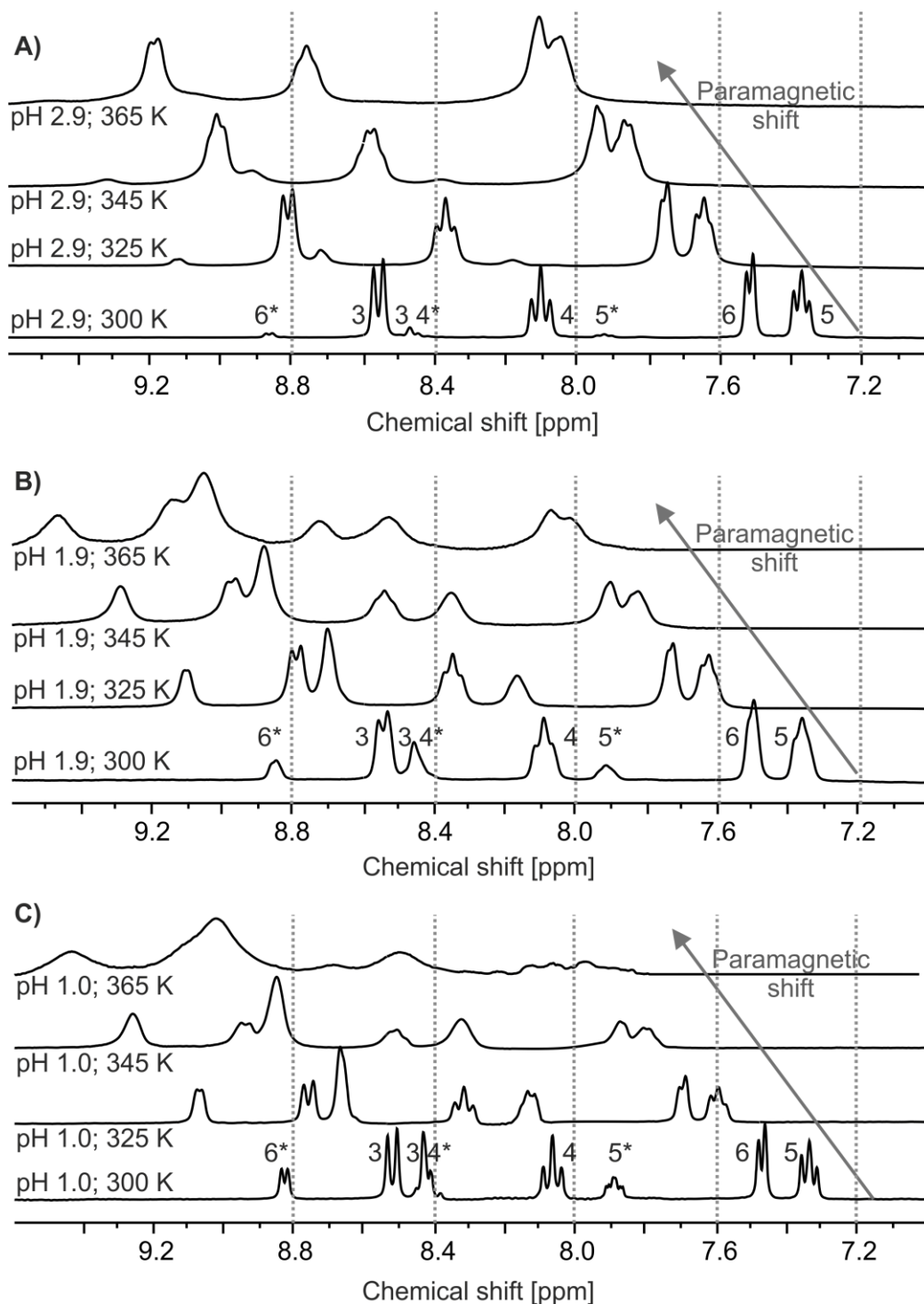


Figure 9. T -dependent $^1\text{H-NMR}$ spectra of $[\text{Fe}(\text{Bpy})_3]^{2+}$ in $\text{D}_2\text{O}/\text{H}_2\text{O}$ at pH 1.0, 1.9 and 2.9.

Results and Discussion

Table 9. Integrals for $[\text{Fe}(\text{Bpy})_3]^{2+}$ at pH 1.0, 1.9, 2.9 and different temperatures.

pH 1.0	300 K	325 K	345 K	365 K
3 (d)	4.151	3.239	2.180	0.000
4 (t)	3.965	2.886	1.905	0.000
5 (t)	4.452	3.232	2.385	0.000
6 (d)	4.416	3.313	2.385	0.000
3* (m)	1.755	2.728	4.031	6.000
4* (m)	1.755	2.728	4.031	6.000
5* (m)	1.715	2.919	3.195	6.000
6* (d)	1.790	2.954	3.887	6.000
Full	24	24	24	24
$[\text{Fe}(\text{Bpy})_3]^{2+}$	0.71	0.53	0.37	0.00
$[\text{Fe}(\text{Bpy})_3\text{H}]^{3+}$	0.29	0.47	0.63	1.00
pH 1.9	300 K	325 K	345 K	365 K
3 (d)	4.947	3.965	3.179	-
4 (t)	4.808	3.850	3.206	-
5 (t)	4.578	3.541	2.862	-
6 (d)	4.610	3.541	2.862	-
3* (m)	1.274	2.277	3.008	-
4* (m)	1.274	2.277	3.008	-
5* (m)	1.209	2.258	2.986	-
6* (d)	1.301	2.289	2.889	-
Full	24	24	24	24
$[\text{Fe}(\text{Bpy})_3]^{2+}$	0.79	0.62	0.50	-
$[\text{Fe}(\text{Bpy})_3\text{H}]^{3+}$	0.21	0.38	0.50	-
pH 2.9	300 K	325 K	345 K	365 K
3 (d)	5.835	5.847	5.552	-
4 (t)	5.736	5.579	5.178	-
5 (t)	5.748	5.501	5.220	-
6 (d)	5.590	5.261	5.220	-
3* (m)	0.292	0.463	0.689	-
4* (m)	0.292	0.463	0.689	-
5* (m)	0.233	0.452	0.721	-
6* (d)	0.274	0.435	0.731	-
Full	24	24	24	24
$[\text{Fe}(\text{Bpy})_3]^{2+}$	0.95	0.92	0.88	-
$[\text{Fe}(\text{Bpy})_3\text{H}]^{3+}$	0.05	0.08	0.12	-

Since the true type of molecular interaction of the complex with surrounding protons is not yet understood a comparison of the $^1\text{H-NMR}$ spectra for the free ligand 2,2'-bipyridine and the complex $[\text{Fe}(\text{Bpy})_3]^{2+}$ was conducted at representative pH-values (5.9, 1.0 and 0.2). For the free ligand at pH 5.9 the unprotonated ligand and at pH 1.0 respectively pH 0.2 (not given since it is identical to 1.0) the protonated ligand is observed in $\text{D}_2\text{O}/\text{H}_2\text{O}$ mixtures. This is in agreement with only one pK_A value reported in the literature ($pK_A = 4.43$).^[133] For the complex, at pH 1.0 the protonated species is observed that is discussed in detail in this work. In contrast to the free ligand, at pH 0.2 a new species is observed which is most likely a double protonated species and it should be noted that this species is also diamagnetic. Details of the different peak positions are given in Table 10. Please note that for the protons 3 and 4 the signal of the protonated complex and the protonated free Bpy ligand is different at pH 1.0 due to differences in the symmetry. Furthermore, all signals of the protonated species are shifted compared to the free ligand and also the multiplet 5* is different to multiplet 5.

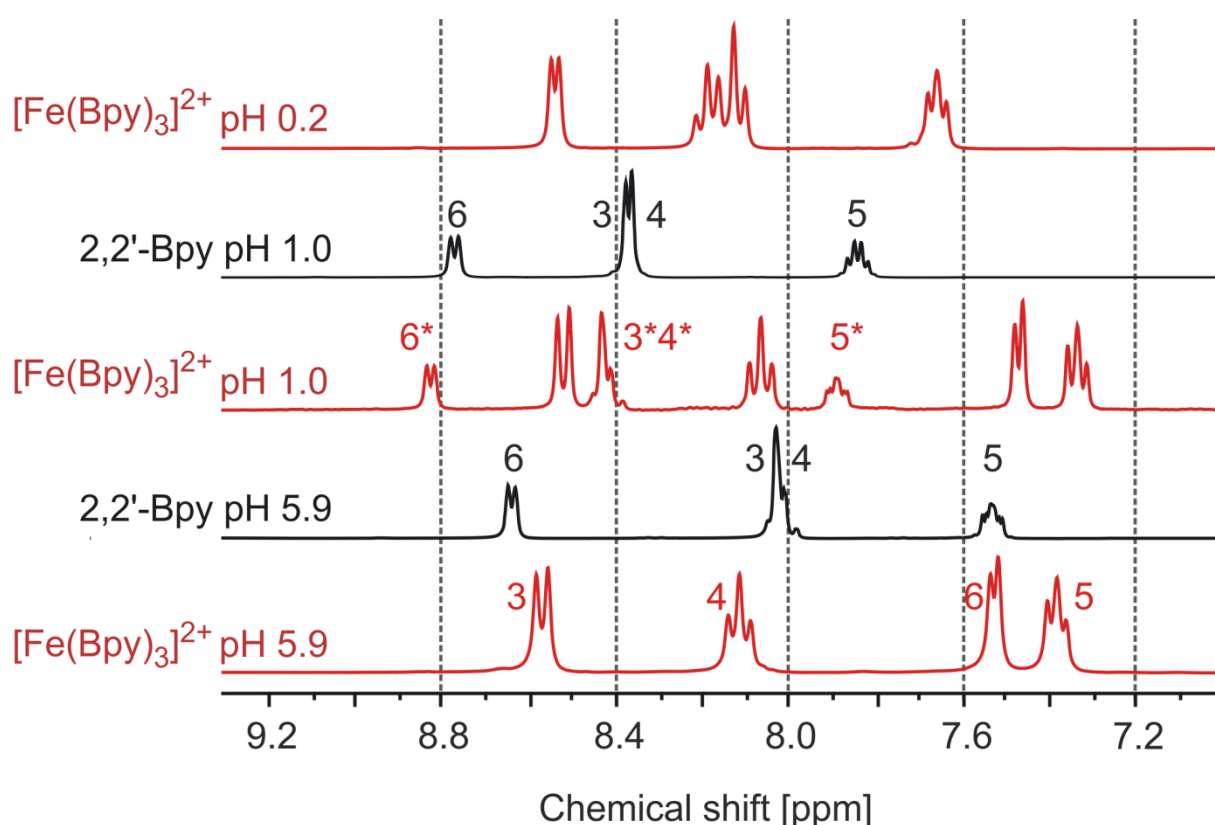


Figure 10. $^1\text{H-NMR}$ spectroscopy comparison of $[\text{Fe}(\text{Bpy})_3]^{2+}$ and the related ligand in $\text{D}_2\text{O}/\text{H}_2\text{O}$ mixtures at different pH-values.

Table 10. ^1H -NMR peak positions in ppm for 2,2'-bipyridine in $\text{D}_2\text{O}/\text{H}_2\text{O}$ at different pH-values.

	3 (m), 4 (d)	5 (m)	6 (d)
pH 5.9	8.007, 8.010, 8.028, 8.046	7.509, 7.531, 7.535, 7.554	8.626, 8.642
pH 1.0	8.358, 8.371	7.816, 7.832, 7.847, 7.863	8.755, 8.772

^1H -NMR spectroscopy has been also used to monitor the molecular interaction between the diamagnetic LS complexes $\text{Fe}(44\text{mBpy})_3\text{Cl}_2$, $\text{Fe}(55\text{mBpy})_3\text{Cl}_2$, $\text{Fe}(4\text{mBpy})_3\text{Cl}_2$ and $\text{Fe}(5\text{mBpy})_3\text{Cl}_2$ with surrounding protons. Signals were assigned according to the literature.^[131] Liquid $\text{H}_2\text{O}/\text{D}_2\text{O}$ mixtures of the complexes ($c = 0.007$ mol/L) were prepared at different pH-values reaching from pH 5.9 to pH 1.0. The results for $[\text{Fe}(44\text{mBpy})_3]^{2+}$ are given in Figure 11A. At pH 5.9 the expected signals for the complex are found. A singlet at 8.345 ppm belonging to position 3 and two signals belonging to position 6 (7.258, 7.277 ppm) and 5 (7.158, 7.177 ppm) are found in the aromatic region. See Appendix A8 and A10 for atom numbering and further NMR data. The methyl group at 4 gives a singlet at 2.508 ppm. At pH 3.8 a new set of signals is observed which indicates a protonated species as it could already be observed for $[\text{Fe}(\text{Bpy})_3]^{2+}$.^[132] This new set of signals consist of doublet 6* (8.634, 8.653 ppm), singlet 3* (8.240 ppm), doublet 5* (7.706, 7.725 ppm) and singlet CH_3^* (2.624 ppm) and becomes more and more pronounced with pH lowering. Interestingly, their occurrence can already be seen slightly at pH 5.9.

In Figure 11B the fraction of the protonated species γH^+ was plotted against the pH (γH^+ was calculated dividing the integrals belonging to the new signals through the overall integral sum). γH^+ rises exponentially with the proton concentration from 0.00 at neutral pH to 0.75 at pH 1.0. Full ^1H -NMR data and determination of the protonated species are given in Table 11.

The temperature dependence of this phenomenon was also evaluated. In Figure 11C the γH^+ versus the temperature is plotted for pH 1.0, 1.9 and 2.9 at 300 K, 325 K, 345K and 365 K. It can readily be observed that γH^+ increases linearly with rising T . The altitude appears here also to be independent from the pH. A paramagnetic shift of the spectra coupled with a significant line broadening is observed upon heating for the solutions (pH 1.0, 1.9, 2.9) which are given in Figure 12 and Table 12. Such observation also hints here towards the presence of

paramagnetic species due to coordinative changes induced by protonation. Full peak positions for the T -dependence are given in the Appendix A10.

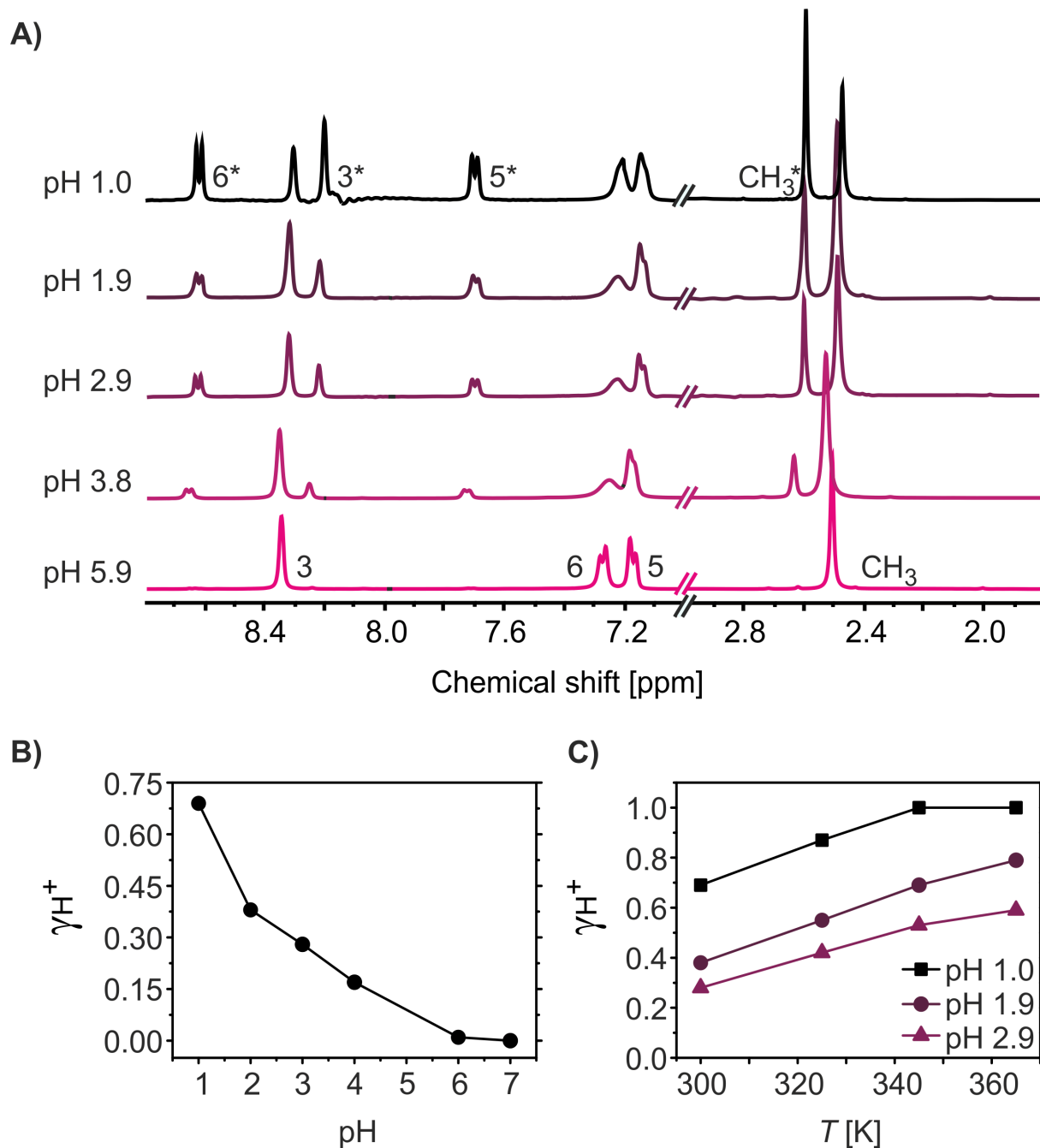


Figure 11. A: ^1H -NMR spectroscopy of $[\text{Fe}(\text{44mBpy})_3]^{2+}$ in $\text{D}_2\text{O}/\text{H}_2\text{O}$ mixtures at different pH-values; **B:** plot of γ_{H^+} (calculated from A) against the pH giving an exponential function; **C:** plot of γ_{H^+} against the temperature for different pH-values showing a linear relationship.

Results and Discussion

Table 11. Peak positions and integrals for $[\text{Fe}(\text{44mBpy})_3]^{2+}$ at 300 K and different pH-values.

$[\text{Fe}(\text{44mBpy})_3]^{2+}$	Peak positions at different pH-values at 300 K				
	pH 5.9	pH 3.8	pH 2.9	pH 1.9	pH 1.0
3 (s)	8.345	8.352	8.319	8.317	8.297
4 (CH₃)	2.508	2.527	2.490	2.489	2.463
5 (d)	7.158, 7.177	7.164, 7.18	7.132, 7.148	7.128, 7.144	7.114, 7.134
6 (d)	7.258, 7.277	7.248	7.219	7.218	7.198, 7.216
3* (s)	-	8.252	8.218	8.216	8.195
4* (CH₃)	-	2.634	2.601	2.599	2.587
5* (d)	-	7.717, 7.733	7.688, 7.706	7.685, 7.704	7.687, 7.705
6* (d)	-	8.647, 8.664	8.614, 8.633	8.612, 8.629	8.603, 8.621
$[\text{Fe}(\text{44mBpy})_3]^{2+}$	Integrals at different pH-values at 300 K				
	pH 5.9	pH 3.8	pH 2.9	pH 1.9	pH 1.0
3 (s)	5.902	5.085	4.091	3.799	2.061
4 (CH₃)	18.273	14.881	12.408	11.212	5.689
5 (d)	5.771	5.249	4.525	3.675	1.695
6 (d)	6.054	4.677	4.177	3.675	1.695
3* (s)	0.000	0.999	1.754	2.306	4.401
4* (CH₃)	0.000	3.166	5.559	6.788	12.340
5* (d)	0.000	0.974	1.816	2.285	4.006
6* (d)	0.000	0.969	1.671	2.260	4.113
Full	36	36	36	36	36
$[\text{Fe}(\text{44mBpy})_3]^{2+}$	1.00	0.83	0.70	0.62	0.31
$[\text{Fe}(\text{44mBpy})_3\text{H}]^{3+}$	0.00	0.17	0.30	0.38	0.69

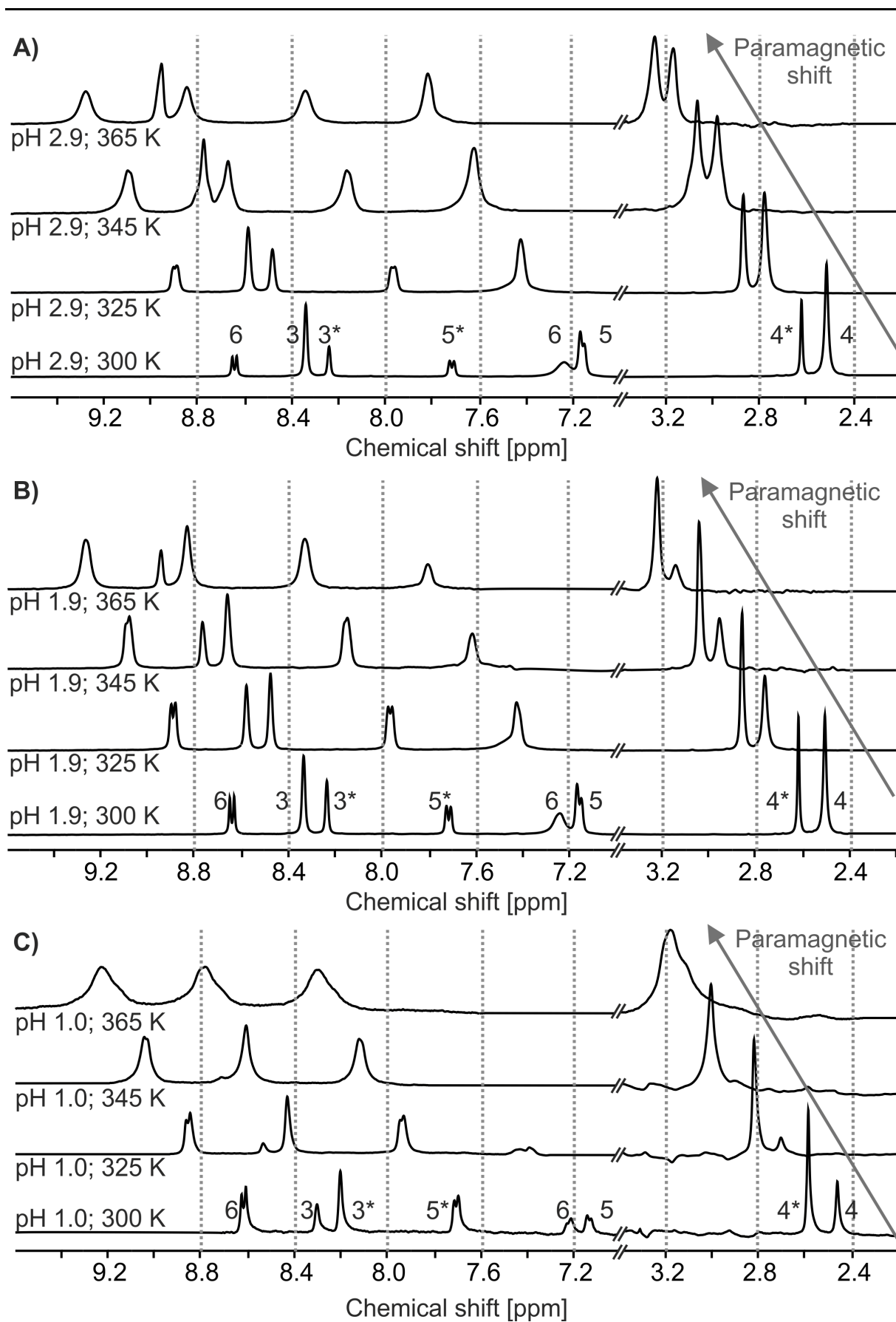
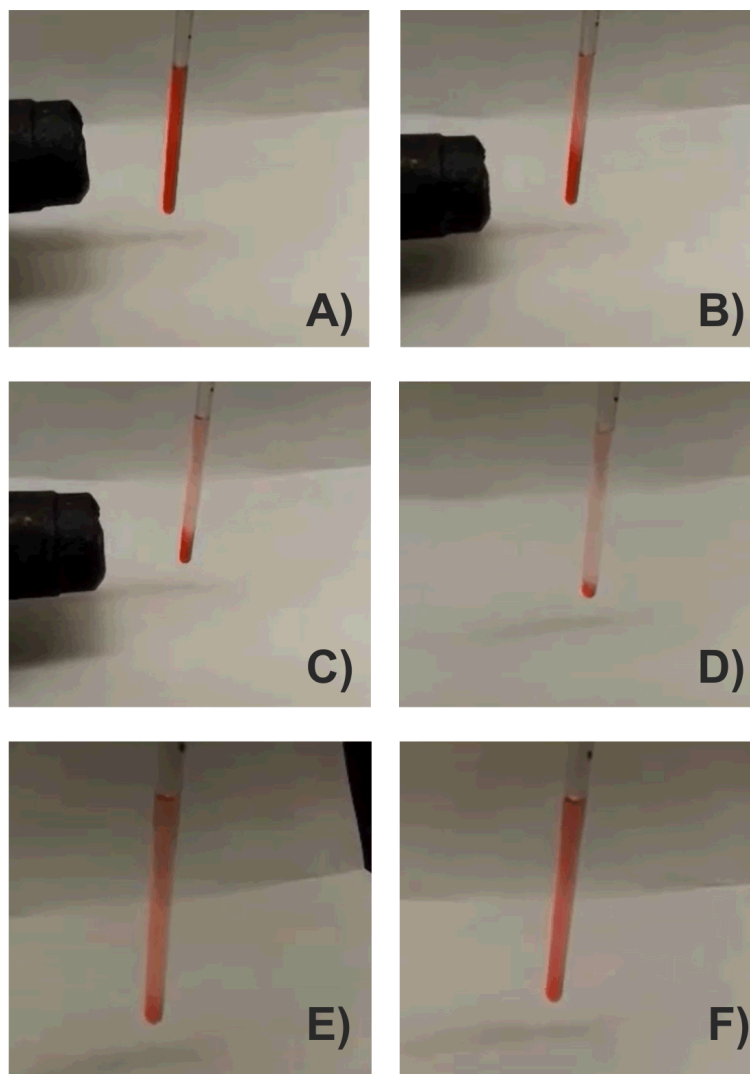


Figure 12. T -dependent ^1H -NMR spectra of $[\text{Fe}(\text{44mBpy})_3]^{2+}$ in $\text{D}_2\text{O}/\text{H}_2\text{O}$ at pH 1.0, 1.9, 2.9.

Table 12. Integrals for $[\text{Fe}(\text{44mBpy})_3]^{2+}$ at pH 1.0, 1.9, 2.9 and different temperatures.

pH 1.0	300 K	325 K	345 K	365 K
3 (s)	2.061	0.897	0.000	0.000
4 (CH ₃)	5.689	2.405	0.000	0.000
5 (d)	1.695	0.742	0.000	0.000
6 (d)	1.695	0.742	0.000	0.000
3* (s)	4.401	5.562	6.001	5.890
4* (CH ₃)	12.340	15.033	16.772	18.169
5* (d)	4.006	5.552	6.673	6.027
6* (d)	4.113	5.066	6.554	5.914
Full	36	36	36	36
$[\text{Fe}(\text{44mBpy})_3]^{2+}$	0.31	0.13	0.00	0.00
$[\text{Fe}(\text{44mBpy})_3\text{H}]^{3+}$	0.69	0.87	1.00	1.00
pH 1.9	300 K	325 K	345 K	365 K
3 (s)	3.799	2.687	1.744	1.436
4 (CH ₃)	11.212	8.087	5.594	3.779
5 (d)	3.675	2.630	1.827	1.249
6 (d)	3.675	2.630	1.827	1.249
3* (s)	2.306	3.217	4.181	4.577
4* (CH ₃)	6.788	9.997	12.431	14.078
5* (d)	2.285	3.423	4.251	4.938
6* (d)	2.260	3.330	4.144	4.694
Full	36	36	36	36
$[\text{Fe}(\text{44mBpy})_3]^{2+}$	0.62	0.45	0.31	0.21
$[\text{Fe}(\text{44mBpy})_3\text{H}]^{3+}$	0.38	0.55	0.69	0.79
pH 2.9	300 K	325 K	345 K	365 K
3 (s)	4.139	3.301	3.423	2.644
4 (CH ₃)	13.458	11.118	7.887	7.611
5 (d)	4.106	3.308	2.886	2.331
6 (d)	4.106	3.308	2.886	2.331
3* (s)	1.768	2.442	2.880	3.305
4* (CH ₃)	5.095	7.576	9.642	10.660
5* (d)	1.629	2.414	3.185	3.568
6* (d)	1.698	2.533	3.211	3.550
Full	36	36	36	36
$[\text{Fe}(\text{44mBpy})_3]^{2+}$	0.72	0.58	0.47	0.41
$[\text{Fe}(\text{44mBpy})_3\text{H}]^{3+}$	0.28	0.42	0.53	0.59



Scheme 14. Completely reversible color change upon heating of $[\text{Fe}(44\text{mBpy})_3]^{2+}$ in $\text{D}_2\text{O}/\text{H}_2\text{O}$ mixture at pH 1.0.

As it can be seen in Scheme 14 the alterations during heating are completely reversible ruling out any decomposition of the discussed systems. The spectra are completely recovered after cooling down. Scheme 14 shows that the proton interaction with the diamagnetic complexes happens alongside a color change from the typical reddish color around RT to a colorless state at elevated temperatures (in this case shown for $[\text{Fe}(44\text{mBpy})_3]^{2+}$ in $\text{D}_2\text{O}/\text{H}_2\text{O}$ at pH 1.0). The color is completely restored when the solution has cooled to RT. This observation applies to all other ^1H -NMR spectra which are completely restored after recovering from elevated temperatures.

$[\text{Fe}(\text{55mBpy})_3]^{2+}$ was analyzed in a similar way via $^1\text{H-NMR}$ spectroscopy featuring also coordinative changes at low pH as it is demonstrated in Figure 13A. At neutral pH 5.9 the complex features two doublets belonging to position 3 (8.362, 8.390 ppm) and 4 (7.89, 7.92 ppm) and two singlets belonging to 6 (7.20 ppm) and the CH_3 -group (2.155 ppm). Analogously to $[\text{Fe}(\text{44mBpy})_3]^{2+}$ or $[\text{Fe}(\text{Bpy})_3]^{2+}$ new sets of signals are appearing at low pH consisting of two singlets and a multiplet. The multiplet (8.213, 8.240, 8.266, 8.293 ppm) belongs to 3* and 4* and could not be separated. The smaller singlet at 8.658 ppm represents proton 6* while the bigger one belongs to the methyl group (2.526 ppm) of the protonated species $[\text{Fe}(\text{55mBpy})_3\text{H}]^{3+}$. It should be noted that essentially no line broadening can be observed here indicating that the newly formed adduct is still diamagnetic.

The γH^+ versus pH is given in Figure 13B rising up to 0.5 at pH 1.0. This value is significantly lower compared to $\text{Fe}[(\text{44mBpy})_3]^{2+}$ where nearly 0.75 were found at the same pH. See Table 13 for further corresponding NMR data. This demonstrates the ability of the substituent at the aromatic ring to influence the proton acceptance at the nitrogen donor and opens up possibilities to tailor this proton acceptability.

Solutions of $[\text{Fe}(\text{55mBpy})_3]^{2+}$ at pH 1.0, 1.9 and 2.9 were heated from 300 K to 365 K what again leads to a linear rise of γH^+ displayed in Figure 13C. For pH 1.0 full protonation is observed at 365 K. At pH 1.9 protonation reaches only 0.6 and only 0.5 at pH 2.9. The spectra have also a strong paramagnetic shift and the line broadening intensifies with rising T (see Table 14 and Figure 14) what would indicate also the presence of a protonated paramagnetic species which cannot be seen in $^1\text{H-NMR}$ spectroscopy as it could be observed previously. It was also not possible to change this by varying the acquisition time and the observed spectral area (see also Appendix A11).

Unfortunately, it was also not possible to investigate the paramagnetic respectively SCO system $[\text{Fe}(\text{Bpp})_2]^{2+}$ with $^1\text{H-NMR}$ spectroscopy since signal-to-noise ratio was too strong and small variations in multi-peak spectra of paramagnetic compounds cannot be sufficiently analyzed as it was the case for the diamagnetic systems. Also $^{13}\text{C-NMR}$ failed to give suitable results for this system.

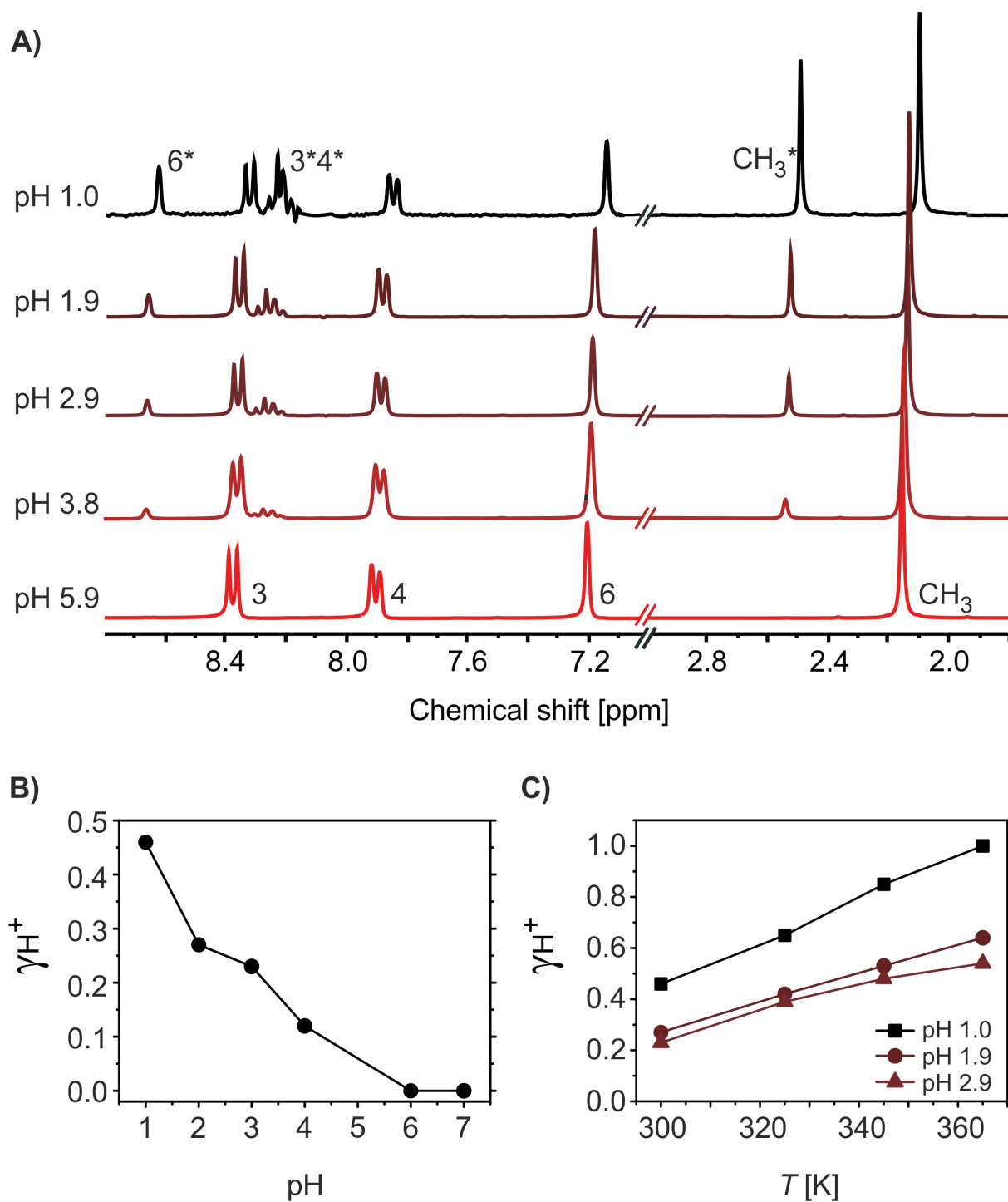


Figure 13. A: ^1H -NMR spectroscopy of $[\text{Fe}(\text{55mBpy})_3]^{2+}$ in $\text{D}_2\text{O}/\text{H}_2\text{O}$ mixtures at different pH-values; **B:** plot of γ_{H^+} (calculated from A) against the pH giving an exponential relationship; **C:** plot of γ_{H^+} against the temperature for different pH-values giving linear functions.

Results and Discussion

Table 13. Peak positions and integrals for $[\text{Fe}(\text{55mBpy})_3]^{2+}$ at 300 K and different pH-values.

$[\text{Fe}(\text{55mBpy})_3]^{2+}$	Peak positions at different pH-values at 300 K				
	pH 5.9	pH 3.8	pH 2.9	pH 1.9	pH 1.0
3 (d)	8.362, 8.390	8.353, 8.381	8.345, 8.373	8.339, 8.367	8.306, 8.334
4 (d)	7.889, 7.916	7.879, 7.906	7.872, 7.898	7.864, 7.892	7.829, 7.857
5 (CH₃)	2.155	2.146	2.137	2.132	2.096
6 (s)	7.200	7.190	7.181	7.174	7.133
3* (m)	-	8.250, 8.280	8.216 - 8.299	8.210 - 8.292	8.183 - 8.255
4* (m)	-	8.250, 8.280	8.216 - 8.299	8.210 - 8.292	8.210 - 8.292
5* (CH₃)	-	2.539	2.531	2.525	2.491
6* (s)	-	8.669	8.661	8.655	8.622
$[\text{Fe}(\text{55mBpy})_3]^{2+}$	Integrals at different pH-values at 300 K				
	pH 5.9	pH 3.8	pH 2.9	pH 1.9	pH 1.0
3 (d)	6.302	5.220	4.908	4.724	3.499
4 (d)	5.906	5.490	4.694	4.537	3.485
5 (CH₃)	17.988	15.617	16.068	15.336	10.389
6 (s)	5.804	5.506	4.785	4.729	3.748
3* (m)	0.000	0.708	0.905	1.093	2.538
4* (m)	0.000	0.708	0.905	1.093	2.538
5* (CH₃)	0.000	2.073	2.850	3.455	7.386
6* (s)	0.000	0.677	0.884	1.033	2.417
Full	36	36	36	36	36
$[\text{Fe}(\text{55mBpy})_3]^{2+}$	1.00	0.88	0.85	0.81	0.59
$[\text{Fe}(\text{55mBpy})_3\text{H}]^{3+}$	0.00	0.12	0.15	0.19	0.41

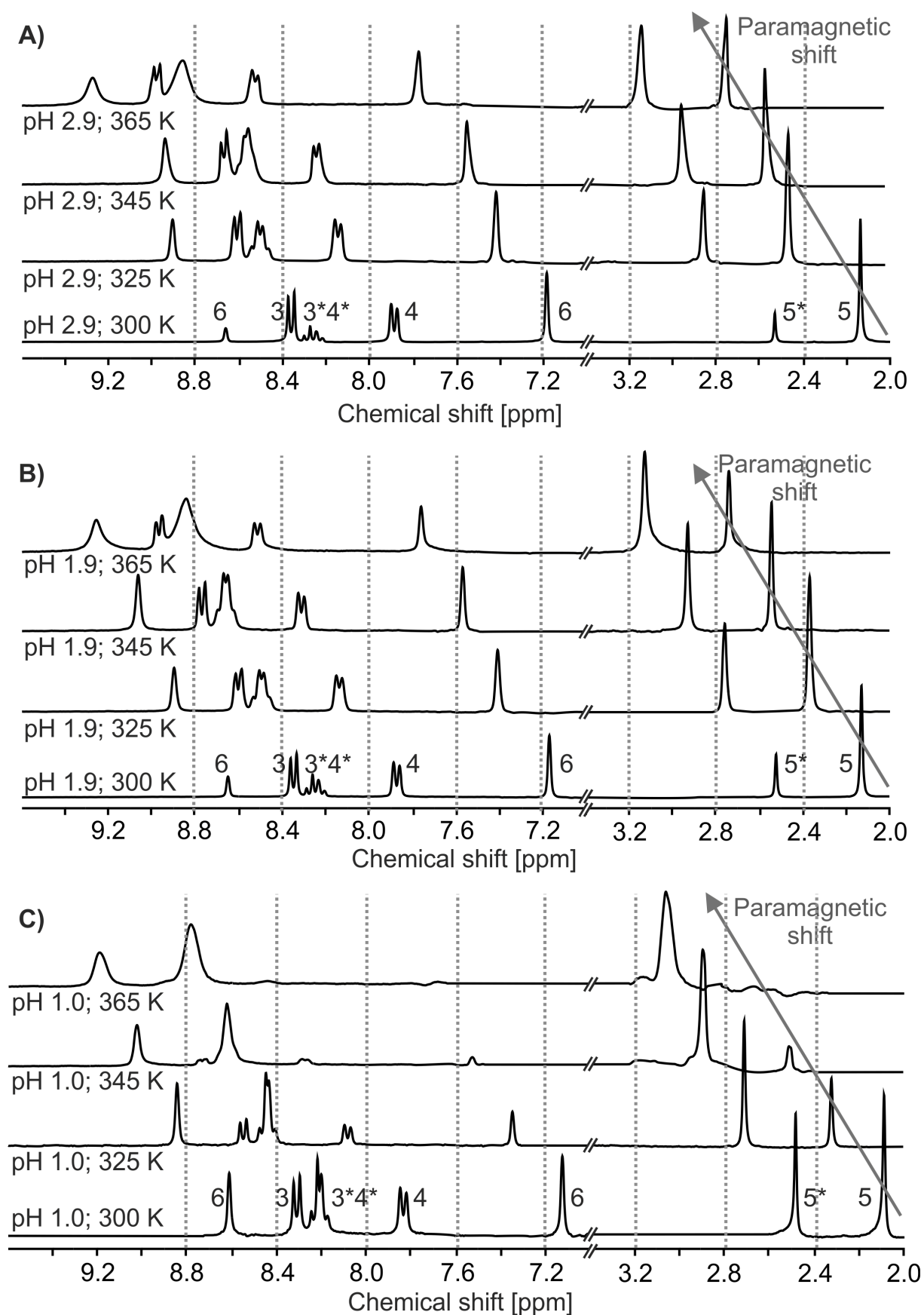


Figure 14. T -dependent ^1H -NMR spectra of $[\text{Fe}(\text{55mBpy})_3]^{2+}$ in $\text{D}_2\text{O}/\text{H}_2\text{O}$ at pH 1.0, 1.9, 2.9.

Results and Discussion

Table 14. Integrals for $[\text{Fe}(\text{55mBpy})_3]^{2+}$ at pH 1.0, 1.9, 2.9 and different temperatures.

pH 1.0	300 K	325 K	345 K	365 K
3 (d)	3.319	2.140	0.993	0.000
4 (d)	3.335	2.078	1.115	0.000
5 (CH₃)	9.764	6.368	2.541	0.000
6 (s)	2.882	1.969	0.667	0.000
3* (m)	2.684	3.942	5.188	6.395
4* (m)	2.684	3.942	5.188	6.395
5* (CH₃)	8.500	11.686	15.218	17.408
6* (s)	2.833	3.876	5.091	5.803
Full	36	36	36	36
$[\text{Fe}(\text{55mBpy})_3]^{2+}$	0.54	0.35	0.15	0.00
$[\text{Fe}(\text{55mBpy})_3\text{H}]^{3+}$	0.46	0.65	0.85	1.00
pH 1.0	300 K	325 K	345 K	365 K
3 (d)	4.619	3.835	2.985	2.335
4 (d)	4.510	3.605	2.958	2.292
5 (CH₃)	12.895	9.986	8.400	6.255
6 (s)	4.222	3.329	2.709	2.085
3* (m)	1.697	2.643	3.391	4.022
4* (m)	1.697	2.643	3.391	4.022
5* (CH₃)	4.649	7.240	8.860	11.112
6* (s)	1.710	2.720	3.305	3.876
Full	36	36	36	36
$[\text{Fe}(\text{55mBpy})_3]^{2+}$	0.73	0.58	0.47	0.36
$[\text{Fe}(\text{55mBpy})_3\text{H}]^{3+}$	0.27	0.42	0.53	0.64
pH 2.9	300 K	325 K	345 K	365 K
3 (d)	4.879	4.029	3.267	2.902
4 (d)	4.633	3.737	3.093	2.926
5 (CH₃)	13.900	10.900	9.516	8.024
6 (s)	4.332	3.378	2.934	2.672
3* (m)	1.381	2.345	2.801	3.269
4* (m)	1.381	2.345	2.801	3.269
5* (CH₃)	4.073	6.872	8.784	9.758
6* (s)	1.422	2.394	2.804	3.180
Full	36	36	36	36
$[\text{Fe}(\text{55mBpy})_3]^{2+}$	0.77	0.61	0.52	0.46
$[\text{Fe}(\text{55mBpy})_3\text{H}]^{3+}$	0.23	0.39	0.48	0.54

In a similar fashion $^1\text{H-NMR}$ spectroscopy was conducted for compound $[\text{Fe}(\text{4mBpy})_3]^{2+}$, the results are given in Figure 15. At pH 5.9 the only signals that could be observed belong to the original complex. At pH 1.0 a γH^+ value of 0.40 was found lower than it was observed for $[\text{Fe}(\text{44mBpy})_3]^{2+}$ and $[\text{Fe}(\text{55mBpy})_3]^{2+}$. Upon heating this amount rises steadily to $\gamma\text{H}^+ = 0.94$, slightly lower than it was observed for $[\text{Fe}(\text{44mBpy})_3]^{2+}$ and $[\text{Fe}(\text{55mBpy})_3]^{2+}$. The pH-response of $[\text{Fe}(\text{5mBpy})_3]^{2+}$ is even more reduced (Figure 16) and at pH 1.0 only 25% of protonated species are found with $\gamma\text{H}^+ = 0.25$. Interestingly, $[\text{Fe}(\text{5mBpy})_3]^{2+}$ can be influenced more strongly by temperature and has at 365 K a $\gamma\text{H}^+ = 0.90$. Full $^1\text{H-NMR}$ data are given in Table 15 and Table 16 (see also Appendix A12).

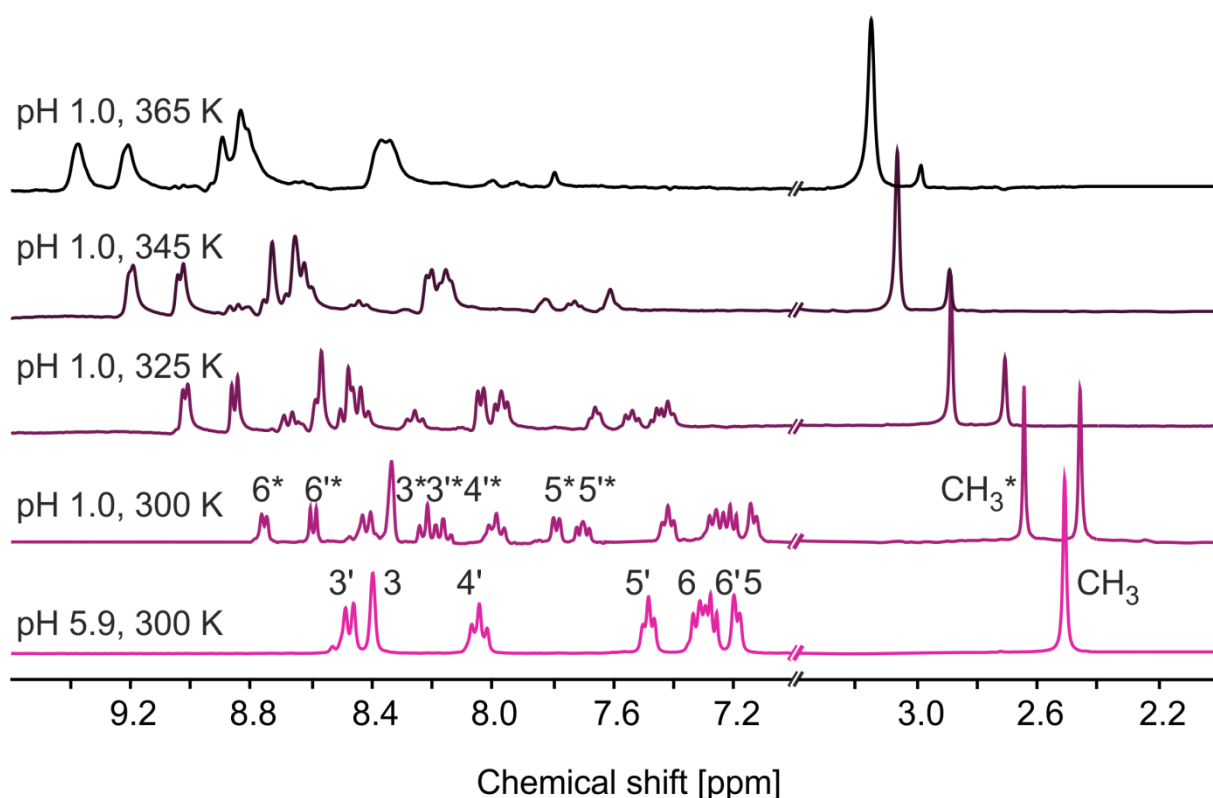


Figure 15. $^1\text{H-NMR}$ spectroscopy of $[\text{Fe}(\text{4mBpy})_3]^{2+}$ in $\text{D}_2\text{O}/\text{H}_2\text{O}$ mixtures at different pH-values and temperatures.

Results and Discussion

Table 15. Peak positions and integrals for $[\text{Fe}(\text{4mBpy})_3]^{2+}$ at different pH and temperatures.

$[\text{Fe}(\text{4mBpy})_3]^{2+}$	Peak positions at different pH and temperatures				
	pH 5.9, 300 K	pH 1.0, 300 K	pH 1.0, 325 K	pH 1.0, 345 K	pH 1.0, 365 K
3	8.396	8.334	8.567 - 8.587	8.732 - 8.758	8.895
4 (CH₃)	2.510	2.450	2.712	2.893	3.070
5	7.176, 7.195	7.12, 7.140	7.395, 7.413	7.588 - 7.607	7.790
6, 6'	7.252 - 7.330	7.187 - 7.276	7.413 - 7.469	7.705 - 7.746	7.912
3'	8.460, 8.487	8.386 - 8.474	8.643 - 8.691	8.814 - 8.872	9.050
4'	8.016 - 8.067	7.960 - 8.011	8.230 - 8.281	8.417 - 8.469	8.650
5'	7.460 - 7.497	7.677 - 7.718	7.641 - 7.671	7.825	7.997
3*	8.396	8.334	8.567 - 8.587	8.732 - 8.758	8.895
4* (CH₃)	-	2.636	2.890	3.068	3.242
5*	-	7.776, 7.795	8.027, 8.046	8.136 - 8.219	8.336 - 8.366
6*	-	8.750, 8.766	9.011, 9.027	9.194, 9.209	9.371
3'* 4'*	-	8.136 - 8.241	8.410 - 8.503	8.598 - 8.685	8.808 - 8.832
5'*	-	7.396 - 7.433	7.948 - 7.988	8.136 - 8.219	8.336 - 8.366
6'*	-	8.585, 8.604	8.846, 8.866	9.026, 9.046	9.207
$[\text{Fe}(\text{4mBpy})_3]^{2+}$	Integrals at different pH and temperatures				
	pH 5.9, 300 K	pH 1.0, 300 K	pH 1.0, 325 K	pH 1.0, 345 K	pH 1.0, 365 K
3	3.012	1.792	1.008	0.527	-
4 (CH₃)	8.938	5.330	2.994	1.571	0.530
5	3.038	1.806	0.995	0.509	-
6, 6'	6.009	3.579	2.015	1.005	-
3'	3.000	1.821	1.017	0.357	-
4'	2.988	1.790	1.024	0.509	-
5'	3.014	1.789	1.008	0.524	-
3*	0.000	1.200	1.987	2.486	-
4* (CH₃)	0.000	3.648	5.948	7.439	8.470
5*	0.000	1.217	1.988	2.527	-
6*	0.000	1.233	2.002	2.507	-
3'* 4'*	0.000	2.431	3.969	4.994	-
5'*	0.000	1.165	2.022	2.527	-
6'*	0.000	1.202	2.023	2.519	-
Full	30	30	30	30	9
$[\text{Fe}(\text{4mBpy})_3]^{2+}$	1.00	0.60	0.34	0.17	0.06
$[\text{Fe}(\text{4mBpy})_3\text{H}]^{3+}$	0.00	0.40	0.66	0.83	0.94

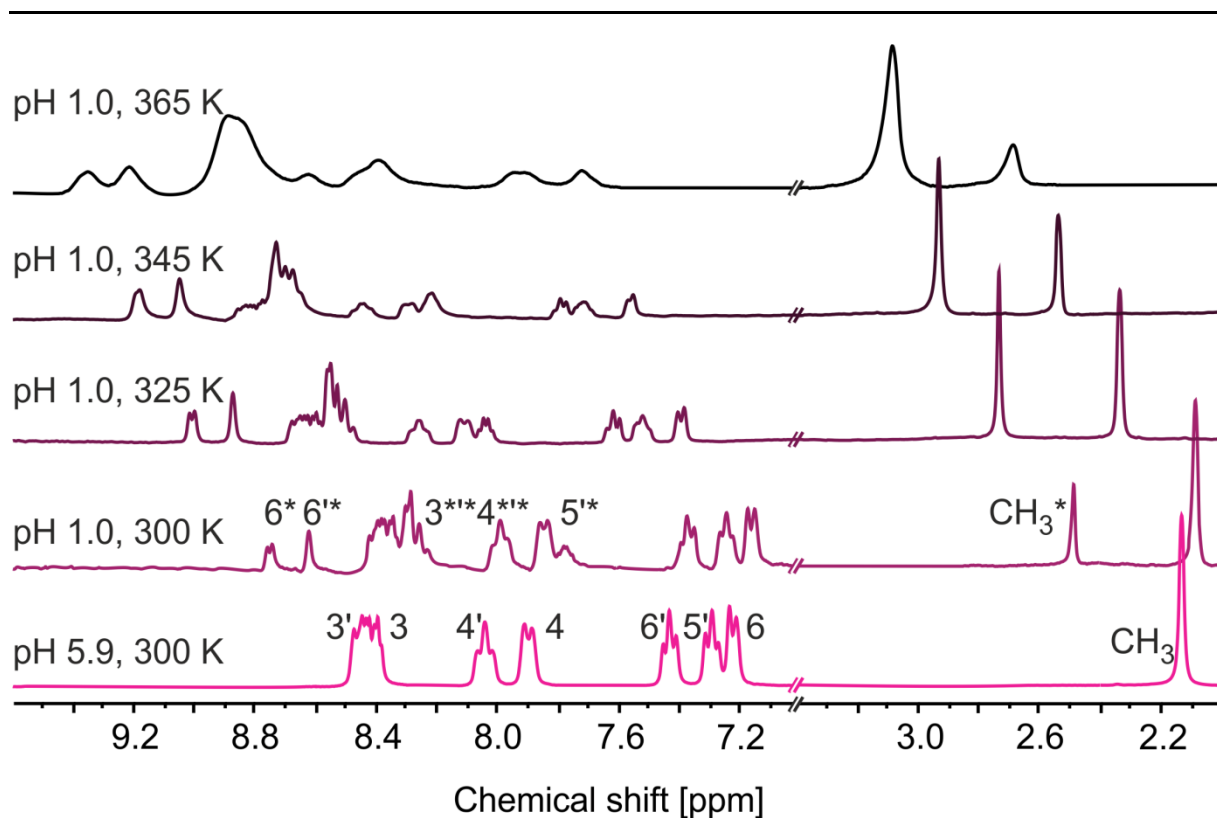


Figure 16. $^1\text{H-NMR}$ spectroscopy of $[\text{Fe}(\text{5mBpy})_3]^{2+}$ in $\text{D}_2\text{O}/\text{H}_2\text{O}$ mixtures at different pH-values and temperatures.

It must be noted that it was difficult to evaluate the integral values of $[\text{Fe}(\text{Bpy})_3]^{2+}$ at elevated temperatures precisely. Due to the strong line broadening this was not possible in all cases. For the methylated derivatives the situation is different since the signal of the characteristic methyl group is also at elevated temperatures sharp and not overlapping with other signals what makes integration always possible. Therefore the overall integral sum in some tables is just mirroring the amount of protons at the methyl group.

Furthermore, it is important to understand that all γH^+ values discussed in this section are of course related to the visible amount which is indeed observable via $^1\text{H-NMR}$ spectroscopy. Obviously, the overall amount of protonated species must be higher because there is an additional portion belonging to the paramagnetic species which is not observable in $^1\text{H-NMR}$ spectroscopy. This should always be kept in mind related to the discussion. Nevertheless, if only protonated species are observed in $^1\text{H-NMR}$ spectra then the complete sample must be protonated. The underlying equilibrium condition will be further analyzed in the following sections and based on this it appeared to be most helpful to talk about γH^+ and γ_{HS} .

Results and Discussion

Table 16. Peak positions and integrals for $[\text{Fe}(\text{5mBpy})_3]^{2+}$ at different pH and temperatures.

$[\text{Fe}(\text{5mBpy})_3]^{2+}$	Peak positions at different pH and temperatures				
	pH 5.9, 300 K	pH 1.0, 300 K	pH 1.0, 325 K	pH 1.0, 345 K	pH 1.0, 365 K
3, 3'	8.380 - 8.469	8.352 - 8.419	8.623 - 6.676	8.811	8.820 - 8.883
4	7.881, 7.905	7.828, 7.854	8.093, 8.126	8.275, 8.299	8.389
5 (CH₃)	2.131	2.082	2.334	2.513	2.689
6	7.204, 7.226	7.142, 7.166	7.380, 7.397	7.544, 7.561	7.713
4'	8.013 - 8.060	7.962 - 8.011	8.22 - 8.282	8.411 - 8.463	8.615
5'	7.263 - 7.306	7.217 - 7.257	7.490 - 7.535	7.707	7.918
6'	7.403 - 7.446	7.344 - 7.388	7.592 - 7.633	7.766 - 7.802	7.918
3* '*, 4* '*	-	8.227 - 8.328	8.490 - 8.558	8.670 - 8.800	8.820 - 8.883
5* (CH₃)	-	2.484	2.733	2.910	3.087
6*	-	8.620	8.899, 9.015	9.178, 9.192	9.349
5'*	-	7.746 - 7.776	8.011 - 8.057	8.153	8.389
6'*	-	8.740, 8.757	8.871	9.047	9.206
$[\text{Fe}(\text{5mBpy})_3]^{2+}$	Integrals at different pH and temperatures				
	pH 5.9, 300 K	pH 1.0, 300 K	pH 1.0, 325 K	pH 1.0, 345 K	pH 1.0, 365 K
3, 3'	6.003	4.416	3.415	1.739	-
4	2.987	2.259	1.623	0.983	-
5 (CH₃)	8.992	6.711	5.026	3.460	0.904
6	3.017	2.310	1.648	0.967	-
4'	2.998	2.301	1.625	0.929	-
5'	2.997	2.233	1.270	0.946	-
6'	3.004	2.195	1.624	0.912	-
3* '*, 4* '*	0.000	3.264	5.454	8.288	-
5* (CH₃)	0.000	1.967	4.279	6.102	8.096
6*	0.000	0.736	1.347	1.898	-
5'*	0.000	0.891	1.326	1.901	-
6'*	0.000	0.717	1.364	1.876	-
Full	30	30	30	30	9
$[\text{Fe}(\text{5mBpy})_3]^{2+}$	1.00	0.75	0.54	0.33	0.10
$[\text{Fe}(\text{5mBpy})_3\text{H}]^{3+}$	0.00	0.25	0.46	0.67	0.90

2.1.3 Behavior in aqueous solution: UV-Visible experiments

UV-Vis spectroscopy of diluted aqueous solutions was conducted between 200 nm and 600 nm since optical changes upon protonation could already be observed with the naked eye. Diluted solutions ($c = 0.010$ mmol/L) of $[\text{Fe}(\text{Bpy})_3]^{2+}$ with varying pH were prepared and analyzed what is given in Figure 17A and Figure 17C ($c = 0.020$ mol/L). The characteristic MLCT-envelope (around 525 nm) is reduced gradually with rising proton concentration. The absorbance goes from 0.13 at pH 5.9 to 0.04 at pH 1.9. The d-d-transition around 350 nm is also reduced. High-energy MLCT-bands are usually observed for LS states ($S = 0$) and move to lower energy or vanish completely for HS states ($S = 2$).^[8] A strong bathochromic shift from 290 nm to 300 nm upon protonation also appears for the π - π^* -transitions what is usually observed for pyridine- or imidazole-like aromatic rings.^[134] The bathochromic shift indicates an interaction at the nitrogen-donor of the aromatic rings since it is known that interaction with protons causes either a bathochromic or hypsochromic shift of the related transition.

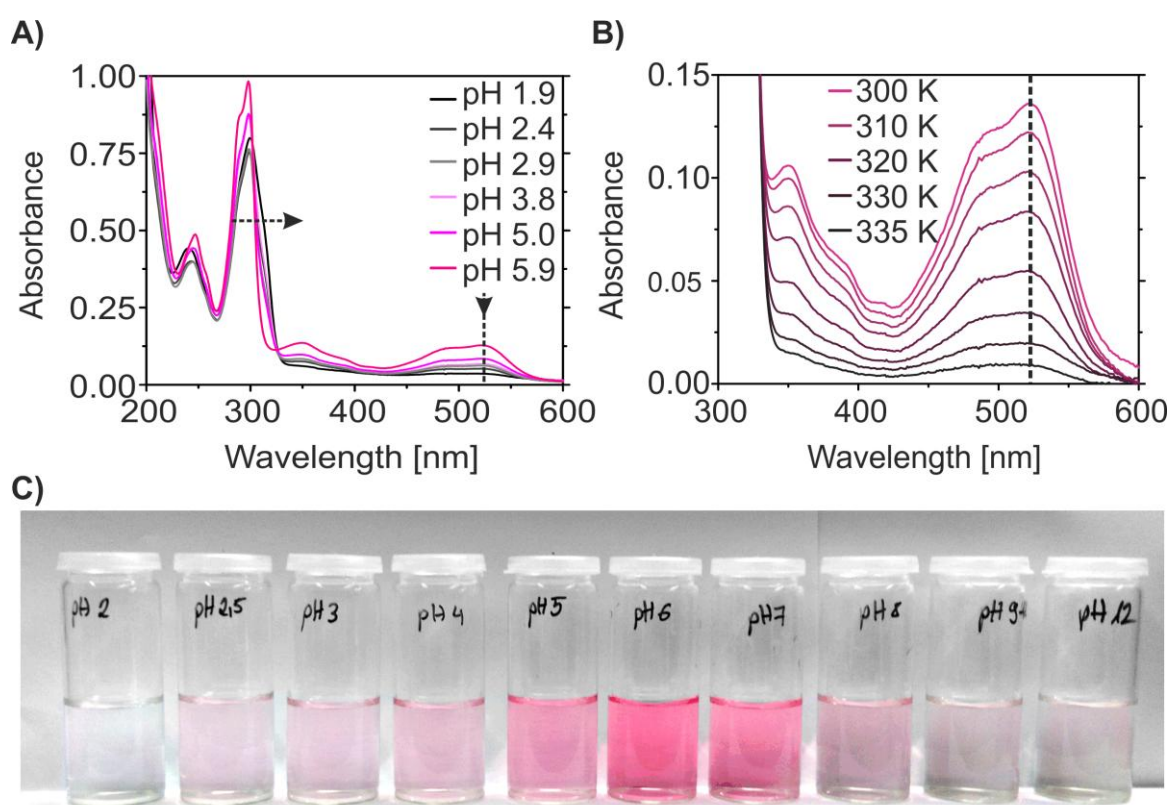


Figure 17. **A:** pH-dependent UV-Vis spectra of $[\text{Fe}(\text{Bpy})_3]^{2+}$ ($c = 0.010$ mmol/L). **B:** Excerpt of the T -dependent UV-Vis spectra of $[\text{Fe}(\text{Bpy})_3]^{2+}$ ($c = 0.084$ mmol/L) at pH 1.9. **C:** Picture of $[\text{Fe}(\text{Bpy})_3]^{2+}$ solutions (for all $c = 0.020$ mmol/L) at different pH.

Temperature-dependent UV-Vis spectra were also recorded for less diluted solutions of $[\text{Fe}(\text{Bpy})_3]^{2+}$ ($c = 0.084 \text{ mmol/L}$) at pH 1.9 still absorbing in the MLCT-region as it can be seen in Figure 17B. The temperature was varied between 300 K and 335 K leading to a nearly complete extinction of the MLCT-envelope in a linear manner as it was already observed during temperature-dependent $^1\text{H-NMR}$ spectroscopy. The absorbance changes reversibly between 0.13 and 0.01 while varying the temperature between 300 K and 335 K. Additional graphs where the absorbance and wavelength of the MLCT-band and $\pi\text{-}\pi^*$ -transition were selectively followed are shown in the Appendix A13.

Changes of the optical properties due to protonation could already be observed with the naked eye during $^1\text{H-NMR}$ spectroscopy upon the heating of acidic complex solutions of $[\text{Fe}(44\text{mBpy})_3]^{2+}$ (see Scheme 14). Therefore, UV-Vis spectroscopy was conducted between 200 nm and 600 nm. Diluted solutions ($c = 0.008 \text{ mmol/L}$) of $[\text{Fe}(44\text{mBpy})_3]^{2+}$ with varying pH were prepared and analyzed given in Figure 18A and Figure 18C ($c = 0.164 \text{ mol/L}$). The typical MLCT-transition (529 nm) is reduced gradually with rising proton concentration. The absorbance goes from 0.12 at pH 5.9 to 0.02 at pH 1.9. The d-d-transition around 350 nm is also reduced. High-energy MLCT-bands are usually observed for LS states ($S = 0$) and move to lower energy or vanish completely for HS states ($S = 2$).^[8] A bathochromic shift from 280 nm to 296 nm is also observed upon protonation for the $\pi\text{-}\pi^*$ -transitions which is usually indicative for pyridine- or imidazole-like aromatic rings.^[134] Isosbestic points appear at 227 nm, 279 nm, 303 nm, 322 nm and 600 nm.

Furthermore, temperature-dependent UV-Vis spectroscopy was also conducted for diluted aqueous solutions of $[\text{Fe}(44\text{mBpy})_3]^{2+}$ ($c = 0.082 \text{ mmol/L}$) at pH 1.9 where they were still absorbing in the MLCT-region as it can be seen in Figure 18B. The temperature was varied between 300 K and 335 K and was leading again to a complete extinction of the MLCT-envelope in a linear manner as it was already observed during temperature-dependent $^1\text{H-NMR}$ spectroscopy. The absorbance is changed reversibly between 0.10 and 0.01 varying the temperature between 300 K and 335 K. Supplementary graphs where the absorbance and wavelength of the MLCT-band and $\pi\text{-}\pi^*$ -transition were selectively followed for $[\text{Fe}(44\text{mBpy})_3]^{2+}$ are also shown in the Appendix A14.

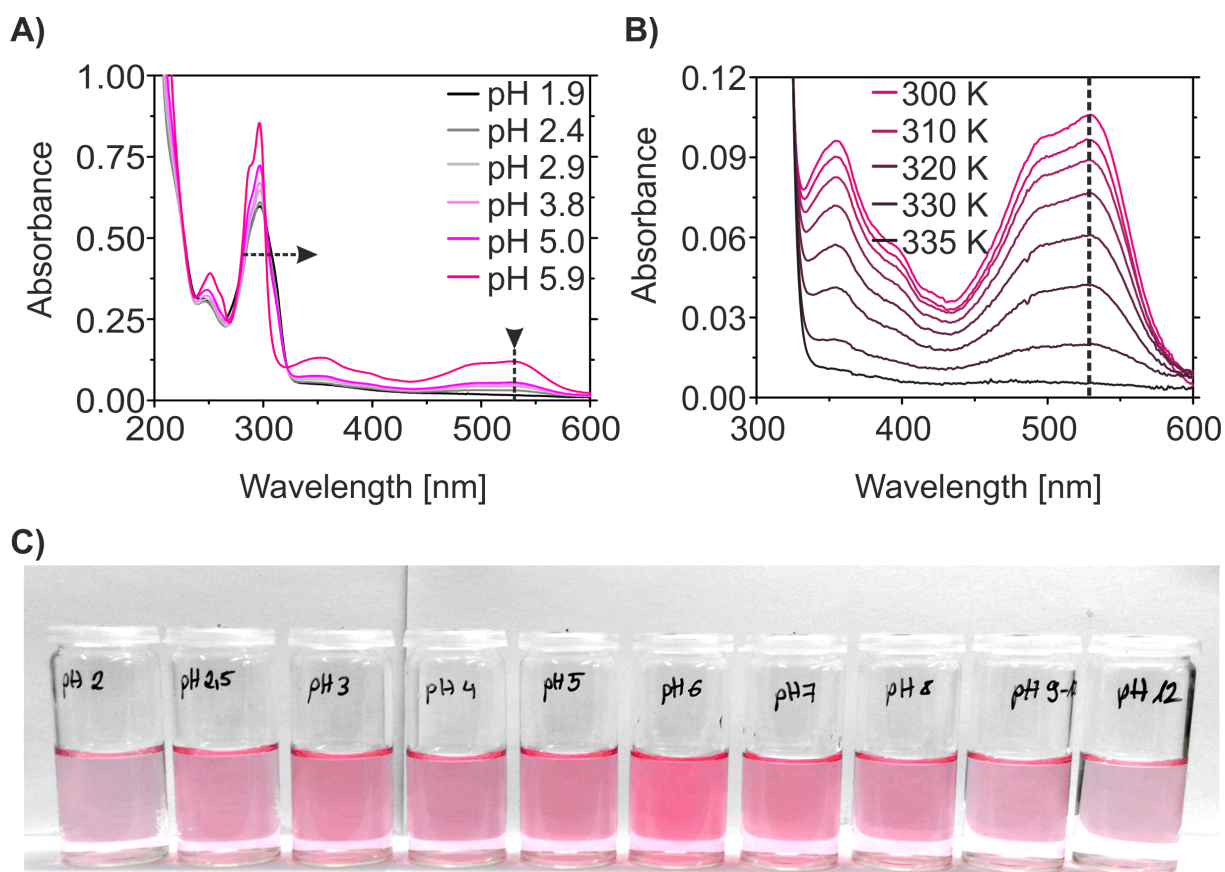


Figure 18. **A:** UV-Vis spectroscopy of $[\text{Fe}(\text{44mBpy})_3]^{2+}$ in H_2O at different pH values ($c = 0.008 \text{ mmol/L}$); **B:** T -dependent UV-Vis spectroscopy of $[\text{Fe}(\text{44mBpy})_3]^{2+}$ at pH 1.9 ($c = 0.082 \text{ mmol/L}$); **C:** Photograph of the variable optical properties of $[\text{Fe}(\text{44mBpy})_3]^{2+}$ due to pH differences ($c = 0.164 \text{ mmol/L}$).

Similar UV-Vis measurements were also conducted for $[\text{Fe}(\text{55mBpy})_3]^{2+}$. In Figure 19A the pH-dependent UV-Vis spectra of $[\text{Fe}(\text{55mBpy})_3]^{2+}$ in aqueous solutions ($c = 0.008 \text{ mmol/L}$) with different pH are given. The MLCT-transition at 509 nm bleaches gradually with rising proton concentration. Lowering the pH from 5.9 to 1.0 reduces the absorbance from 0.10 to 0.01. The d-d-transition around 350 nm is simultaneously reduced. The π - π^* -transition is bathochromically shifted from 292 nm to 308 nm. Isosbestic points are found at 243 nm, 314 nm, 337 nm and 585 nm. An aqueous solution of $[\text{Fe}(\text{55mBpy})_3]^{2+}$ at pH 1.9 ($c = 0.082 \text{ mmol/L}$) measured between 300 K and 335 K bleaches completely in a reversible way. The absorbance of the MLCT-transition at 509 nm is reduced from 0.3 to 0.0 upon heating as it can be seen in Figure 19B. This finding is again highly congruent with T -dependent $^1\text{H-NMR}$ where a reversible process was found. The variation at different pH can

still be seen with the naked eye as given in Figure 19C where the typical red color bleaches with rising proton concentration.

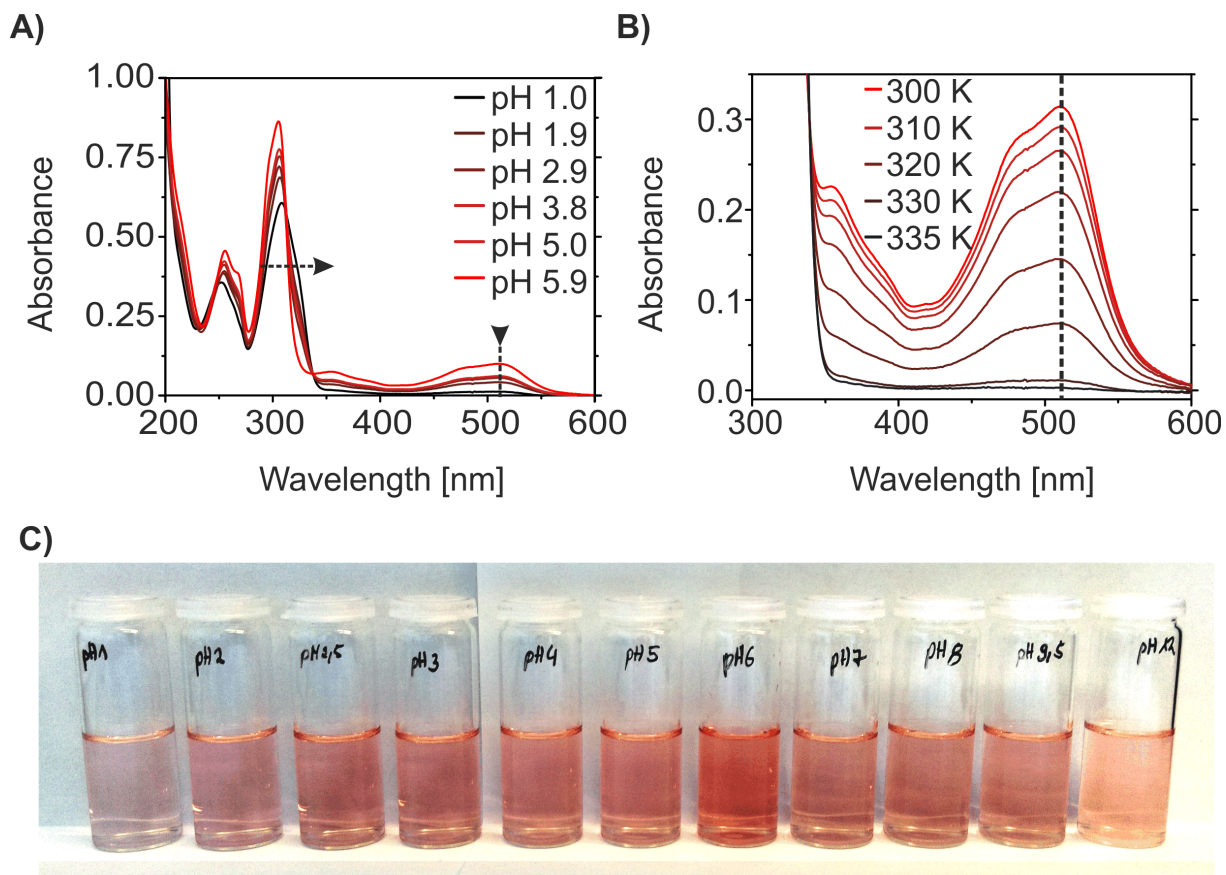


Figure 19. **A:** UV-Vis spectroscopy of $[\text{Fe}(\text{55mBpy})_3]^{2+}$ in H_2O at different pH values ($c = 0.008$ mmol/L); **B:** T -dependent UV-Vis spectroscopy of $[\text{Fe}(\text{55mBpy})_3]^{2+}$ at pH 1.9 ($c = 0.082$ mmol/L); **C:** Photograph of the variable optical properties of $[\text{Fe}(\text{55mBpy})_3]^{2+}$ due to pH differences ($c = 0.164$ mmol/L).

The three discussed LS systems $[\text{Fe}(\text{Bpy})_3]^{2+}$, $[\text{Fe}(\text{44mBpy})_3]^{2+}$ and $[\text{Fe}(\text{55mBpy})_3]^{2+}$ show pH-dependent optical properties. The vanishing of the MLCT suggests a LS to HS transition upon protonation since the later is commonly colorless due to occupation of t_{2g} orbitals by unpaired electrons.^[8] The bathochromic shift of the π - π^* -transition with rising proton concentration indicates an interaction of the protons with the aromatic nitrogen-donor acting as a base. These findings in acidic media are in line with the ¹H-NMR experiments and suggest the formation of a protonated HS species. Therefore it appeared logically compelling

to study the interaction of protons with SCO systems and if they could also trigger a similar behavior.

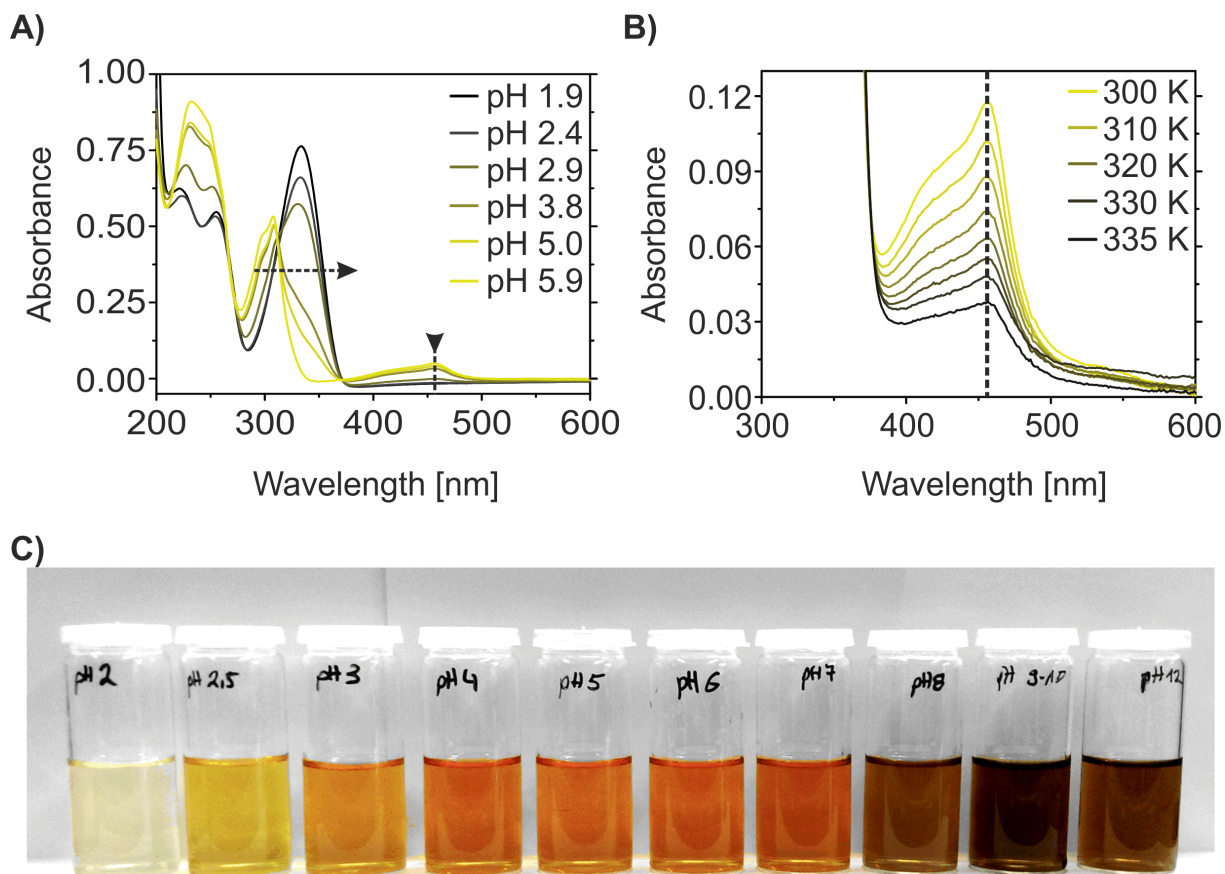


Figure 20. **A:** UV-Vis spectroscopy of $[\text{Fe}(\text{Bpp})_2]^{2+}$ in H_2O at different pH values ($c = 0.011 \text{ mmol/L}$); **B:** Temperature-dependent UV-Vis spectroscopy of $[\text{Fe}(\text{Bpp})_2]^{2+}$ at pH 1.9 ($c = 0.104 \text{ mmol/L}$); **C:** Photograph of the variable optical properties of $[\text{Fe}(\text{Bpp})_2]^{2+}$ due to pH differences ($c = 0.210 \text{ mmol/L}$).

In Figure 20A the pH-dependent UV-Vis spectra of the SCO complex $[\text{Fe}(\text{Bpp})_2]^{2+}$ in aqueous solution ($c = 0.011 \text{ mmol/L}$) are depicted. Upon lowering of the pH from 5.9 to 1.9 the intensity of the characteristic MLCT-transition at 458 nm is reduced from 0.06 to 0.00. This hints towards a modulation of the SCO properties of the sample. A very large bathochromic shift of the $\pi-\pi^*$ -transition is observed in line with the additional number of nitrogen-donor groups compared to bipyridine-like systems. The $\pi-\pi^*$ -transition moves from

300 nm to 330 nm and gains remarkably in intensity upon protonation. Isosbestic points appear at 266 nm, 311 nm, 371 nm and 577 nm. The differences in optical behavior can be easily observed with the unaided eye since the brown solution becomes yellowish respectively colorless during proton addition (see Figure 20C).

Acidic solutions at pH 1.9 ($c = 0.104$ mmol/L) were also measured temperature-dependent what is displayed in Figure 20B. Similarly to the previous findings a further vanishing of the MLCT-envelope is observed when the temperature is raised from 300 K to 335 K. The absorbance is reduced linearly from 0.12 to 0.03 now caused by an interplay between SCO behavior and protonation-induced coordinative changes. This proves that the optical properties of SCO systems like $[\text{Fe}(\text{Bpp})_2]^{2+}$ can be modulated in solution via protonation of the near vicinity. Additional graphs where the absorbance and wavelength of the MLCT-band and π - π^* -transition were selectively followed are shown in the Appendix A15.

2.1.4 Behavior in aqueous solution: Magnetic susceptibility studies

The change of magnetism upon protonation is confirmed by T -dependent SQUID measurements of aqueous $[\text{Fe}(\text{Bpy})_3]^{2+}$ solutions (H_2O , $c = 0.168 \text{ mol/L}$). These experiments were performed at different pH values and are given in Figure 21A as plot of the relative HS fraction γ_{HS} ($\gamma_{\text{HS}} = (\chi_{\text{MT}}T)/(\chi_{\text{MT}}T)_{(S=2)}$ where $(\chi_{\text{MT}}T)_{(S=2)}$ is the theoretical value for a complex with the total spin S of 2) versus T .

At pH 7 γ_{HS} is with 0.03 almost negligible. When lowering the pH γ_{HS} increases first slowly, and below pH 2.5 more abruptly with γ_{HS} values between 0.14 and 0.27 for pH 2 and 1. The solutions are now clearly paramagnetic. This observation can be explained with a pH-dependent spin state switch between a diamagnetic iron(II) LS species and a paramagnetic iron(II) HS species, starting around pH 2.5. As already indicated by NMR spectroscopy, this spin state switch is temperature dependent. At pH 1 γ_{HS} varies between 0.21 and 0.46 while going from 260 K to 350 K. Please note that this pH- and T -dependent change is completely reversible. In Figure 21B the γ_{HS} is plotted against the pH for 300 K and 350 K. It becomes obvious that the T -dependence sets in below pH 3 and increases with the proton concentration as it was already observed in ^1H -NMR spectroscopy.

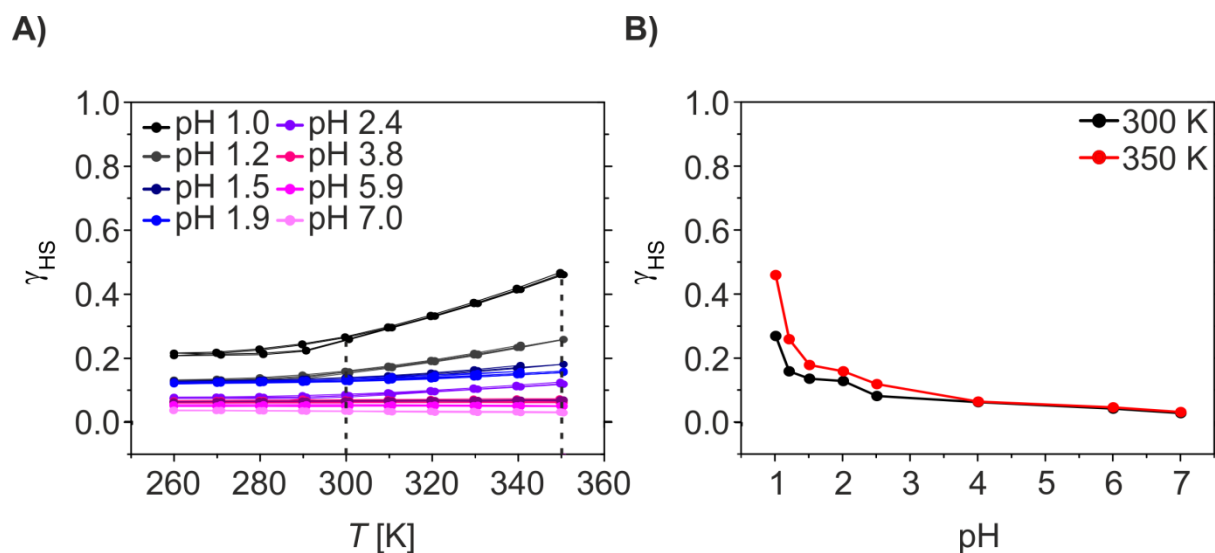


Figure 21. Magnetic characterization of $[\text{Fe}(\text{Bpy})_3]^{2+}$ in aqueous solution ($c = 0.168 \text{ mol/L}$). **A:** Plot of γ_{HS} versus T for the different solutions showing an increasing γ_{HS} by proton concentration and temperature. **B:** pH-dependence of γ_{HS} at 300 K and 350 K calculated from the SQUID data.

The significant changes observed upon protonation via pH- and T -dependent $^1\text{H-NMR}$ and UV-Vis spectroscopy suggest also a proton-driven coordination-induced spin state switch (PD-CISSS) for $[\text{Fe}(\text{44mBpy})_3]^{2+}$, $[\text{Fe}(\text{55mBpy})_3]^{2+}$, $[\text{Fe}(\text{4mBpy})_3]^{2+}$ and $[\text{Fe}(\text{5mBpy})_3]^{2+}$ as we have already seen it for $[\text{Fe}(\text{Bpy})_3]^{2+}$. To monitor the presence of paramagnetic species in solution SQUID measurements were conducted in H_2O . The results are given in Figure 22–26 as a plot of the high-spin fraction γ_{HS} vs T and γ_{HS} vs pH.

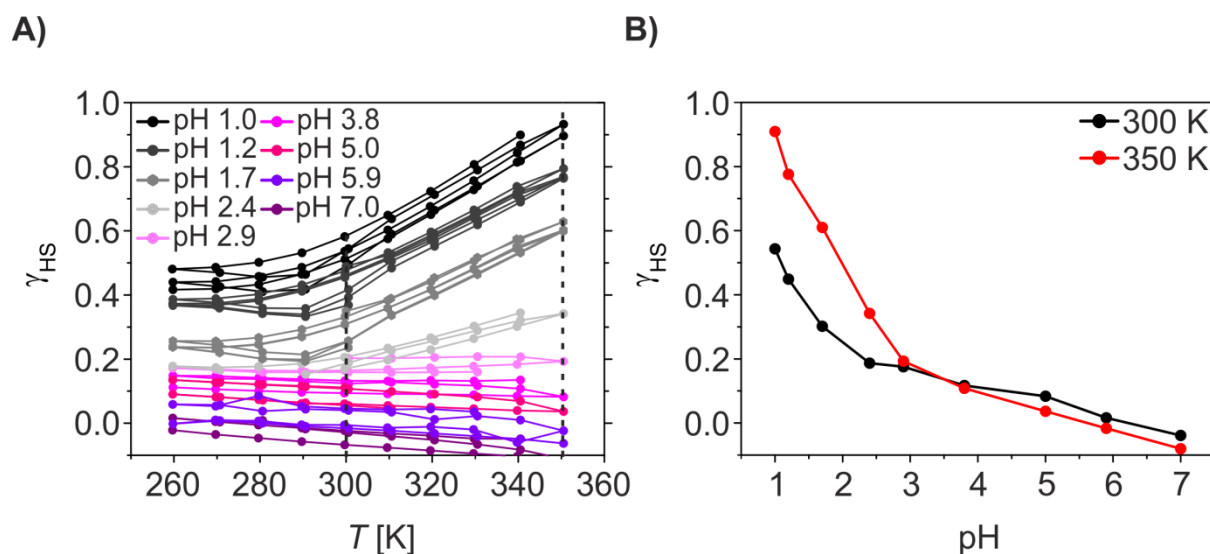


Figure 22. Magnetism of $[\text{Fe}(\text{44mBpy})_3]^{2+}$ in aqueous solution ($c = 29.35$ mmol/L). **A:** Plot of γ_{HS} versus T for the different solutions showing an increasing γ_{HS} by H^+ concentration and temperature. **B:** pH-dependence of γ_{HS} at 300 K and 350 K calculated from the SQUID data.

In Figure 22 the results for $[\text{Fe}(\text{44mBpy})_3]^{2+}$ are given. As it can be seen in Figure 22A is $[\text{Fe}(\text{44mBpy})_3]^{2+}$ essentially diamagnetic ($\gamma_{\text{HS}} = 0.00$) at pH 7.0 over the complete temperature range. At pH 3.0 already 20% ($\gamma_{\text{HS}} = 0.20$) of the molecules are in a HS state. At pH 1.7 already 30% ($\gamma_{\text{HS}} = 0.30$) are in a HS state what can be increased up to 60% ($\gamma_{\text{HS}} = 0.60$) at 350 K. At pH 1.0 at RT 50% ($\gamma_{\text{HS}} = 0.50$) of the molecules are paramagnetic increasing to nearly 100% ($\gamma_{\text{HS}} \sim 1.0$) at 350 K. It should be noted that the switching process is completely reversible. In Figure 22B it becomes obvious that the temperature dependence comes into play below pH 3.0 where a significant amount of paramagnetic $[\text{Fe}(\text{44mBpy})_3\text{H}]^{3+}$ is present. It is quite remarkable that the naturally diamagnetic $[\text{Fe}(\text{44mBpy})_3]^{2+}$ can be converted completely into a paramagnetic compound by protonation. The results are in excellent

agreement with the $^1\text{H-NMR}$ spectroscopy where also complete protonation (γH^+) was found at pH 1.0 at elevated temperatures and with the UV-Vis spectroscopy.

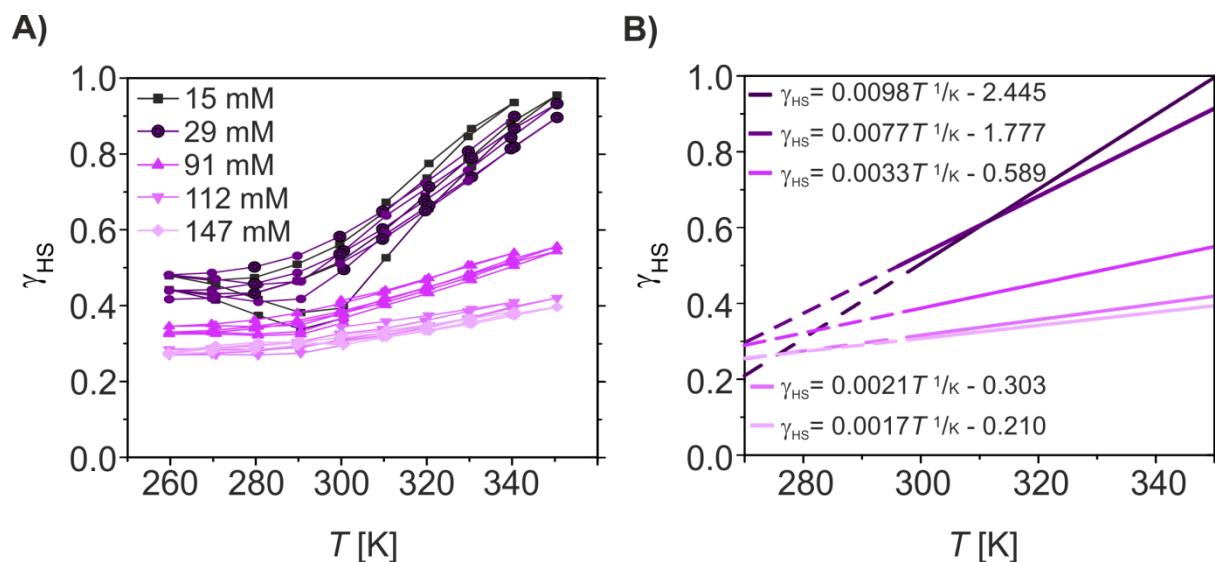


Figure 23. Concentration-dependent magnetism of $[\text{Fe}(44\text{mBpy})_3]^{2+}$ in aqueous solution at pH 1.0. **A:** Plot of γ_{HS} versus T showing an increasing γ_{HS} when lowering the complex to proton concentration. **B:** Linear fit of **A** between 300 K and 350.

Additionally, the influence of the complex to proton ratio was analyzed by varying the concentration of $[\text{Fe}(44\text{mBpy})_3]^{2+}$ (see Figure 23). We find that the amount of paramagnetic $[\text{Fe}(44\text{mBpy})_3\text{H}]^{3+}$ is increased from 30% ($\gamma_{\text{HS}} = 0.30$) to 60% ($\gamma_{\text{HS}} = 0.60$) at RT and from 40% ($\gamma_{\text{HS}} = 0.40$) to 95% ($\gamma_{\text{HS}} = 0.95$) at 350 K when the concentration is reduced from 147 mmol/L to 15 mmol/L. This highlights that the sensitivity of PD-CISSS rises with lowered complex concentration as it would be expected for an equilibrium condition. Furthermore the curves were fitted linearly between 300 K and 350 K given in Figure 23B (below 300 K heat capacity influences the results as it can be seen in Figure 23A). The altitude of T rises correlated to concentration showing that the switching process becomes more likely the fewer complexes are competing with more protons. It starts with an altitude of 0.0017 K^{-1} at 147 mmol/L and ends up with 0.0098 K^{-1} at 15 mmol/L.

In Figure 24A it can be seen that the pH-response of $[\text{Fe}(\text{55mBpy})_3]^{2+}$ is reduced compared to $[\text{Fe}(\text{44mBpy})_3]^{2+}$ in complete agreement with the SQUID and UV-Vis data. $[\text{Fe}(\text{55mBpy})_3]^{2+}$ is also completely diamagnetic with $\gamma_{\text{HS}} = 0.00$ at RT and pH 7.0 (see Figure 24A). In contrast to $[\text{Fe}(\text{44mBpy})_3]^{2+}$ at pH 2.9 no significant paramagnetism is observed for $[\text{Fe}(\text{55mBpy})_3]^{2+}$. At pH 1.0 only 30% ($\gamma_{\text{HS}} = 0.30$) are in a HS state at RT going up reversibly to 60% at 350 K ($\gamma_{\text{HS}} = 0.60$). In the ^1H -NMR spectra of $[\text{Fe}(\text{55mBpy})_3]^{2+}$ it could already be seen that γ_{H^+} is significantly lower compared to $[\text{Fe}(\text{44mBpy})_3]^{2+}$ at similar pH levels. In the UV-Vis spectra the MLCT-intensity was also always higher. This is reflected in Figure 24B where it can be seen that γ_{HS} rises only below pH 1.5 with no significant T -dependence above. The same concentration dependence of $[\text{Fe}(\text{44mBpy})_3]^{2+}$ is found for $[\text{Fe}(\text{55mBpy})_3]^{2+}$ given in Figure 25A. The switching progress can be raised from 15% ($\gamma_{\text{HS}} = 0.15$) to 30% ($\gamma_{\text{HS}} = 0.30$) at pH 1.0 and 300K when lowering the initial complex concentration from 147 mmol/L to 15 mmol/L. The altitude of the conversion goes from 0.0021 K^{-1} to 0.0078 K^{-1} , distinctively slower compared to $[\text{Fe}(\text{44mBpy})_3]^{2+}$ (see Figure 25B). This can be explained by the ligand substitution what is discussed in detail in the conclusion.

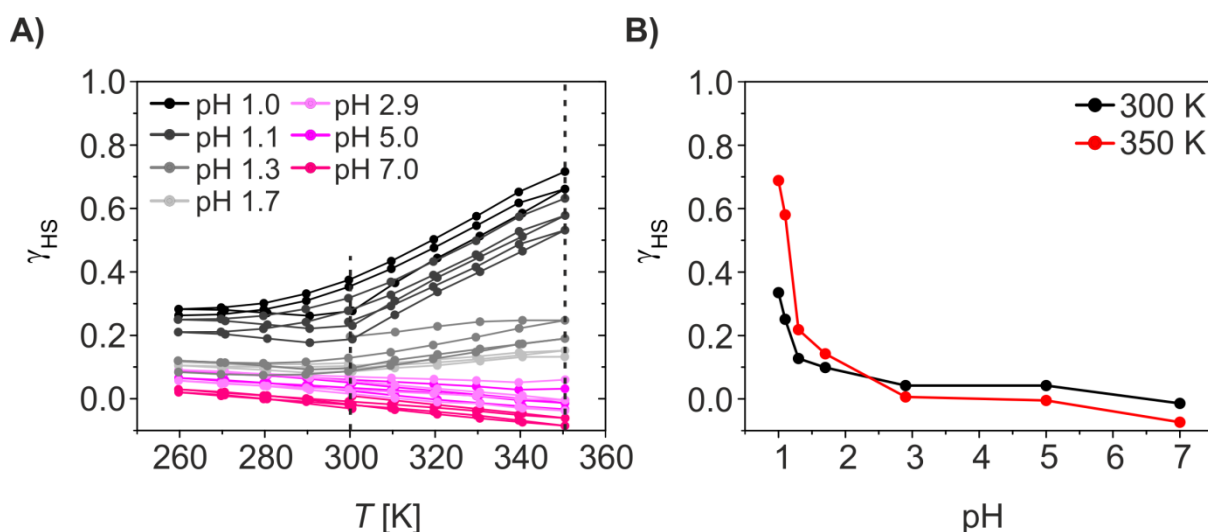


Figure 24. Magnetism of $[\text{Fe}(\text{55mBpy})_3]^{2+}$ in aqueous solution ($c = 29.4 \text{ mmol/L}$). **A:** Plot of γ_{HS} versus T for the different solutions showing an increasing γ_{HS} by proton concentration and temperature. **B:** pH-dependence of γ_{HS} at 300 K and 350 K calculated from the SQUID data.

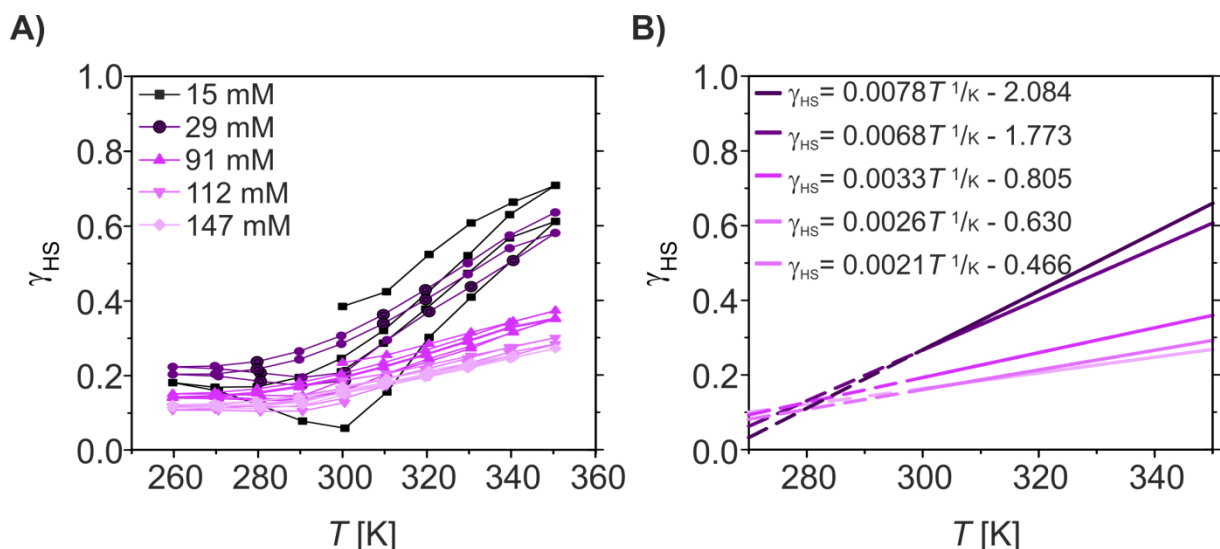


Figure 25. Concentration-dependent magnetism of $[\text{Fe}(55\text{mBpy})_3]^{2+}$ in aqueous solution at pH 1.0. **A:** Plot of γ_{HS} versus T showing an increasing γ_{HS} when lowering the complex to proton concentration. **B:** Linear fit of **A** between 300 K and 350.

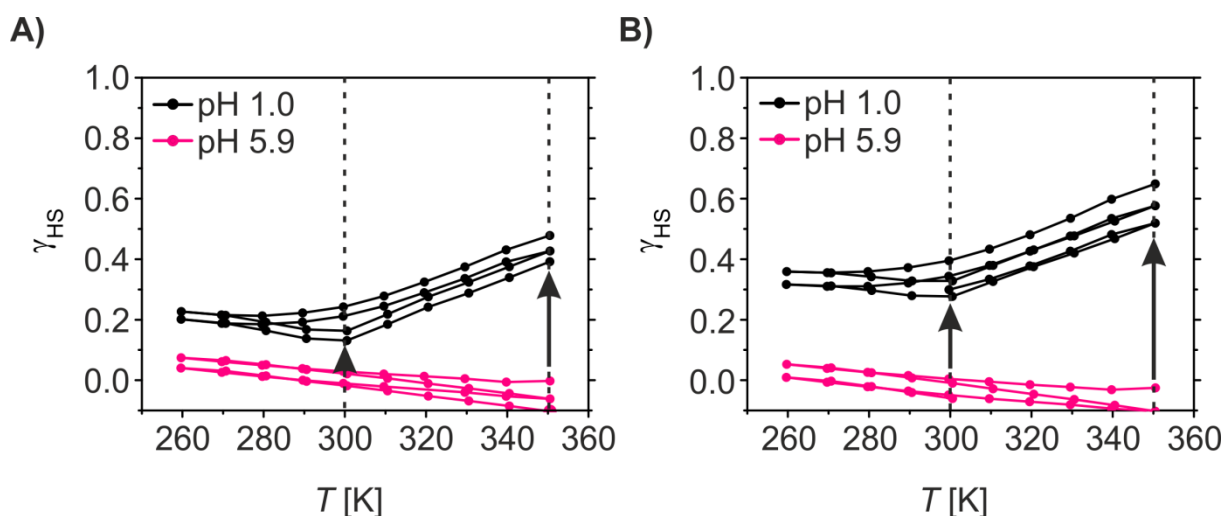


Figure 26. Magnetism of $[\text{Fe}(4\text{mBpy})_3]^{2+}$ (**A**) and $[\text{Fe}(5\text{mBpy})_3]^{2+}$ (**B**) in aqueous solution ($c = 31.28 \text{ mmol/L}$). The plot of γ_{HS} versus T for the different solutions shows an increasing γ_{HS} by proton concentration and temperature.

In Figure 26 the pH-responsive magnetism of $[\text{Fe}(4\text{mBpy})_3]^{2+}$ and $[\text{Fe}(5\text{mBpy})_3]^{2+}$ is depicted. As it can be seen in Figure 26A is $[\text{Fe}(4\text{mBpy})_3]^{2+}$ at pH 7.0 essentially diamagnetic ($\gamma_{\text{HS}} = 0.00$) over the complete temperature range. At pH 1.0 at 300 K already 21%

($\gamma_{\text{HS}} = 0.21$) of the molecules are in a HS state. At pH 1.0 it is found that 44% ($\gamma_{\text{HS}} = 0.44$). $[\text{Fe}(\text{5mBpy})_3]^{2+}$ can be increased from a complete LS state at pH 7.0 to 33% ($\gamma_{\text{HS}} = 0.33$) at pH 1.0 and 300 K. At pH 1.0 at 350 K 58% ($\gamma_{\text{HS}} = 0.58$) of the molecules are paramagnetic. The switching process is here also completely reversible.

Consequently, the magnetic behavior of $[\text{Fe}(\text{Bpp})_2]^{2+}$ was monitored in solution with different pH values (see Figure 27). At pH 7 we observe a significant stabilization of the LS state in H_2O with a γ_{HS} around 0.3 which is in very good agreement with the literature data measured in D_2O . Upon protonation the overall amount of the paramagnetic species is shifted towards 80% ($\gamma_{\text{HS}} = 0.80$) at RT and towards 100% ($\gamma_{\text{HS}} = 1.0$) at 350K what is in excellent agreement with the UV-Vis spectra. The process is again completely reversible over the measured temperature range which is why we rule out partial detachment of the ligand although precise $^1\text{H-NMR}$ was not available for $[\text{Fe}(\text{Bpp})_2]^{2+}$. In Figure 27B it can be seen nicely how the spin state of $[\text{Fe}(\text{Bpp})_2]^{2+}$ is modulated via pH and temperature.

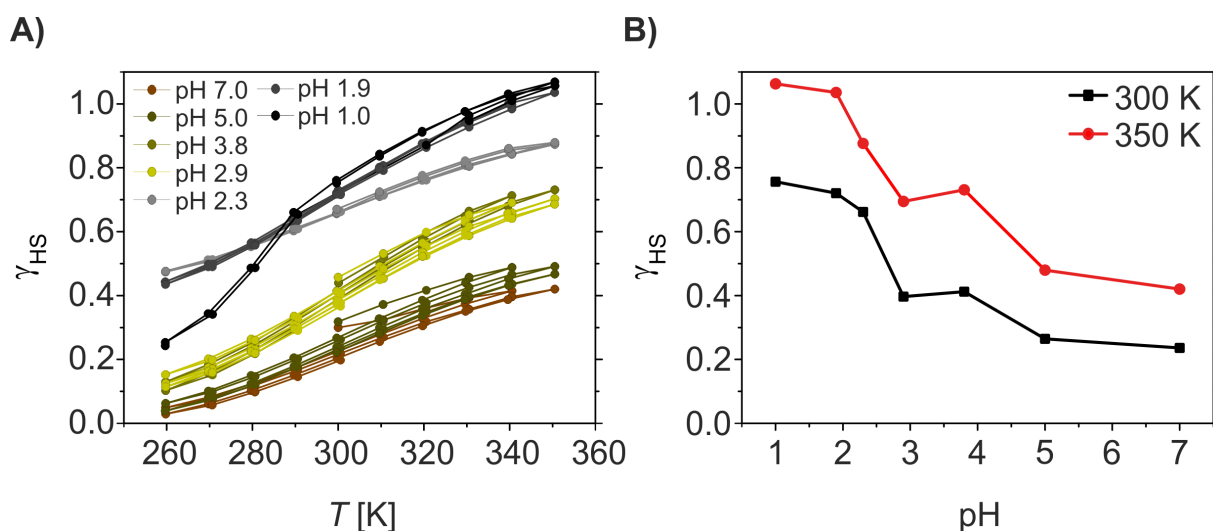


Figure 27. Magnetic characterization of $[\text{Fe}(\text{Bpp})_2]^{2+}$ in aqueous solution ($c = 36.40$ mmol/L). **A:** Plot of γ_{HS} versus T for the different solutions showing an increasing γ_{HS} by proton concentration and temperature. **B:** pH-dependence of γ_{HS} at 300 K and 350 K calculated from the SQUID data.

2.1.5 Behavior in aqueous solution: Field-cycling ^1H -NMR relaxometry

MRI makes use of the tissue based differences in ^1H longitudinal relaxation times T_1 of water molecules.^[22,28] Paramagnetic molecules or SCO complexes shorten T_1 and lead to a better imaging contrast.^[22,28,42] It was shown in the previous sections that especially $[\text{Fe}(\text{Bpy})_3]^{2+}$ -like systems have a pH-responsive magnetism which should influence relaxation times in a pH-dependent fashion. Here, field-cycling (FC) ^1H -NMR relaxometry data are provided for $[\text{Fe}(\text{Bpy})_3]^{2+}$, $[\text{Fe}(44\text{mBpy})_3]^{2+}$ and $[\text{Fe}(\text{Bpp})_2]^{2+}$ yielding Larmor frequency ν -dependent, concentration-dependent and pH-dependent measurements of T_1 , as well as the observed longitudinal relaxation rate $r_{1\text{Obs}}$ and molar relaxivity Δr_1 . $[\text{Fe}(55\text{mBpy})_3]^{2+}$, $[\text{Fe}(4\text{mBpy})_3]^{2+}$ and $[\text{Fe}(5\text{mBpy})_3]^{2+}$ have not been investigated since it could be inferred from the SQUID data that they will perform less than the other systems. Aqueous solutions of $[\text{Fe}(\text{Bpy})_3]^{2+}$ ($c = 0.168$ mol/L), $[\text{Fe}(44\text{mBpy})_3]^{2+}$ ($c = 0.147$ mol/L) and $[\text{Fe}(\text{Bpp})_2]^{2+}$ ($c = 0.036$ mol/L) were characterized with FC ^1H -NMR relaxometry ($\nu = 0.01$ MHz and 10 MHz with $\nu = \gamma B/2\pi$ where γ is the gyromagnetic ratio and B is the external magnetic field) at different pH.

Initially, the concentration-dependent changes of $r_{1\text{Obs}}$ upon addition of $[\text{Fe}(\text{Bpy})_3]^{2+}$ to a neutral aqueous solution and at pH 1.0 were measured at two different Larmor frequencies ν . The corresponding graphs are depicted in Figure 28. One can see easily that the complex does not influence the relaxation rate in neutral media significantly. For the observed concentration range an overall change between 0.3 s $^{-1}$ and 1.4 s $^{-1}$ is observed which is negligible and can be traced back to very small paramagnetic impurities not visible via Mössbauer spectroscopy or to coordination changes happening already at pH 5.9. Paramagnetic relaxation saturation appears also to be reached already at 0.220 mol/L. In acidic media (pH 1.0) the situation is completely different as it can be seen in Figure 28B. For 10 MHz as well as for 0.005 MHz the concentration dependence appears to be linear and rises steadily from 0.3 s $^{-1}$ to 20 s $^{-1}$ (10 MHz) and to 39 s $^{-1}$ (0.005 MHz) at a concentration around 0.220 mol/L.

These results already show that the pH-responsive magnetism which was observed via ^1H -NMR spectroscopy, UV-Vis spectroscopy and SQUID magnetometry is indeed able to serve as the basis for pH-responsive paramagnetic relaxation enhancement and highlights drastic changes at the iron(II) core during protonation.

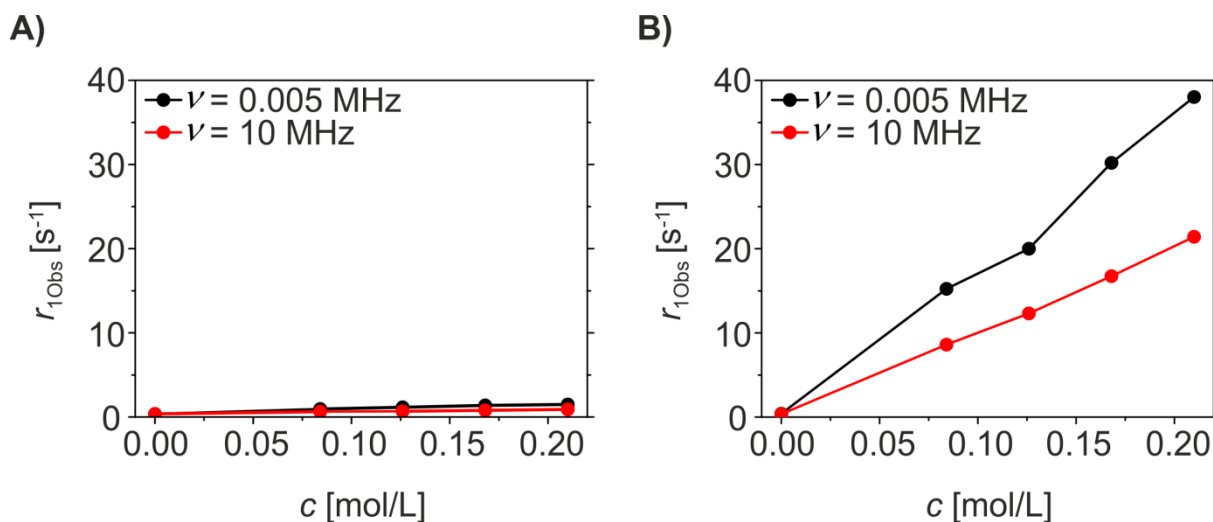


Figure 28. Concentration-dependent longitudinal relaxation rate $r_{1\text{Obs}}$ of $[\text{Fe}(\text{Bpy})_3]^{2+}$ in neutral aqueous solution at pH 5.9 (left) and at pH 1.0 (right) measured at two different Larmor frequencies ν (0.005 MHz and 10 MHz).

Consequently, aqueous solutions of $[\text{Fe}(\text{Bpy})_3]^{2+}$ ($c = 0.168$ mol/L) were characterized with field-cycling (FC) ¹H-NMR relaxometry at different pH-values since the results given in Figure 28 could be easily explained via a coordination change at the iron(II) center induced by protonation. Most reasonable, protonation should appear at the most basic entities of the complex which are the nitrogen atoms of the pyridyl rings. Protons would therefore compete with the iron for the bond to the nitrogen. This can lead to a bond break between iron and nitrogen what could be described as proton-driven coordination-induced spin state switch (PD-CISSS). Such mechanism predicts the formation of a free coordination spot at the paramagnetic iron center that should increase dramatically the relaxivity of water. The system shows initially only outer sphere relaxation while it could also undergo inner sphere relaxation after the protonation induced bond break since water molecules can be exchanged directly at the paramagnetic iron(II) center.^[22,28,101] In Figure 29 the longitudinal relaxation time T_1 and molar relaxivity (characteristic feature of contrast agents) Δr_1 are plotted against pH. There, $r_{1\text{Obs}}$ is the observed longitudinal relaxation rate and R_1^{LM} the longitudinal solvent relaxation rate.

$$\text{Thereby is } \Delta r_1 = \frac{r_{1\text{Obs}} - R_1^{\text{LM}}}{c}; \quad R_1^{\text{LM}} = 1 / T_1^{\text{LM}}; \quad \text{and } r_{1\text{Obs}} = 1 / T_1;$$

In Figure 29 the longitudinal relaxation time T_1 and the molar relaxivity Δr_1 are plotted against the pH. The experiments yield ^1H -relaxation times of the water molecules which are influenced by the exchange at free coordination spots of paramagnetic centers.^[22,28,101] For $[\text{Fe}(\text{Bpy})_3]^{2+}$ a strong pH dependence of Δr_1 is observed. At pH values below 4, a significant increase is observed in line with the proposed formation of a free coordination spot. For $[\text{Fe}(\text{Bpy})_3]^{2+}$ Δr_1 is between $0.00(1) \text{ s}^{-1}\text{mmol}^{-1}\text{L}$ (pH 7, LS, no coordination spot) and $0.18 \text{ s}^{-1}\text{mmol}^{-1}\text{L}$ (pH 1, $\gamma_{\text{HS}} = 0.27$, free coordination spot) – corresponding to an increase of the molar relaxivity by a factor of 18. This increase is significantly higher than the one observed for switchable nickel(II) complexes with a factor of 3–7^[45] or gadolinium-based systems with a factor of 1–5 (see Table 1).^[21,44]

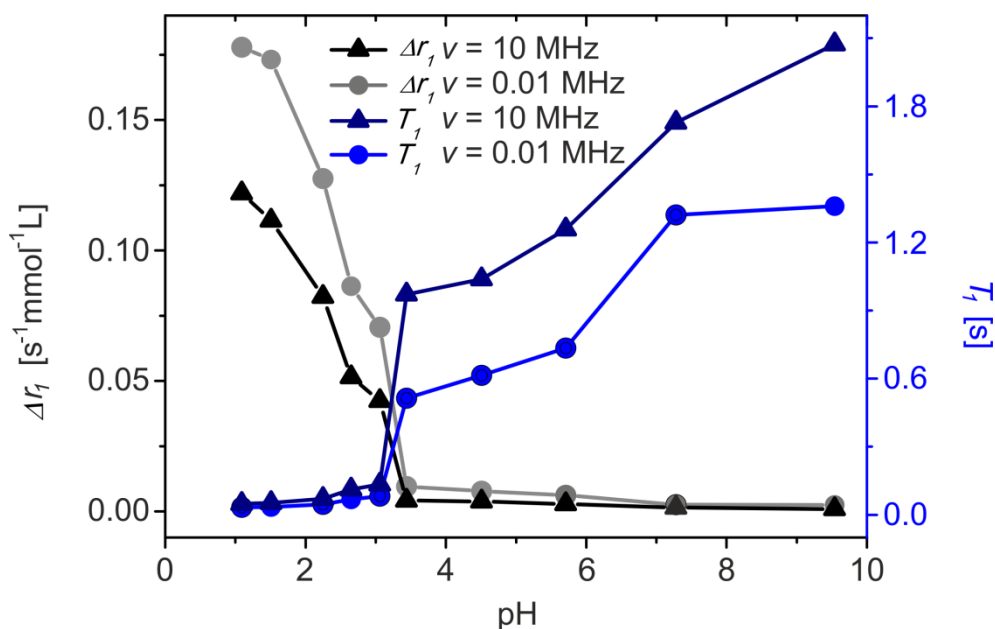


Figure 29. FC ^1H -NMR measurements of T_1 (blue) and Δr_1 (black) at an aqueous solution of $[\text{Fe}(\text{Bpy})_3]^{2+}$ ($c = 0.168 \text{ mol/L}$); at a Larmor frequency ν of 0.01 MHz (circle) and 10 MHz (triangle) at RT.

The relaxometry of $[\text{Fe}(44\text{mBpy})_3]^{2+}$ is depicted in Figure 30. T_1 is diminished gradually from 0.5 s to 0.02 s alongside lowering of the pH. T_1 is already reduced compared to neutral water in line with ^1H -NMR for $[\text{Fe}(44\text{mBpy})_3]^{2+}$. Δr_1 is very stable between pH 9 and 4 where only a small decrease from $0.02 \text{ s}^{-1}\text{mmol}^{-1}\text{L}$ to $0.04 \text{ s}^{-1}\text{mmol}^{-1}\text{L}$ is observed. The dispersion among

0.01 MHz and 10 MHz is very narrow, in line with the presence of mostly LS complexes of $[\text{Fe}(\text{44mBpy})_3]^{2+}$ for which nearly no dispersion should be detectable. Below pH 4 a large increase of Δr_1 to $0.13 \text{ s}^{-1}\text{mmol}^{-1}\text{L}$ (10 MHz) and $0.16 \text{ s}^{-1}\text{mmol}^{-1}\text{L}$ (0.1 MHz) is observed as it would be caused by a magnetic change under opening of a free coordination spot. The dispersion is much larger compared to neutral pH which is indicative for a paramagnetic protonated species. The relaxivity gap between LS and HS is characterized by a factor of 10.

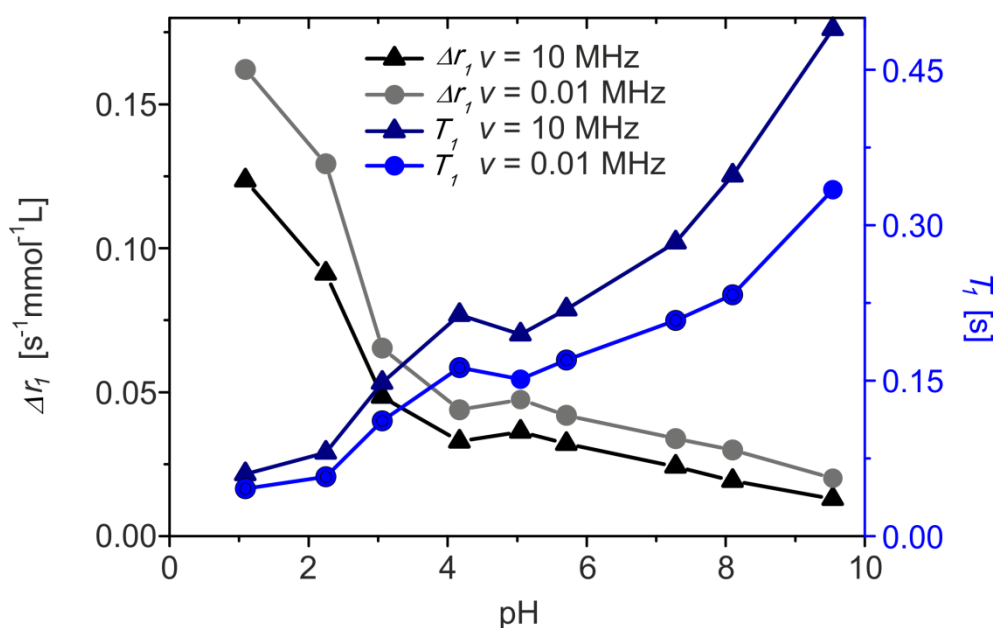


Figure 30. FC ^1H -NMR measurements of T_1 (blue) and Δr_1 (black) at an aqueous solution of $[\text{Fe}(\text{44mBpy})_3]^{2+}$ ($c = 0.147 \text{ mol/L}$); at a Larmor frequency of 0.01 MHz (circle) and 10 MHz (triangle) at RT.

Consequently, also concentration-dependent measurements of $[\text{Fe}(\text{Bpp})_2]^{2+}$ in neutral aqueous solution were conducted at two different Larmor frequencies ν depicted in Figure 31. Since $[\text{Fe}(\text{Bpp})_2]^{2+}$ is a SCO complex we observe a saturation behavior for the concentration dependence. Around 0.01 mol/L $r_{1\text{Obs}}$ is with 0.5 more or less identical for both frequencies. At 0.036 mol/L the solution is already at a point at which $r_{1\text{Obs}}$ cannot be further reduced by supplementary complex addition. At 0.01 MHz $r_{1\text{Obs}} = 2.9 \text{ s}^{-1}$ and at 10 MHz $r_{1\text{Obs}} = 2.3 \text{ s}^{-1}$ are found. Such a behavior is commonly observed for paramagnetic systems. Since at 0.036 mol/L paramagnetic relaxation saturation appears to be reached already this concentration was also used for further pH-dependent measurements.

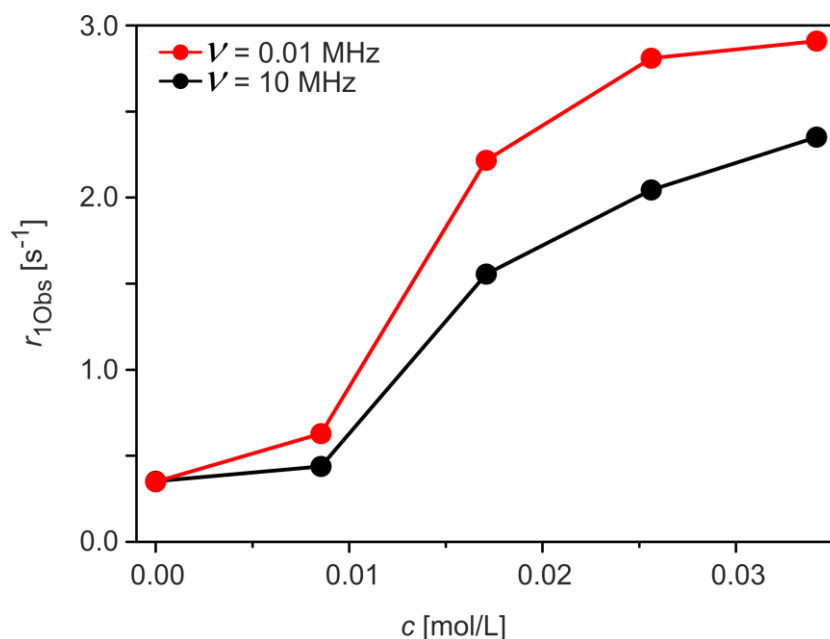


Figure 31. Concentration-dependent longitudinal relaxation rate $r_{1\text{Obs}}$ of $[\text{Fe}(\text{Bpp})_2]^{2+}$ in neutral aqueous solution measured at two Larmor frequencies ν (0.01 MHz, 10 MHz).

For comparison, aqueous solutions of the SCO complex $[\text{Fe}(\text{Bpp})_2]^{2+}$ ($c = 0.036$ mol/L) were investigated also in a pH-dependent fashion (see Figure 32). The aqueous solution of the spin-crossover complex is paramagnetic at room temperature ($\gamma_{\text{HS}} \cong 0.5$). When the pH is lowered, the same PD-CISSS mechanism as for $[\text{Fe}(\text{Bpy})_3]^{2+}$ could be observed. Significant differences in the relaxivity values of $[\text{Fe}(\text{Bpp})_2]^{2+}$ when the pH is lowered support the proposed mechanism. For the complex a strong pH-dependence of Δr_1 is observed. The molar relaxivity varies between 0.06 s⁻¹mmol⁻¹L and 0.57 s⁻¹mmol⁻¹L corresponding to a factor of 9.5. The increase of the relaxivity of $[\text{Fe}(\text{Bpp})_2]^{2+}$ starts at a slightly higher pH indicating an influence of the used ligand. $[\text{Fe}(\text{Bpy})_3]^{2+}$ and $[\text{Fe}(\text{Bpp})_2]^{2+}$ have different Δr_1 values at pH 7 due to differences in the spin state and the ligand. At room temperature $[\text{Fe}(\text{Bpy})_3]^{2+}$ is a diamagnetic LS complex without exchangeable protons at the ligand. In D₂O solution at room temperature $[\text{Fe}(\text{Bpp})_2]^{2+}$ is a SCO complex with exchangeable protons at the ligand.^[9,130] Please note, that at pH 7 γ_{HS} of $[\text{Fe}(\text{Bpp})_2]^{2+}$ is 0.5 with a molar relaxivity of 0.06 s⁻¹mmol⁻¹L whereas at pH 1 γ_{HS} of $[\text{Fe}(\text{Bpy})_3]^{2+}$ is with 0.27 smaller while the molar relaxivity is with 0.18 s⁻¹mmol⁻¹L significantly larger. The drastic increase of Δr_1 at low pH values can only be explained with the formation of a free coordination spot at the iron center. We observe a small relaxation

dispersion for the complex solutions which is slightly more pronounced for the paramagnetic than for the diamagnetic species. This effect must originate solely from the complex since the solvent (H₂O) is essentially free from dispersion and does not show any changes under varying acidity as it would be expected.

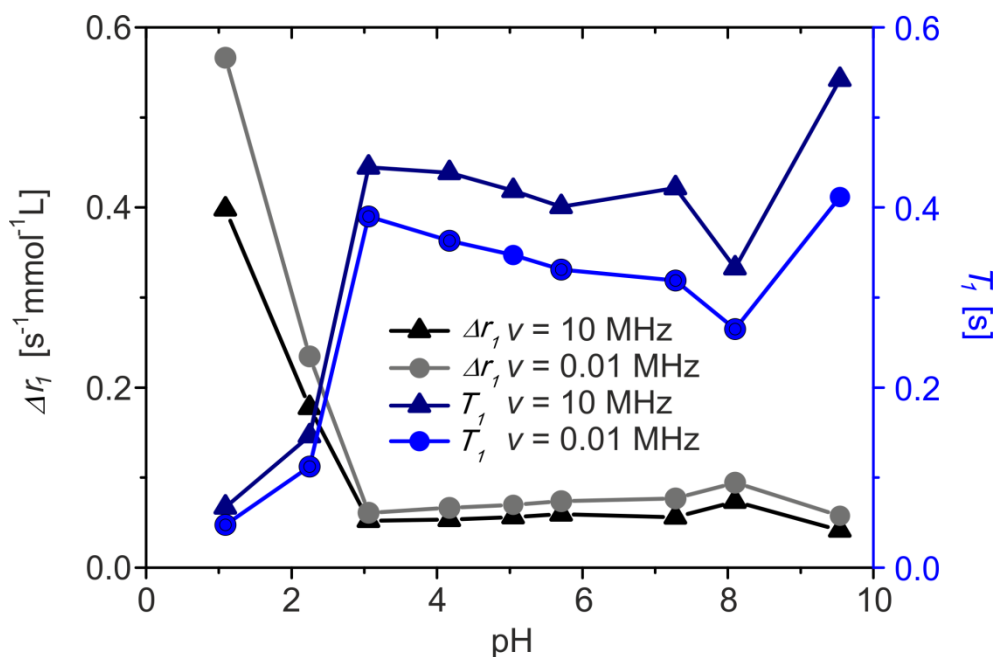
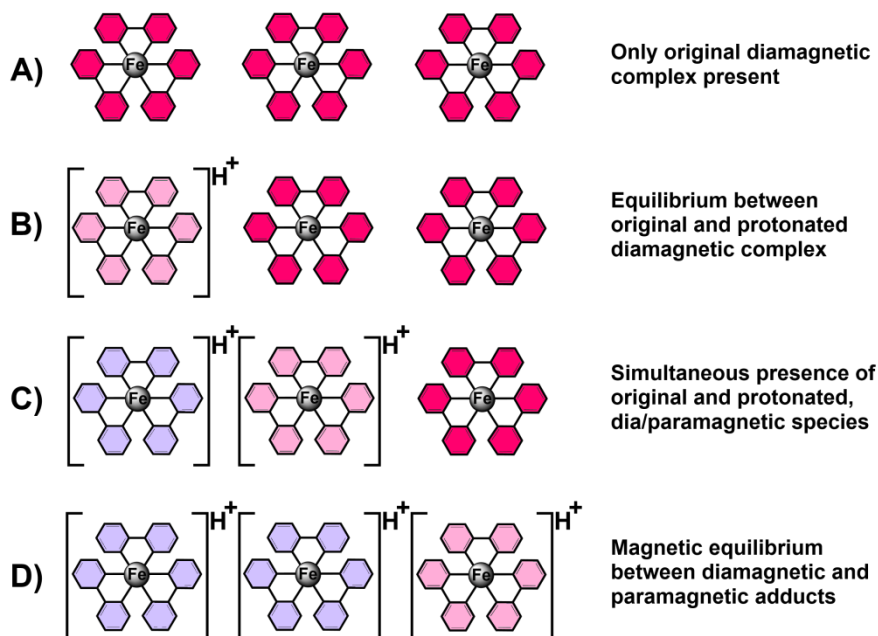


Figure 32. FC ¹H-NMR measurements of T_1 (blue) and Δr_1 (black) at an aqueous solution of $[Fe(Bpp)_2]^{2+}$ ($c = 0.036$ mol/L); at a Larmor frequency ν of 0.01 MHz (circle) and 10 MHz (triangle) at RT.

Parts of this section (2.1 Homoleptic iron(II) complexes) have been reproduced by permission of the Royal Society of Chemistry. Findings have been published in an article with the DOI:10.1039/C6CC08618G which can be found on the website of the Royal Society of Chemistry.

2.2 Proton-driven coordination-induced spin state switch

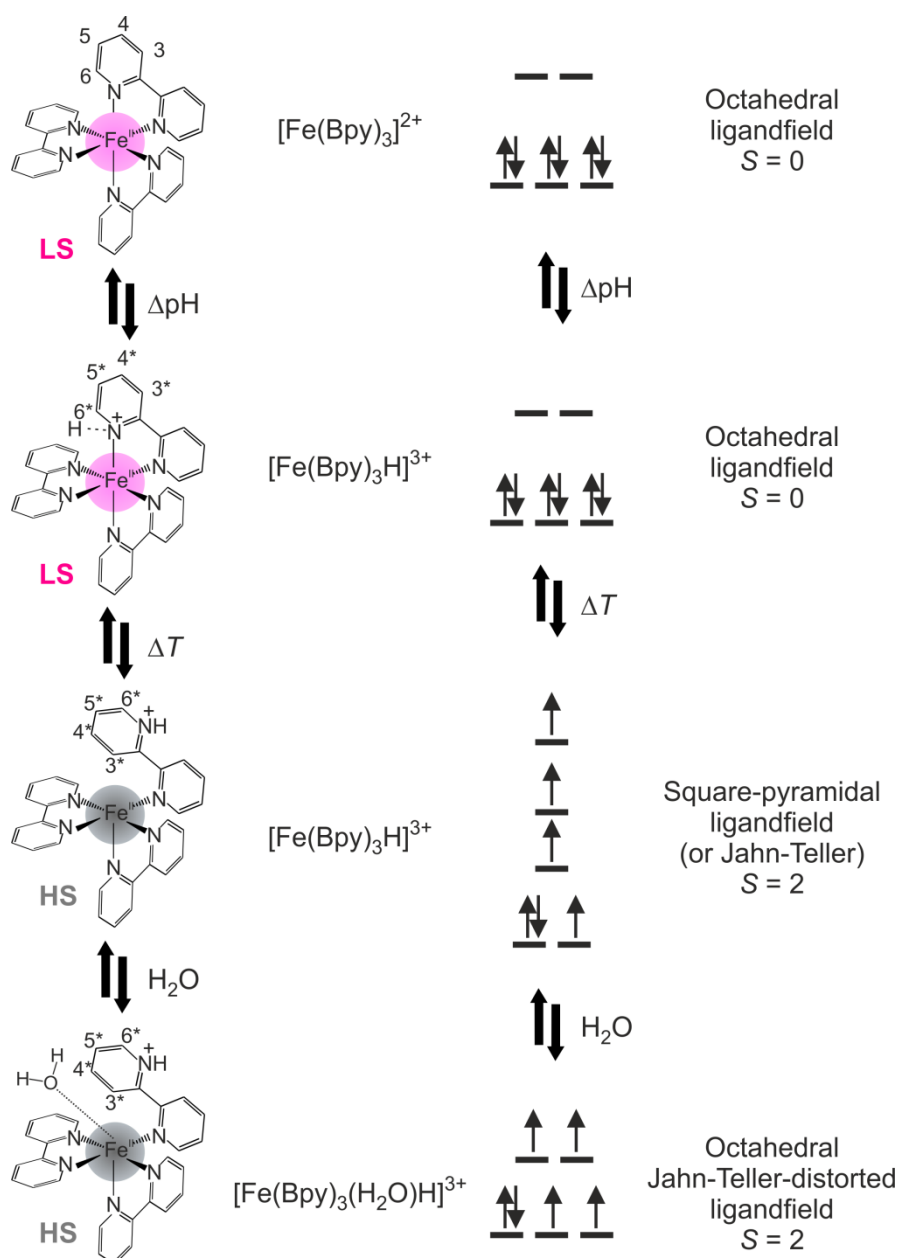
2.2.1 Observations and systematic trends



Scheme 15. Different iron(II) species in aqueous solutions in relation to the pH; **A:** Neutral solution; **B:** Slightly acidic solution; **C:** Acidic solution; **D:** Highly acidic solution.

The existing data verifies a pH-responsive magnetism for $[\text{Fe}(\text{Bpy})_3]^{2+}$, $[\text{Fe}(44\text{mBpy})_3]^{2+}$, $[\text{Fe}(55\text{mBpy})_3]^{2+}$, $[\text{Fe}(4\text{mBpy})_3]^{2+}$, $[\text{Fe}(5\text{mBpy})_3]^{2+}$ and $[\text{Fe}(\text{Bpp})_2]^{2+}$ which was followed via $^1\text{H-NMR}$, UV-Vis spectroscopy and magnetic measurements. From this data it can be concluded that they interact with surrounding protons. While $[\text{Fe}(\text{Bpy})_3]^{2+}$, $[\text{Fe}(44\text{mBpy})_3]^{2+}$, $[\text{Fe}(55\text{mBpy})_3]^{2+}$, $[\text{Fe}(4\text{mBpy})_3]^{2+}$ and $[\text{Fe}(5\text{mBpy})_3]^{2+}$ are completely diamagnetic in neutral media an increase of the H^+ concentration does lead to the formation of a diamagnetic protonated species. This protonated species is in an equilibrium condition with a paramagnetic one that has distinctly different optical, magnetic and structural properties. This equilibrium is found to be pH-, temperature- and concentration-dependent enabling a near 100% conversion of the diamagnetic to a paramagnetic species. This remarkable conversion rate allows PD-CISSS systems to compete with SCO systems regarding their switchability and pH-response as it was shown for $[\text{Fe}(\text{Bpp})_2]^{2+}$. Additionally, it was demonstrated via FC $^1\text{H-NMR}$

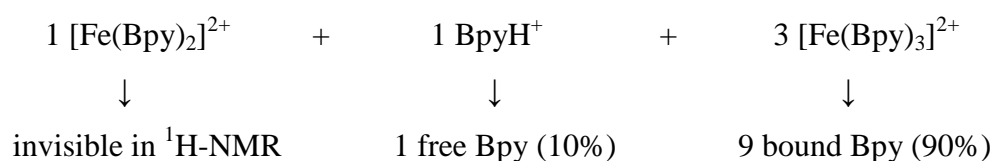
relaxometry that the pH-responsive magnetism leads to a paramagnetic relaxation enhancement at surrounding water protons. This is indicative for the opening of a free coordination spot at the iron core where water molecules are exchanged and serves as the basis for smart CA's in *fMRI*. Species appearing during this process are illustrated in Scheme 15. Furthermore it was possible to modulate $[\text{Fe}(\text{Bpp})_2]^{2+}$ towards the HS state via protonation what was monitored via UV-Vis spectroscopy and SQUID magnetometry.



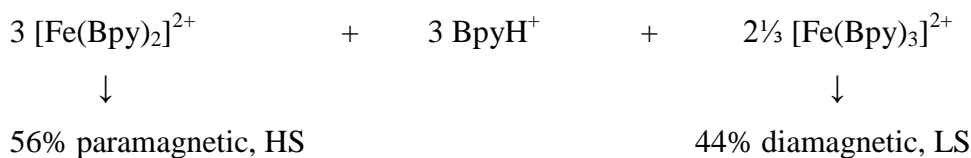
Scheme 16. Mechanism of the proton-driven coordination-induced spin state switch with all emerging species and the respective ligand field splitting given exemplarily for $[\text{Fe}(\text{Bpy})_3]^{2+}$.

The overall mechanism of the PD-CISSS is given in Scheme 16 exemplary for $[\text{Fe}(\text{Bpy})_3]^{2+}$. Initially the iron(II) core is in an octahedral ligand field with a rather large splitting forcing the electrons to pair and therefore to be in the LS state ($S = 0$). A first equilibrium exists between the diamagnetic $[\text{Fe}(\text{Bpy})_3]^{2+}$, and the protonated form $[\text{Fe}(\text{Bpy})_3\text{H}]^{3+}$ which is still diamagnetic (LS, $S = 0$) and the proton is delocalized over the nitrogen donor atoms. This is evident in the ^1H -NMR spectra where two different species can be observed upon protonation which are clearly diamagnetic. This protonated species $[\text{Fe}(\text{Bpy})_3\text{H}]^{3+}$ participates at a second equilibrium which can be triggered by variation of temperature. During increase of the thermal energy molecular dynamics are accelerated and a half-bonded species of $[\text{Fe}(\text{Bpy})_3\text{H}]^{3+}$ is generated. This half-bonded species has a square pyramidal coordination geometry and is consequently paramagnetic (HS, $S = 2$). The mainly temperature induced presence of this species was precisely traceable by SQUID magnetometry and led to a paramagnetic shift as well as paramagnetic line broadening in ^1H -NMR spectroscopy. Furthermore, the change of the electronic structure is observable via UV-Vis spectroscopy by a vanishing of the typical MLCT transition of this complex. A large bathochromic shift proves interaction between the protons and the nitrogen base. In a final, very fast step the half-bonded $[\text{Fe}(\text{Bpy})_3\text{H}]^{3+}$ – which is of course a transient species – is coordinated by water molecules since the experiments take place in aqueous solution and iron(II) is known to favor an octahedral coordination. The measurable formation of $[\text{Fe}(\text{H}_2\text{O})(\text{Bpy})_3\text{H}]^{3+}$ which should rapidly exchange water molecules is proven by the paramagnetic relaxation enhancement of the water protons in FC ^1H -NMR relaxometry. It should be noted that the Δr_1 values in acidic media of $[\text{Fe}(\text{Bpy})_3]^{2+}$ ($0.18 \text{ s}^{-1}\text{mmol}^{-1}\text{L}$, pH 1, $\gamma_{\text{HS}} = 0.3$) are essentially higher than in neutral aqueous solution of $[\text{Fe}(\text{Bpp})_2]^{2+}$ ($0.06 \text{ s}^{-1}\text{mmol}^{-1}\text{L}$, pH 7, $\gamma_{\text{HS}} = 0.5$) with an enclosed coordination shell. Therefore the opening of a free coordination spot is evident.

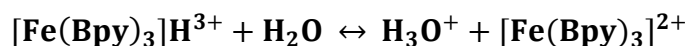
It is necessary to point out that the data does not support acid decomposition under complete dissociation of the complex $[\text{Fe}(\text{Bpy})_3]^{2+}$ into $[\text{Fe}(\text{Bpy})_2]^{2+}$ and BpyH^+ in the presented pH-area. The SQUID data at pH 1.0 and 300 K verify that around 25% of all iron complexes are in a paramagnetic HS state. When we assume the above mentioned dissociation process would take place the overall composition would be as follows:



This 10% of protonated compound (1:9 ratio) can't be observed in $^1\text{H-NMR}$. Instead nearly 30% of a protonated species appear which fully supports our depicted half-bonded, three-step mechanism. If we assume again a complete dissociation based on around 30% of protonated species as found at pH 1.0 and 300 K via $^1\text{H-NMR}$ we would get following composition:



Since 25% of paramagnetic molecules and not 56% are found via SQUID measurements it fully supports our depicted mechanism and shows that essentially no complete acid decomposition is taking place. Furthermore UV-Vis, $^1\text{H-NMR}$ and SQUID experiments are fully reversible in contrast to the acid decomposition of $[\text{Fe}(\text{Bpy})_3]^{2+}$ below pH 1.0 reported in the literature which is totally irreversible.^[123,124] Furthermore it was shown in the initial section that the color of $\text{Fe}(\text{Bpy})_2\text{Cl}_2$ is black while we observe in acidic solution a completely colorless species. pK_A values have been determined for $[\text{Fe}(\text{Bpy})_3]^{2+}$ based on the experimental $^1\text{H-NMR}$ and SQUID data for the acid-base-reaction as follows:



$$K = \frac{c[\text{H}_3\text{O}^+] * c[\text{Fe}(\text{Bpy})_3]^{2+}}{c[\text{H}_2\text{O}] * c[\text{Fe}(\text{Bpy})_3\text{H}]^{3+}} ; \text{ where } c[\text{H}_2\text{O}] = \text{const.}$$

$$K_A = K * c[\text{H}_2\text{O}] = \frac{c[\text{H}_3\text{O}^+] * c[\text{Fe}(\text{Bpy})_3]^{2+}}{c[\text{Fe}(\text{Bpy})_3\text{H}]^{3+}} ; pK_A = -\log \left(K_A * 1 \frac{\text{mol}}{\text{L}} \right)$$

$$pK_A = -\log \left\{ \frac{c[\text{H}_3\text{O}^+] * c[\text{Fe}(\text{Bpy})_3]^{2+}}{c[\text{Fe}(\text{Bpy})_3\text{H}]^{3+}} * 1 \frac{\text{mol}}{\text{L}} \right\}$$

pH 1.0, 300 K:

$$c[\text{H}_3\text{O}^+] = 0.1 \frac{\text{mol}}{\text{L}}, c[\text{Fe}(\text{Bpy})_3]^{2+} = 3.08 \frac{\text{mmol}}{\text{L}}, c[\text{Fe}(\text{Bpy})_3\text{H}]^{3+} = 3.92 \frac{\text{mmol}}{\text{L}}$$

$$pK_A = 1.1$$

pH 2.0, 300 K:

$$c[\text{H}_3\text{O}^+] = 0.01 \frac{\text{mol}}{\text{L}}, c[\text{Fe}(\text{Bpy})_3]^{2+} = 5.04 \frac{\text{mmol}}{\text{L}}, c[\text{Fe}(\text{Bpy})_3\text{H}]^{3+} = 1.96 \frac{\text{mmol}}{\text{L}}$$

$$pK_A = 1.5$$

$$\overline{pK_A} = 1.3$$

We find an average pK_A value of 1.3 for the described adduct $[\text{Fe}(\text{Bpy})_3\text{H}]^{3+}$ and an corresponding average pK_B value of 12.7 for the complex $[\text{Fe}(\text{Bpy})_3]^{2+}$. For comparison: $pK_A(\text{HCl}) = -7$; $pK_A(\text{Fe}(\text{H}_2\text{O})_6^{3+}) = 2.5$.^[133,135]

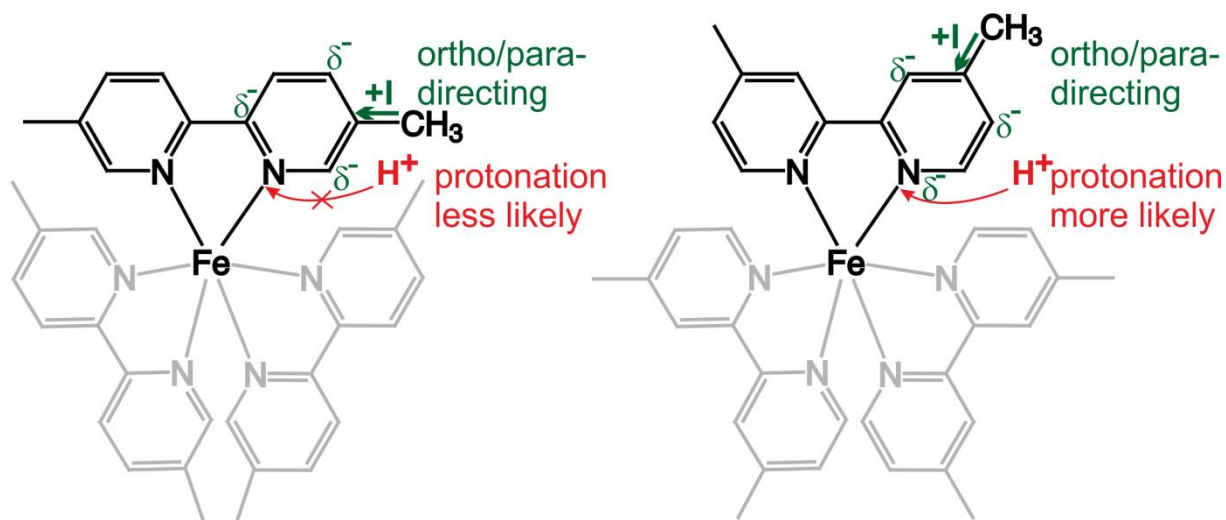
2.2.2 Consequences and predictions

It has been congruently demonstrated via $^1\text{H-NMR}$, UV-Vis, FC $^1\text{H-NMR}$ spectroscopy as well as SQUID magnetometry that the six compounds $[\text{Fe}(\text{Bpy})_3]^{2+}$, $[\text{Fe}(44\text{mBpy})_3]^{2+}$, $[\text{Fe}(55\text{mBpy})_3]^{2+}$, $[\text{Fe}(4\text{mBpy})_3]^{2+}$, $[\text{Fe}(5\text{mBpy})_3]^{2+}$ and $[\text{Fe}(\text{Bpp})_2]^{2+}$ behave severely different regarding PD-CISSS. $[\text{Fe}(44\text{mBpy})_3]^{2+}$ was already showing protonated species at pH 5.9 and could be completely converted into $[\text{Fe}(44\text{mBpy})_3\text{H}]^{3+}$ via a combination of temperature and pH. Simultaneously, a complete disappearance of the MLCT was observed by UV-Vis spectroscopy. The diamagnetism of $[\text{Fe}(44\text{mBpy})_3]^{2+}$ could also be completely converted into paramagnetism via protonation. In contrast to this, no complete protonation did appear for $[\text{Fe}(55\text{mBpy})_3]^{2+}$ in $^1\text{H-NMR}$ spectroscopy and also the MLCT-intensity was always higher compared to $[\text{Fe}(44\text{mBpy})_3]^{2+}$ at a similar pH. Neither the γ_{HS} of $[\text{Fe}(55\text{mBpy})_3]^{2+}$ could be heightened by variation of pH nor by temperature or concentration as much as it happened for $[\text{Fe}(44\text{mBpy})_3]^{2+}$. The reason for this must be clearly grounded in the nature of the ligand and especially the position of the methyl group. The nitrogen donor at the pyridyl rings of $[\text{Fe}(55\text{mBpy})_3]^{2+}$ is in *meta* position to the methyl group. This directs electron density via its inductive effect towards the *ortho* and *para* direction to the hydrogen atoms and does not influence the bond between iron and nitrogen. In contrast to this is the nitrogen donor of $[\text{Fe}(44\text{mBpy})_3]^{2+}$ in the *para* direction to the methyl group. Therefore, in this case electron density is donated from the methyl group directly towards the nitrogen which becomes partially more negatively charged. The nitrogen becomes a harder base which is more likely to interact with protons as a hard acid. Consequently, protonation is most likely for compound $[\text{Fe}(44\text{mBpy})_3]^{2+}$, least likely for compound $[\text{Fe}(4\text{mBpy})_3]^{2+}$ and $[\text{Fe}(5\text{mBpy})_3]^{2+}$, while $[\text{Fe}(55\text{mBpy})_3]^{2+}$ should be located in between. In exactly this order it was observed in the presented experiments.

The second equilibrium step – twisting of the pyridyl ring – should be influenced mainly by the sterical demand of the substituent what is indeed mirrored by the γ_{HS} values. A summary of the characteristic γ_{H^+} and γ_{HS} values is given in Table 17. The described inductive effect is illustrated in Scheme 17.

Table 17. Summary of γ_{H^+} and γ_{HS} values found for the discussed complexes at pH 1.0.

	γ_{H^+} (300 K)	γ_{H^+} (365 K)	γ_{HS} (300 K)	γ_{HS} (350 K)
$[\text{Fe}(\text{Bpy})_3]^{2+}$	0.29	1.00	0.26	0.46
$[\text{Fe}(\text{44mBpy})_3]^{2+}$	0.69	1.00	0.55	0.91
$[\text{Fe}(\text{55mBpy})_3]^{2+}$	0.46	1.00	0.33	0.69
$[\text{Fe}(\text{4mBpy})_3]^{2+}$	0.40	0.94	0.21	0.44
$[\text{Fe}(\text{5mBpy})_3]^{2+}$	0.25	0.90	0.33	0.58
$[\text{Fe}(\text{Bpp})_2]^{2+}$	-	-	0.75	1.00



Scheme 17. Structural representation of $[\text{Fe}(\text{44mBpy})_3]^{2+}$ (right) and $[\text{Fe}(\text{55mBpy})_3]^{2+}$ (left). The inductive effect of the methyl group explains the observed differences in pH-responsive magnetism.

Nevertheless, the data from Table 17 has some disadvantages that need to be addressed. The first is that γ_{H^+} does not reflect the overall percentage in the respective sample since only the diamagnetic protonated species is visible in ^1H -NMR spectroscopy. Secondly, values are only

comparable if they were measured at the same pH, the same temperature and under identical complex concentrations. From the measurements in Figure 24 and Figure 27 it becomes obvious that concentration dependencies only play a role when the complex concentration is around the same value as the proton concentration or below. For an aqueous hydrochloric solution at pH 1.0 this is 100 mM. Below, concentration effects can be neglected as it was shown for 15 mM and 29 mM solutions of $[\text{Fe}(\text{44mBpy})_3]^{2+}$ and $[\text{Fe}(\text{55mBpy})_3]^{2+}$ which yielded exactly the same γ_{HS} values at different complex concentrations. It appears quite plausible that below a certain complex to proton ratio the overall proton concentration doesn't affect the protonation equilibrium itself anymore. This is also the reason why variations of c during ^1H -NMR spectroscopy did not yield any significant changes. Due to this finding it is possible to directly compare the ^1H -NMR results where concentrations around 7 mM were used with the SQUID data where concentrations around 30 mM were used. Furthermore, ^1H -NMR spectroscopy and SQUID magnetometry were conducted analogously around 300 K and 350 K. Therefore, more representative parameters have been calculated at 300 K and 350 K for the complexes at pH 1.0. γ_{HS} is directly converted into $\gamma_{\text{H}^+_{\text{Para}}}$ since it is a real percentage of the protonated paramagnetic species in a sample. From the remaining fraction $(1 - \gamma_{\text{H}^+_{\text{Para}}})$ $\gamma_{\text{H}^+_{\text{Dia}}}$ and γ_{Dia} have been calculated using the percentages from γ_{H^+} . This approach generates fully representative numbers reflecting the overall equilibrium conditions in aqueous solution with pH 1.0. The corresponding values are summed up in Table 18.

Table 18. Calculation of $\gamma_{\text{H}^+_{\text{Para}}}$, $\gamma_{\text{H}^+_{\text{Dia}}}$ and γ_{Dia} for the discussed complexes at pH 1.0.

Temperature	300 K			350 K		
Complex	$\gamma_{\text{H}^+_{\text{Para}}}$	$\gamma_{\text{H}^+_{\text{Dia}}}$	γ_{Dia}	$\gamma_{\text{H}^+_{\text{Para}}}$	$\gamma_{\text{H}^+_{\text{Dia}}}$	γ_{Dia}
$[\text{Fe}(\text{Bpy})_3]^{2+}$	0.26	0.21	0.53	0.46	0.34	0.20
$[\text{Fe}(\text{5mBpy})_3]^{2+}$	0.33	0.17	0.50	0.58	0.28	0.14
$[\text{Fe}(\text{4mBpy})_3]^{2+}$	0.21	0.32	0.47	0.44	0.46	0.10
$[\text{Fe}(\text{55mBpy})_3]^{2+}$	0.33	0.27	0.40	0.69	0.26	0.04
$[\text{Fe}(\text{44mBpy})_3]^{2+}$	0.55	0.13	0.32	0.91	0.09	0.00

$\gamma_{\text{H}^+_{\text{Para}}}$, $\gamma_{\text{H}^+_{\text{Dia}}}$ and γ_{Dia} are perfectly representative values to evaluate the actual sample composition. γ_{Dia} decreases steadily with the number of methyl groups present at the pyridyl

rings. The inductive effect is also perfectly reassembled by the values and shows that the PD-CISSS can easily be tuned by substitution. This effect which accounts for the first equilibrium condition (the protonation of the complex) is found in exactly the same order for 300 K and 350 K. To get a deeper insight into the second equilibrium condition between the protonated diamagnetic and the protonated paramagnetic species it appeared helpful to calculate further values. $\gamma\text{H}^+_{\text{Para}}$ and $\gamma\text{H}^+_{\text{Dia}}$ represent the overall sample composition. To reflect just the protonated species they were converted into $\gamma\text{H}^+_{\text{Para}}(100)$ and $\gamma\text{H}^+_{\text{Dia}}(100)$ which are the paramagnetic and diamagnetic fraction of only the protonated species. Together they represent 100% of the protonated species and are given in Table 19.

Table 19. Calculation of $\gamma\text{H}^+_{\text{Para}}(100)$ and $\gamma\text{H}^+_{\text{Dia}}(100)$ for the discussed complexes at pH 1.0.

Temperature	300 K		350 K	
Complex	$\gamma\text{H}^+_{\text{Para}}(100)$	$\gamma\text{H}^+_{\text{Dia}}(100)$	$\gamma\text{H}^+_{\text{Para}}(100)$	$\gamma\text{H}^+_{\text{Dia}}(100)$
$[\text{Fe}(\mathbf{44mBpy})_3]^{2+}$	0.81	0.19	0.91	0.09
$[\text{Fe}(\mathbf{55mBpy})_3]^{2+}$	0.55	0.45	0.72	0.28
$[\text{Fe}(\mathbf{4mBpy})_3]^{2+}$	0.40	0.60	0.49	0.51
$[\text{Fe}(\mathbf{5mBpy})_3]^{2+}$	0.66	0.34	0.67	0.33
$[\text{Fe}(\mathbf{Bpy})_2]^{2+}$	0.55	0.45	0.58	0.42

Firstly, the values support again the concept of the +I-effect for the dimethylated compounds which have the highest $\gamma\text{H}^+_{\text{Para}}(100)$ values of all samples. For the monomethylated and unmethylated compounds the situation is more difficult to explain and it is obvious that the twisting of the pyridyl rings here is also influenced by sterical interactions. Furthermore, the substitution differences appearing on one single ligand should also be taken into account. So far we assumed that protonation is equally distributed among the available nitrogen donors at one complex but this is a simplification. It borders on certainty that especially for the monomethylated compounds basicity differences at one ligand are important. Additionally, the influence of CH- π -, polar- π - and ion- π -interactions must be considered. Water for example is well known to undergo polar- π -interactions with benzene molecules.^[136] Surprisingly, a former undetected feature becomes observable. It appears that the equilibrium between $\gamma\text{H}^+_{\text{Para}}(100)$ and $\gamma\text{H}^+_{\text{Dia}}(100)$ stays nearly identical for the monomethylated and

unmethylated compounds between 300 K and 350 K. The magnetic equilibrium here is a steady-state condition not influenced by the temperature. The overall rise in magnetism is solely generated by further temperature induced protonation happening in the same time domain as the ring-flip. This is not the case for the dimethylated compounds where the magnetic equilibrium is shifted strongly to the side of the paramagnetic species with rising temperature. This is most likely a result of the increased molecular motion exerted by the methyl groups on the ligand.

Hence, it is presented in detail how the magnetism of diamagnetic complexes as well as SCO systems can be modulated towards the HS state via PD-CISSS. Additionally it is shown that the performance is highly pH-, temperature- and concentration-dependent and can be modified towards 100% switchability. In combination it is highlighted via ligand substitution how the responsiveness can be modulated easily. This opens up new possibilities to enhance PD-CISSS effects via substitution for example with long alkyl chains with a strong inductive effect or other groups able to donate whole electron pairs like for example ethers. Due to these opportunities it should be possible to design more advanced pH-responsive probes that could be triggered around neutral pH to serve as smart CA's in fMRI visualizing tissue-pH.

Parts of this section (2.2 Proton-driven coordination-induced spin state switch) have been reproduced by permission of the Royal Society of Chemistry. Findings have been published in an article with the **DOI:10.1039/C6CC08618G** which can be found on the website of the Royal Society of Chemistry.

2.3 Iron(II) complexes under small confinement

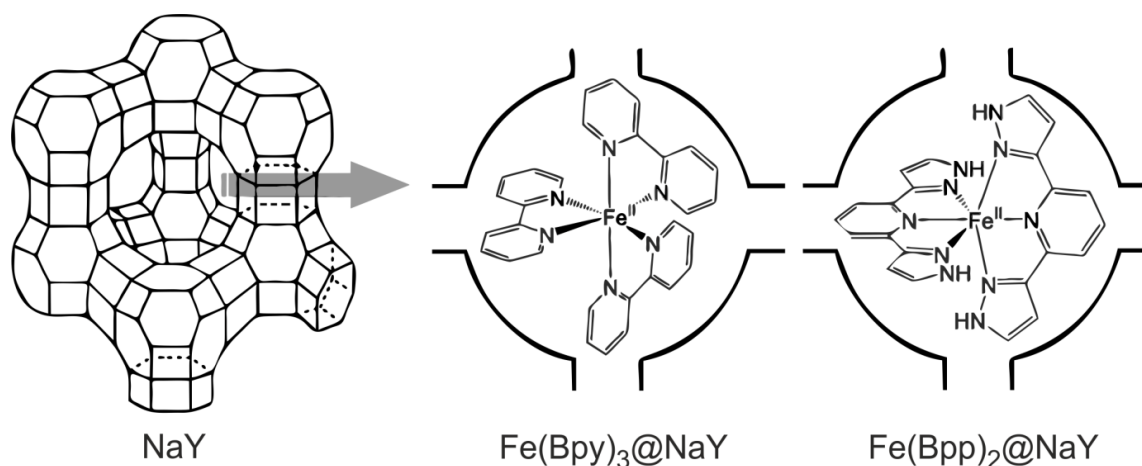
Zeolites play an important role in the fields of catalysis as well as in separation and sieving due to their defined porous architecture and their ion exchange ability.^[58-60] Recently there is also a rising interest in using these materials in biomedical applications since they provide an outstanding biocompatibility paired with the possibility of precise nanostructuring.^[90-97] In formidable experiments zeolites have been used already as imaging reporter, drug carrier or medical nanoprobe and have given a significant impetus to the rise of medical nanotechnology.^[114] One particular interesting medical application is the use of zeolites as carrier for smart CA's.^[90-97] Those are considered as a key development for an early and effective detection of cancerous tissue.^[20,22] Therefore we decided to investigate the potential of iron complexes as smart CA's by synthesizing zeolite hybrids which are consist of a faujasite carrier and an iron reporter function.

The following samples were prepared by a wet impregnation approach which was carried out in methanol and yielded $\text{Fe}(\text{Bpy})_3@NaY$ and $\text{Fe}(\text{Bpp})_2@NaY$. During the impregnation process the major species in solution is $[\text{Fe}(\text{Bpy})_3]^{2+}/[\text{Fe}(\text{Bpp})_2]^{2+}$. For a very small amount of the iron centers, one or two of the Bpy/Bpp ligands are replaced partially by methanol. These species can access the small channels and since they are always partially coordinated they can only be located in the supercages. Wet impregnation was also applied to obtain $\text{Fe}(\text{Bpy})_3@NH_4Y$, $\text{Fe}(\text{Bpy})_3@KY$, $\text{Fe}(\text{Bpy})_3@CaY$ and $\text{Fe}(\text{Bpy})_3@LaY$ from simple ion exchanged zeolites. The faujasite carrier exhibits common bulk properties since the particles are micro-sized. For comparison also a La-blocked sample $\text{Fe}(\text{Bpy})_3@FeLaY$ is analyzed.

2.3.1 General information and characterization

For the ion exchanged sample $\text{Fe}(\text{Bpy})_3@FeLaY$ around 2.4 wt% of iron were determined. Thus an iron center can be found nearly in every pseudo cell. In case of the impregnated sample $\text{Fe}(\text{Bpy})_3@NaY$ 0.13 wt% iron (AAS) were detected. This is more than twenty times less than for an iron exchange due to the small dissociation constant. For both samples a slight excess of the Bpy ligand (0.05 wt%) is detected. The results indicate that one $[\text{Fe}(\text{Bpy})_3]^{2+}$ unit is present in every 2.4 unit cells. Consequently, one complex is surrounded by 18 empty pseudo cells making direct interactions between the iron cores impossible. The loading of the

samples $\text{Fe}(\text{Bpy})_3@ \text{NH}_4\text{Y}$, $\text{Fe}(\text{Bpy})_3@ \text{CaY}$ and $\text{Fe}(\text{Bpy})_3@ \text{KY}$ is even lower with loadings of 0.07 wt%, 0.09 wt% and 0.08 wt%. $\text{Fe}(\text{Bpy})_3@ \text{LaY}$ was found to have an iron content of 0.12 wt%. $\text{Fe}(\text{Bpp})_2@ \text{NaY}$ has an iron content of 0.36 wt%. The significantly higher value compared to the Bpy-samples can be traced back to the longer reaction time and the fact that only one ligand has to dissociate to allow the complex to trespass the nanochannels of NaY. The nitrogen excess is also below 0.05 wt% and is most likely to be caused by entrapped ligand. One complex is found in every unit cell. In this sample there is one layer of empty supercages between every iron center. A schematic representation of the impregnated samples is given in Scheme 18. The overall composition of the impregnated samples is summed up in Table 20. See the literature for further sample explanations.^[67,132,137]



Scheme 18. Illustration of the homoleptic iron complexes $[\text{Fe}(\text{Bpy})_3]^{2+}$ and $[\text{Fe}(\text{Bpp})_2]^{2+}$ small enough to be encapsulated inside the supercages of zeolite NaY (Bpp = 2,6-bis(1*H*-pyrazol-3-yl)pyridine, Bpy = 2,2'-bipyridine).

Table 20. Iron contents together with elemental analysis of the impregnated samples.

	Fe [wt%]	N [wt%]	C [wt%]	H [wt%]
$\text{Fe}(\text{Bpy})_3@ \text{NaY}$	0.13	0.26	12.31	3.05
$\text{Fe}(\text{Bpy})_3@ \text{KY}$	0.08	0.14	9.53	2.15
$\text{Fe}(\text{Bpy})_3@ \text{CaY}$	0.09	0.94	12.88	2.20
$\text{Fe}(\text{Bpy})_3@ \text{NH}_4\text{Y}$	0.07	3.66	10.66	3.06
$\text{Fe}(\text{Bpy})_3@ \text{LaY}$	0.12	1.61	14.21	2.22
$\text{Fe}(\text{Bpp})_2@ \text{NaY}$	2.18	11.81	26.81	3.14

For the Mössbauer spectra of the samples prepared with the wet impregnation approach, only one LS doublet is detected in all cases. As typical representative the Mössbauer spectrum of the sample $\text{Fe}(\text{Bpy})_3@NaY$ is given in Figure 33A. The observed doublet can be clearly assigned to $[\text{Fe}(\text{Bpy})_3]^{2+}$ and no indications of other species (e.g. mono- and bis-coordinated bipyridine species)^[127] are observed, in agreement with results of Lunsford *et al.*^[72-74,80] The Mössbauer spectrum of $\text{Fe}(\text{Bpp})_2@NaY$ (Figure 33B) is also in agreement with the formation of the homoleptic complex $[\text{Fe}(\text{Bpp})_2]^{2+}$ inside of the zeolite.^[130] The fitting parameters are given in Table 21. For the remaining samples the iron content was too small to be characterized using Mössbauer spectroscopy.

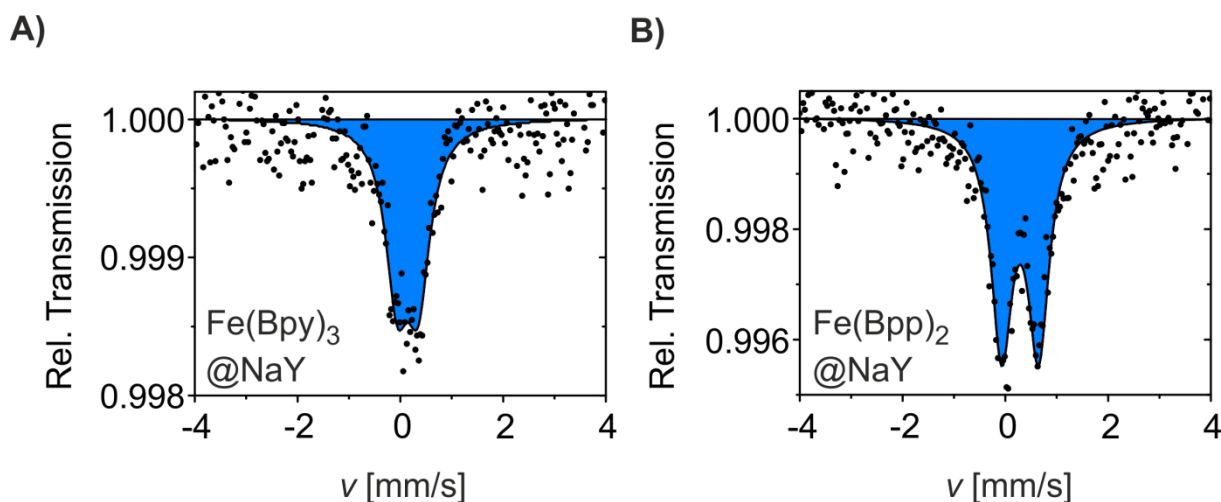


Figure 33. Room temperature Mössbauer spectra of $\text{Fe}(\text{Bpy})_3@NaY$ (A) and $\text{Fe}(\text{Bpp})_2@NaY$ (B). The black dots correspond to the measured transmission and the solid line corresponds to the fit with the refinement parameters given in Table 21. In both cases a doublet (blue) characteristic for the diamagnetic iron(II) LS species is observed.

Table 21. Compilation of the Mössbauer parameters of $\text{Fe}(\text{Bpy})_3@NaY$ and $\text{Fe}(\text{Bpp})_2@NaY$.

	Spin state	δ [mm s ⁻¹]	ΔE_Q [mm s ⁻¹]	$\Gamma/2$ [mm s ⁻¹]
$\text{Fe}(\text{Bpy})_3@NaY$	LS	0.23(3)	0.34(6)	0.24(5)
$\text{Fe}(\text{Bpp})_2@NaY$	LS	0.29(2)	0.72(4)	0.25(3)

Evanescent-wave-IR measurements show that no adhesion of complexes on the surface is taking place for all samples. This proves the incorporation of the complex in the zeolite. The corresponding spectra are given in Figure 34. Vibrations between 600 cm^{-1} and 1200 cm^{-1} belong to the zeolite lattice while the small vibrations around 1600 cm^{-1} belong to water which is incorporated in the zeolite framework.^[68] Next to these results EDX measurements were conducted as the amount of iron complexes on the surface of the impregnated samples could be too small to be detected by IR spectroscopy. The measurement of $\text{Fe}(\text{Bpy})_3@NaY$ revealed the presence of O, Na, Al and Si which all belong to the zeolite framework. The carbon belongs most likely to organic solvent molecules or to the ligand sphere of the complexes visible for the electron beam through the zeolite windows. Nevertheless, no iron can be detected what highlights the ability of the impregnation method to incorporate complexes inside of the voids. The SEM images (see Appendix A18–19) together with the EDX results confirm the absence of complex particles on the surface.

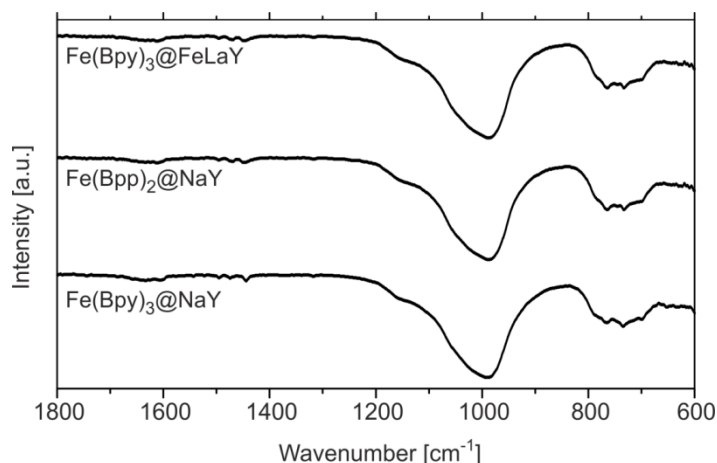


Figure 34. Evanescent-wave-IR measurements of $\text{Fe}(\text{Bpy})_3@NaY$, $\text{Fe}(\text{Bpp})_2@NaY$ and a La-blocked iron exchanged sample $\text{Fe}(\text{Bpy})_3@FeLaY$. Relative transmission is plotted against the wave number. The spectra were recorded between 600 cm^{-1} and 1800 cm^{-1} .

Discrepancies in the literature can be explained by different preparation methods.^[72-74,77,80] Contact solutions are not able to exchange complexes into the zeolite, most likely due to the very short contact time compared to stirring the zeolite in the complex solution for several hours or days. Another important fact is the pre-heat-treatment and a proper degassing.

Especially the latter was already taken into account for having a huge impact on the complex formation and loading.^[72-74,77,80] Powder diffraction is in fine agreement with the literature (see Figure 35).^[84,127,138] Only reflexes are detected which belong to the zeolite. All measurements verify that the complexes are encapsulated in the zeolite, that there is essentially no surface adhesion and that no crystalline bulk material is present.

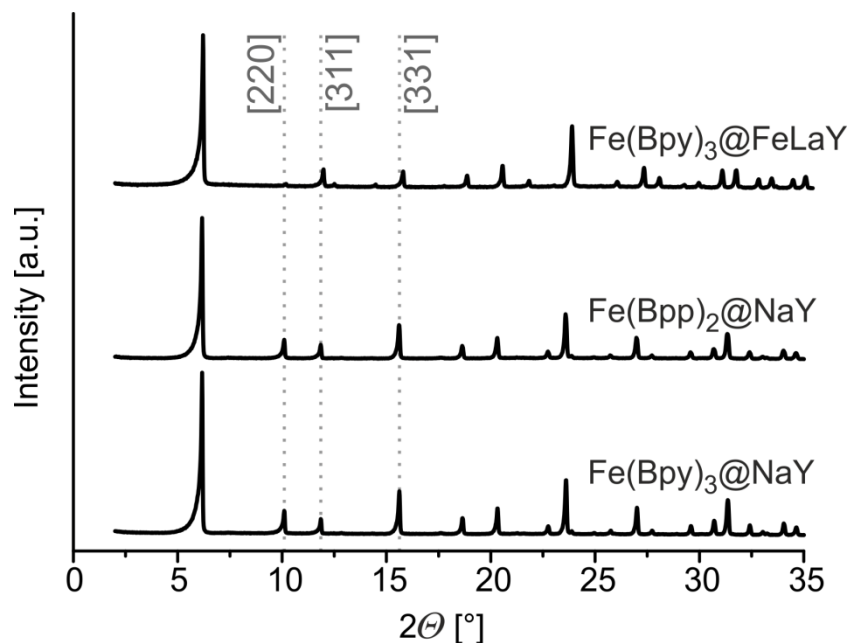


Figure 35. XRD patterns for $\text{Fe}(\text{Bpy})_3@NaY$, $\text{Fe}(\text{Bpp})_2@NaY$ and $\text{Fe}(\text{Bpy})_3@FeLaY$. The intensity is plotted against the diffraction angle 2θ .

^{29}Si , ^{23}Na , ^{27}Al and ^1H MAS NMR spectra were recorded to characterize the samples completely, especially to analyze the presence of Brønsted acid sites. In Figure 36 the ^{29}Si , ^{27}Al and ^{23}Na MAS spectra of the sample $\text{Fe}(\text{Bpy})_3@NaY$ as well as the free zeolite NaY are compared. The spectra of both compounds are very similar with a slight shift of the resonances. The ^{27}Al MAS spectra of those samples show that extra-framework aluminum is factually not present.^[139] The ^{23}Na and ^{29}Si signals are in a commonly observed range and in very good agreement to literature data.^[139] ^1H MAS NMR spectra are given in Figure 37. The Brønsted acid sites in the zeolite pointing towards the supercage are typically observed between 3.5 ppm and 4.5 ppm depending on the zeolite source.^[139,140] In the NaY starting material they were observed at 3.6 ppm and their presence in $\text{Fe}(\text{Bpy})_3@NaY$ is confirmed by

a peak at 3.8 ppm. The environment is highly acidic due to a shift of 0.2 ppm from 3.6 ppm as shown by Yan *et al.*^[139,140] Incorporated water is found at 3.0 ppm (NaY) and 3.4 ppm ($\text{Fe}(\text{Bpy})_3@ \text{NaY}$). The impregnated sample was washed with toluene which signals appear at 2.6 ppm and 7.4 ppm; 0.2 ppm deep-field-shifted compared to solution.^[139,141] Due to the low complex loading the resonances of the ligand are hidden by the toluene signals.

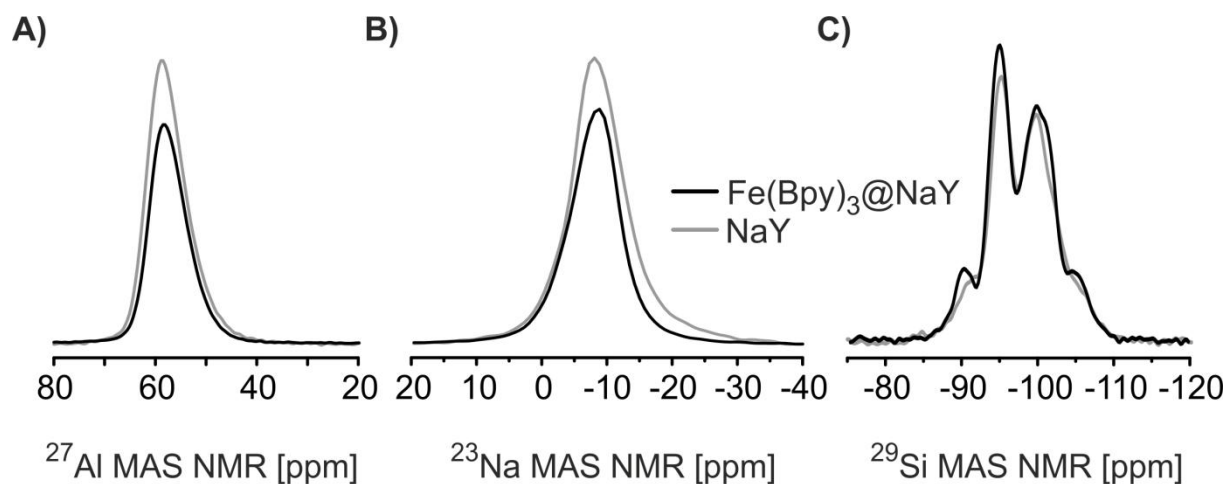


Figure 36. ^{27}Al (A), ^{23}Na (B) and ^{29}Si (C) solid state MAS NMR spectra of NaY (grey) and $\text{Fe}(\text{Bpy})_3@ \text{NaY}$ (black). The chemical shift is given in ppm.

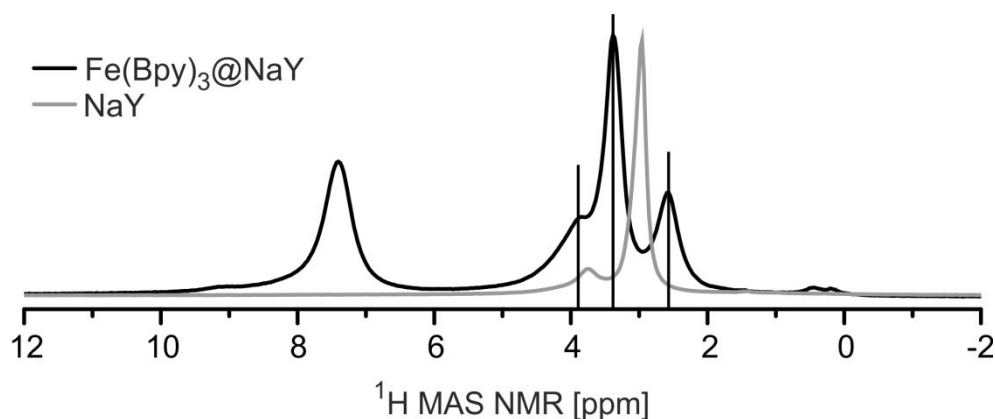


Figure 37. ^1H solid state MAS NMR spectra of NaY (grey) and $\text{Fe}(\text{Bpy})_3@ \text{NaY}$ (black). The chemical shift is given in ppm. Brønsted sites appear typically between 3.5 ppm and 4.5 ppm.

2.3.2 Optical characterization and chromaticity

The optical spectra as received after synthesis revealed only small differences between the hybrid materials and the bulk complex. The maximum of the MLCT-envelope of $\text{Fe}(\text{Bpy})_3@NaY$ is shifted towards 530 nm compared to 520 nm of the bulk complex what is characteristic for the small confinement.^[62,78] The d-d-transition at 350 nm is Laporte-forbidden and therefore very weak.^[142] The optical spectrum of $\text{Fe}(\text{Bpp})_2@NaY$ is mostly identical to the one reported by Halcrow *et al.*^[9,130] The MLCT-envelope is slightly red-shifted from 450 nm to 460 nm as it is observed for the bulk material in DMF. In our case it is also attributed to the interaction with the supercage. The shoulder at 550 nm is not assigned in the literature but belongs probably also to the MLCT-envelope. The $\pi-\pi^*$ transition appears at 310 nm. A d-d-transition is not observed what highlights the high symmetry of the complex. Upon heating a color change is observed for both samples that is displayed in Figure 38 and Figure 39. The color change is similar to the one already observed in solutions of the bare complex at different pH values.

First indications for the possibility to switch the spin state of the incorporated complexes were observed upon heating of the neat composite materials. For both samples, a completely reversible color change from red to colorless ($\text{Fe}(\text{Bpy})_3@NaY$), respectively yellow to colorless ($\text{Fe}(\text{Bpp})_2@NaY$) is observed upon heating that can be also followed by reflective Kubelka-Munk spectroscopy (loss of the MLCT-band from red/yellow to colorless). This color change is linked to a loss of water in the cavities of the zeolite as derived from TG analysis (see Appendix A16–17) and the red, respective yellow color is restored when $\text{Fe}(\text{Bpy})_3@NaY$, respective $\text{Fe}(\text{Bpp})_2@NaY$ are treated with a drop of water or equilibrated at air for some time. Interestingly, in the case of $\text{Fe}(\text{Bpp})_2@NaY$ the same reversible color change is observed upon heating although the bulk complex itself is known to undergo SCO at low temperatures.^[9,130] No indication for a color change upon cooling is observed and the Mössbauer spectrum at room temperature confirms, that the encapsulated complex is in a LS state. This indicates that the magnetic properties are significantly influenced by the zeolite environment, in agreement with some preliminary results on encapsulated cobalt(II) and iron(II) complexes.^[76,80-84] Remarkably, the properties of $[\text{Fe}(\text{Bpp})_2]^{2+}$ and $[\text{Fe}(\text{Bpy})_3]^{2+}$ in the supercage of the zeolite are very similar although the first system is well known for its SCO properties while the latter is a stable LS complex.^[8,9,130]

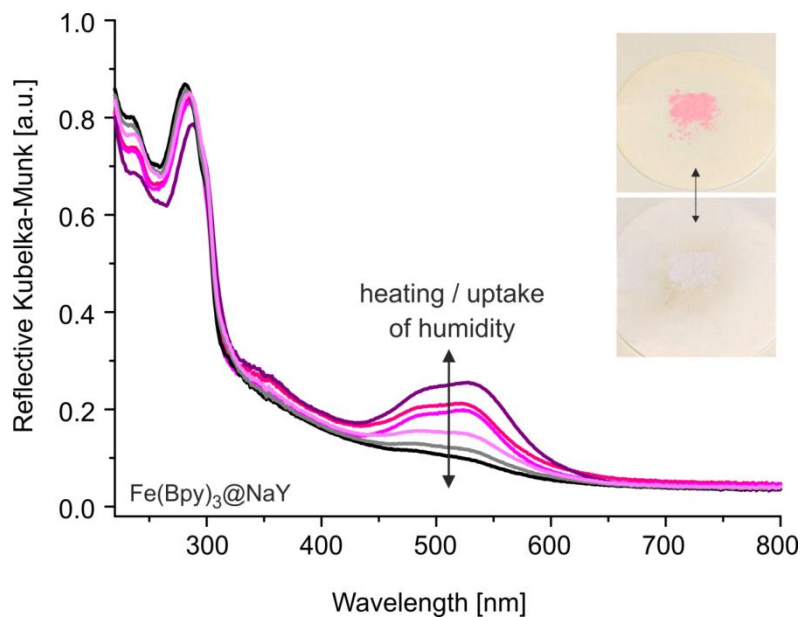


Figure 38. Reflective Kubelka-Munk measurements of $\text{Fe}(\text{Bpy})_3@NaY$. Baseline correction and 100% transmission reference are omitted for clarity. Heating to 370 K corresponds to the black line where a complete absence of the MLCT-band is observed. It recovers when a droplet of $\text{MeOH}/\text{H}_2\text{O}$ is added or is left at humid air (violet and red lines).

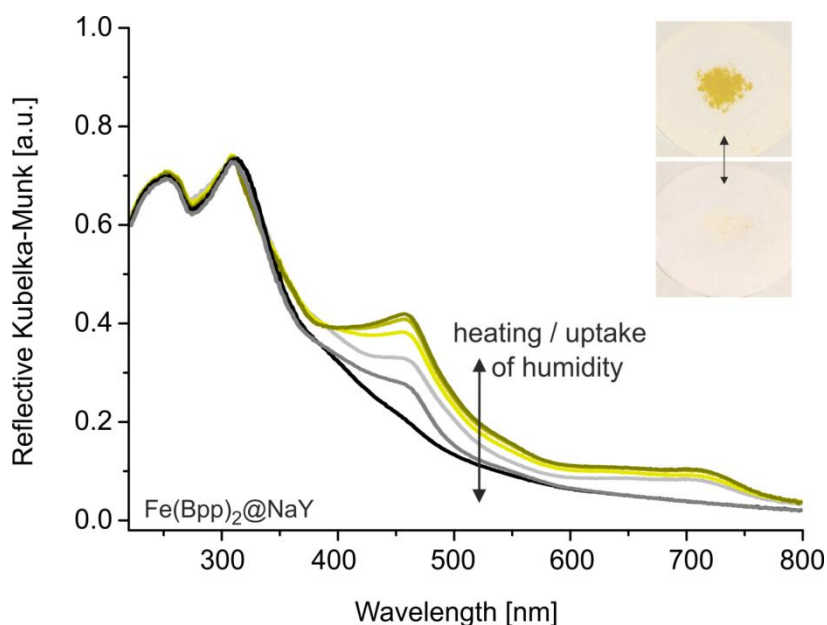
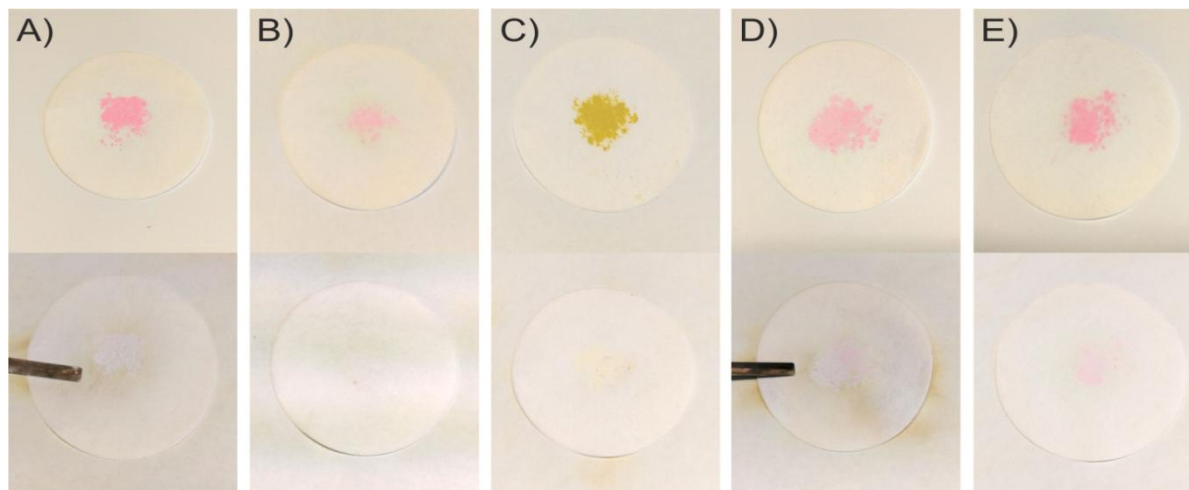


Figure 39. Reflective Kubelka-Munk measurements of $\text{Fe}(\text{Bpp})_2@NaY$. Baseline correction and 100% transmission reference are omitted for clarity. Heating to 370 K corresponds to the black line where a complete absence of the MLCT-band is observed. It recovers when a droplet of $\text{MeOH}/\text{H}_2\text{O}$ is added or is left at humid air (yellow and grey lines).

A color change upon heating or uptake of humidity from the air can be observed for all impregnated samples. The corresponding pictures for $\text{Fe}(\text{Bpy})_3@NaY$, $\text{Fe}(\text{Bpy})_3@NH_4Y$, $\text{Fe}(\text{Bpp})_2@NaY$, $\text{Fe}(\text{Bpy})_3@KY$ and $\text{Fe}(\text{Bpy})_3@CaY$ are given in Scheme 19.



Scheme 19. Reversible color change of the discussed hybrid materials upon heating. From left to right: **A)** $\text{Fe}(\text{Bpy})_3@NaY$, **B)** $\text{Fe}(\text{Bpy})_3@NH_4Y$, **C)** $\text{Fe}(\text{Bpp})_2@NaY$, **D)** $\text{Fe}(\text{Bpy})_3@KY$ and **E)** $\text{Fe}(\text{Bpy})_3@CaY$.

The reflective Kubelka-Munk measurements were accompanied with temperature-dependent measurements of the overall reflectivity. The results for $\text{Fe}(\text{Bpy})_3@NaY$ are given in Figure 40. The sample measurement starts at 250 K with an overall reflectivity of 9.1 which is maintained till 330 K. Above 330 K the reflectivity rises steadily up to 12.5. Further cooling and heating cycles are performed where the overall reflectivity stays more or less the same and varies slightly between 12.5 and 12.8 when the temperature is shuffled between 250 K and 400 K. The results are in line with the observed color change from a red to a colorless state. The reflectivity does not recover after cooling since the measurements are performed under vacuum. Similar measurements were performed for $\text{Fe}(\text{Bpp})_2@NaY$ and are displayed in Figure 41. The sample measurement starts at 250 K with an overall reflectivity of 6.8 which is maintained till 350 K. Above 350 K the reflectivity rises steadily up to 11.0. Further cooling and heating cycles are performed where the overall reflectivity stays more or less the same and varies slightly between 11.0 and 8.7 when the temperature is shuffled between 250 K and 400 K. Nevertheless, a broader variation as it was observed for $\text{Fe}(\text{Bpy})_3@NaY$. The results are in line with the observed color change from a yellow to a colorless state.

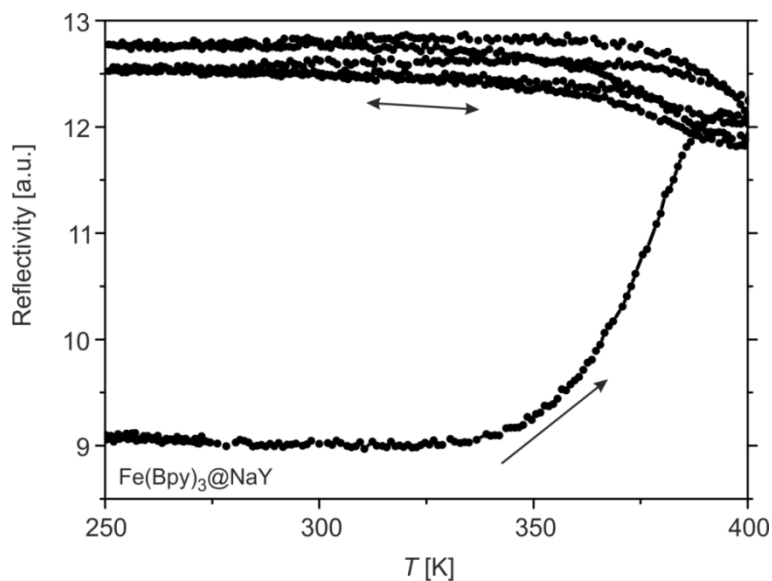


Figure 40. The overall reflectivity of the sample Fe(Bpy)₃@NaY is plotted against the temperature during several heating modes between 250 K and 400 K.

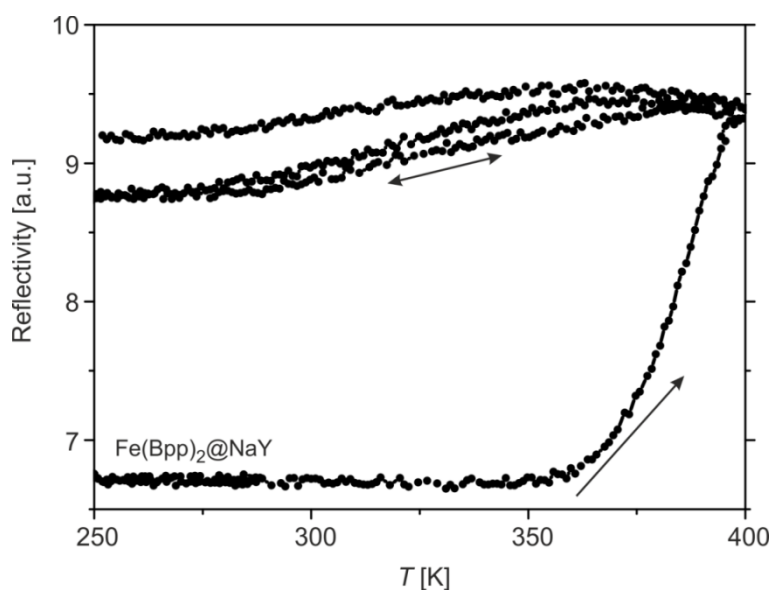


Figure 41. The overall reflectivity of the sample Fe(Bpp)₂@NaY is plotted against the temperature during several heating modes between 250 K and 400 K.

Interestingly, essentially no change of the overall reflectivity is observed for the La-blocked and iron exchanged sample Fe(Bpy)₃@FeLaY which stays constantly around 3.0 over the complete investigated temperature range. This finding is in line with the corresponding magnetic measurements.^[132] Furthermore, also no color change could be observed upon heating of this hybrid materials. The corresponding measurements are given in Figure 42.

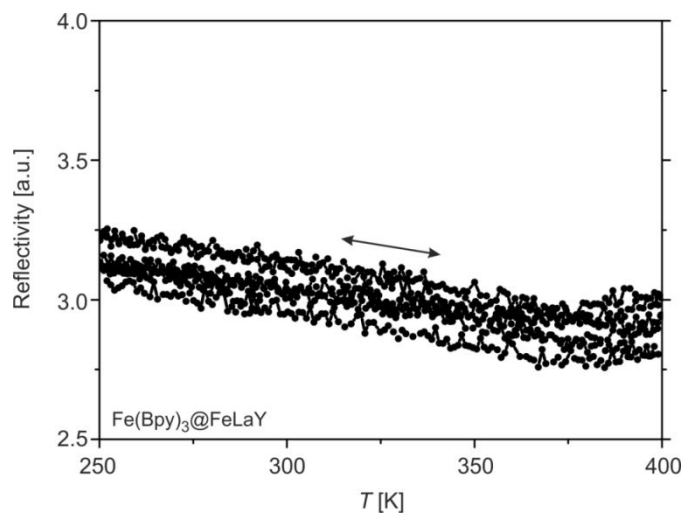


Figure 42. The overall reflectivity of the sample $\text{Fe}(\text{Bpy})_3@ \text{FeLaY}$ is plotted against the temperature during several heating modes between 250 K and 400 K.

2.3.3 Magnetism of zeolite hybrid materials

The observed color change is characteristic for a spin state change. This was analyzed using magnetic measurements in the 150–400 K temperature range. The data are given in Figure 43 for $\text{Fe}(\text{Bpy})_3@ \text{NaY}$ and in Figure 44 for $\text{Fe}(\text{Bpp})_2@ \text{NaY}$. The RT magnetic susceptibility χ_{Mass} of $\text{Fe}(\text{Bpy})_3@ \text{NaY}$ and $\text{Fe}(\text{Bpp})_2@ \text{NaY}$ is strongly negative ($-6 \cdot 10^{-3} \text{ cm}^3 \text{ g}^{-1}$ at 300 K for both samples), characteristic for diamagnetic zeolite samples. Due to the absence of paramagnetic iron centers, the room temperature mass susceptibility of those samples is also diamagnetic. Upon cooling and heating between RT and 150 K no significant changes are observed. Subsequent heating of both samples to 400 K reveals a significant increase in the mass susceptibility in both cases, with a χ_{Mass} value at 300 K of $-3 \cdot 10^{-3} \text{ cm}^3 \text{ g}^{-1}$ for $\text{Fe}(\text{Bpy})_3@ \text{NaY}$ and $3 \cdot 10^{-3} \text{ cm}^3 \text{ g}^{-1}$ for $\text{Fe}(\text{Bpp})_2@ \text{NaY}$. This corresponds to a change of the mass susceptibility ($\Delta\chi_{\text{Mass}}$) at room temperature of $3 \cdot 10^{-3} \text{ cm}^3 \text{ g}^{-1}$ for $\text{Fe}(\text{Bpy})_3@ \text{NaY}$ and $9 \cdot 10^{-3} \text{ cm}^3 \text{ g}^{-1}$ for $\text{Fe}(\text{Bpp})_2@ \text{NaY}$. In the case of $\text{Fe}(\text{Bpp})_2@ \text{NaY}$ the increase of $\Delta\chi_{\text{Mass}}$ is more pronounced in line with the higher iron contents (three fold). From this the generation of a paramagnetic complex inside the composite materials can be concluded. Subsequent cooling and heating cycles reveal a slight increase of the χ_{Mass} with decreasing temperatures as expected for paramagnetic samples due to the Curie law. The increase of χ_{Mass} is correlated with the color change. This indicates, that the spin state of the iron center changes from a diamagnetic LS to a paramagnetic HS state for both samples.

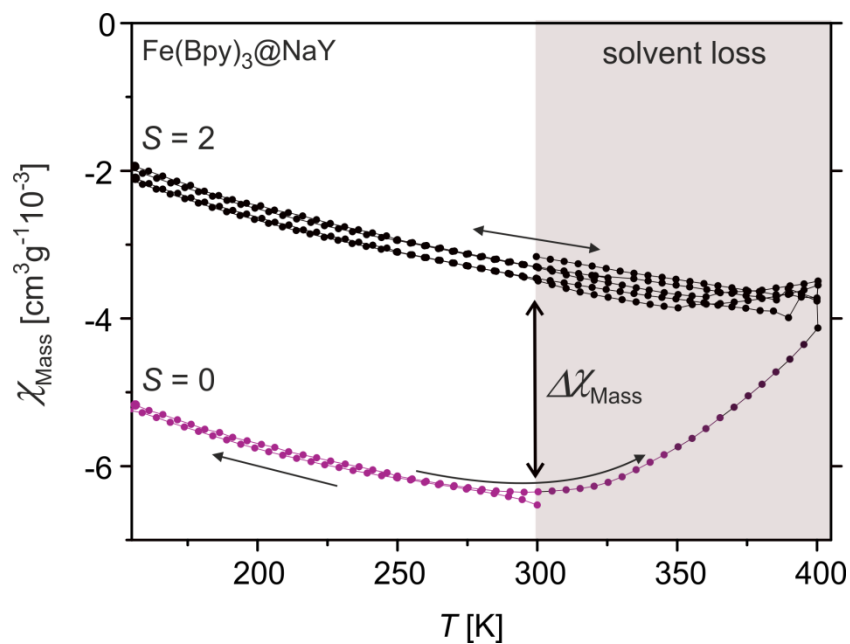


Figure 43. Magnetic behavior of $\text{Fe}(\text{Bpy})_3@NaY$. χ_{Mass} is plotted against the temperature in a range between 150 K and 400 K. The measurements were performed at 20000 Oe in the settle mode. The measurement was started at 300 K and cooled down at first.

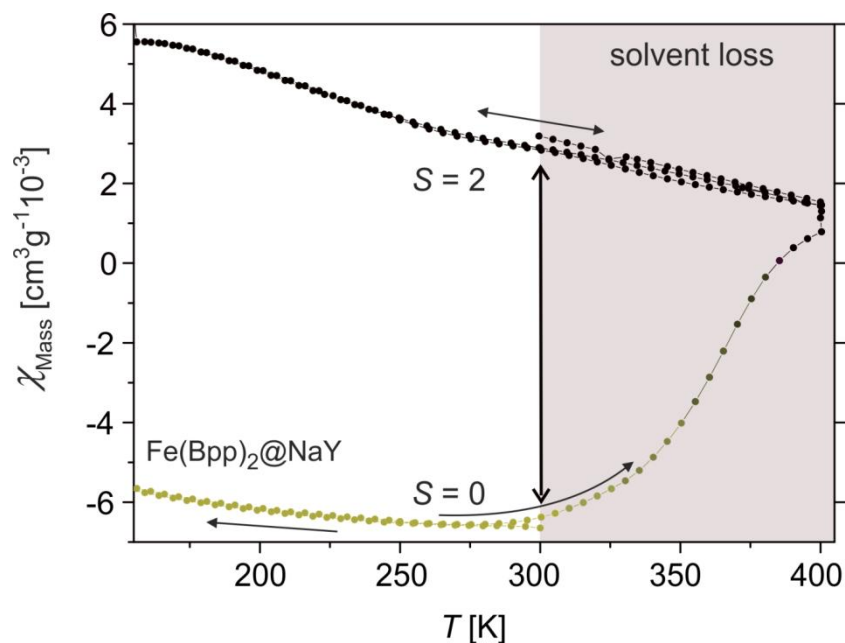


Figure 44. Magnetic behavior of sample $\text{Fe}(\text{Bpp})_2@NaY$. χ_{Mass} is plotted against the temperature in a range between 150 K and 400 K. The measurements were performed at 20000 Oe in the settle mode. The measurement was started at 300 K and cooled down at first.

The same behavior appears for $\text{Fe}(\text{Bpy})_3@ \text{NH}_4\text{Y}$, $\text{Fe}(\text{Bpy})_3@ \text{CaY}$, $\text{Fe}(\text{Bpy})_3@ \text{LaY}$ and $\text{Fe}(\text{Bpy})_3@ \text{KY}$ as it can be seen in Figure 45. They also show a pronounced rise of the magnetic susceptibility alongside the typical color change when heated above 300 K and also don't recover inside of the SQUID. $\text{Fe}(\text{Bpy})_3@ \text{CaY}$, $\text{Fe}(\text{Bpy})_3@ \text{LaY}$ and $\text{Fe}(\text{Bpy})_3@ \text{KY}$ start around the same value of χ_{Mass} but $\text{Fe}(\text{Bpy})_3@ \text{NH}_4\text{Y}$ is slightly reduced. Nevertheless, $\text{Fe}(\text{Bpy})_3@ \text{NH}_4\text{Y}$ shows the most pronounced rise of χ_{Mass} while $\text{Fe}(\text{Bpy})_3@ \text{LaY}$ has the most moderate rise of χ_{Mass} upon heating to 400 K. This can be traced back to the different counter cations. NH_4^+ itself is an acid which should increase the observed PD-CISSS effects what is exactly the case since the largest $\Delta\chi_{\text{Mass}}$ value is found. Furthermore, this sample has the lowest iron loading. In the literature it is known that La-blocking and exchange leads to the removal of Brønsted acid sites. Consequently, the lowest $\Delta\chi_{\text{Mass}}$ value is observed for $\text{Fe}(\text{Bpy})_3@ \text{LaY}$.

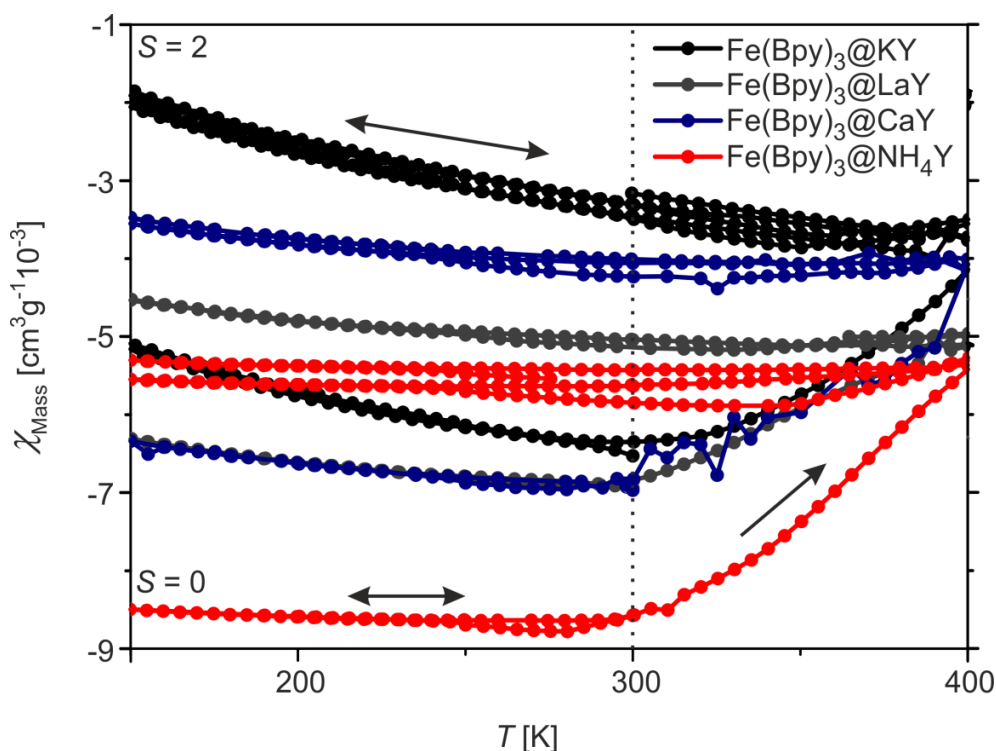


Figure 45. Magnetic behavior of $\text{Fe}(\text{Bpy})_3@ \text{NH}_4\text{Y}$ (red), $\text{Fe}(\text{Bpy})_3@ \text{CaY}$ (blue), $\text{Fe}(\text{Bpy})_3@ \text{LaY}$ (grey) and $\text{Fe}(\text{Bpy})_3@ \text{KY}$ (black). χ_{Mass} is plotted against the temperature in a range between 150 K and 400 K. The measurements were performed at 20000 Oe in the settle mode. They were started at 300 K and cooled down at first.

For a better comparison of the samples the differences between the average values for the magnetic mass susceptibility at 300 K were determined before and after reaching 400 K during the first heating cycle. In Figure 46 those values ($\Delta\chi_{\text{Mass}}$) were plotted against the iron weight content of all the discussed samples where iron(II) complexes have been incorporated inside of microsized NaY. A direct proportional correlation between the complex loading and the rise of the magnetic susceptibility is indicated. The grey dots represent $\text{Fe}(\text{Bpy})_3@ \text{NH}_4\text{Y}$ and $\text{Fe}(\text{Bpy})_3@ \text{LaY}$ which behave slightly different than expected and were explained previously and therefore were not considered for the fitting.

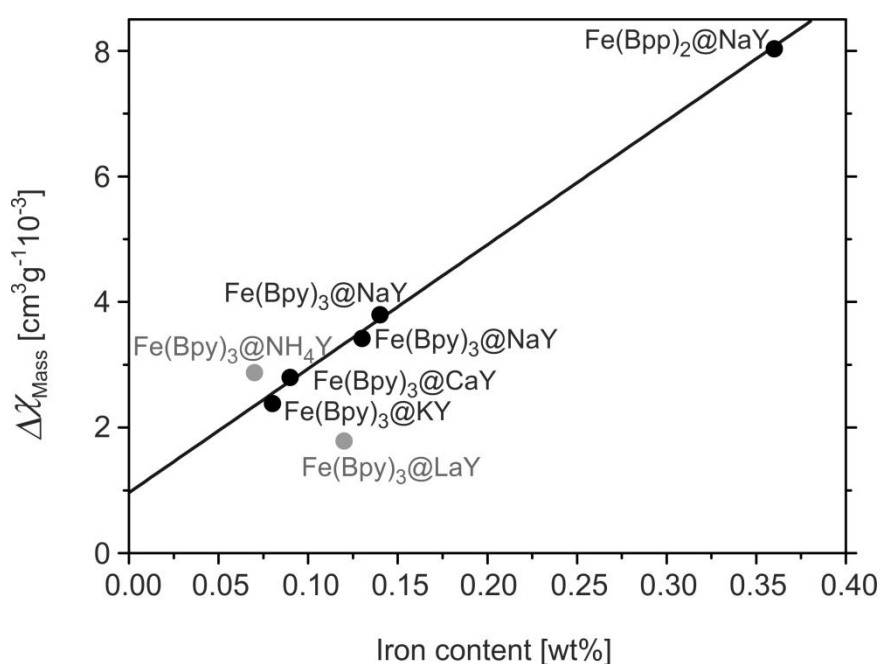
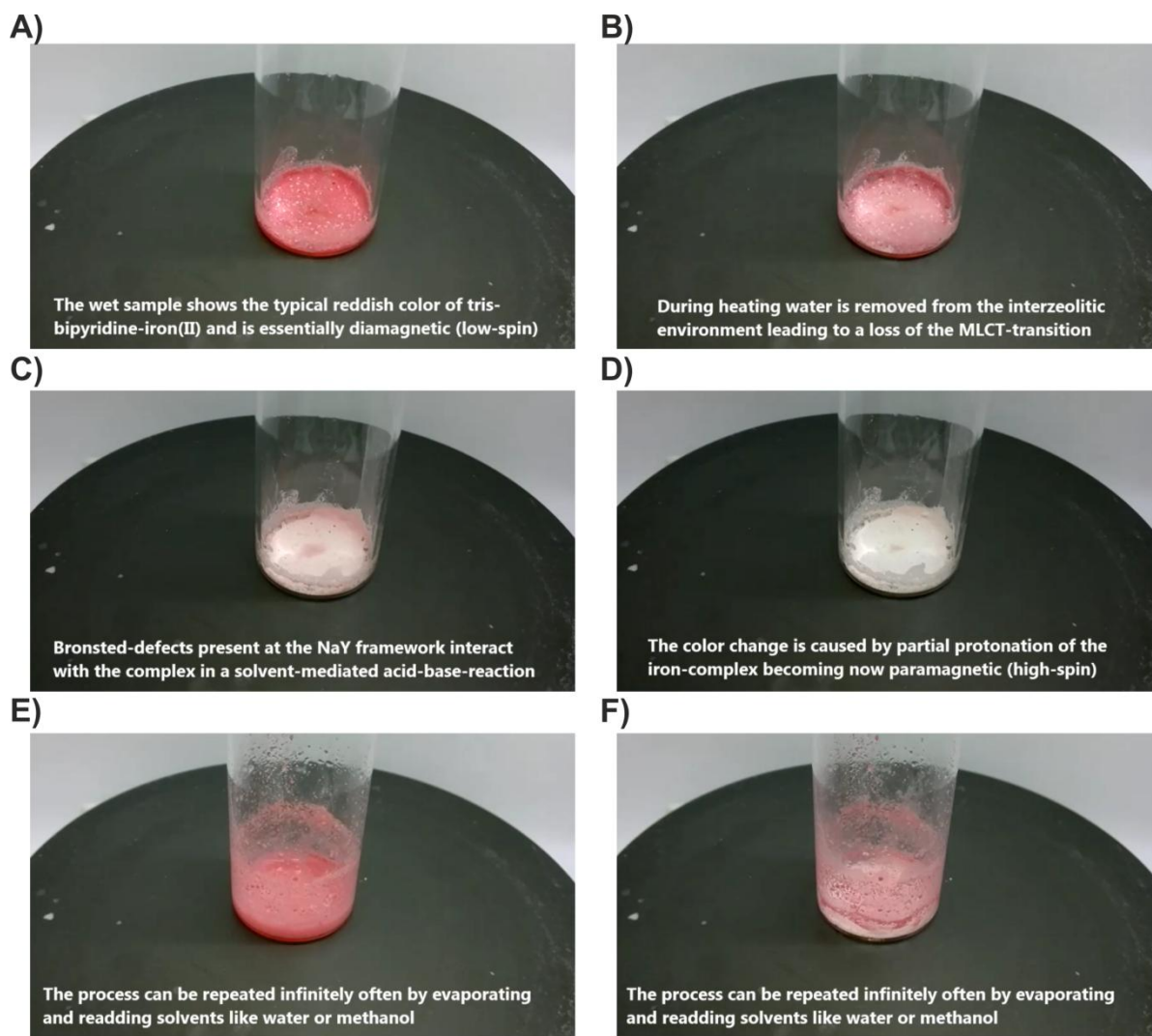


Figure 46. Plot of $\Delta\chi_{\text{Mass}}$ of the discussed samples against their iron content. $\Delta\chi_{\text{Mass}}$ was taken at 300 K before and after the first heating cycle. A direct proportional correlation is found between the complex loading and $\Delta\chi_{\text{Mass}}$ which is reassembled by the black line.

In Scheme 20 photographs of a video are given where $\text{Fe}(\text{Bpy})_3@ \text{NaY}$ was heated on a heating plate.^[132] Due to the rise in temperature water is removed from the intrazeolitic channels what lowers the intrazeolitic pH. This leads to the formation of protonated paramagnetic species triggered by a PD-CISSS. This effect is completely reversible since the color recovers completely when a droplet of MeOH or water is added. The cycle can be repeated infinitely often.



Scheme 20. Photographs of the reversible color change exhibited by $\text{Fe}(\text{Bpy})_3@ \text{NaY}$ upon solvent removal during heating and subsequent recovering by addition of MeOH.

Please note, that this spin state change and the associated color change can also be observed for suspensions of the composite material $\text{Fe}(\text{Bpy})_3@ \text{NaY}$ in water, when the pH is lowered in small steps by the use of hydrochloric acid. A picture of this series where the pH was varied between 6.0 and 2.0 is given at the bottom of Scheme 21 together with the investigated mechanism. Similar results could be obtained for $\text{Fe}(\text{Bpy})_3@ \text{FeLaY}$ which couldn't be switched upon heating but in acidic solution. In line with the proposed coordination change at the iron center, a significant T_1 shortage of the intrazeolitic water is found for the solid composite material $\text{Fe}(\text{Bpp})_2@ \text{NaY}$ between the wet (water vapour saturation) state (27.79 ms) and dry (heated at 100 °C) state (11.06 ms) with solid state NMR (see Figure 47).

The composite material $\text{Fe}(\text{Bpy})_3@ \text{NaY}$ was saturated with 0.1 M HCl and heated in a solid state NMR experiment; T_1 is reduced gradually from 26.66 ms at 300 K, 19.38 ms at 320 K and 15.73 ms at 340 K to 11.93 ms at 375 K (Figure 47). It can be concluded that inside the zeolite a proton-driven coordination-induced spin state switch (PD-CISSS) takes place.

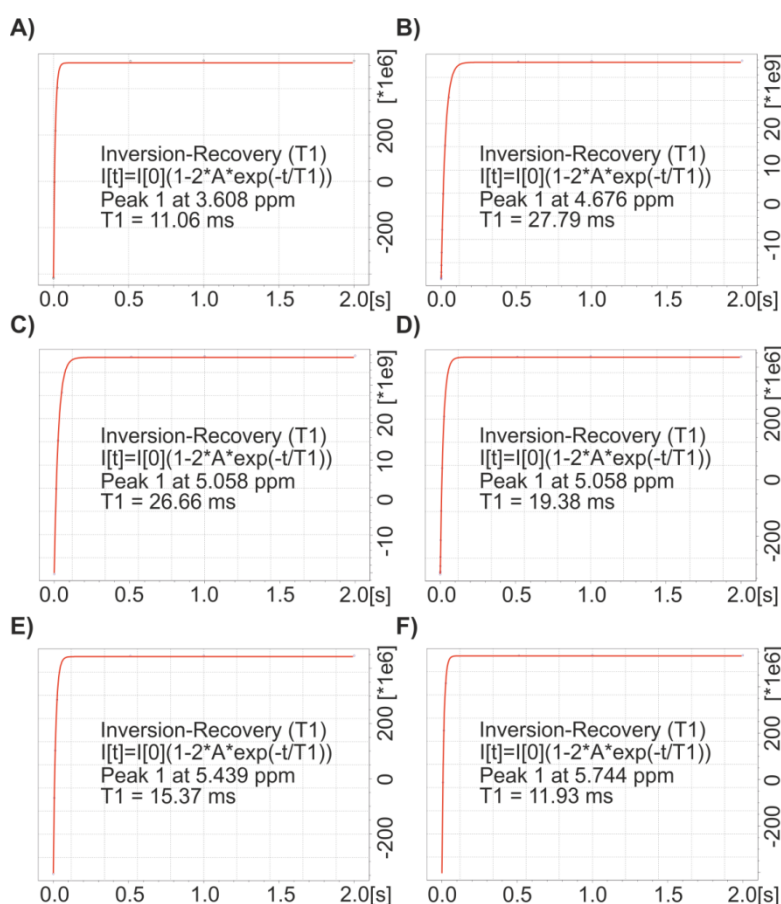


Figure 47. ^1H inversion-recovery experiments via solid state NMR to determine the relaxation time T_1 of the water bound inside the intrazeolitic channels. Sample $\text{Fe}(\text{Bpp})_2@ \text{NaY}$ dried *in vacuo* at 400 K (A) and saturated above water vapor for one day (B). Sample $\text{Fe}(\text{Bpy})_3@ \text{NaY}$ was treated with a droplet of 0.1 M HCl and saturated above water vapor for one day. Relaxation times T_1 have been measured at 300 K (C), 320 K (D), 340 K (E) and 375 K (F).

Parts of this section (2.3 Iron(II) complexes under small confinement) have been reproduced by permission of the Royal Society of Chemistry. Findings have been published in an article with the DOI:10.1039/C6CC08618G which can be found on the website of the Royal Society of Chemistry.

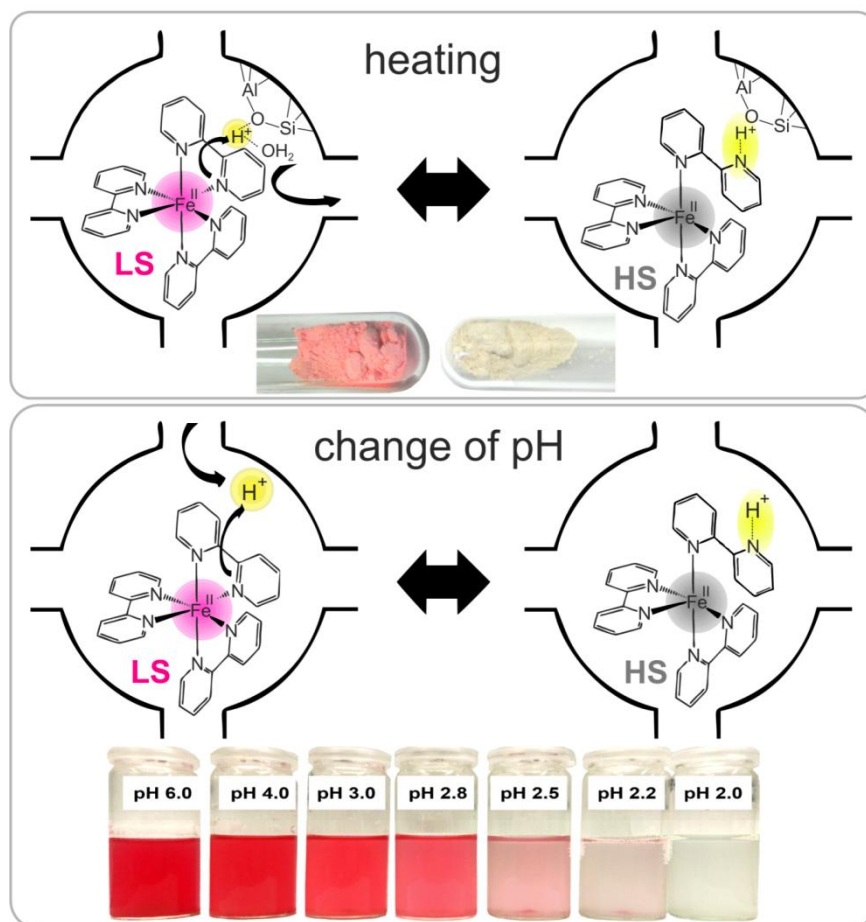
2.4 pH-Responsive magnetism in zeolites

2.4.1 Observations and systematic trends

Diamagnetic iron complexes have been entrapped inside the small nanovoids of micro-sized zeolite NaY and have been found to detect changes of the intrazeolitic environment by undergoing a proton-driven coordination-induced spin state switch (PD-CISSS) when present at a sufficiently low concentration. This behavior is not reported in literature yet since high zeolite loadings are usually desired, calcinations above 700 K remove Brønsted acid defects and uncomplexed iron can form stable diamagnetic adducts inside the supercages.^[72,74,143] All those conditions lead to stable LS complexes. Only samples of Fe(Bpy)₃@NaY and Fe(Bpp)₂@NaY prepared by wet impregnation exhibit temperature-dependent optical and magnetic properties. The spin state change is induced by Brønsted acid defects as it could be inferred from the alteration of the MLCT transition, the MAS NMR spectroscopy and SQUID magnetometry. The observed mechanism follows exactly the result which could already be generated in solution.

The fact that the alteration of the complex' optical properties is not observed for the La-blocked samples makes an involvement of Brønsted acid sites even more reasonable. Protons interact with the most basic part in the hybrids which are the *N*-donor atoms of the aromatic rings what consequently leads to differences in MLCT-transition as it has already been observed for aqueous solutions of the complex. All analysis verifies the presence of only the octahedral coordinated complexes inside of the zeolite. Additionally, for zeolites it is generally known that they carry proton defects and the complex loadings of the impregnated samples are in a region where interaction with them is shifted into an observable region.^[139,143] Therefore the observed effect under small confinement must be a spin state change with coordination change caused by Brønsted acid defects. Especially [Fe(Bpy)₃]²⁺ under small confinement is shown to exhibit reversible magnetic bistability upon protonation. Brønsted acid sites present in NaY zeolite are shielded from interaction with the nitrogen-donors of the 2,2'-bipyridine-backbone as long as intrazeolitic solvent is present. Upon solvent removal a competitive acid-base reaction takes place between the nitrogen-donor and the hydroxyl group that leads to the protonation of the iron complex and alters simultaneously its magnetic properties. The resulting protonated complex – a half-bonded species – becomes paramagnetic. This allows monitoring the Brønsted acidity via changes of the magnetic

moment. A free coordination spot becomes present where water molecules are exchanged rapidly as it was observed by paramagnetic relaxation enhancement in inversion-recovery experiments.



Scheme 21. Two different mechanisms leading to the formation of a protonated and hexacoordinated species inside the supercage. Top: Intrazeolitic proton defects undergo a competitive acid-base reaction with ligands in the near surrounding and change thereby the magnetism of the iron centers. Bottom: External protons attach to the nitrogen-donor.

In the wet state, the water in the zeolite cavities interacts with the Brønsted acid sites (hydrogen bonds) and thus prevents an interaction of those sites with the complex in the supercages. Upon heating, water is removed and now the Bpy (or the Bpp) ligand can interact with the Brønsted acid sites leading to a protonation of the nitrogen donor. This induces a coordination change at the iron center from six to five in line with a spin state change from a

diamagnetic low-spin state to a paramagnetic high-spin state. If this mechanism is correct, a similar color change should be observed for a suspension of the complex in an acid solution. In order to test the theory, a small amount of $\text{Fe}(\text{Bpy})_3@ \text{NaY}$ has been suspended in an aqueous solution where the pH was adjusted in small steps by the use of hydrochloric acid. With the bare eye it could be already seen that the suspensions lose their intense reddish-pink color and turn colorless with a rising proton concentration (what could be also observed for the La-blocked zeolite with high complex loading). A picture of the solution where the pH was varied between pH 6.0 and pH 2.0 is given in Scheme 21. This optical behavior is caused by the addition of protons to the nitrogen donor of the 2,2'-bipyridine ligands as it would be expected for an acid-base reaction. All color changes are similar to the changes observed upon solvent removal what indicates that both processes are caused by protons in the near surrounding of the iron complexes. Inside the zeolite a proton-driven coordination-induced spin state switch takes place.

2.4.2 Consequences and predictions

The presented system is not only an ultra precise proton detector but serves rather as attractive prototype for smart contrast agents in functional magnetic resonance imaging (*f*MRI). The ligand flexibility of the encapsulated system provides the basis for pH-detection via water relaxation since a free coordination spot becomes vacant upon proton attachment. It is most likely that the pH-responsive magnetism of the iron(II) reporter functions can be modulated via ligand substitution in a similar way as it has been presented in the initial part of this work. Therefore, it should be a promising approach to synthesize nanozeolite hybrids incorporating the complexes which were already investigated in solution. Those should lead to stable suspensions and the use of $[\text{Fe}(44\text{mBpy})_3]^{2+}$ for example should allow to increase the proton sensitivity also inside of the zeolites in a similar way as it has already been observed in acidic solution.

Parts of this section (2.4 pH-Responsive magnetism in zeolites) have been reproduced by permission of the Royal Society of Chemistry. Findings have been published in an article with the DOI:10.1039/C6CC08618G which can be found on the website of the Royal Society of Chemistry.

2.5 Iron(II) complexes encapsulated in nanozeolites

When biological applications for example as smart CA's are envisioned it is obvious that nanosized zeolite carriers need to be used. They can be easily transported through the blood vessels and are excreted completely over the kidney.^[144] Furthermore such Gd(III) based hybrid materials are already clinically used as CA's for gastrointestinal imaging. Therefore, the experimental procedures of the previous section where homoleptic iron(II) complexes were incorporated via impregnation into microsized zeolites were repeated for nanozeolites. The synthesis itself was basically maintained to avoid paramagnetic impurities and was just adjusted at steps where it was necessary to acknowledge the nanoparticulate structure of the hybrid materials (see Experimental Section). Nonetheless, it was found to be helpful to prepare initially iron(II) exchanged samples of the nanosized zeolites. This has two advantages. At first it is possible to compare the received Mössbauer spectra with the ones of the impregnated samples what is helpful for a correct signal assignment. Mössbauer data for nanosized zeolites are so far not available in the literature. Secondly, it appeared compelling to evaluate the two different preparation procedures with each other since the large surface of nanosized zeolites should make impregnation approaches more favorable.

2.5.1 Iron exchange experiments

The nanosized zeolites NaA, NaY and NaX have been subjected to an iron(II) exchange procedure. They were suspended in aqueous solutions with 10 wt%, 5 wt% and 2 wt% of $\text{FeCl}_2 \cdot 4 \text{H}_2\text{O}$ and were left in contact for the exchange equilibrium to be reached. The resulting Mössbauer spectra which were recorded after drying of the samples *in vacuo* are displayed in the following. For all exchanged NaA samples two characteristic doublets appear (see Figure 48) which belong to the iron(II) species in the sodalite cages (outer doublet, OD) and to hexaaquo iron(II) inside of the supercage (inner doublet, ID). The potential difference between the two exchange sites does not allow a selective incorporation of iron(II). Both sites are occupied unaffectedly by the overall iron concentration in solution although it can be observed that the amount of OD decreases with the iron concentration. In the resulting samples 2.6 wt%, 1.1 wt% and 0.6 wt% iron are found via AAS. The received percentages are the lowest for all samples since the extremely confined NaA has a drastically decreased water exchange rate.^[97] Full parameters and percentages are given in Table 22 and Table 23.

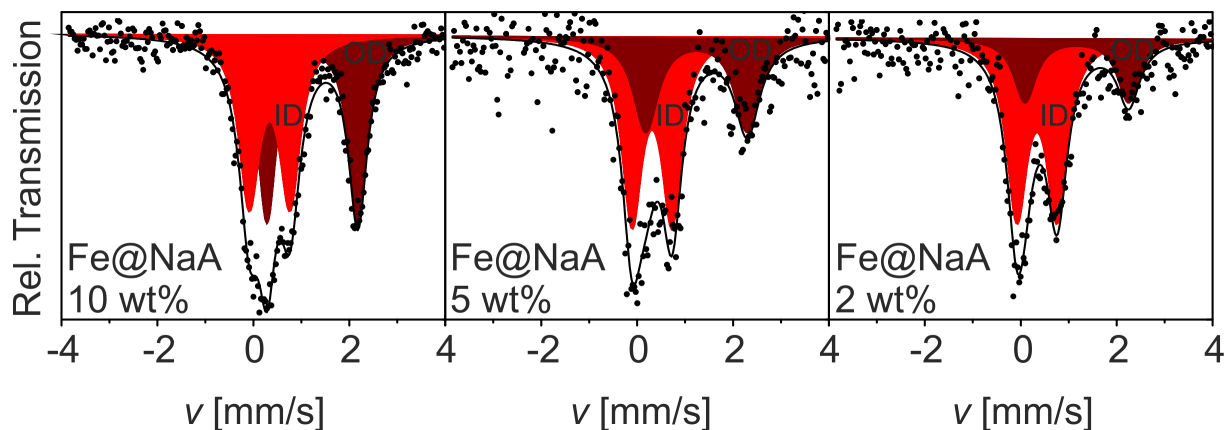


Figure 48. Room temperature Mössbauer spectra of iron(II) exchanged NaA with different iron ratios. The black dots correspond to the measured transmission and the solid line corresponds to the fit with the refinement parameters.

The situation is completely different for NaX where the potential difference between the sites in the supercage and the sodalite cages leads indeed to a variable occupation (see Figure 49). Since NaX possesses a large number of sites in the supercage a very dominant ID is found at 10 wt% and a small amount for the OD. Already at 5 wt% the OD vanishes almost completely although small traces are still present in the sodalite cages which could not any longer be fitted with Recoil. At 2 wt% only the ID is found which means that iron(II) was selective incorporated into the supercage. The potential difference leads to the initial occupation of sites inside the supercage. When those are fully occupied iron(II) starts to be exchanged into the sodalite cages whose site positions are higher in energy.^[71] In the resulting samples 3.4 wt%, 1.8 wt% and 0.8 wt% iron are found via AAS. Full parameters and percentages are given in Table 22 and Table 23.

A similar behavior is found for NaY where at 10 wt% the ID and OD are present with a more pronounced OD compared to NaX but a less pronounced OD compared to NaA (see Figure 50). At 5 wt% still both sites are occupied mirrored by the simultaneous presence of an ID and OD. Only at 2 wt% it appears that the potential difference comes into play and allows a selective occupation of the sites in the supercage. Only the ID can be found which represents 100% of all iron(II) species. In the resulting samples 3.6 wt%, 2.0 wt% and 0.7 wt% iron are found via AAS. Full parameters and percentages are given in Table 22 and Table 23.

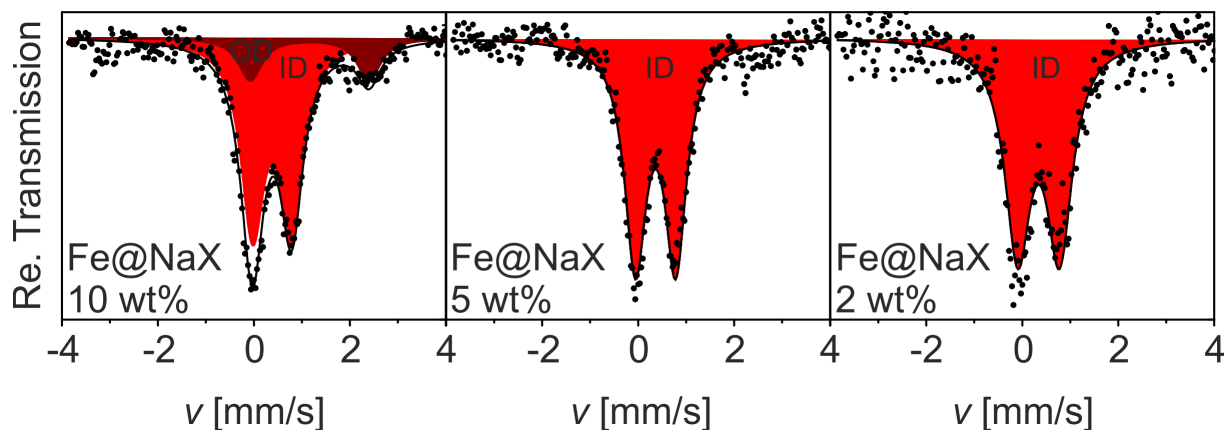


Figure 49. Room temperature Mössbauer spectra of iron(II) exchanged NaX with different iron ratios. The black dots correspond to the measured transmission and the solid line corresponds to the fit with the refinement parameters.

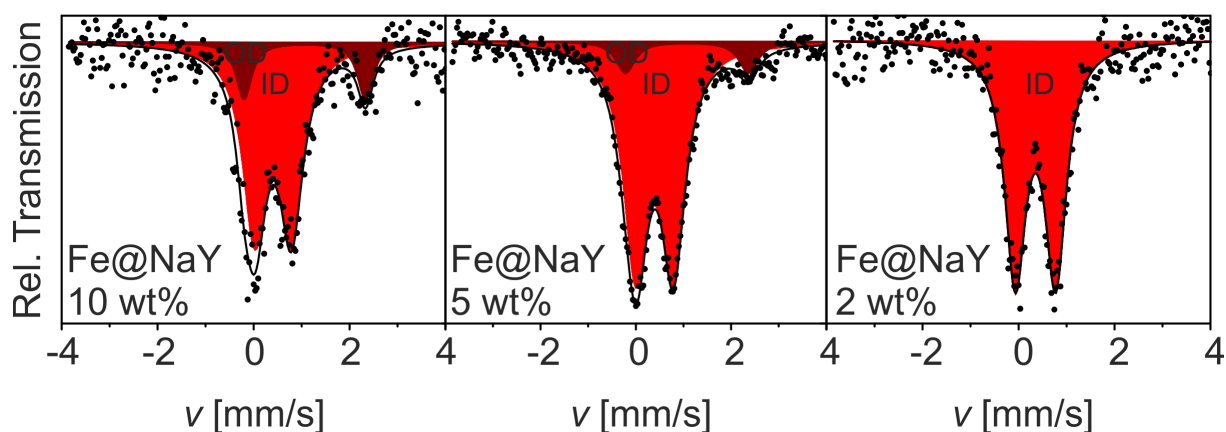


Figure 50. Room temperature Mössbauer spectra of iron(II) exchanged NaY with different iron ratios. The black dots correspond to the measured transmission and the solid line corresponds to the fit with the refinement parameters.

Table 22. Percentages of iron (wt%) in the sodalite cages (OD) and in the supercage (ID).

Fe(II) in solution	NaA		NaX		NaY	
	ID	OD	ID	OD	ID	OD
10 wt%	1.23 wt%	1.37 wt%	2.76 wt%	0.64 wt%	2.98 wt%	0.62 wt%
5 wt%	1.08 wt%	0.72 wt%	1.80 wt%	0.00 wt%	1.80 wt%	0.20 wt%
2 wt%	0.43 wt%	0.17 wt%	0.80 wt%	0.00 wt%	0.70 wt%	0.00 wt%

Table 23. Full Mössbauer parameter of the iron exchanged nanozeolites NaA, NaX and NaY.

Zeolite	Fe(II) [wt%]	Doublet	δ [mm/s]	ΔE_Q [mm/s]	$I/2$ [mm/s]	Population [%]
NaA	10	ID	0.532(18)	0.46(3)	0.24(3)	47.2(3)
	10	OD	1.055(15)	2.25(3)	0.25(2)	52.8(5)
NaA	5	ID	0.31(3)	0.83(6)	0.25(4)	59.9(8)
	5	OD	1.23(6)	2.12(11)	0.31(10)	40.0(12)
NaA	2	ID	0.34(2)	0.84(5)	0.26(4)	71.3(7)
	2	OD	1.17(7)	2.16(14)	0.28(11)	28.7(9)
NaX	10	ID	0.38(4)	0.81(8)	0.29(2)	81.1(4)
	10	OD	1.16(19)	2.5(4)	0.29(11)	18.9(6)
NaX	5	ID	0.362(10)	0.840(18)	0.273(14)	100
	5	OD	-	-	-	0.00
NaX	2	ID	0.34(2)	0.87(4)	0.32(3)	100
	2	OD	-	-	-	0.00
NaY	10	ID	0.41(3)	0.76(5)	0.29(4)	82.9(7)
	10	OD	1.07(7)	2.53(13)	0.20(10)	17.1(8)
NaY	5	ID	0.396(11)	0.785(18)	0.304(16)	89.8(3)
	5	OD	1.08(6)	2.58(12)	0.24(9)	10.2(4)
NaY	2	ID	0.353(16)	0.84(3)	0.27(2)	100
	2	OD	-	-	-	0.00

In summary it is found that the occupation of cation sites in all described zeolites can be influenced to a certain extent by exploiting the potential difference between the supercage and sodalite cage positions. The potential difference is the lowest for NaA which results always in an OD and ID regardless the used iron percentage although the occupation of the sodalite cages can be slightly reduced at low iron concentrations. For NaY this potential difference is larger and at 2 wt% selectively the supercage can be occupied. The largest effect is found for NaX which possesses also the highest number of exchangeable cation sites inside the supercage.^[145-148] Already at 5 wt% nearly only the sites inside of the supercage are occupied. Unfortunately, the low concentrations in solution lead to an even lower percentage inside the resulting material (equilibrium condition) which is effectively in the same range as it can be generated with the impregnation method for nanosized zeolites. Therefore, the impregnation method is still the most promising approach and was consequently used in the further syntheses.

2.5.2 General characterization of impregnated nanozeolites

A number of analytical methods are suitable to characterize the molecular nature of the prepared hybrid nanomaterials. XRD, SEM/EDX and IR spectroscopy are mainly used to ensure purity of the samples while Mössbauer spectroscopy and SQUID magnetometry can be used to validate the coordination geometry of the encapsulated complexes. Powder diffraction was performed to verify the encapsulation of the homoleptic iron(II) complexes inside the supercages of the faujasite. Powder diffraction is used to analyze the crystallinity of a material and helps therefore to prove the absence of bulk material on the surface of the zeolite nanoparticles.^[137,138] In Figure 51 the results of the NaY encapsulated samples are given. It appears that NaY, Fe(Bpy)₃@NaY, Fe(44mBpy)₃@NaY and Fe(55mBpy)₃@NaY show exactly the same reflexes and no additional ones. This proves the complete purity of the synthesized samples. It is noteworthy that the relative intensity of the [220] reflex is reduced for the hybrid materials compared to the bare NaY. Such variation in relative reflex intensity is usually observed when large cations (like the used homoleptic iron(II) complexes) are incorporated inside of the zeolite nanovoids.^[84,127,137,138] This is a further prove for successful incorporation. In Figure 52 the results of the NaX encapsulated samples are given. It appears here also NaX, Fe(Bpy)₃@NaX, Fe(44mBpy)₃@NaX and Fe(55mBpy)₃@NaX show exactly the same reflexes and no additional ones. This proves again complete purity of the synthesized samples. In this case we don't observe a noteworthy reduction of the relative intensity of the [220] reflex compared with [311] and [331]. This is totally in line with the overall increased amount of cation sites in the NaX supercage compared to NaY.^[145-148] Without a doubt, the powder diffraction proves the incorporation inside the voids.

SEM in combination with EDX showed that the nanoparticular structure of the zeolites could be preserved during the impregnation process. Before, particles between 100 nm and 150 nm are found for NaX and particles between 100 nm and 200 nm are found for NaY. After the impregnation similar size ranges are found for all samples. All SEM pictures are given in the Appendix A20–27. EDX measurements confirm basically O, Si, Al, Na and small amounts of Fe what is visible to EDX through the smaller windows of the zeolite. The resulting iron values are slightly higher compared to AAS what can be traced back to the used synthetic procedure. While EDX analyzes the outer section of the particles, AAS accounts for the complete sample. The iron complex density is therefore higher in surface near areas in line with findings in literature.^[72-74,80] EDX data are also given in the Appendix A20–27.

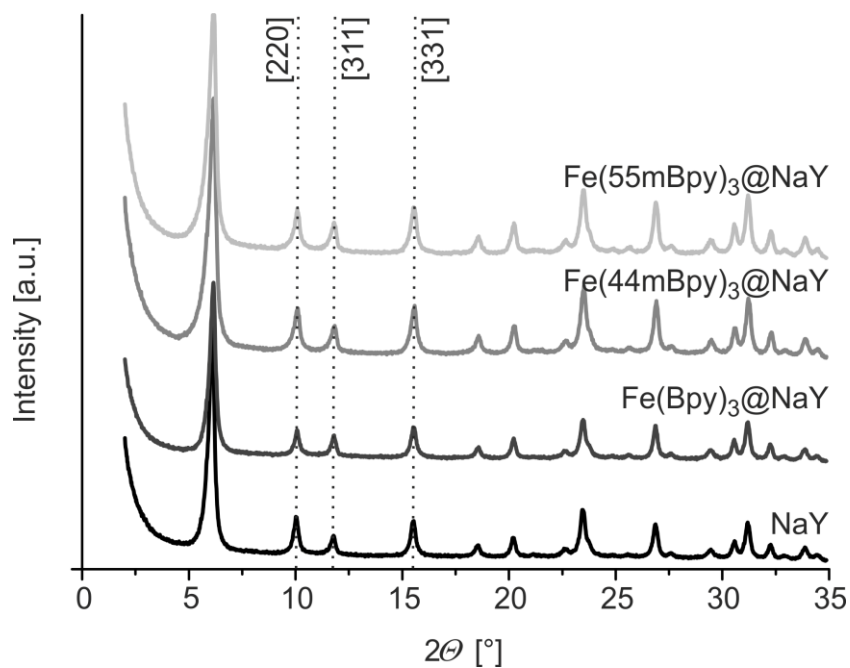


Figure 51. Powder XRD patterns of bare NaY, Fe(Bpy)₃@NaY, Fe(44mBpy)₃@NaY and Fe(55mBpy)₃@NaY. The intensity is plotted against the diffraction angle 2θ .

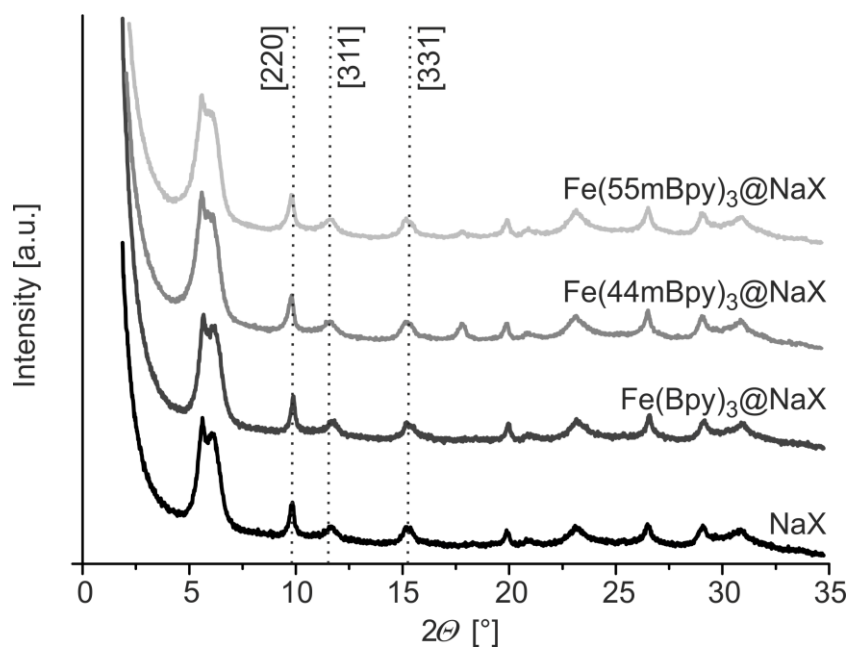


Figure 52. Powder XRD patterns of bare NaX, Fe(Bpy)₃@NaX, Fe(44mBpy)₃@NaX and Fe(55mBpy)₃@NaX. The intensity is plotted against the diffraction angle 2θ .

Evanescent-wave-IR spectroscopy was used to characterize the sample composition and complement XRD. This technique is not able to penetrate the zeolite deeply and therefore only yields information about the sample surface. In this case it is an excellent method to verify the absence of surface depositions or crystalline bulk material probably still present after the synthesis procedure.^[84,127,138] In Figure 53 the IR spectra of NaY, Fe(Bpy)₃@NaY and Fe(Bpy)₃Cl₂ are given representatively for all other NaY incorporated samples since the synthetic procedure was kept meticulously the same. One can see easily that no crystalline bulk material is present since the spectrum of NaY is totally identical to the one of Fe(Bpy)₃@NaY. No signals belonging to Fe(Bpy)₃Cl₂ can be detected. The broad band around 3400 cm⁻¹ present in Fe(Bpy)₃@NaY can be assigned to OH-stretching frequencies of H₂O and MeOH molecules. Signals around 1000 cm⁻¹ are associated with the NaY zeolite lattice.^[68] In Figure 54 the IR spectra of NaX, Fe(Bpy)₃@NaX and Fe(Bpy)₃Cl₂ are given exemplarily for all NaX incorporated samples. One can see easily that also here the spectrum of the hybrid materials does not differ from the bare NaX and that essentially no reflexes of crystalline bulk material appear verifying the encapsulation. All signals around 1000 cm⁻¹ are associated with the NaX zeolite lattice.^[68] The band around 3400 cm⁻¹ in Fe(Bpy)₃@NaX can be also assigned to OH-stretching frequencies of H₂O and MeOH molecules.^[68,149]

AAS was used to determine the iron content of all nanosized hybrid materials. This is important to calculate loading capacities and to gain representative data from Mössbauer spectroscopy and SQUID magnetometry. The loadings are given in wt% in Table 24. An overall very similar loading is found for all samples except for Fe(55mBpy)₃@NaY which has with 0.39 wt% the lowest loading. Furthermore, a higher loading capacity is generally achieved in NaX in line with the additional number of exchangeable ion sites in the supercage accessible for small organic molecules.^[145-148] Overall, around two complexes are found per unit cell which consists out of eight supercages. Additionally the complex loading of the nanosized particles is around five times higher compared to microsized zeolite impregnations what is obviously related to the better accessibility caused by the larger surface.

Table 24. Summary of the iron loadings in wt% for the discussed, impregnated nanozeolites.

	NaX	NaY
[Fe(44mBpy) ₃] ²⁺	0.51 wt%	0.51 wt%
[Fe(55mBpy) ₃] ²⁺	0.59 wt%	0.39 wt%
[Fe(Bpy) ₃] ²⁺	0.59 wt%	0.48 wt%

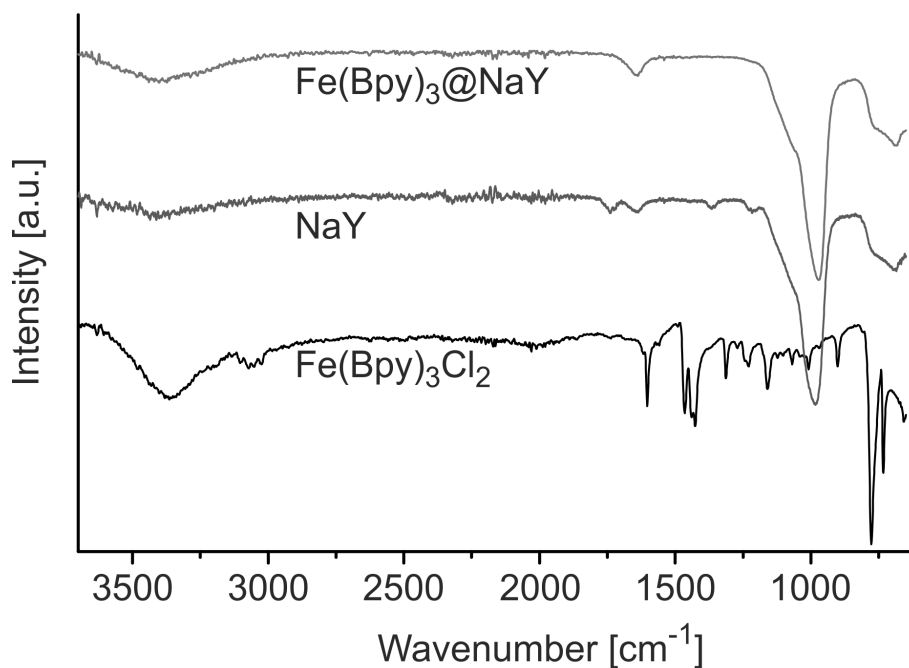


Figure 53. Representative evanescent-wave-IR measurements of NaY, Fe(Bpy)₃@NaY and Fe(Bpy)₃Cl₂. The relative transmission is plotted against the wave number. The spectra were recorded between 600 cm⁻¹ and 3750 cm⁻¹.

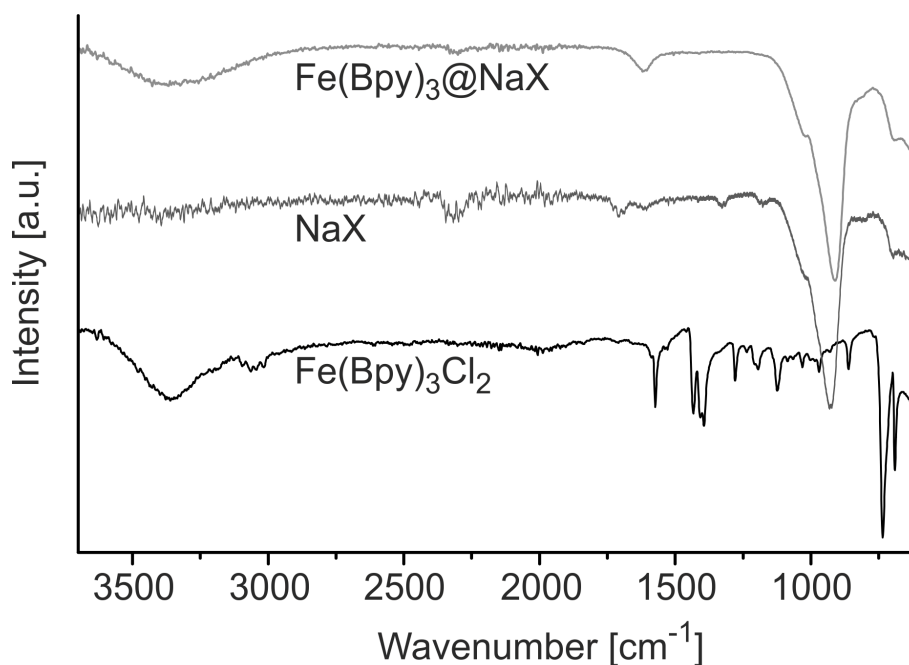


Figure 54. Representative evanescent-wave-IR measurements of NaX, Fe(Bpy)₃@NaX and Fe(Bpy)₃Cl₂. The relative transmission is plotted against the wave number. The spectra were recorded between 600 cm⁻¹ and 3750 cm⁻¹.

2.5.3 Solid state investigations

Reflective Kubelka-Munk measurements were conducted to gain UV-Vis spectra of the impregnated nanozeolites. The electronic spectra give information about the coordination of the iron(II) center due to characteristic electronic transitions which are influenced by geometry and spin pairing.^[8] The spectra are given for all samples together with the spectrum of the corresponding complex in neutral aqueous solution. The d-d-transition of $\text{Fe}(\text{Bpy})_3@NaX$ and $\text{Fe}(\text{Bpy})_3@NaY$ is located around 350 nm where it is also observed for the bulk material (see Figure 55). The $\pi-\pi^*$ -transitions appear between 250 nm and 300 nm nearly identical for the encapsulated and the bulk complex. A difference is observed for the MLCT-envelope which is located around 530 nm. For $\text{Fe}(\text{Bpy})_3@NaY$ it is bathochromically shifted to higher wavelengths what is considered as indicative for the encapsulation.^[62,78] Such feature cannot be observed for $\text{Fe}(\text{Bpy})_3@NaX$ where the MLCT-envelope is strongly broadened due to increased π -cation interaction inside NaX. The transitions and shape of the spectra verify the incorporation of the homoleptic iron(II) complexes inside the nanovoids. From the sharp $\pi-\pi^*$ -transitions paramagnetic iron(II) in the sodalite cages can be excluded.

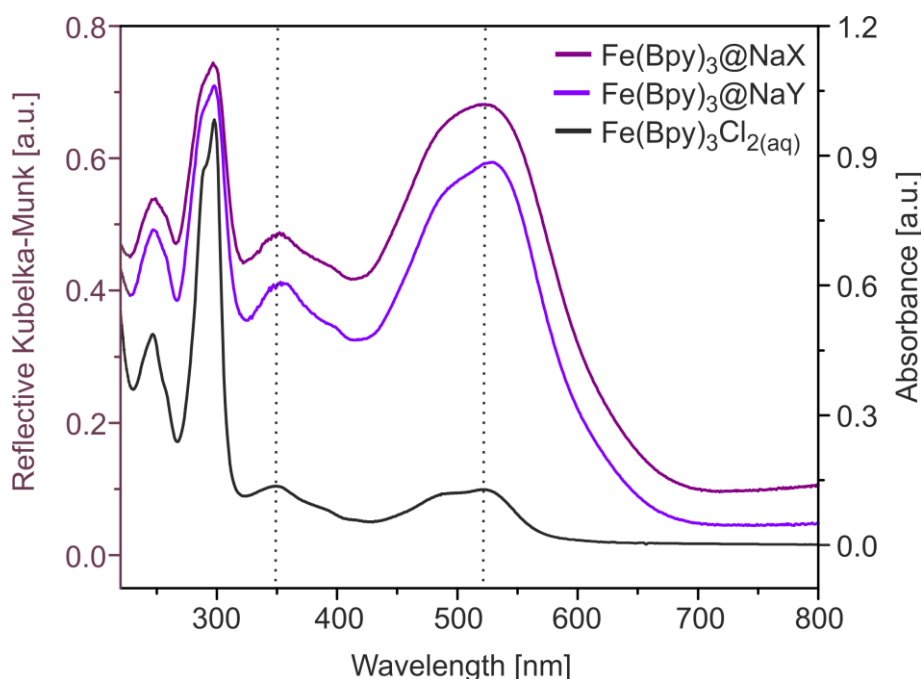


Figure 55. Reflective Kubelka-Munk measurements of $\text{Fe}(\text{Bpy})_3@NaX$ and $\text{Fe}(\text{Bpy})_3@NaY$ together with the UV-Vis spectrum of $\text{Fe}(\text{Bpy})_3\text{Cl}_2$ in H_2O . Baseline correction and 100% transmission reference are omitted for clarity. Reflectivity is plotted against the wavelength.

In Figure 56 the reflective Kubelka-Munk measurements of $\text{Fe}(55\text{mBpy})_3@NaX$ and $\text{Fe}(55\text{mBpy})_3@NaY$ are given. The d-d-transition of both compounds is located around 355 nm. For $\text{Fe}(55\text{mBpy})_3@NaX$ it is bathochromically shifted what would be indicative for a stronger distortion of the complex inside NaX compared to NaY. This will be confirmed in the further sections by Mössbauer spectroscopy. The $\pi-\pi^*$ -transitions appear between 250 nm and 300 nm nearly identical for the encapsulated and the bulk complex. The bathochromical shift of the MLCT-envelope is crucially less pronounced than it was observed for $\text{Fe}(\text{Bpy})_3@NaY$. The MLCT-envelope is located around 530 nm and for $\text{Fe}(\text{Bpy})_3@NaX$ it is again broadened due to increased π -cation interaction inside NaX. The transitions and shape of the spectra verify also here the incorporation of the homoleptic iron(II) complexes inside the nanovoids. From the sharp $\pi-\pi^*$ -transitions paramagnetic iron(II) in the sodalite cages can be excluded. It should be noted that $[\text{Fe}(55\text{mBpy})_3]^{2+}$ is distinctly larger than $[\text{Fe}(\text{Bpy})_3]^{2+}$ and these methylated complexes represent most likely the size limit of systems able to be encapsulated.

In Figure 57 the reflective Kubelka-Munk measurements of $\text{Fe}(44\text{mBpy})_3@NaX$ and $\text{Fe}(44\text{mBpy})_3@NaY$ are given. It can be directly seen that the whole spectrum of the hybrid materials is hypsochromically shifted compared to the complex in aqueous solution. The d-d-transition of $\text{Fe}(44\text{mBpy})_3@NaX$ and $\text{Fe}(44\text{mBpy})_3@NaY$ is moved towards 350 nm compared to 360 nm for the bulk material. The $\pi-\pi^*$ -transitions appear below 300 nm strongly shifted compared to the bulk complex. The MLCT-envelope is hypsochromically shifted towards 525 nm and is not broadened. Nevertheless, the transitions and shape of the spectra verify also here the incorporation of the homoleptic iron(II) complexes inside the nanovoids. It should be noted that the $\pi-\pi^*$ -transitions are not as sharp as observed for the complex in solution what would be indicative for the presence of paramagnetic complex molecules and what will be further proven by Mössbauer spectroscopy and SQUID magnetometry. The shift of the complete spectra to lower wavelengths corresponds to an absorbance of more energy-rich rays. This behavior mirrors a stabilization (lowering of the orbitals) of the complexes inside of the nanovoids. Such a stabilization could be the presence of a highly ionic species like for example $[\text{Fe}(44\text{mBpy})_3\text{H}]^{3+}$ which would energetically fit to the superpolar and highly charged voids of the zeolite.^[145]

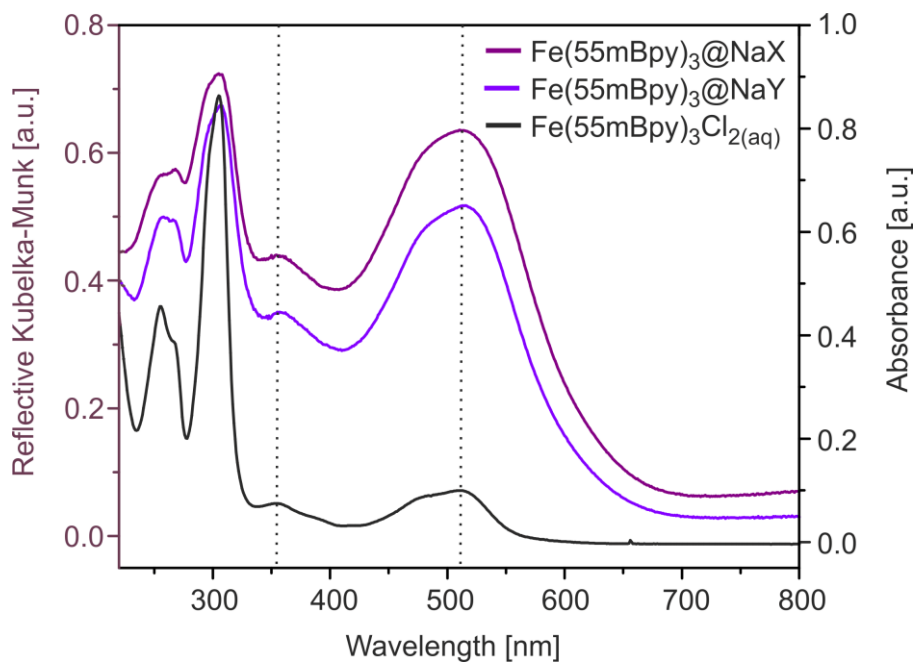


Figure 56. Kubelka-Munk reflectivity of Fe(55mBpy)₃@NaX and Fe(55mBpy)₃@NaY together with the UV-Vis spectrum of Fe(55mBpy)₃Cl₂ in H₂O. Baseline correction and 100% transmission reference are omitted for clarity. Reflectivity is plotted against the wavelength.

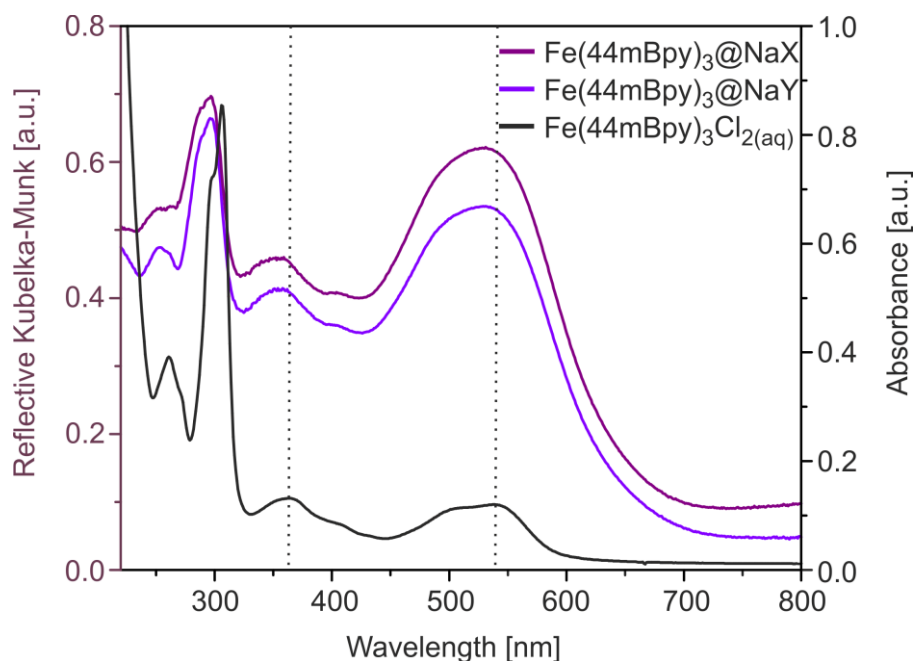


Figure 57. Kubelka-Munk reflectivity of Fe(44mBpy)₃@NaX and Fe(44mBpy)₃@NaY together with the UV-Vis spectrum of Fe(44mBpy)₃Cl₂ in H₂O. Baseline correction and 100% transmission reference are omitted for clarity. Reflectivity is plotted against the wavelength.

Mössbauer spectroscopy was used to characterize the iron reporter functions inside of the zeolite nanoparticles. The used synthetic strategy allows to incorporate selectively the diamagnetic iron(II) species inside the large supercages of the nanosized zeolites NaY and NaX without any paramagnetic impurities. Those paramagnetic species are usually HS iron(II) ions located inside of the sodalite cages via ion exchange procedures.^[72-75] We found that this species can only be partially removed afterwards which is why the impregnation is a very favorable and elegant method to incorporate complexes inside of zeolites. Consequently there are essentially no signals observed for Fe(II) ions in the sodalite cages. In Figure 58 the RT Mössbauer spectra of Fe(Bpy)₃@NaY and Fe(Bpy)₃@NaX are given as they were received after synthesis. One can see easily that only the typical diamagnetic signal is present for Fe(Bpy)₃@NaY. $\delta = 0.27$ mm/s and $\Delta E_Q = 0.51$ mm/s are in very good agreement with literature values and the parameters shown in this work for Fe(Bpy)₃Cl₂.^[77] For Fe(Bpy)₃@NaX also a LS doublet is observed with a significantly larger ΔE_Q compared to the bulk material. This broadening is characteristic for all NaX samples and has therefore to be related to the zeolite properties. The highly charged supercage most likely exerts a larger field splitting on the incorporated complexes than the one of NaY in line with a higher number of counter cations.^[145-148] For Fe(Bpy)₃@NaX $\delta = 0.35$ mm/s and $\Delta E_Q = 0.69$ mm/s are observed. A complete summary of the fitted Mössbauer parameters is given in Table 25.

Table 25. Summary of the observed Mössbauer parameters for the impregnated nanozeolites.

	Doublet	δ [mm/s]	ΔE_Q [mm/s]	$\Gamma/2$ [mm/s]	Population [%]
Fe(Bpy)₃@NaY	ID	0.27(4)	0.51(6)	0.32(6)	100
Fe(Bpy)₃@NaX	ID	0.35(3)	0.69(6)	0.27(5)	100
Fe(55mBpy)₃@NaY	ID	0.32(5)	0.71(7)	0.32(7)	100
Fe(55mBpy)₃@NaX	ID	0.35(4)	0.74(8)	0.24(6)	100
Fe(44mBpy)₃@NaY	ID	0.25(9)	0.66(16)	0.35(12)	79(3)
Fe(44mBpy)₃@NaY	OD	0.45(7)	1.0(14)	0.13(14)	21(3)
Fe(44mBpy)₃@NaX	ID	0.28(5)	0.65(9)	0.25(2)	60(11)
Fe(44mBpy)₃@NaX	OD	0.44(6)	1.0(13)	0.23(3)	40(10)

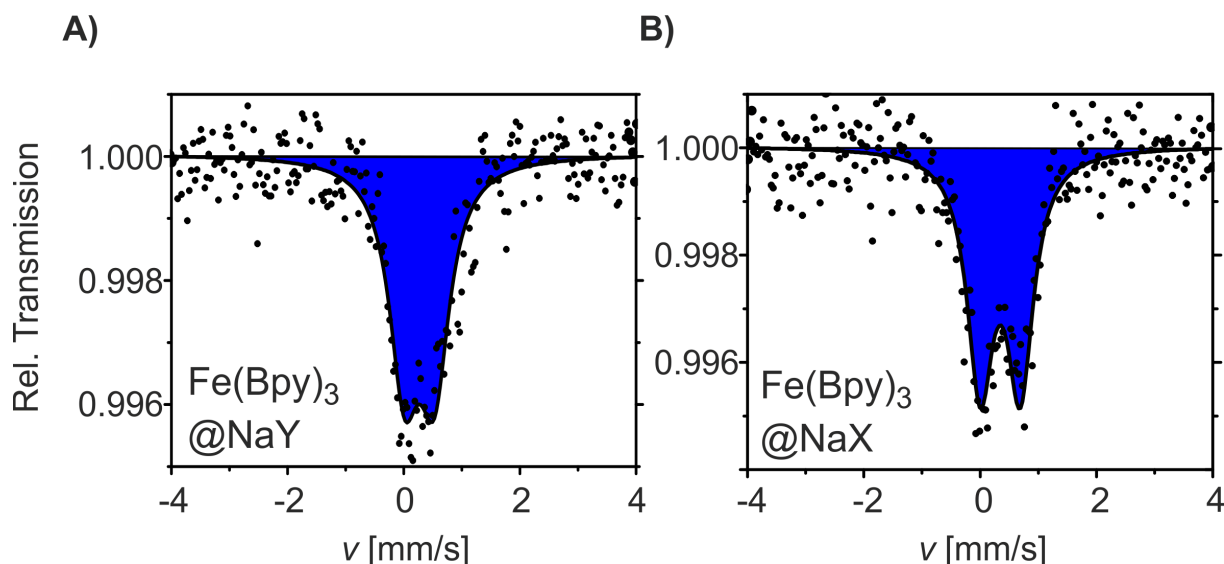


Figure 58. Room temperature Mössbauer spectra of $\text{Fe}(\text{Bpy})_3@NaY$ (A) and $\text{Fe}(\text{Bpy})_3@NaX$ (B). The black dots correspond to the measured transmission and the solid line corresponds to the fit with the refinement parameters given in Table 25. In both cases a doublet (blue) characteristic for the diamagnetic iron(II) low-spin species is observed.

Mössbauer measurements (see Figure 59) were also conducted for $\text{Fe}(\text{55mBpy})_3@NaY$ and $\text{Fe}(\text{55mBpy})_3@NaX$. It should be noted, that the iron percentage for $\text{Fe}(\text{55mBpy})_3@NaY$ is with 0.39 wt% the lowest achieved loading. Therefore the spectrum has a very low signal-to-noise ratio. Nevertheless it was the best spectrum that could be generated after leaving it for 9 days in the Mössbauer apparatus. For this compound also a LS doublet is observed which has a larger ΔE_Q value than it is found for the bulk material. In this case the broadening originates most likely from a strong distortion of the complex similar to the findings of the reflective Kubelka-Munk measurements. The methyl substituent increases the overall extent and allows encapsulation just under distorted coordination. For $\text{Fe}(\text{55mBpy})_3@NaY$ $\delta = 0.32$ mm/s and $\Delta E_Q = 0.71$ mm/s are observed. Very similar values are found for $\text{Fe}(\text{55mBpy})_3@NaX$ with $\delta = 0.35$ mm/s and $\Delta E_Q = 0.74$ mm/s. The complex is also distorted as it is found for all complexes incorporated in NaX nanoparticles. In summary the results verify the octahedral coordination of the encapsulated complexes inside the nanozeolites which are completely diamagnetic at room temperature similar to neutral aqueous complex solutions.

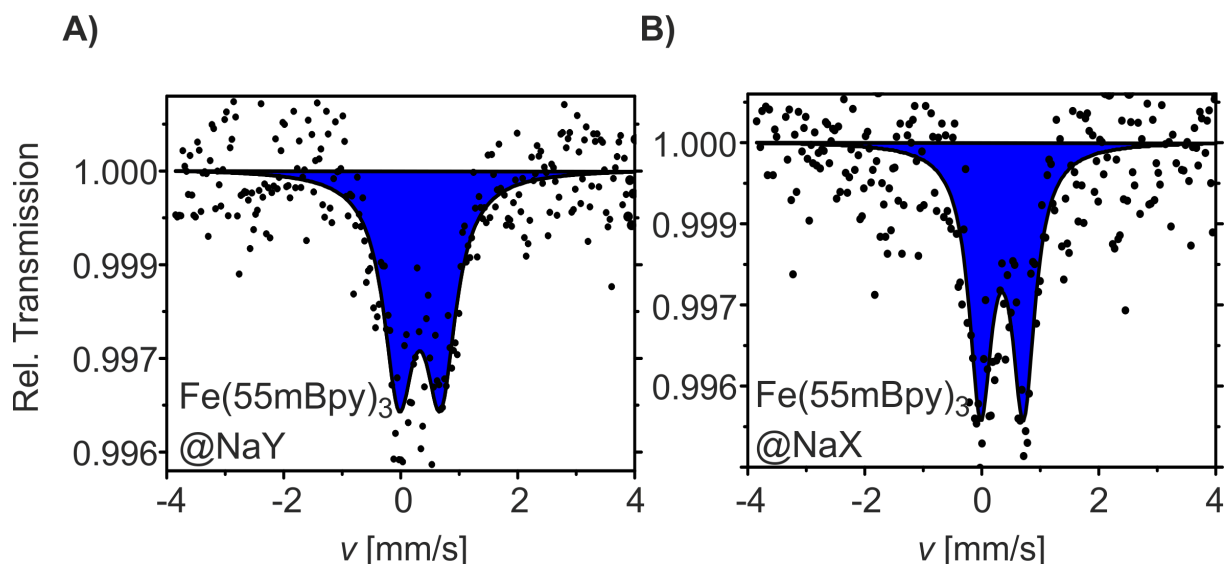


Figure 59. Room temperature Mössbauer spectra of $\text{Fe}(55\text{mBpy})_3@NaY$ (A) and $\text{Fe}(55\text{mBpy})_3@NaX$ (B). The black dots correspond to the measured transmission and the solid line corresponds to the fit with the refinement parameters given in Table 25. In both cases a doublet (blue) characteristic for the diamagnetic iron(II) low-spin species is observed.

For $\text{Fe}(44\text{mBpy})_3@NaY$ the Mössbauer spectroscopy reveals a so far unexpected feature. A slightly broadened inner doublet is observed belonging to the Fe(II) LS species associated with the supercage incorporated complex. Parameters of $\delta = 0.28$ mm/s and $\Delta E_Q = 0.65$ mm/s are found representing 79% of all iron species. The values are in line with the overall observed LS doublets belonging to the octahedral coordinated complex. Furthermore a Fe(II) HS species is observed with $\delta = 0.45$ mm/s and $\Delta E_Q = 1.0$ mm/s which accounts for 21% of all iron species. From the isomer shift it becomes clear, that this species is also located in the supercage. The ΔE_Q is in a common range for paramagnetic Fe(II) ions in the supercage (see for example the Mössbauer parameters of $\text{Fe}(\text{H}_2\text{O})_6@NaY$).^[75,77] This is indicative for a partial switching of the $[\text{Fe}(44\text{mBpy})_3]^{2+}$ ion caused by Brønsted acids as it was shown in the previous section. The finding is in line with the increased sensitivity of this ligand towards protons as it was shown in the first section of this work. Additionally, it corresponds very well to the results from the reflective Kubelka-Munk measurements where a strong hypsochromic shift of the spectrum was observed. This hypsochromic shift can be also observed for the microsized zeolites $\text{Fe}(\text{Bpy})_3@NaY$ upon heating as it was shown earlier in this work.^[132] The Mössbauer spectrum is given in Figure 60.

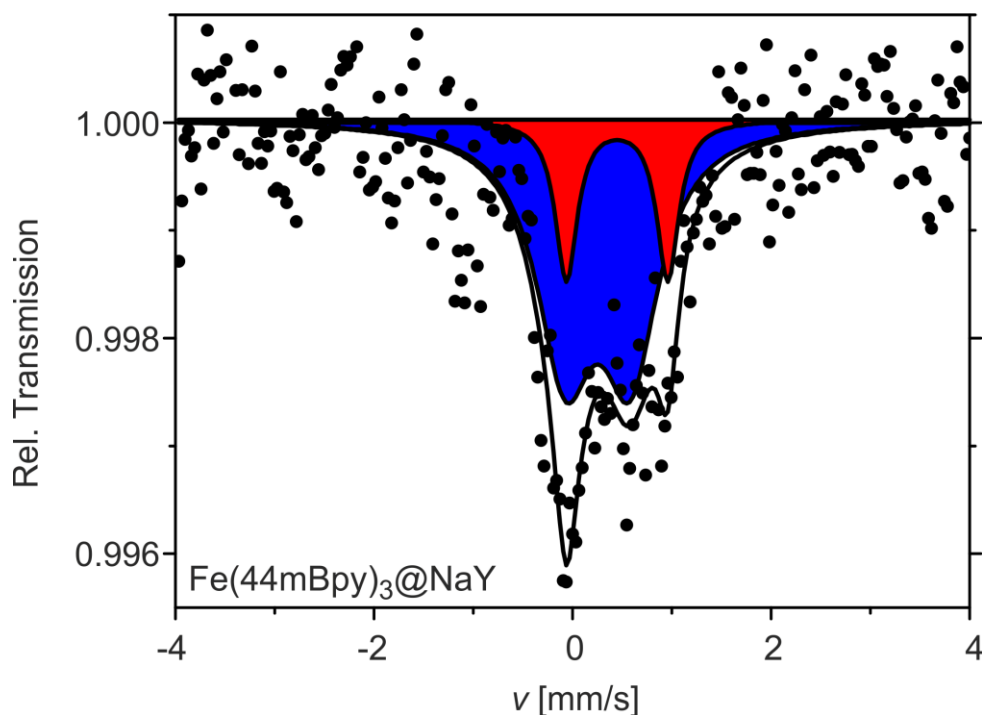


Figure 60. Room temperature Mössbauer spectrum of $\text{Fe}(44\text{mBpy})_3@NaY$. The black dots correspond to the measured transmission and the solid line corresponds to the fit with the refinement parameters given in Table 25.

A similar situation can be observed for $\text{Fe}(44\text{mBpy})_3@NaX$. The inner doublet is again slightly broadened and belongs to the Fe(II) LS species associated with the supercage incorporated complex. Parameters of $\delta = 0.25$ mm/s and $\Delta E_Q = 0.66$ mm/s are found representing 60% of all iron species in line with the octahedral coordinated complex. A paramagnetic Fe(II) HS species is observed with $\delta = 0.44$ mm/s and $\Delta E_Q = 1.00$ mm/s which represents 40% of all iron species. The isomer shift verifies a location in the supercage. Inside NaX also a partial switching of the $[\text{Fe}(44\text{mBpy})_3]^{2+}$ ion caused by Brønsted acids is found similar to the results for NaY. The results are again in line with the increased sensitivity of this ligand towards protons. Furthermore, a larger amount of paramagnetic complexes is observed as it would be expected for the NaX. Additionally, a strong hypsochromic shift of the spectrum of $\text{Fe}(44\text{mBpy})_3@NaX$ was observed during reflective Kubelka-Munk measurements what corresponds very well to this results. The Mössbauer spectrum is given in Figure 61.

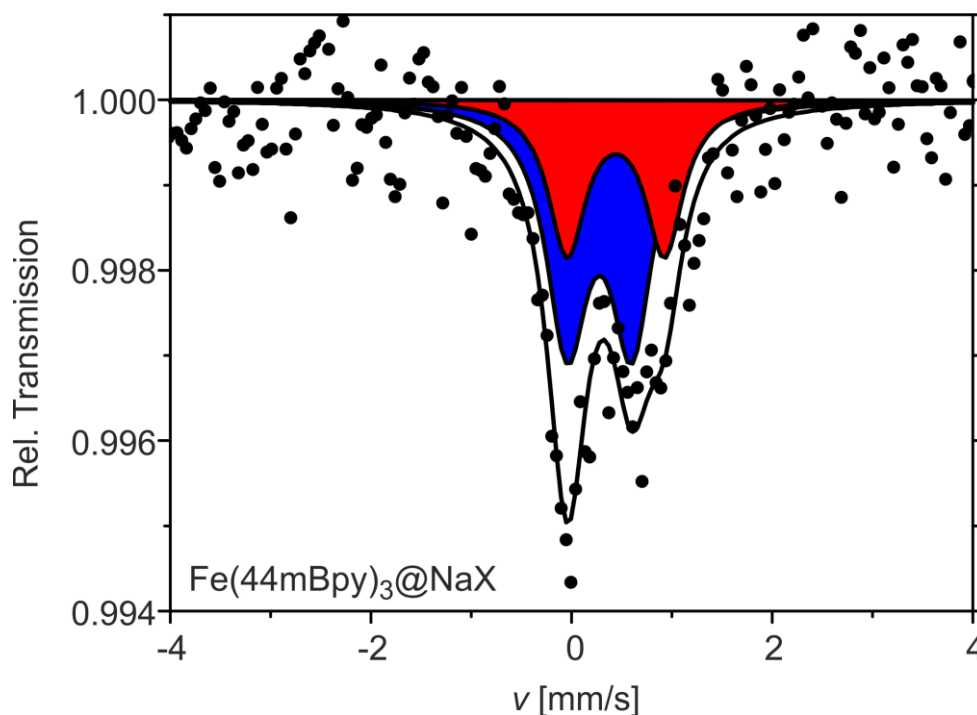


Figure 61. Room temperature Mössbauer spectrum of $\text{Fe}(44\text{mBpy})_3@NaX$. The black dots correspond to the measured transmission and the solid line corresponds to the fit with the refinement parameters given in Table 25.

All nanosized hybrids were furthermore characterized via SQUID magnetometry in a temperature range between 150 K and 400 K. All measurements were conducted in the settle-mode and samples were dried *in vacuo* before. $\text{Fe}(\text{Bpy})_3@NaY$ has a $\chi_{\text{Mass}} = -3.08 \cdot 10^{-3} \text{ cm}^3 \text{ g}^{-1}$ at RT corresponding to a complete LS state as it was observed already via Mössbauer spectroscopy. The corresponding graph is given in Figure 62. Similar values are found for $\text{Fe}(55\text{mBpy})_3@NaY$. Both samples don't change their magnetic state upon cooling but start at 310 K to rise steadily as it was already observed for microsized zeolite particles in the previous section. Interestingly, the overall $\Delta\chi_{\text{Mass}}$ values are very different. While $\text{Fe}(\text{Bpy})_3@NaY$ goes up to $\chi_{\text{Mass}} = 0.95 \cdot 10^{-3} \text{ cm}^3 \text{ g}^{-1}$ the compound $\text{Fe}(55\text{mBpy})_3@NaY$ is going up to $\chi_{\text{Mass}} = 5.74 \cdot 10^{-3} \text{ cm}^3 \text{ g}^{-1}$. The high susceptibility remains stable over several cycles as the magnetometer is operating under vacuum. For $\text{Fe}(44\text{mBpy})_3@NaY$ an increased $\chi_{\text{Mass}} = 1.44 \cdot 10^{-3} \text{ cm}^3 \text{ g}^{-1}$ is yet observed at the first cycle in congruency with the Mössbauer spectra. The amount of paramagnetic complexes is raised up to $\chi_{\text{Mass}} = 8.33 \cdot 10^{-3} \text{ cm}^3 \text{ g}^{-1}$. This is also the highest value observed and correlates well with the results in solution for the incorporated complex. All characteristic SQUID data are given in Table 26.

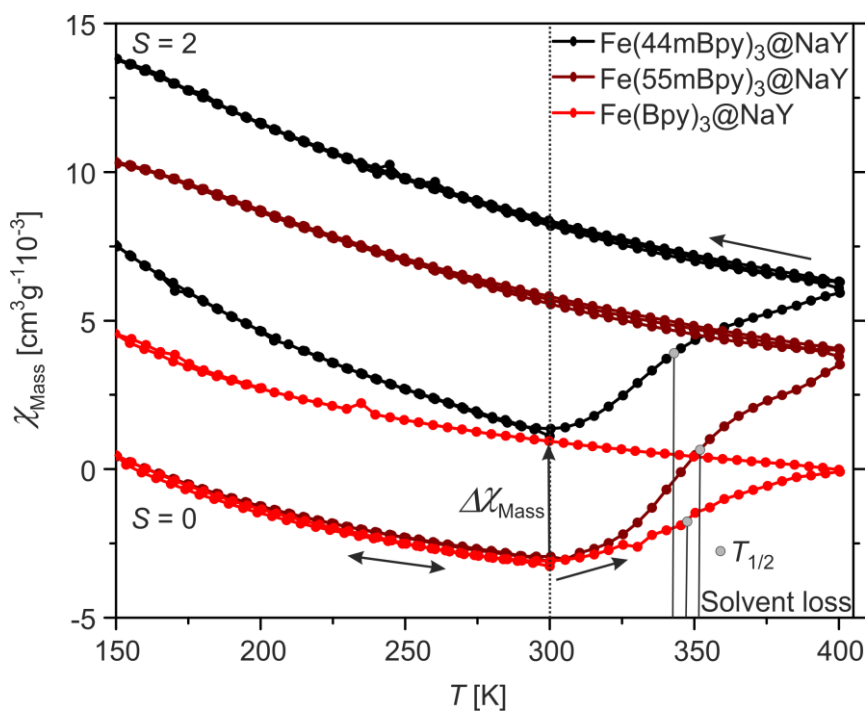


Figure 62. Magnetic behavior of $\text{Fe}(44\text{mBpy})_3@NaY$ (black), $\text{Fe}(55\text{mBpy})_3@NaY$ (brown) and $\text{Fe}(\text{Bpy})_3@NaY$ (red). χ_{Mass} is plotted against the temperature in a range between 150 K and 400 K. They were measured in the settle-mode, started at 300 K and cooled down at first.

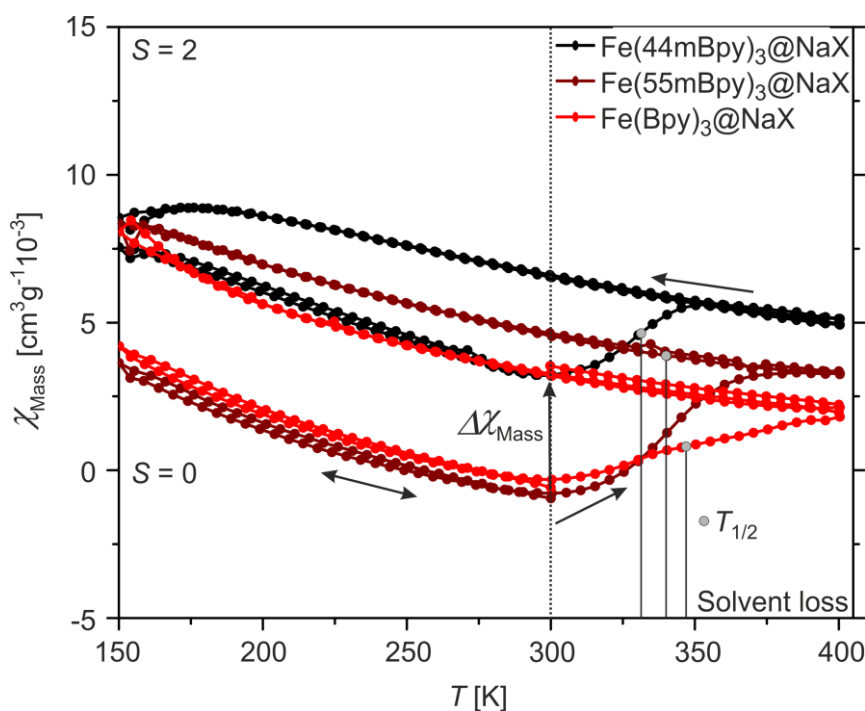


Figure 63. Magnetic behavior of $\text{Fe}(44\text{mBpy})_3@NaX$ (black), $\text{Fe}(55\text{mBpy})_3@NaX$ (brown) and $\text{Fe}(\text{Bpy})_3@NaX$ (red). χ_{Mass} is plotted against the temperature in a range between 150 K and 400 K. They were measured in the settle-mode, started at 300 K and cooled down at first.

For the samples which were incorporated inside of NaX exactly the same sensitivity is found but the overall $\Delta\chi_{\text{Mass}}$ values are drastically reduced compared to NaY (see Figure 63). Again $\text{Fe}(\text{Bpy})_3@NaX$ and $\text{Fe}(55mBpy)_3@NaX$ start around the same values at 300 K (with values of $\chi_{\text{Mass}} = -0.34 \cdot 10^{-3} \text{ cm}^3 \text{ g}^{-1}$ and $\chi_{\text{Mass}} = -0.96 \cdot 10^{-3} \text{ cm}^3 \text{ g}^{-1}$). $\text{Fe}(\text{Bpy})_3@NaX$ rises up to $\chi_{\text{Mass}} = 3.21 \cdot 10^{-3} \text{ cm}^3 \text{ g}^{-1}$ while the dimethylated compound $\text{Fe}(55mBpy)_3@NaX$ reaches $\chi_{\text{Mass}} = 4.71 \cdot 10^{-3} \text{ cm}^3 \text{ g}^{-1}$ at the second cycle and 300 K. $\text{Fe}(44mBpy)_3@NaX$ goes from an already increased $\chi_{\text{Mass}} = 3.21 \cdot 10^{-3} \text{ cm}^3 \text{ g}^{-1}$ up to $\chi_{\text{Mass}} = 6.62 \cdot 10^{-3} \text{ cm}^3 \text{ g}^{-1}$. It should be noted that the magnetic behavior depends essentially on the used ligand type and follows the proton acceptability controlled by the +I-effect also inside the zeolite supercages. All characteristic SQUID data are given in Table 26.

Table 26. χ_{Mass} of impregnated nanozeolites at 300 K before (I) and after (II) reaching 400 K.

$\chi_{\text{Mass}} [10^{-3} \text{ cm}^3 \text{ g}^{-1}]$	NaX, 300 K, I	NaX, 300 K, II	NaY, 300 K, I	NaY, 300 K, II
$[\text{Fe}(44mBpy)_3]^{2+}$	3.21	6.62	1.44	8.33
$[\text{Fe}(55mBpy)_3]^{2+}$	-0.96	4.71	-3.08	5.74
$[\text{Fe}(\text{Bpy})_3]^{2+}$	-0.34	3.21	-3.08	0.95

To gain a better insight into the pH-responsiveness of the hybrid nanoparticles $\Delta\chi_{\text{Mass}}$ was calculated by subtracting the lowest observed χ_{Mass} at 300 K of the corresponding zeolite from the highest achieved χ_{Mass} at 300 K after heating to 400 K of the respective sample. For NaX $-0.34 \cdot 10^{-3} \text{ cm}^3 \text{ g}^{-1}$ and for NaY $-3.08 \cdot 10^{-3} \text{ cm}^3 \text{ g}^{-1}$ were used for all complexes since it is obvious from the Mössbauer spectroscopy that $\text{Fe}(44mBpy)_3@NaX$ and $\text{Fe}(44mBpy)_3@NaY$ are already partially switched at RT in line with the magnetic measurements. The calculated values are given in Table 27.

From this data one can see easily that $\Delta\chi_{\text{Mass}}$ follows for all samples exactly the behavior which was already observed during heating of acidic solutions of the complexes itself. The largest conversion to the HS state can be generated for $\text{Fe}(44mBpy)_3@NaX$ and $\text{Fe}(44mBpy)_3@NaY$. $\text{Fe}(44mBpy)_3@NaX$, $\text{Fe}(44mBpy)_3@NaY$, $\text{Fe}(55mBpy)_3@NaX$ and $\text{Fe}(55mBpy)_3@NaY$ are influenced the most by the type of zeolite which is used. The behavior of $\text{Fe}(\text{Bpy})_3@NaY$ and $\text{Fe}(\text{Bpy})_3@NaX$ can be considered as independent from the zeolite host. This is remarkable since it correlates with the possibility of interaction with the

zeolite void. Since $[\text{Fe}(\text{Bpy})_3]^{2+}$ fits nicely into the supercage it will have the least interaction with the void while the methylated derivatives are strongly distorted as it could be seen in the Mössbauer spectra. The distortion can be easily compensated via a ring-flip which is indeed happening during a PD-CISS. The π -cation interactions in NaX can be considered as much stronger than in NaY what should therefore reduce the paramagnetic response in NaX exactly in the way as it is found.^[145-148]

Table 27. $\Delta\chi_{\text{Mass}}$ of the impregnated nanozeolites between 300 K before and after heating.

$\Delta\chi_{\text{Mass}} [10^{-3} \text{ cm}^3 \text{ g}^{-1}]$	NaX	NaY
$[\text{Fe}(\mathbf{44mBpy})_3]^{2+}$	7.58	11.40
$[\text{Fe}(\mathbf{55mBpy})_3]^{2+}$	5.67	8.81
$[\text{Fe}(\mathbf{Bpy})_3]^{2+}$	4.17	4.03

Since the ligand substitution influences strongly the proton acceptance of the nitrogen donor it appeared intuitive to calculate the temperature $T_{1/2}$ where 50% of the difference between the χ_{Mass} values at 300 K are reached. The results are given in Table 28. $T_{1/2}$ is shifted towards higher values for NaY compared to NaX in line with the usually higher number of Brønsted acid sites.^[143,145-148] It should be noted that for $\text{Fe}(\text{Bpy})_3@ \text{NaY}$ and $\text{Fe}(\text{Bpy})_3@ \text{NaX}$ this is not the case. Exactly the same was already found in solution for this complex where the T -dependence of the γ_{HS} was mainly a steady-state condition. Furthermore, the $T_{1/2}$ values are the lowest for $\text{Fe}(\mathbf{44mBpy})_3@ \text{NaX}$ exactly as it would be expected. Consequently, this system is the most T -dependent similarly to the behavior in solutions with acidic pH. $T_{1/2}$ follows all in all the observed influence of the +I-effect and is in total agreement with the pH-responsive magnetism in solution.

Table 28. $T_{1/2}$ values indicating where 50% of χ_{Mass} between 300 K and 400 K are reached.

	NaX	NaY
$[\text{Fe}(\mathbf{Bpy})_3]^{2+}$	346 K	348 K
$[\text{Fe}(\mathbf{55mBpy})_3]^{2+}$	340 K	351 K
$[\text{Fe}(\mathbf{44mBpy})_3]^{2+}$	332 K	343 K

2.5.4 Investigations in solution

Besides the observation that PD-CISSS effects were found to be preserved inside micro-sized and nano-sized zeolite particles another unexpected effect of the hybrid materials was investigated which is happening this time in aqueous suspension. All systems like $\text{Fe}(\text{Bpy})_3@ \text{NaY}$ which were encapsulated in NaY nanoparticles are completely stable in neutral aqueous suspension. Below pH 2 the nanozeolite host starts to dissolve, initiated by acid-triggered dealumination. In the micro-sized particles this is only happening below pH 1. For systems encapsulated in NaX this behavior is completely different. Aqueous suspensions of $\text{Fe}(\text{Bpy})_3@ \text{NaX}$ show an unexpected color change in the inverse way as it has been observed in the previous section. Suspensions around pH 3 are completely stable and show no change in color or leaching of the complex. When the pH is raised gradually up to pH 6 the suspensions start to bleach during a storage time of one week. Thereby the observed color correlates with the pH and for pH 6 a completely colorless suspension is formed which shows also no leaching of the complex. Since the reaction times are very long it is clear that the underlying mechanism is a thermodynamically controlled one. $\text{Fe}(\text{Bpy})_3@ \text{NaX}$ is obviously a kinetically stable product which is formed in MeOH while upon suspension in aqueous solution a pH-dependent thermodynamically stable product is formed. A lowered pH obviously favors the kinetically stable product. Pictures of the discussed suspensions of $\text{Fe}(\text{Bpy})_3@ \text{NaX}$ are given together with suspensions of NaX and $\text{Fe}(\text{Bpy})_3@ \text{NaY}$ for comparison in Scheme 22.



Scheme 22. Coloring of solutions with different pH of $\text{Fe}(\text{Bpy})_3@ \text{NaX}$, $\text{Fe}(\text{Bpy})_3@ \text{NaY}$ and NaX after several days of storage. NaX and $\text{Fe}(\text{Bpy})_3@ \text{NaY}$ are given for comparison.

It was possible to follow this color change to some extent with UV-Vis spectroscopy in aqueous suspension what can be seen in Figure 64. One should be aware of the fact that suspensions are difficult to be measured and most UV-Vis spectroscopy apparatuses are not made for such measurements. The suspensions were freshly dispersed by the use of ultrasound directly before the measurements. The solvent and the spectrum at pH 6 were used as baseline correction to be able to follow directly the change of the MLCT-transition related to its intensity at various pH values. One can see easily that the typical MLCT-envelope is vanishing with rising pH as it could be already observed with the naked eye. It's lowered from 0.20 at pH 2.9 to 0.10 at pH 5.0 and down to 0.0 at pH 5.9. This highlights drastic coordination changes at the iron(II) center.

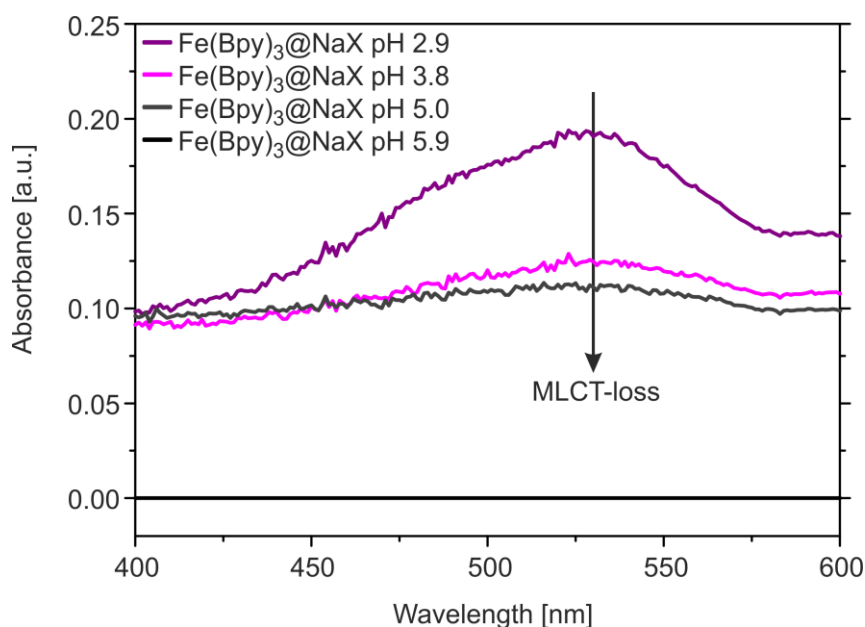


Figure 64. UV-Vis measurement of aqueous suspensions of Fe(Bpy)₃@NaX at different pH values after several days of storage. The absorbance is plotted against the wavelength at nm. The data was baseline corrected by using the spectrum of the solvent and the suspension at a pH of 5.9.

DLS measurements were conducted to ensure the structural integrity of the nanoparticles. Suspensions between pH 2.9 and pH 5.9 were measured and found to be completely stable in the observed pH range. The maximum of the particle size distribution is for all experiments

centered around 120 nm (hydrodynamic radius) which corresponds well to the SEM measurements where an extension up to 150 nm was found. The lowered pH does not affect the overall shape and size of the particles. The results are given in Figure 65 for pH 2.9 and pH 5.9. All others were omitted for clarity since all measurements are essentially equal.

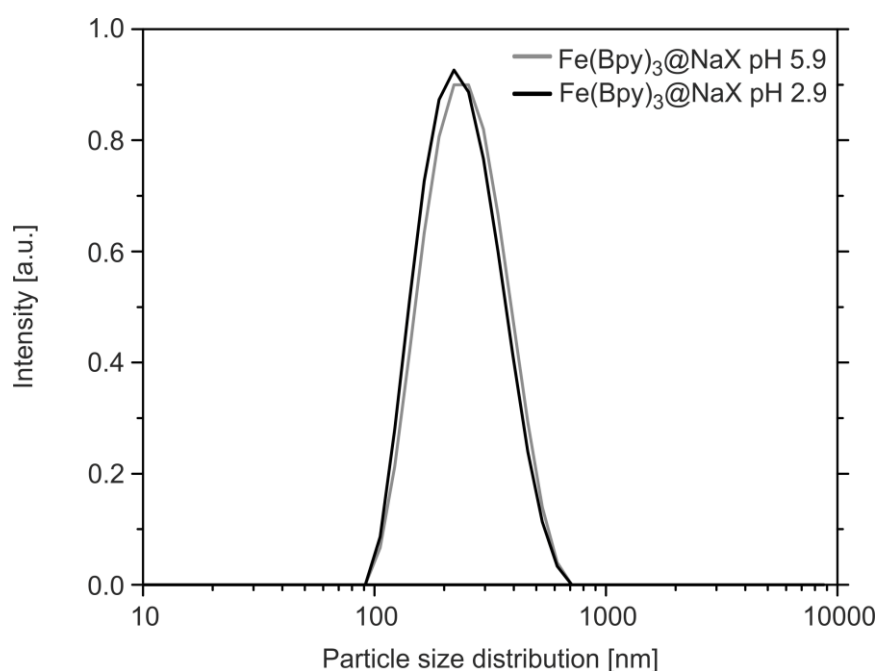


Figure 65. Dynamic light scattering of aqueous suspensions of Fe(Bpy)₃@NaX at two pH values after one week of storage. The intensity is plotted against the particle size distribution (hydrodynamic radius). Complete structural integrity is found in the observed pH range.

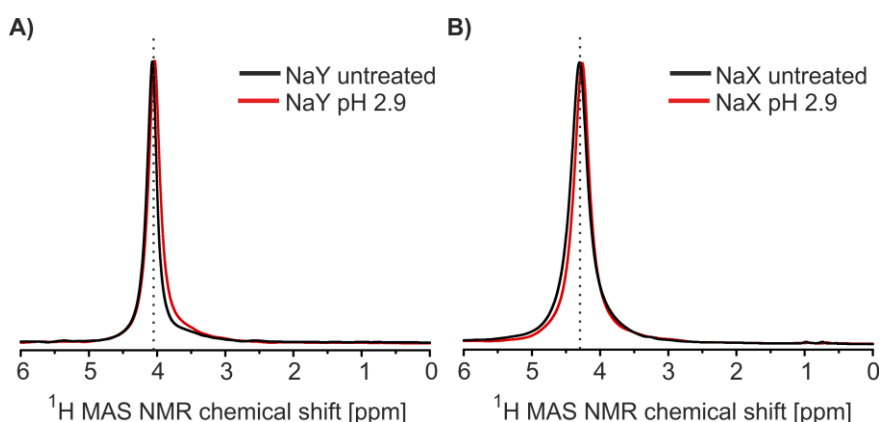


Figure 66. ¹H MAS NMR spectroscopy of bare NaY (A) and NaX (B) stored for one week in neutral aqueous media and at pH 2.9. The chemical shift is given in ppm.

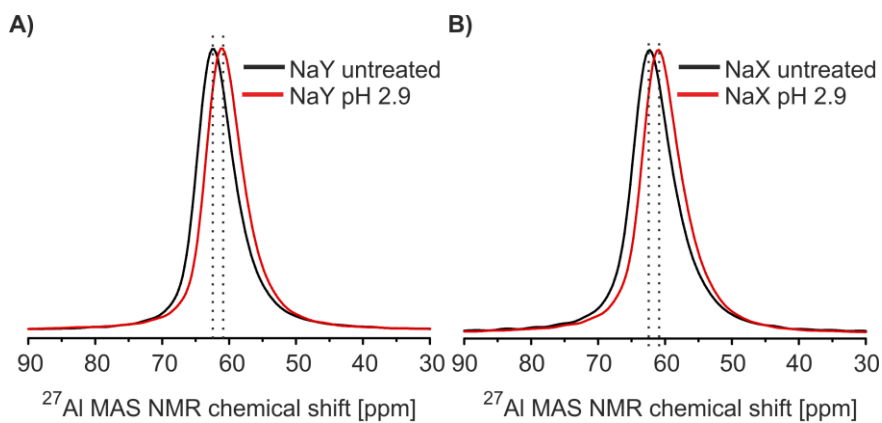


Figure 67. ^{27}Al MAS NMR spectroscopy of bare NaY (A) and NaX (B) stored for one week in neutral aqueous media and at pH 2.9. The chemical shift is given in ppm.

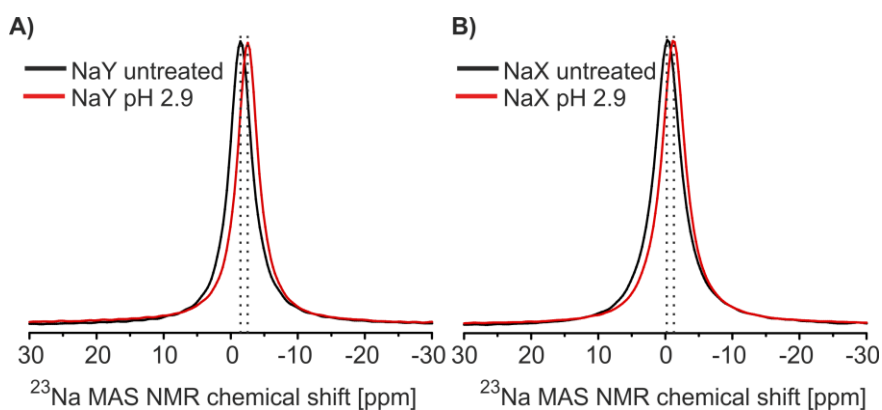


Figure 68. ^{23}Na MAS NMR spectroscopy of bare NaY (A) and NaX (B) stored for one week in neutral aqueous media and at pH 2.9. The chemical shift is given in ppm.

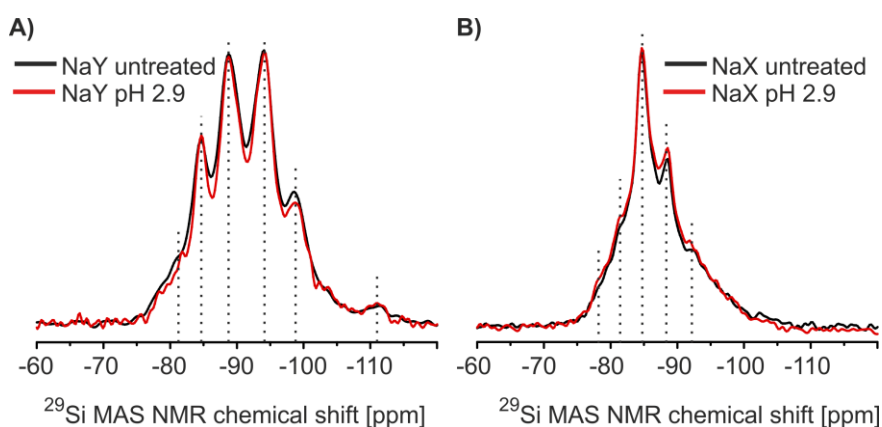


Figure 69. ^{29}Si MAS NMR spectroscopy of bare NaY (A) and NaX (B) stored for one week in neutral aqueous media and at pH 2.9. The chemical shift is given in ppm.

MAS NMR spectroscopy was thought to be able to observe structural differences between the untreated zeolite NaY and NaX and the ones which were stored for one week in aqueous suspension at pH 2.9. Spectra were recorded for the ^1H , ^{27}Al , ^{23}Na and ^{29}Si cores which are given in the Figures 66–69. The Brønsted acid sites in the zeolite pointing towards the supercage are typically observed between 3.5 ppm and 4.5 ppm depending on the zeolite source.^[139,140] It can be stated that the acidic treatment does essentially not alter the properties of the zeolite nanoparticles. For none of the cores a distinct difference is observed. This leads to the conclusion that the thermodynamically triggered color change has to originate solely from the complex coordination itself and the interaction between the confined complex and the void. SQUID magnetometry in a temperature range between 150 K and 400 K is displayed for the colorless compound $\text{Fe}(\text{Bpy})_3@ \text{NaX}$ after one week of storage at pH 2.9 together with the corresponding measurement of the untreated sample – for comparative reasons – in Figure 70. A huge difference is observed between both samples highlighting a completely paramagnetic behavior of $\text{Fe}(\text{Bpy})_3@ \text{NaX}$ after one week of storage at pH 2.9 in total congruency to the observed vanishing of the MLCT-transition. The sample has at 300 K a χ_{Mass} value of $10 \cdot 10^{-3} \text{ cm}^3 \text{ g}^{-1}$. A drastic change of the coordination geometry can be inferred from this measurement.

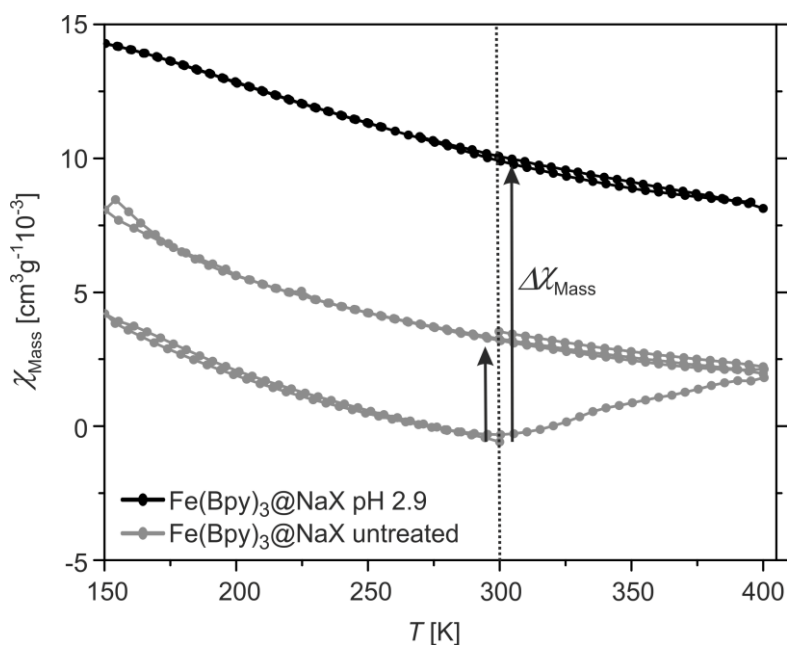


Figure 70. Magnetic behavior of $\text{Fe}(\text{Bpy})_3@ \text{NaX}$ after several days of storage at pH 2.9 given together with the untreated sample. χ_{Mass} is plotted against the temperature in a range between 150 K and 400 K. The measurements were performed at 20000 Oe in the settle mode.

It appears that two possibilities can lead to the observed effect. It should be noted that Mössbauer spectroscopy verifies an unusual distortion of $[\text{Fe}(\text{Bpy})_3]^{2+}$ inside of NaX which is not taking place for NaY. Furthermore the observed color change is taking place only for $[\text{Fe}(\text{Bpy})_3]^{2+}$ in NaX and not for NaY over a very long time range. The formed colorless compound is for NaX obviously the thermodynamically stable product while the homoleptic, octahedrally coordinated complex is the kinetically stable product in NaX. The strong π -cation interaction in NaX has to be responsible for the distortion. This distorted mode is obviously energetically unfavorable why the complex transits to a paramagnetic species. This species can be a dissociation product, a half-bonded species with coordinated water or a protonated species.

Since the effect itself is pH-dependent and takes place only around neutral pH the second alternative is the one that is most likely. Highly ionic, acidic, aqueous solutions are exchanged much slower inside of the zeolite and lead therefore to a decreased water exchange rate. Therefore, at pH 2.9 the water exchange is strongly limited and only happens at the surface of the particles. At pH 6.0 water molecules can be exchanged more easily throughout the intrazeolitic channels and interact with the entrapped complexes. For NaY this does not lead to any alterations since the confined complex is already the thermodynamically and kinetically stable product. Inside of NaX the situation is different and the complex is strongly distorted. The rapid exchange of water molecules allows here the formation of a partially H_2O coordinated species under Fe-N bond-break and twisting of one or more pyridyl-rings towards the cation sites under π -cation interaction. This product has reduced sterical interactions and is therefore now the thermodynamically stable product.

2.6 PD-CISSS of iron(II) complexes in nanozeolites

2.6.1 Observations and systematic trends

$[\text{Fe}(44\text{mBpy})_3]^{2+}$, $[\text{Fe}(55\text{mBpy})_3]^{2+}$ and $[\text{Fe}(\text{Bpy})_3]^{2+}$ have been incorporated by a wet impregnation technique inside the voids of NaY and NaX nanoparticles. Encapsulation has been found to proceed without formation of paramagnetic impurities or presence of crystalline bulk material. This was confirmed by IR and Mössbauer spectroscopy as well as by powder diffraction and SEM/EDX measurements. The achieved loadings are up to five times higher than it was found for microsized zeolites. This can be traced back to the large accessible surface area of the nanoparticles. Furthermore, the achieved loadings can compete with iron exchange procedures which are only able to occupy selectively the large cavity at similar loadings. This makes impregnation an effective and reliable preparation technique especially for zeolite nanoparticles. Approximately two complexes are found per unit cell which consists out of eight supercages.

Mössbauer spectroscopy verifies the predominant formation of the diamagnetic, octahedral coordinated iron(II) complexes inside the voids. For $\text{Fe}(\text{Bpy})_3@ \text{NaY}$ this happens under complete preservation of the Mössbauer parameters. For all encapsulated complexes in NaX nanoparticles a distortion of the coordination geometry compared to the bulk material is observed which is most pronounced for the methylated derivatives as a result of the higher sterical demand. $\text{Fe}(44\text{mBpy})_3@ \text{NaY}$ and $\text{Fe}(44\text{mBpy})_3@ \text{NaX}$ incorporate a diamagnetic and a paramagnetic species inside the supercages what is mirrored by a higher χ_{Mass} value at RT during SQUID magnetometry. This is in line with the findings in solution where this system was found to transit most easily to a paramagnetic state caused by a PD-CISSS. All encapsulated compounds undergo this PD-CISSS in NaY as well as in NaX caused by Brønsted acid sites (visible in ^1H MAS NMR) in total analogy to the behavior of the bulk complexes in acidic solution. This was followed via SQUID magnetometry. The overall change of $\Delta\chi_{\text{Mass}}$ was found to be larger for NaY but $T_{1/2}$ was found to be significantly shifted to lower temperatures in NaX in congruency to the theoretically larger amount of Brønsted acid sites. Interestingly the same $T_{1/2}$ value was found for $[\text{Fe}(\text{Bpy})_3]^{2+}$ in both zeolites in congruency to the T -independent steady-state condition for this complex in solution.

Furthermore the confined complexes in NaX were identified as the kinetically stable compounds which are converted in neutral aqueous solution over a long time range to a

thermodynamically stable, paramagnetic species. This species was found to be most likely partially coordinated by H₂O molecules in order to reduce sterical constraints and undergo π -cation interaction as a result of the increased number of cation sites in the supercage of NaX.

2.6.2 Consequences and predictions

It was shown that zeolite nanoparticles can be used as carrier for iron(II) reporter functions which preserve PD-CISSS effects under encapsulation. The resulting pH-responsive magnetism depends essentially on the used ligand, the zeolite host and the temperature. For further experiments USY zeolites should be considered which are generated by initial acid dealumination.^[139,140,143] This increases the stability in acidic solutions and leads to a faster water exchange as a result of partial destruction of the zeolite lattice.^[95] This should allow an observable paramagnetic relaxation enhancement in solution as a result of increased water exchange.^[95,97] A further reduction of the particle diameter will lead to full loadings where up to one complex should be able to be incorporated in every supercage. The impregnation is with no doubt the most reliable preparation method and is excellently suitable for nanoparticles and should therefore be continuously used for further experiments. Although the zeolite voids limit drastically the number of incorporable systems several complexes can be imagined which should lead to higher paramagnetic fractions. Ethers or long alkyl chains should be very suitable for this, pushing more electron density into the pyridyl rings. Another interesting feature so far unexplored is the general paramagnetic relaxation enhancement of bare iron exchanged zeolites where hexaaquo iron(II) or iron(III) is present only in the supercages. Ions in the sodalite cages don't contribute to paramagnetic relaxation enhancement and iron ions in the supercages will allow a fast water exchange rate.^[95,97] The reduced thermal motion upon immobilization in the zeolite host should increase the paramagnetic relaxation enhancement dramatically and it is very likely that hexaaquo iron(II) or iron(III) also displays a significant pH-response due to ligand exchange. More sophisticated ligands could be used which have pH-labile groups like hydrazones or thiomaleamic acids which allow a direct modification of the spin state around neutral pH or which are only stable at slightly basic pH values.

3. Summary

3.1 Summary (in English)

In the first part of this study a series of homoleptic iron(II) complexes of twelve different bidentate and tridentate ligands was synthesized and investigated with regard to the observation of a pH-responsive magnetism in aqueous solution. The five, at room temperature diamagnetic, aprotic iron(II) complexes $[\text{Fe}(\text{Bpy})_3]^{2+}$, $[\text{Fe}(44\text{mBpy})_3]^{2+}$, $[\text{Fe}(55\text{mBpy})_3]^{2+}$, $[\text{Fe}(4\text{mBpy})_3]^{2+}$ and $[\text{Fe}(5\text{mBpy})_3]^{2+}$ show the necessary long-term stability in solution and a pH-responsive magnetism. The corresponding chloride salts were characterized in the solid state using magnetic measurements, Mössbauer spectroscopy, powder diffraction, thermo gravimetric analysis and single crystal X-ray structure analysis. All five complexes show a spin state change above room temperature due to a loss of solvent molecules included in the crystal packing. Solutions of the complexes at different pH were investigated in detail using $^1\text{H-NMR}$ and UV-Vis spectroscopy as well as magnetic measurements to analyze their suitability as smart imaging probe due to a pH-responsive paramagnetic relaxation enhancement. It is demonstrated that the low-spin (LS) complexes can be converted reversibly into high-spin (HS) complexes as function of the pH, temperature and concentration. In a first step the diamagnetic $[\text{Fe}(\text{L})_3]^{2+}$ (L = bipyridine or its mentioned derivatives) is protonated, leading to a diamagnetic six-coordinated species $[\text{Fe}(\text{L})_2(\text{LH})]^{3+}$, where LH^+ is still a bidentate ligand. This diamagnetic species is in a temperature-dependent equilibrium with a paramagnetic species $[\text{Fe}(\text{L})_2(\text{HL})(\text{H}_2\text{O})]^{3+}$, where HL acts as monodentate ligand and the sixth coordination site is occupied by a water molecule that is exchanged rapidly. Both equilibria influence each other thus the whole proton-driven coordination-induced spin state switch (PD-CISSS) is pH-, temperature- and concentration-dependent. Additionally, it is demonstrated that also spin-crossover (SCO) complexes like $[\text{Fe}(\text{Bpp})_2]^{2+}$ can be modulated towards the HS state via PD-CISSS. Furthermore, it is shown that the pH range and completeness of the underlying PD-CISSS depend on the substitution pattern of the ligand and especially the inductive effect of the methyl substituents. In the case of $[\text{Fe}(44\text{mBpy})_3]^{2+}$, indications for a protonated species were already observed at pH 6 and the magnetic measurements revealed a complete conversion to the HS state at pH 1 and elevated temperatures. At room temperature and pH 1, γ_{HS} is twice as high as for $[\text{Fe}(\text{Bpy})_3]^{2+}$. The molar relaxivity Δr_1 at pH 1 is slightly lower, although a higher fraction of paramagnetic centers is present. An explanation for this is a difference in the water exchange rates. The

performance of the other three complexes is in between $[\text{Fe}(\text{44mBpy})_3]^{2+}$ and $[\text{Fe}(\text{Bpy})_3]^{2+}$. This can be coherently explained by the different positions of the methyl group. Generally, each methyl group increases the electron density in the pyridine ring due to its inductive effect. The inductive effect is *ortho* and *para* directing. The pyridine nitrogen of $[\text{Fe}(\text{55mBpy})_3]^{2+}$ is in *meta* position to the methyl group and the electron density is not as strongly increased as in the case of $[\text{Fe}(\text{44mBpy})_3]^{2+}$, where it is *para* to the methyl group. In case of $[\text{Fe}(\text{4mBpy})_3]^{2+}$ and $[\text{Fe}(\text{5mBpy})_3]^{2+}$ with only one methyl group the effect is weaker. Therefore, electron density at the pyridine nitrogen is increased the most for $[\text{Fe}(\text{44mBpy})_3]^{2+}$. The nitrogen becomes a harder base which is more likely to interact with protons as a hard acid. Consequently, protonation is most likely for $[\text{Fe}(\text{44mBpy})_3]^{2+}$, least likely for $[\text{Fe}(\text{4mBpy})_3]^{2+}$ and $[\text{Fe}(\text{5mBpy})_3]^{2+}$, while $[\text{Fe}(\text{55mBpy})_3]^{2+}$ is located in between. This is in excellent agreement with the experimental results. The second equilibrium step involves a twisting of the pyridyl ring and a Fe-N bond break. The twisting is mainly influenced by the sterical demand of the substituents and is most likely not relevant for solution experiments. However, the increased electron density at the pyridine nitrogen strengthens the Fe-N bond. This is mirrored in the γ_{HS} values that do not increase in the same extent as the γ_{H^+} values. The counteracting influence of the increased electron density (more likely protonation vs. strengthening of the Fe-N bond) explains why the increase of γ_{HS} starts at lower pH in the case of $[\text{Fe}(\text{55mBpy})_3]^{2+}$ (strengthening of the Fe-N bond dominates) and at a slightly higher pH in the case of $[\text{Fe}(\text{44mBpy})_3]^{2+}$ (more protonation due to *para* directing effect) compared to $[\text{Fe}(\text{Bpy})_3]^{2+}$. For the presented complexes, in field-cycling (FC) $^1\text{H-NMR}$ relaxometry factors between 10 and 20 are found for the LS-HS relaxivity gap. This is – to the best of our knowledge – the largest LS-HS relaxivity gap reported so far in the literature. The results highlight that iron(II) complexes should indeed be considered as pH-responsive alternative to toxic gadolinium(III) complexes in the development of smart contrast agents. Due to the very acidic conditions needed so far, the application potential of the presented systems is most likely in the area of gastrointestinal imaging.

In the second part of this study, diamagnetic iron(II) complexes have been encapsulated in the supercages of micro-sized zeolite NaY and have been found to detect changes of the intrazeolitic environment by undergoing a PD-CISSS if the complex concentration is sufficiently low. Especially the hybrids $\text{Fe}(\text{Bpy})_3@ \text{NaY}$ and $\text{Fe}(\text{Bpp})_2@ \text{NaY}$ exhibit temperature-dependent optical and magnetic properties when prepared via wet impregnation. Under small confinement, the spin state change is induced by Brønsted acid sites as it could

be inferred from the alteration of the MLCT-transition, MAS NMR spectroscopy and magnetic measurements. The observed interaction follows exactly the result which could already be observed and explained in solution. Mössbauer spectroscopy, powder diffraction and SEM/EDX verify the presence of solely the octahedral coordinated complexes inside of the zeolite. Additionally, for zeolites it is generally known that they carry proton defects which were also found via MAS NMR and the complex loadings of the impregnated materials are in a region where interaction with protons is shifted into an observable region. Brønsted acid sites interact with the most basic part in the hybrids which are the *N*-donor atoms of the aromatic rings what consequently leads to differences in MLCT-transition. All color changes upon heating followed via reflective Kubelka-Munk measurements are similar to the changes observed in solution what indicates that both processes are caused by protons in the near surrounding of the iron complexes. Therefore, the observed effect under small confinement must be a spin state change with coordination change caused by Brønsted acid sites. Especially $[\text{Fe}(\text{Bpy})_3]^{2+}$ under small confinement is shown to exhibit a reversible magnetic bistability upon protonation. In the wet state, the water in the zeolite cavities interacts with the Brønsted acid sites (hydrogen bonds) and thus prevents an interaction of those sites with the complexes in the supercages. Upon heating, water is removed and now the Bpy (or the Bpp) ligand can interact with the Brønsted acid sites leading to a protonation of the nitrogen donor. This induces a coordination change at the iron center from six to five in line with a spin state change from a diamagnetic LS state to a paramagnetic HS state. A free coordination spot is formed where water molecules are exchanged rapidly as it could be followed by paramagnetic relaxation enhancement in inversion-recovery experiments. In summary it has been demonstrated that inside the zeolite a proton-driven coordination-induced spin state switch can take place, too. This is essential since hybrid materials – especially zeolites – are known for their outstanding biocompatibility which is highly necessary for *in vivo* applications and the design of safe and stable smart contrast agents. Additionally, the PD-CISSS allows here to monitor the temperature-dependent Brønsted acidity via changes of the magnetic moment.

In the third part of this study, wet impregnation was used to insert $[\text{Fe}(44\text{mBpy})_3]^{2+}$, $[\text{Fe}(55\text{mBpy})_3]^{2+}$ and $[\text{Fe}(\text{Bpy})_3]^{2+}$ in the supercages of zeolite NaY and NaX nanoparticles. IR and Mössbauer spectroscopy confirmed encapsulation without the formation of paramagnetic species in the sodalite cages. It turned out that the nanosized particles are very suitable for the wet impregnation technique due to the higher surface accessibility. The achieved loadings are up to five times higher than it was found for microsized zeolites and are

therefore in a region comparable to iron exchange procedures. This highlights wet impregnation as an effective and reliable preparation technique for zeolite nanoparticles. All hybrid materials were analyzed with Mössbauer spectroscopy where predominantly the formation of the diamagnetic, octahedral coordinated iron(II) complexes inside the voids was detected. For all encapsulated complexes in NaX nanoparticles a distortion of the coordination geometry compared to the bulk material is observed which is most pronounced for the methylated derivatives as a result of the higher sterical demand. In the case of $\text{Fe}(44\text{mBpy})_3@NaX$ and $\text{Fe}(44\text{mBpy})_3@NaY$ a diamagnetic and a paramagnetic species are observed inside the supercages what is mirrored by a higher χ_{Mass} value at RT during SQUID magnetometry. This is in line with the solution measurements of the chloride complex which transits most easily via PD-CISSS to a paramagnetic state. The Mössbauer parameters of the paramagnetic species could be captured and correspond nicely to a paramagnetic, asymmetric iron(II) complex in the supercage as it would be indicative for a half-bonded, protonated adduct. Magnetic measurements show that all composite materials undergo PD-CISSS – in NaY as well as in NaX – caused by Brønsted acid sites in total analogy to the behavior of the bulk complexes in acidic solution. The overall change of $\Delta\chi_{\text{Mass}}$ was found to be larger for NaY while $T_{1/2}$ was found to be significantly shifted to lower temperatures in NaX in congruency to the theoretically larger amount of Brønsted acid sites. Interestingly the same $T_{1/2}$ value was found for $[\text{Fe}(\text{Bpy})_3]^{2+}$ in both zeolites in congruency to the T -independent steady state condition for this complex in solution. The results highlight that iron(II) zeolite hybrid nanoparticles should be considered for the design of new smart contrast agents. The interplay between the complexes and the solid state material leads to multiresponsiveness, increases the biocompatibility and generates a broader property spectrum what is important to shift the desired features into the biological window.

In summary, a family of compounds was identified displaying a pH-responsive magnetism in aqueous solution. The underlying mechanism is a proton-driven coordination-induced spin state switch that leads to a paramagnetic relaxation enhancement above a specific proton concentration due to a free coordination site where water molecules can be exchanged. The PD-CISSS was found to be temperature-, concentration- and pH-dependent and to be alterable via ligand substitution. Thereby, the influence of the ligand is mainly determined by the electron donating ability of the methyl groups. The pH-responsiveness is not only limited to complex solutions but can also be observed under small confinement. It was demonstrated

that microsized zeolite particles loaded with the presented complexes can show also PD-CISSS effects under removal and addition of water from the intrazeolitic channels. A similar behavior can also be generated in zeolite nanoparticles and the sensitivity of the pH-response is under small confinement still controllable via ligand substitution as it has been observed in solution. The presented PD-CISSS and the amalgamation with biocompatible zeolite nanoparticles is doubtlessly a new impetus for the design of smart contrast agents based on nontoxic iron(II) complexes.

3.2 Summary (in German)

Im ersten Teil dieser Arbeit wurde eine Serie von homoleptischen Eisen(II)-Komplexen, aus zwölf verschiedenen zwei- und dreizähligen Liganden, synthetisiert und im Hinblick auf das Auftreten eines pH-responsiven Magnetismus untersucht. Die fünf, bei Raumtemperatur diamagnetischen und aprotischen Eisen(II)-Komplexe $[\text{Fe}(\text{Bpy})_3]^{2+}$, $[\text{Fe}(44\text{mBpy})_3]^{2+}$, $[\text{Fe}(55\text{mBpy})_3]^{2+}$, $[\text{Fe}(4\text{mBpy})_3]^{2+}$ und $[\text{Fe}(5\text{mBpy})_3]^{2+}$ zeigen in Lösung die notwendige Langzeitstabilität als auch einen pH-responsiven Magnetismus. Die korrespondierenden Chloride wurden im festen Zustand mittels Magnetmessungen, Mössbauerspektroskopie, Pulverdiffraktometrie, Thermogravimetrie und Röntgen-Einkristallstrukturanalyse analysiert. Alle fünf Systeme zeigen einen Wechsel des Spinzustands oberhalb von Raumtemperatur, ausgelöst durch den Verlust von Lösungsmittelmolekülen im Kristallgitter. Lösungen der Komplexe wurden sowohl mittels ^1H -NMR- und UV-Vis-Spektroskopie bei unterschiedlichen pH-Werten detailliert untersucht, als auch mittels Magnetmessungen, um deren Eignung als intelligentes Kontrastmittel, basierend auf einer pH-responsiven paramagnetischen Verstärkung der Relaxation zu untersuchen. Es konnte demonstriert werden, dass die *low-spin* (LS) Komplexe in Abhängigkeit des pH-Wertes, der Temperatur und der Konzentration, reversibel in den *high-spin* (HS) Zustand überführt werden können. Einleitend wird zuerst der diamagnetische Komplex $[\text{Fe}(\text{L})_3]^{2+}$ ($\text{L} = 2,2'$ -Bipyridin oder seine Derivate) protoniert, was zu einer diamagnetischen, sechsfach koordinierten Spezies $[\text{Fe}(\text{L})_2(\text{LH})]^{3+}$ führt, bei welcher LH^+ immer noch ein zweizähliger Ligand ist. Die diamagnetische Spezies befindet sich in einem temperaturabhängigen Gleichgewicht mit der paramagnetischen Spezies $[\text{Fe}(\text{L})_2(\text{HL})(\text{H}_2\text{O})]^{3+}$, wobei HL als einzähliger Ligand fungiert und die sechste freie Koordinationsstelle von einem Wassermolekül besetzt wird, welches schnell ausgetauscht werden kann. Beide Gleichgewichte beeinflussen sich gegenseitig und dementsprechend ist der vollständige protonengetriebene, koordinationsinduzierte Wechsel des Spinzustands (PD-CISSS) pH-, temperatur- und konzentrationsabhängig. Zusätzlich konnte demonstriert werden, dass sich auch *Spin-Crossover* (SCO) Komplexe wie $[\text{Fe}(\text{Bpp})_2]^{2+}$ mittels PD-CISSS in den HS Zustand überführen lassen. Desweiteren konnte gezeigt werden, dass der pH-Bereich und die Vollständigkeit des zugrundeliegenden PD-CISSS vom Substitutionsmuster des Liganden und im Speziellen vom induktiven Effekt der Methylgruppen abhängen. Im Fall von $[\text{Fe}(44\text{mBpy})_3]^{2+}$ konnten Anzeichen für eine Protonierung bereits bei pH 6 beobachtet werden und Magnetmessungen bestätigten eine vollständige Konversion in den HS Zustand bei pH 1 und erhöhter Temperatur. Bei pH 1 und Raumtemperatur ist γ_{HS} daher für diese

Verbindung doppelt so hoch wie für $[\text{Fe}(\text{Bpy})_3]^{2+}$. Obwohl ein größerer Anteil von paramagnetischen Zentren vorliegt, ist die molare Relaxivität Δr_1 bei pH 1 etwas niedriger. Eine mögliche Erklärung dafür sind Unterschiede in der Austauschrate der Wassermoleküle. Das Verhalten der anderen drei Komplexe liegt zwischen $[\text{Fe}(44\text{mBpy})_3]^{2+}$ und $[\text{Fe}(\text{Bpy})_3]^{2+}$. Dies kann zufriedenstellend mit den unterschiedlichen Positionen der Methylgruppen erklärt werden. Generell erhöht jede Methylgruppe die Elektronendichte in den Pyridinringen aufgrund ihres induktiven Effekts. Der induktive Effekt ist *ortho*- und *para*-dirigierend. Der Stickstoff am Pyridinring von $[\text{Fe}(55\text{mBpy})_3]^{2+}$ befindet sich in *meta*-Stellung zur Methylgruppe und daher ist die Elektronendichte nicht so stark erhöht wie im Fall von $[\text{Fe}(44\text{mBpy})_3]^{2+}$, wo er sich *para*-ständig zur Methylgruppe befindet. Im Fall von $[\text{Fe}(4\text{mBpy})_3]^{2+}$ und $[\text{Fe}(5\text{mBpy})_3]^{2+}$ mit nur jeweils einer Methylgruppe ist der Effekt dementsprechend schwächer. Folglich ist für $[\text{Fe}(44\text{mBpy})_3]^{2+}$ die Elektronendichte am Stickstoff der Pyridinringe am höchsten. Der Stickstoff wird dadurch zu einer härteren Base für welche es wahrscheinlicher ist mit einem Proton als harte Säure zu interagieren. Somit ist die Protonierung am wahrscheinlichsten für $[\text{Fe}(44\text{mBpy})_3]^{2+}$, am unwahrscheinlichsten für $[\text{Fe}(4\text{mBpy})_3]^{2+}$ und $[\text{Fe}(5\text{mBpy})_3]^{2+}$, während sich $[\text{Fe}(55\text{mBpy})_3]^{2+}$ genau dazwischen befindet. Exakt diese Reihenfolge wurde experimentell bestätigt. Das zweite Gleichgewicht beinhaltet die Drehung der Pyridinringe und einen Fe-N-Bindungsbruch. Die Drehung wird zudem vom sterischen Anspruch der Substituenten beeinflusst und ist höchstwahrscheinlich nicht relevant für Lösungsexperimente. Nichtsdestotrotz stärkt die erhöhte Elektronendichte an den Pyridinstickstoffen die Fe-N-Bindung. Dies spiegelt sich in den γ_{HS} Werten wider, welche nicht in gleichem Maße wie die γ_{H^+} Werte ansteigen. Der gegenläufige Einfluss der erhöhten Elektronendichte (wahrscheinlichere Protonierung vs. Stärkung der Fe-N-Bindung) erklärt, weshalb der Anstieg von γ_{HS} bei $[\text{Fe}(55\text{mBpy})_3]^{2+}$ (Stärkung der Fe-N-Bindung dominiert) bei einem niedrigeren pH-Wert startet und für $[\text{Fe}(44\text{mBpy})_3]^{2+}$ bei einem höheren pH-Wert (mehr Protonierung durch *para*-dirigierenden Effekt) verglichen mit $[\text{Fe}(\text{Bpy})_3]^{2+}$. Für die präsentierten Komplexe werden mittels FC ^1H -NMR-Relaxometrie, Faktoren zwischen 10 und 20 für den LS-HS Relaxationsunterschied gefunden. Nach bestem Wissen, ist dies der größte LS-HS Relaxationsunterschied der bis jetzt in der Literatur beschrieben ist. Die Resultate unterstreichen, dass Eisen(II)-Verbindungen tatsächlich als pH-responsive Alternative zu toxischen Gadolinium(III)-Komplexen bei der Entwicklung von intelligenten Kontrastmitteln in Betracht gezogen werden sollten. Aufgrund der bisher benötigten, stark

sauren Bedingungen, liegt das Anwendungspotential der beschriebenen Systeme am wahrscheinlichsten im Bereich der gastrointestinalen bildgebenden Diagnostik.

Im zweiten Teil dieser Studie wurden diamagnetische Eisen(II)-Komplexe in den *Supercages* von Zeolith-Mikropartikeln eingeschlossen. Es konnte festgestellt werden, dass intra-zeolithische Veränderungen durch einen PD-CISS detektiert werden können, solange die Konzentration der Komplexe innerhalb der Kavitäten ausreichend gering ist. Besonders die Hybridmaterialien $\text{Fe}(\text{Bpy})_3@NaY$ und $\text{Fe}(\text{Bpp})_2@NaY$ zeigen temperaturabhängige, optische und magnetische Eigenschaften, wenn sie mittels der beschriebenen Imprägnationstechnik hergestellt werden. Durch die Verkapselung im Zeolith wird der Wechsel des Spinzustands über Brønsted-Säuren induziert. Dies kann aus den Veränderungen des MLCT-Übergangs, der MAS NMR Spektroskopie und den Magnetmessungen abgeleitet werden. Die beobachtbare Interaktion folgt exakt den Resultaten, welche bereits in Lösung erzeugt und erklärt werden konnten. Mössbauerspektroskopie, Pulverdiffraktometrie und SEM/EDX verifizieren die ausschließliche Präsenz von oktaedrisch koordinierten Komplexen im Zeolith. Zusätzlich ist bekannt, dass Zeolithe Brønsted-saure Zentren besitzen welche auch mittels MAS NMR nachgewiesen werden konnten. Desweiteren liegt die Komplexbeladung der imprägnierten Proben in einem Bereich in welchem die Interaktion mit Protonen in ein beobachtbares Areal verschoben ist. Die Brønsted-sauren Zentren interagieren mit dem basischsten Teil der Hybridmaterialien. Dies sind die Stickstoffdonoratome der aromatischen Ringe, was in Konsequenz zu Unterschieden im MLCT-Übergang führt. Alle auftretenden Farbwechsel während des Aufheizens – verfolgt mittels reflektiver Kubelka-Munk-Spektroskopie – sind identisch zu den Änderungen welche bereits in Lösung auftraten. Dies ist symptomatisch dafür, dass beide Prozesse durch Protonen in der näheren Komplexumgebung ausgelöst werden. Deshalb muss der beobachtete Effekt im Hybridmaterial ebenfalls ein Wechsel des Spinzustands mit Änderung der Koordinationsgeometrie – verursacht durch Brønsted-saure Zentren – sein. Besonders $\text{Fe}(\text{Bpy})_3@NaY$ zeigt unter Verkapselung eine reversible magnetische Bistabilität durch Protonierung. Im hydratisierten Zustand interagieren die Wassermoleküle in den Kavitäten mit den Brønsted-Zentren (Wasserstoffbrückenbindungen) und verhindern so die Interaktion dieser Zentren mit den Komplexen im *Supercage*. Durch Erhitzen wird das Wasser entfernt und die Bpy (oder Bpp) Liganden können mit den Brønsted-Zentren interagieren, was zu einer Protonierung am Stickstoffdonor führt. Dies induziert am Eisenzentrum einen Koordinationswechsel von sechs zu fünf, übereinstimmend mit einem Wechsel des Spinzustands von einem diamagnetischen

LS zu einem paramagnetischen HS Zustand. Dabei wird eine Koordinationsstelle frei, an welcher Wassermoleküle schnell ausgetauscht werden können. Dies konnte anhand der Verstärkung der paramagnetischen Relaxation in *Inversion-Recovery* Experimenten nachvollzogen werden. Zusammengefasst konnte demonstriert werden, dass auch in Zeolithen ein PD-CISSS stattfinden kann. Dies ist wichtig, da Hybridmaterialien und vor allem Zeolithe für ihre herausragende Biokompatibilität bekannt sind. Dieses ist für *in vivo* Anwendungen und das Design von sicheren und stabilen, intelligenten Kontrastmitteln besonders nötig. Zusätzlich erlaubt der PD-CISSS hier die temperaturabhängige Brønsted-Acidität über Änderungen des magnetischen Moments zu überwachen.

Im dritten Teil dieser Studie wurden $[\text{Fe}(44\text{mBpy})_3]^{2+}$, $[\text{Fe}(55\text{mBpy})_3]^{2+}$ und $[\text{Fe}(\text{Bpy})_3]^{2+}$ mittels Imprägnation in die *Supercages* von NaY und NaX Nanopartikeln eingebracht. IR- und Mössbauerspektroskopie bestätigten die Einlagerung ohne Bildung von paramagnetischen Nebenprodukten in den Sodalith-Käfigen. Es stellte sich heraus, dass die Nanopartikel aufgrund ihrer großen zugänglichen Oberfläche sehr gut für die Imprägnationstechnik geeignet sind. Die erzielten Beladungen sind bis zu fünf Mal so hoch wie für die Mikropartikel und liegen daher in einem Beladungsbereich der vergleichbar mit Eisenaustauschprozeduren ist. Dies hebt die Imprägnation als effektive und verlässliche Präparationstechnik für beladene Zeolith-Nanopartikel hervor. Alle Hybridmaterialien wurden mittels Mössbauerspektroskopie analysiert, wobei vorrangig die Bildung von diamagnetischen, oktaedrischen Eisen(II)-Komplexen innerhalb der großen Kavitäten bestätigt wurde. Für alle Komplexe welche in NaX eingeschlossen wurden, tritt im Vergleich zum Feststoff eine Verzerrung der Koordinationsgeometrie auf. Aufgrund des höheren sterischen Anspruchs ist diese für die methylierten Derivate ausgeprägter. Sowohl $\text{Fe}(44\text{mBpy})_3@NaX$ als auch $\text{Fe}(44\text{mBpy})_3@NaY$ weisen eine diamagnetische und eine paramagnetische Spezies in den *Supercages* auf, was sich in erhöhten χ_{Mass} Werten bei RT widerspiegelt. Die Mössbauerparameter der paramagnetischen Spezies konnten bestimmt werden und korrespondieren vollständig mit denen paramagnetischer, asymmetrischer Eisen(II)-Komplexe im *Supercage*, wie man es für ein halb-gebundenes, protoniertes Addukt erwarten würde. Alle eingeschlossenen Verbindungen durchlaufen bei Erhöhung der Temperatur während der Magnetmessung einen PD-CISSS – sowohl in NaY als auch in NaX. Dies wird durch Brønsted-Zentren verursacht, in Analogie zum Verhalten welches bereits bei den Komplexen in Lösung beobachtet werden konnte. Die gesamte Änderung $\Delta\chi_{\text{Mass}}$ fällt für NaY stärker aus während $T_{1/2}$ für NaX signifikant zu niedrigeren Temperaturen verschoben ist, in Über-

einstimmung mit dem theoretisch höheren Gehalt von Brønsted-Zentren. Interessanterweise wurden für $[\text{Fe}(\text{Bpy})_3]^{2+}$ in beiden Zeolithen identische $T_{1/2}$ Werte gefunden, übereinstimmend mit dem temperaturunabhängigen, stationären Zustand dieser Komplexe in Lösung. Die Ergebnisse zeigen, dass Hybride aus Eisen(II)-Komplexen und Zeolith-Nanopartikeln für die Konzeptionierung neuer, intelligenter Kontrastmittel in Betracht gezogen werden sollten. Die Verbindung von Komplexen und Trägermaterialien führt zu Multiresponsivität, erhöht die Biokompatibilität und generiert ein breiteres Eigenschaftsspektrum, welches wichtig ist um die Anwendbarkeit in das biologische Fenster zu verschieben.

Alles in allem wurde eine Klasse von Verbindungen identifiziert, welche einen pH-responsiven Magnetismus in wässriger Lösung aufweisen. Der verantwortliche, molekulare Mechanismus ist ein PD-CISSS, welcher aufgrund des Austauschs von Wassermolekülen an einer freien Koordinationsstelle, zu einer Verstärkung der paramagnetischen Relaxation oberhalb einer spezifischen Protonenkonzentration führt. Der PD-CISSS ist sowohl temperatur-, konzentrations-, als auch pH-abhängig und kann durch Substitution der Liganden beeinflusst werden. Dabei wird der Einfluss des Liganden maßgeblich durch die Elektronendonorfunktion der Methylgruppen bestimmt. Die pH-Responsivität ist nicht auf Lösungen von Komplexen beschränkt, sondern kann auch unter Einschluss in Hybridmaterialien beobachtet werden. Es konnte demonstriert werden, dass mit den beschriebenen Komplexen beladene Zeolith-Mikropartikel PD-CISSS Eigenschaften unter Entfernung und Zuführung von Wasser in den intrazeolithischen Kanälen aufweisen können. Ein ähnliches Verhalten konnte auch für Zeolith-Nanopartikel generiert werden, wobei die pH-Responsivität auch unter Einschluss immer noch durch Substitution der Liganden kontrolliert werden kann, wie es bereits in Lösung der Fall war. Der präsentierte PD-CISSS und dessen Verknüpfung mit biokompatiblen Zeolith-Nanopartikeln ist zweifellos ein neuer Impuls für das Design von intelligenten Kontrastmitteln basierend auf ungiftigen Eisen(II)-Komplexen.

4. Experimental Section

4.1 General procedures and instrumentation

pH-Determination of aqueous solutions with different pH-values has been carried out by using a Mettler Toledo MP 220 pH meter. All measurements have been conducted three times after stabilization. The pH Meter was calibrated with a buffer solution of pH 7.00 from Fluka. Acidic solutions between pH 6 and pH 1 have been prepared by adjusting the pH with 0.1 M HCl solution which was purchased from Grüssing. This solution was found to have a pH of 1.0 while the used distilled water was found to have a pH of 5.9. Acidic solutions below pH 1 have been adjusted with distilled water and conc. HCl which was purchased from Bernd Kraft. Solutions more basic than the used water have been adjusted with 0.1 M NaOH from Grüssing.

Magnetic susceptibility data were collected using a MPMSXL-5 SQUID magnetometer. Powdered bulk samples were measured under an applied field of 5000 Oe in a temperature range between 50 K and 400 K while the zeolite probes were measured under an applied field of 20 000 Oe in a temperature range between 150 K and 400 K. All samples were prepared in gelatin capsules placed in a plastic straw and were measured in the settle mode with a cooling and heating rate of 5 K between each measurement point. The measured values were corrected for the diamagnetism of the sample holder and the ligand by using tabulated Pascal's constants (suitable values can be estimated as $\chi_{\text{Dia}} \approx 0.5 \cdot 10^{-6} M_{\text{complex}}$).^[150] For the zeolite probes χ_{Mass} was calculated. Solution measurements were performed in the settle mode under an applied field of 20 000 Oe in a temperature range between 260 K and 350 K and a heating rate of 10 K between each measurement point. The liquid samples were held within a plastic straw that was sealed (two junctions in a distance around 18 mm welded two times in each case and rotated through 90°) to give a suitable reservoir containing 0.1 mL of aqueous complex solution with different concentrations. The data were corrected for the diamagnetic contributions of the ligand by using tabulated Pascal's constants, the neutral solvent and the sample holder.^[150] The high spin molar fraction was calculated as $\gamma_{\text{HS}} = (\chi_{\text{MT}})/(\chi_{\text{MT}})_{(S=2)}$ where $(\chi_{\text{MT}})_{(S=2)}$ is the theoretical value for a complex with the total spin S of 2. All measurements were analyzed by using the CGS system mode. The treatment of all magnetic data was done with the ORIGIN software.^[151]

⁵⁷Fe Mössbauer spectra were recorded in transmission geometry in a constant-acceleration mode using a conventional Mössbauer spectrometer operating at room temperature which was equipped with a 50mCi ⁵⁷Co(Rh) source. The bulk samples of the iron complexes were prepared under ambient conditions. Samples of impregnated zeolites were prepared under inert conditions. Extra inert conditions were used for iron exchanged zeolites since small traces of oxygen lead immediately to oxidation. The spectra were fitted using Recoil 1.05 Mössbauer Analysis Software.^[152] Lorentzian lineshapes were used for the least-squares fitting of the experimental data. The isomer shift values were reported with respect to α -Fe as a reference at room temperature.

¹H-NMR spectra in solution were recorded on a Varian Unity Inova 300 spectrometer from Agilent Technologies at 300 MHz in D₂O/H₂O mixtures; pH-values were adjusted in D₂O with 0.1 M HCl and concentrated HCl. Data had been calibrated by D₂O (4.79 ppm) and fitted with Spinworks software.^[153] γ H⁺ values were calculated from the integral values and correspond to the ratio between the signal intensity of the protonated species against the signal intensity of all observed signals at the corresponding pH.

NMR spectra of solid samples were recorded on a Bruker Avance III HD 400 spectrometer operating at a B_0 field of 9.4 T using a double-resonance 4 mm Bruker MAS probe at a rotation frequency of 5 kHz. Chemical shifts of ¹H were referenced indirectly to TMS using adamantane. The ¹H one-pulse experiments were acquired using a 90° pulse lengths of 3.0 μ s with a recycle delay of 0.5 s. T_1 measurements were done without spinning using the inversion-recovery scheme with inter-pulse delays varying from 50 μ s up to 2.0 s. The resulting curve was then fitted using the equation $I(t) = I_{(0)}\{1 - [2 \cdot A \cdot \exp(-t / T_1)]\}$.

Field-cycling (FC) ¹H-NMR of liquids was used to monitor the longitudinal relaxation time T_1 with a STELAR FFC 2000 relaxometer. The measurements were conducted in an extended glass straw and at 300 K \pm 1 K. The Larmor-frequency was varied between 10 kHz and 10 MHz with $\nu = \gamma B_0 / 2\pi$ where γ is the gyromagnetic ratio and B_0 is the external magnetic field. The molar relaxivity Δr_1 was calculated from $\Delta r_1 = (R_1 - R_1^{LM}) \cdot c^{-1}$; where R_1 is the

observed longitudinal relaxation, R_1^{LM} the observed longitudinal relaxation of the solvent and c the complex concentration. All R_1^{LM} are measured values and were determined for all used pH values although they were found to be stable over the used pH range. R_1 values can be calculated from the reciprocal T_1 .

Ultraviolet-Visible spectra were recorded on a Lambda 19 from Perkin Elmer. Samples were measured as highly diluted solution in quartz glass cuvettes from Carl Roth GmbH & Co. KG and water was used as a reference. The temperature was adjusted by an external temperature control regulating the sample holder in a sweep mode. Suspensions of zeolite particles were treated with ultrasound and were filtered prior to measurement.

Diffuse reflectance spectra at room temperature were recorded in the UV-Vis region on a Cary 300 UV-Vis from Agilent Technologies with a special sample holder for solids and powders in the reflective mode. The data was treated with classical *Kubelka-Munk* function and theory. For calibration a reference sample with 100% transmission was used after the background has been subtracted.

Temperature dependent reflectivity measurements were done by Nathalie Daro, in collaboration with Cédric Desplanches and Guillaume Chastanet, in October 2016. They used an ICMCB homemade apparatus where the sample is illuminated with white light via an optical fiber. The reflected light is then collected by a photomultiplier, on the whole light spectrum. For each compound the reflectivity data were collected during a cooling mode from 290 K to 250 K and then during three cycles between 250 K and 400 K. The reflectivity unit is arbitrary. The $T_{1/2}$ value corresponds to the temperature obtained at half of the transition.

Infrared-Spectra were recorded on a Spectrum 100 FT-IR spectrometer produced by Perkin Elmer. The spectrometer works with an attenuated total reflectance unit (germanium ATR crystal) able to measure in the solid and liquid phase without further preparation. The unit of determined absorption bands is given in wave numbers.

Elemental analysis (carbon, hydrogen and nitrogen contents) was done on a Vario EL III produced by Elementar Analysensysteme GmbH. Samples were placed in tin boats and were measured at least twice while the average of both measurements was used. Acetanilide was measured as standard reference after every sixth sample. For the weighed portion a precision balance was used ($\Delta m = 0.001$ mg).

Iron percentages of all discussed zeolite samples were determined with atomic absorption spectroscopy. The zeolite samples were solubilized completely with HF prior to measurement (acid digestion). The spectra itself were recorded on a Varian AA100. All measurements were done at least twice for two different spots of one batch. The mean value was calculated for all samples and is given as wt%.

X-Ray powder diffractograms were recorded on a STOE StadiP diffractometer in transmission geometry between 5° and 45° of 2θ using Ge monochromated $\text{CuK}\alpha 1$ radiation and a Mythen1K detector. Samples were placed in sealed capillaries and were prepared under ambient conditions.

Mass spectra were recorded on a Finnigan MAT 8500 mass spectrometer with the data system MASPEC II [II32/A304] and ionization energy of 70 eV. Insertion of the samples was conducted via direct entry.

Scanning electron microscope micrographs were recorded on a BIMF Leo 1530 from Zeiss made in Oberkochen (Germany) with different optical magnification. The acceleration voltage was up to 5 kV and the materials were sputter-coated with a 1.3 nm platinum layer.

Energy dispersive X-ray spectroscopy was also done using a BIMF Leo 1530 from Zeiss. Spectra were processed using all peaks and an iteration of seven. C, O, Na, Al, Si, Cl and Fe were usually analyzed.

Thermogravimetric analysis was carried out on a TG Libra F1 from Netzsch with an auto sampler under nitrogen atmosphere (20 mL/min) in the temperature range between 300 K and 900 K with a heating rate around 5 K/min similar to the magnetic measurements. Weighed portions were between 5.0 and 7.0 mg. A temperature calibration was done with six points prior to measurement.

X-ray crystal-structure analysis was performed on a Stoe StadiVari diffractometer instrument that was equipped with an Oxford Cryostream low-temperature unit using graphite-monochromated radiation ($\lambda(\text{Mo}_{K\alpha}) = 0.71073 \text{ \AA}$). The data were corrected for Lorentz and polarization effects. The structures were solved by direct methods (SIR-97)^[154] and refined by fullmatrix least-square techniques against $F_o^2 - F_c^2$ (SHELXL-97).^[155] All hydrogen atoms were calculated in idealised positions with fixed displacement parameters. ORTEP-III^[156] was used for the structure representation, SCHAKAL-99^[157] to illustrate molecule packing. CCDC 1533186 and 1533187 contain the supplementary crystallographic data for this work. These data can be obtained free of charge from the Cambridge Crystallographic Data Centre.

Dynamic light scattering was done by using a Malvern Zetasizer Nano ZS system. The samples were measured in suspension in disposable plastic cuvettes. The suspensions were treated with ultrasound prior to measurement and were cleansed from dust particles with suitable filters. Filtering was found not to affect the particle size distribution.

4.2 Synthesis

Iron(II) complexes in general are mostly sensitive towards oxidation. Furthermore dried zeolites are likely to adsorb oxygen from the surrounding air. Therefore all syntheses of iron(II) complexes were carried out under argon as inert gas by using *Schlenk* tube techniques even when the final product was air stable.^[158] The analytics of bulk complexes and complexes incorporated into zeolite hosts were carried out under ambient conditions. The analytics of iron exchanged zeolites was carried out under strictly inert conditions. All zeolite samples were dried *in vacuo* before measurement if not stated otherwise. All solvents were purified as described in the literature and distilled under argon.^[158] This was not the case for H₂O and the described HCl solutions. H₂O was consequently taken from the same source and was degassed for several hours with argon prior to use. The HCl solutions were used as received since proper degassing is not possible. All the commercially available ligands were dried before usage. All raw zeolites were washed before use several times with deionized water to remove impurities and were dried at air. Before all preparations the raw zeolites were degassed several times and heated under vacuum to ensure that the interzeolitic channels are unclogged and accessible. All toxic materials were disposed of in accordance with “*Prudent Practices in the laboratory*”.^[159]

The following substances used during this work have been purchased and were used as received if not stated otherwise in the previous or in the synthesis section:

2,2'-bipyridine	99+%	Acros
2,2'-dimethoxyethylamine	99%	Alfa Aesar
2,6-dibromopyridine	≥ 98%	TCI
2-acetylpyridine	99%	Sigma Aldrich
2-amino-4-methylpyridine	99%	Sigma Aldrich
2-amino-5-methylpyridine	99%	Alfa Aesar
2-amino-6-methylpyridine	99%	Alfa Aesar
2-bromo-3-methylpyridine	≥ 97%	TCI
2-bromo-5-methylpyridine	98+%	Alfa Aesar
2-bromopyridine	99%	Alfa Aesar
2-cyanopyridine	p.a.	Fluka

Experimental Section

2-cyanopyrimidine	99%	Acros
2-methoxyethyl ether	99%	Acros
4,4'-dimethyl-2,2'-bipyridine	98%	Alfa Aesar
5,5'-dimethyl-2,2'-bipyridine	98%	Alfa Aesar
Acetic acid	99.8%	Sigma Aldrich
Ammonium acetate	≥ 98%	Sigma Aldrich
Ammonium chloride	p.a.	Fluka
Calcium chloride	p.a.	Grüssing
Ethylendiaminetetraacetic acid	99%	Merck
Faujasite-type zeolite NaX	≥ 99%	Zeo-Tech
Faujasite-type zeolite NaX, 150 nm particles	≥ 99%	NanoScape
Faujasite-type zeolite NaY	≥ 99%	ZeoLyst
Faujasite-type zeolite NaY, 150 nm particles	≥ 99%	NanoScape
Iodine, pallets	99.50%	Acros
Iodomethane	99%	Alfa Aesar
Iron, fine powdered	98%	Merck
Lanthanum chloride	99%	Sigma Aldrich
Linde-type zeolite LTA, 100 nm particles	≥ 99%	NanoScape
Lithium(I) chloride, anhydrous	98+%	Alfa Aesar
Methacrolein	90%	Acros
Potassium	99.95%	Sigma Aldrich
Potassium carbonate	p.a.	VWR
Pyrazole	98%	Fluka
Pyridine	100%	VWR
Sodium methoxide	98%	Alfa Aesar
Sodium nitrite	98%	Alfa Aesar
Sodium sulfate	≥ 99%	Roth
Sulfuric acid	95% - 97%	Sigma Aldrich
Tert-butyllithium solution	1.7 M in pentane	Sigma Aldrich
Tetrakis(triphenylphosphine)palladium(0)	98%	Carbolution
Triethylamine	99%	Acros
Trifluoromethanesulfonic anhydride	98%	Carbolution
Zinc(II) chloride, anhydrous	99%	Grüssing

4.2.1 Synthesis of the iron(II) starting salts

Iron(II)chloride tetrahydrate: The synthesis of iron(II)bromide tetrahydrate is described in the literature.^[160] In the style of this was the synthesis of iron(II)chloride tetrahydrate done with several adjustments. 10.0 g ($n = 0.18$ mol) of elemental iron ($M = 55.845$ g/mol) are put into a three-necked round bottom flask. A reflux condenser is fitted on top and everything is set under inert conditions. A dropping funnel is installed during argon flow. It is filled with 100 ml of conc. aqueous HCl (37%). The solution is slowly trickled over the iron powder. After vapor deposition has stopped the white solution is stirred for three hours. The mixture is filtered and remaining parts washed several times with distilled water. The gained green solution is subjected to a cold distillation giving green crystals. The mixture is filtered and washed with cold ether. Drying *in vacuo* yields 17.9 g ($n = 0.09$ mol, 50%) of $\text{FeCl}_2 \cdot 4 \text{H}_2\text{O}$ ($M = 198.81$ g/mol). The substance can be transferred into the dehydrated form by heating it in an evacuation furnace for several days but is not necessary for further synthesis.

Iron(II)acetate dehydrate: Iron(II)acetate dihydrate was synthesized according to Weber *et al.*^[161] All of the amounts were multiplied 1.5 times.

4.2.2 Synthesis of mono- and di-methylated 2,2'-bipyridines

The synthesis of 4-, 5- and 6-methyl-2,2'-bipyridine is described by Smith *et al.* in the literature.^[162] Over time, it was modified largely to give better results, reduce the required steps and increase reliability. Additionally, it was found that unsymmetrical di-methylated 2,2'-bipyridines can be also synthesized using the general procedure what is so far not reported in the literature. Therefore is the synthesis for the mono- and di-methylated 2,2'-bipyridines given explicitly in the following. The position of the proton/methyl group is given as R (4, 5 or 6) respectively R' (4', 5' or 6'). It is most likely that also the position of the nitrogen at the pyridyl rings can be changed to a certain extent.

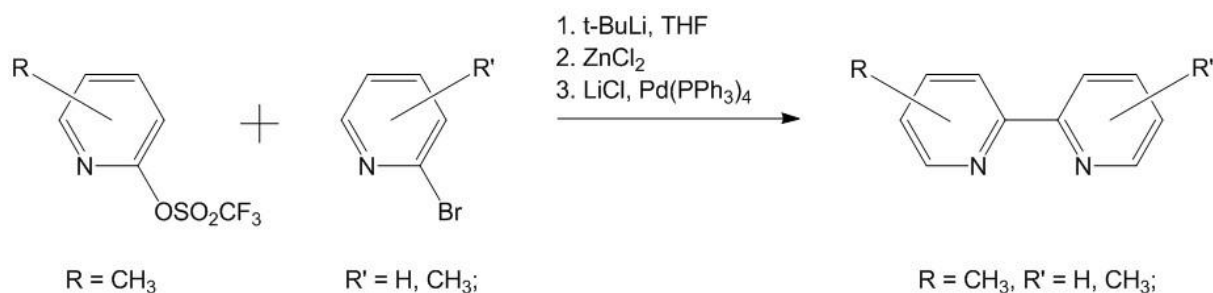
Synthesis of 2-hydroxy-R-methylpyridine: 200 mL of H_2O were put into a 500 mL, three-necked, round-bottom flask with an internal thermometer and magnetic stirrer. 55.0 g of

concentrated sulfuric acid (H_2SO_4 , 97%) are slowly added and the solution is cooled below $0\text{ }^\circ\text{C}$ by immersion in an acetone/ice bath. 25.0 g ($n = 231\text{ mmol}$) of the desired 2-amino-R-methylpyridine ($M = 108.14\text{ g/mol}$) are added. A solution of sodium nitrite is prepared by dissolving 20.5 g ($n = 297\text{ mmol}$) of sodium nitrite ($M = 68.99\text{ g/mol}$) in 50 mL H_2O . After complete dissolution of both batches the reaction mixture is infused slowly with the aqueous sodium nitrite solution. Thereby, the temperature was always kept below $0\text{ }^\circ\text{C}$ and the resulting mixture was stirred for 3 h at $0\text{ }^\circ\text{C}$. Subsequently it was left stirring overnight to come slowly to room temperature under vapor deposition. Afterwards a white-yellow solid precipitated which was found to be already the product. The solid was filtered off and washed with H_2O . Drying *in vacuo* yielded 2-hydroxy-R-methylpyridine ($M = 109.13\text{ g/mol}$) as a pale-brown powder ($m = 18.9\text{ g}$, $n = 173.3\text{ mmol}$, 75%; for 2-hydroxy-4-methylpyridine).

Synthesis of R-methyl-2-(trifluoromethanesulfonyl)oxypyridine: This powder was directly used for further synthesis and 5.5 g ($n = 50.4\text{ mmol}$) were filled into a 250 mL *Schlenk* flask that was degassed intensively. 150 mL of pyridine used as received were transferred into the flask via syringe. After complete dissolution was the reaction solution cooled to $-12\text{ }^\circ\text{C}$ by immersion in an acetone/ice bath. A rubber septum was installed through which an excess of 17.0 g ($n = 60.3\text{ mmol}$) trifluoromethanesulfonic anhydride ($M = 282.13\text{ g/mol}$) was added. The solution was stirred for 3 h at $0\text{ }^\circ\text{C}$ and was quenched with 150 mL of H_2O after having reached room temperature. The mixture was extracted with dichloromethane till the aqueous phase became colorless. The organic fraction was dried with anhydrous sodium sulfate and concentrated on a rotary evaporator. A column was prepared using silica gel deactivated in a mixture of 10% triethylamine in hexane and subsequent flushing with hexane. Flash chromatography was done once of the complete received substance with 10% ethylacetate and 90% hexane giving only the product R-methyl-2-(trifluoromethanesulfonyl)oxypyridine ($M = 241.18\text{ g/mol}$) as a yellow oil ($m = 11.4\text{ g}$, $n = 47.4\text{ mmol}$, 94%; for 4-methyl-2-(trifluoromethanesulfonyl)oxypyridine). $^1\text{H-NMR}$ (CDCl_3 , 300 MHz) δ : 2.44 (s, 3 H), 6.99 (s, 1 H), 7.19 (d, 1 H, $J = 5.1$), 8.24 (d, 1 H, $J = 5.1$);

Synthesis of R,R'-dimethyl-2,2'-bipyridine and R-methyl-2,2'-bipyridine: 120 mL of freshly distilled tetrahydrofuran in a three-necked, round-bottom flask are cooled to $-78\text{ }^\circ\text{C}$ via immersion in an acetone/dry ice bath. Subsequently, 50 mL of a 1.7 M solution of tert-

butyllithium ($n = 85$ mmol) in pentane are added. 43 mmol of the desired 2-bromo- R' -methylpyridine ($m = 7.4$ g, $M = 172.03$ g/mol) or 2-bromopyridine ($m = 6.8$ g, $M = 158.00$ g/mol) were added slowly through the argon flow in order to keep the temperature at -78 °C. After 90 min at -78 °C, the immersion bath was removed and 12.3 g ($n = 90$ mmol) of freshly dried and degassed zinc chloride ($M = 136.29$ g/mol) added through the argon flow. After 3 h at room temperature 9.6 g ($n = 40$ mmol) R -Methyl-2-(trifluoromethanesulfonyl)oxypyridine ($M = 241.18$ g/mol), anhydrous lithium chloride ($m = 3.18$ g, $n = 75$ mmol) and 2.5 g ($n = 2.1$ mmol) of degassed tetrakis(triphenylphosphine)palladium(0) ($M = 1155.59$ g/mol) are added. The mixture was heated for a short time without reflux to remove pentane from the solution till the reaction temperature reached at least 70 °C. Further THF was added if necessary. Thereafter, the reaction mixture was heated to reflux for 30 h and then cooled to room temperature. 60 g ($n = 161$ mmol) EDTA in 500 mL H₂O are added and the pH adjusted to pH 8 with a sodium bicarbonate solution. The solution was stirred for 30 min and then extracted with dichloromethane till the aqueous phase became colorless. The organic fraction was dried with anhydrous sodium sulfate and concentrated on a rotary evaporator. A column was prepared using silica gel deactivated in a mixture of 10% triethylamine in hexane and subsequent flushing with hexane. Flash chromatography was done once of the complete received mixture with 10% ethylacetate and 90% hexane to remove the pre fraction and the remaining catalyst. 10% ethylacetate and 90% hexane were used again to separate in the mixed fraction R -methyl-2-(trifluoromethanesulfonyl)oxypyridine from the product R -methyl-2,2'-bipyridine ($M = 170.21$ g/mol) respectively R,R' -dimethyl-2,2'-bipyridine ($M = 184.24$ g/mol) that was received as a yellow oil. The general reaction procedure is displayed in the following scheme and the yielded products together with their analysis are given after it.



Scheme 23. Synthesis of mono- and dimethylated 2,2'-bipyridines via *Negishi-Coupling*.

4-methyl-2,2'-bipyridine: $m = 5.6$ g, $n = 33$ mmol, 83%; MS [DEI(+), 70 eV]: $m/z = 170.0$ [4mBpy]⁺. 4-methyl-2,2'-bipyridine ($M = 170.22$ g/mol): C₁₁H₁₀N₂ calcd. C 77.62, H 5.92, N 16.46; found C 78.13, H 6.00, N 17.23; ¹H-NMR (CDCl₃, 300 MHz) δ : 2.49 (s, 3 H), 7.24 (d, 1 H, $J = 6.0$), 7.34 (t, 1 H, $J = 5.1$), 7.87 (m, 1 H, $J = 7.5$), 8.32 (s, 1 H), 8.52 (d, 1 H, $J = 7.5$), 8.59 (d, 1 H, $J = 4.2$), 8.70 (s, 1 H);

5-methyl-2,2'-bipyridine: $m = 3.1$ g, $n = 18$ mmol, 45%; MS [DEI(+), 70 eV]: $m/z = 170.0$ [5mBpy]⁺. 5-methyl-2,2'-bipyridine ($M = 170.22$ g/mol): C₁₁H₁₀N₂ calcd. C 77.62, H 5.92, N 16.46; found C 77.87, H 6.21, N 16.72; ¹H-NMR (CDCl₃, 300 MHz) δ : 2.42 (s, 3 H), 7.33 (t, 1 H, $J = 5.4$), 7.69 (d, 1 H, $J = 7.8$), 7.85 (t, 1 H, $J = 7.5$), 8.36 (d, 1 H, $J = 7.8$), 8.44 (d, 1 H, $J = 7.5$), 8.54 (s, 1 H), 8.69 (d, 1 H, $J = 4.5$);

6-methyl-2,2'-bipyridine: $m = 3.3$ g, $n = 19$ mmol, 48%; MS [DEI(+), 70 eV]: $m/z = 170.0$ [6mBpy]⁺. 6-methyl-2,2'-bipyridine ($M = 170.22$ g/mol): C₁₁H₁₀N₂ calcd. C 77.62, H 5.92, N 16.46; found C 76.94, H 5.98, N 15.99; ¹H-NMR (CDCl₃, 300 MHz) δ : 2.70 (s, 3 H), 7.25 (t, 1 H, $J = 7.5$), 7.38 (t, 1 H, $J = 5.4$), 7.78 (t, 1 H, $J = 7.8$), 7.91 (t, 1 H, $J = 7.8$), 8.30 (d, 1 H, $J = 7.8$), 8.55 (d, 1 H, $J = 8.1$), 8.72 (d, 1 H, $J = 4.5$); ¹³C-NMR (CDCl₃, 75 MHz) δ : 24.3, 109.9, 110.0, 118.9, 122.0, 123.9, 124.0, 137.9, 138.0, 158.0, 171.2;

3,6'-methyl-2,2'-bipyridine: $m = 1.7$ g, $n = 9$ mmol, 23%; MS [DEI(+), 70 eV]: $m/z = 184.1$ [36mBpy]⁺. 3,6'-dimethyl-2,2'-bipyridine ($M = 184.10$ g/mol): C₁₂H₁₂N₂ calcd. C 78.23, H 6.57, N 15.21; found C 79.01, H 6.21, N 15.84;

5,6'-methyl-2,2'-bipyridine: $m = 3.3$ g, $n = 18$ mmol, 45%; MS [DEI(+), 70 eV]: $m/z = 184.1$ [56mBpy]⁺. 5,6'-dimethyl-2,2'-bipyridine ($M = 184.10$ g/mol): C₁₂H₁₂N₂ calcd. C 78.23, H 6.57, N 15.21; found C 78.03, H 6.61, N 14.89; ¹H-NMR (CDCl₃, 300 MHz) δ : 2.02 (s, 3 H), 2.32 (s, 3 H), 7.16 (t, 1 H, $J = 5.0$), 7.19 (d, 1 H, $J = 4.9$), 7.48 (d, 2 H, $J = 7.7$), 8.39 (d, 1 H, $J = 4.6$), 8.43 (s, 1 H);

4.2.3 Alternative synthesis of 5-methyl-2,2'-bipyridine

1-(2-pyridylacetyl)pyridinium iodide was synthesized via the 1-phenacylpyridinium iodide synthesis of King *et al.*^[163] 25.4 g ($n = 0.1$ mol) of iodine were dissolved in 50 mL of pyridine and stirred for 30 min at room temperature. 12.0 g ($n = 0.1$ mol) 2-acetylpyridine were added and the mixture was refluxed for 30 min and left stirring for 24 h. The pyridine was removed

to dryness on a rotary evaporator. The remaining residue was suspended in H₂O to separate the 1-(2-pyridylacetyl)pyridinium iodide from the pyridine hydroiodide which is water soluble. After filtering and drying *in vacuo* 1-(2-pyridylacetyl)pyridinium iodide was received as a black powder.

5-methyl-2,2'-bipyridine: The synthesis from 1-(2-pyridylacetyl)pyridinium iodide was done via the procedure of Polin *et al.*^[164] No further column chromatography and just filtering was necessary to receive the product 5-methyl-2,2'-bipyridine ($m = 8.00$ g, $n = 47$ mmol, 90%) as yellow oil. Analysis gave the following results: MS [DEI(+), 70 eV]: $m/z = 170.0$ [5mBpy]⁺. 5-methyl-2,2'-bipyridine ($M = 170.22$ g/mol): C₁₁H₁₀N₂ calcd. C 77.62, H 5.92, N 16.46; found C 77.87, H 6.21, N 16.72; ¹H-NMR (CDCl₃, 300 MHz) δ : 2.42 (s, 3 H), 7.33 (t, 1 H, $J = 5.4$), 7.69 (d, 1 H, $J = 7.8$), 7.85 (t, 1 H, $J = 7.5$), 8.36 (d, 1 H, $J = 7.8$), 8.44 (d, 1 H, $J = 7.5$), 8.54 (s, 1 H), 8.69 (d, 1 H, $J = 4.5$);

4.2.4 Synthesis of pyrazolyl and imidazolyl ligands

Synthesis of 2,6-di(1H-pyrazol-1-yl)pyridine: The 2,6-di(1H-pyrazol-1-yl)pyridine ligand was synthesized according to the literature of Jameson *et al.*^[165] Analysis gave the following results: MS [DEI(+), 70 eV]: $m/z = 211.1$ [L]⁺. 2,6-di(1H-pyrazol-1-yl)pyridine ($M = 211.23$ g/mol): C₁₁H₉N₅ calcd. C 62.55, H 4.29, N 33.16; found C 64.00, H 4.50, N 31.66; The ¹H-NMR data were identical to the literature data.^[165]

Synthesis of 2,6-di(1H-pyrazol-3-yl)pyridine: The 2,6-di(1H-pyrazol-3-yl)pyridine ligand was synthesized according to literature of Sugiyarto *et al.*^[166] Analysis gave following results: MS [DEI(+), 70 eV]: $m/z = 211.1$ [L]⁺. 2,6-di(1H-pyrazol-3-yl)pyridine ($M = 211.23$ g/mol): C₁₁H₉N₅ calcd. C 62.55, H 4.29, N 33.16; found C 64.23, H 4.89, N 31.00; ¹H-NMR (CDCl₃, 300 MHz) δ : 6.51 (s, 2 H), 7.77 (s, 2 H), 7.86 (d, 2 H, $J = 7.0$), 7.96 (m, 1 H, $J = 6.6$), 8.58 (d, 2 H, $J = 2.4$);

Synthesis of 2-(1*H*-imidazol-2-yl)pyridine: 2-(1*H*-imidazol-2-yl)pyridine was synthesized according to the literature of Voss *et al.*^[167] Analysis gave the following results: MS [DEI(+), 70 eV]: $m/z = 145.2$ [L]⁺. 2-(1*H*-imidazol-2-yl)pyridine ($M = 145.17$ g/mol): C₈H₇N₃ calcd. C 66.19, H 4.86, N 28.95; found C 66.02, H 5.00, N 26.98; ¹H-NMR (DMSO-*d*₆, 300 MHz) δ : 7.06 (s, 1 H), 7.21 (s, 1 H), 7.35 (t, 1 H, $J = 5.6$), 7.76 (t, 1 H, $J = 4.3$), 8.04 (m, 1 H), 8.77 (d, 1 H, $J = 4.3$), 12.74 (s, 1 H);

Synthesis of 2-(1*H*-imidazol-2-yl)pyrimidine: 2-(1*H*-imidazol-2-yl)pyrimidine was synthesized according to the literature of Voss *et al.*^[167] Analysis gave the following parameters: MS [DEI(+), 70 eV]: $m/z = 146.2$ [L]⁺. 2-(1*H*-imidazol-2-yl)pyrimidine ($M = 146.15$ g/mol): C₇H₆N₄ calcd. C 57.53, H 4.14, N 38.34; found C 58.72, H 3.98, N 39.23; ¹H-NMR (DMSO-*d*₆, 300 MHz) δ : 7.21 (s, 2 H), 7.43 (t, 1 H, $J = 4.8$), 8.86 (d, 2 H, $J = 4.8$), 12.98 (s, 1 H);

Synthesis of the 2-(1-methyl-1*H*-imidazol-2-yl)pyrimidine: 2-(1-methyl-1*H*-imidazol-2-yl)pyrimidine was synthesized in the style of the general imidazole methylation in the literature of Vlasova *et al.*^[168] 5.0 g ($n = 43$ mmol) of 2-(1*H*-imidazol-2-yl)pyrimidine ($M = 146.15$ g/mol) were dissolved in 50 mL of acetone and an excess of powdered KOH ($m = 2.8$ g, $n = 50$ mmol) was added. The mixture was cooled to 0 °C with an ice bath. During vigorous stirring 6.4 g ($n = 45$ mmol) methyl iodide ($M = 141.94$ g/mol) were added slowly under retention of the initial temperature. The solution was stirred for 5 h at 0 °C and was allowed to warm up till room temperature. Acetone was evaporated and the remaining residue was extracted with CHCl₃ which was dried and evaporated on a rotary evaporator. It wasn't necessary to do column chromatography since both possible isomers are identical due to the position of the imidazole nitrogens. 2-(1*H*-imidazol-2-yl)pyrimidine ($M = 160.18$ g/mol) remained as brown solid (5.1 g, 32 mmol, 75%). Analysis gave following results: MS [DEI(+), 70 eV]: $m/z = 159.9$ [L]⁺. 2-(1-methyl-1*H*-imidazol-2-yl)pyrimidine ($M = 160.18$ g/mol): C₈H₈N₄ calcd. C 59.99, H 5.03, N 34.98; found C 61.20, H 4.98, N 35.43; ¹H-NMR (DMSO-*d*₆, 300 MHz) δ : 4.04 (s, 3 H), 6.91 (s, 1 H), 7.05 (s, 1 H), 7.14 (t, 1 H, $J = 5.4$), 7.67 (t, 1 H, $J = 7.8$), 8.09 (d, 1 H, $J = 8.0$), 8.51 (d, 1 H, $J = 4.3$);

4.2.5 Synthesis of the iron(II) chloride complexes

Initially it should be mentioned that to the best of my knowledge all described chloride salts except $\text{Fe}(\text{Bpy})_3\text{Cl}_2$ are not described in the literature so far.^[116-120] The iron(II) cations tris(3,6'-dimethyl-2,2'-bipyridine)iron(II) chloride, tris(5,6'-dimethyl-2,2'-bipyridine)iron(II) chloride, tris(2-(1*H*-imidazol-2-yl)pyrimidine)iron(II) chloride and tris(2-(1-methyl-1*H*-imidazol-2-yl)pyrimidine)iron(II) chloride are completely unknown.

Synthesis of $\text{Fe}(\text{Bpy})_3\text{Cl}_2$: The complex was synthesized using standard procedures. The product was found to be associated with two water molecules. MS [DEI(+), 70 eV]: $m/z = 156.07$ $[\text{Bpy}]^+$. $\text{Fe}(\text{Bpy})_3\text{Cl}_2 \cdot 2 \text{H}_2\text{O}$ (631.34): $\text{C}_{30}\text{H}_{28}\text{Cl}_2\text{FeO}_2\text{N}_6$ calcd. C 56.89, H 4.77, N 13.27; found C 56.05, H 4.74, N 12.95; $^1\text{H-NMR}$ (D_2O , 300 MHz) δ : 7.38 (t, 6 H, $J = 6.6$), 7.52 (d, 6 H, $J = 5.1$), 8.11 (t, 6 H, $J = 7.5$), 8.57 (d, 6 H, $J = 8.1$);

Synthesis of $\text{Fe}(\text{4mBpy})_3\text{Cl}_2$: All steps in this synthesis were carried out using *Schlenk* tube techniques and argon as inert gas. 565 mg of $\text{FeCl}_2 \cdot 4 \text{H}_2\text{O}$ ($M = 198.81$ g/mol, $n = 2.84$ mmol) were used as starting material and were put in a 25 mL flask. 3.1 equivalents of 4-methyl-2,2'-bipyridine ($M = 170.21$ g/mol, $m = 1500$ mg, $n = 8.81$ mmol) were added. The mixture was subsequently dissolved in 20 mL of dry MeOH and boiled under reflux conditions for 1 h. After cooling to room temperature the solution was reduced and left in the fridge for some days. After one week the solid was isolated via filtering with a filter drain (porosity 4). The resulting dark red powder was dried *in vacuo*. The product was found to be associated with one H_2O and one MeOH molecule. MS [DEI(+), 70 eV]: $m/z = 170.0$ $[\text{4mBpy}]^+$. $\text{Fe}(\text{4mBpy})_3\text{Cl}_2 \cdot \text{H}_2\text{O} \cdot \text{MeOH}$ (689.46): $\text{C}_{34}\text{H}_{38}\text{Cl}_2\text{FeO}_2\text{N}_6$ calcd. C 59.23, H 5.56, N 12.19; found C 59.61, H 6.11, N 11.63; $^1\text{H-NMR}$ (D_2O , 300 MHz) δ : 2.51 (s, 9 H), 7.19 (t, 3 H, $J = 5.7$), 7.27 (t, 3 H, $J = 6.3$), 7.33 (t, 3 H, $J = 6.6$), 7.48 (t, 3 H, $J = 5.7$), 8.04 (t, 3 H, $J = 7.5$), 8.40 (s, 3 H), 8.48 (d, 3 H, $J = 8.1$);

Synthesis of $\text{Fe}(\text{44mBpy})_3\text{Cl}_2$: All steps in this synthesis were carried out using *Schlenk* tube techniques and argon as inert gas. 1500 mg of $\text{FeCl}_2 \cdot 4 \text{H}_2\text{O}$ ($M = 198.81$ g/mol, $n = 7.55$ mmol) were used as starting material and were put in a 50 mL flask. 3.1 equivalents of 4,4'-dimethyl-2,2'-bipyridine ($M = 184.24$ g/mol, $m = 4310$ mg, $n = 23.41$ mmol) were

added. The mixture was subsequently dissolved in 20 mL of dry MeOH and boiled under reflux conditions for 1 h. After cooling to room temperature the solution was reduced and left in the fridge for several days. After one week the solid was isolated via filtering with a filter drain (porosity 4). The resulting dark red powder was dried *in vacuo*. The product was found to be associated with one water molecule and two MeOH molecules. MS [DEI(+), 70 eV]: $m/z = 184.1$ [44mBpy]⁺. Fe(44mBpy)₃Cl₂ · H₂O · 2 MeOH (763.59): C₃₈H₄₆Cl₂FeO₃N₆ calcd. C 59.77, H 6.34, N 11.01; found C 60.12, H 6.45, N 10.30; ¹H-NMR (D₂O, 300 MHz) δ: 2.51 (s, 18 H), 7.17 (d, 6 H, *J* = 5.7), 7.27 (d, 6 H, *J* = 5.7), 8.35 (s, 6 H);

Synthesis of Fe(5mBpy)₃Cl₂: All steps in this synthesis were carried out using Schlenk tube techniques and argon as inert gas. 754 mg of FeCl₂ · 4 H₂O (*M* = 198.81 g/mol, *n* = 3.79 mmol) were used as starting material and were put in a 25 mL flask. 3.1 equivalents of 5-methyl-2,2'-bipyridine (*M* = 170.21 g/mol, *m* = 2000 mg, *n* = 11.75 mmol) were added. The mixture was subsequently dissolved in 20 mL of dry MeOH and boiled under reflux conditions for 1 h. After cooling to room temperature the solution was reduced and left in the fridge for some days. After one week the solid was isolated via filtering with a filter drain (porosity 4). The resulting dark red powder was dried *in vacuo*. The product was found to be associated with two water molecules. MS [DEI(+), 70 eV]: $m/z = 170.0$ [5mBpy]⁺. Fe(5mBpy)₃Cl₂ · 2 H₂O (675.44): C₃₃H₃₆Cl₂FeO₂N₆ calcd. C 58.68, H 5.37, N 12.44; found C 59.13, H 6.65, N 12.29; ¹H-NMR (D₂O, 300 MHz) δ: 2.13 (s, 9 H), 7.21 (d, 3 H, *J* = 6.6) 7.28 (t, 3 H, *J* = 6.6), 7.42 (t, 3 H, *J* = 6.0), 7.89 (d, 3 H, *J* = 5.7), 8.04 (t, 3 H, *J* = 6.9), 8.39 (m, 3 H, *J* = 6.6), 8.44 (m, 3 H, *J* = 7.8);

Synthesis of Fe(55mBpy)₃Cl₂: All steps in this synthesis were carried out using *Schlenk* tube techniques and argon as inert gas. 1500 mg of FeCl₂ · 4 H₂O (*M* = 198.81 g/mol, *n* = 7.55 mmol) were used as starting material and were put in a 50 mL flask. 3.1 equivalents of 5,5'-dimethyl-2,2'-bipyridine (*M* = 184.24 g/mol, *m* = 4310 mg, *n* = 23.41 mmol) were added. The mixture was subsequently dissolved in 20 mL of dry MeOH and boiled under reflux conditions for 1 h. After cooling to room temperature the solution was reduced and left in the fridge for several days. After one week the solid was isolated via filtering with a filter drain (porosity 4). The resulting dark red powder was dried *in vacuo*. The product was found to be associated with two water molecules. MS [DEI(+), 70 eV]: $m/z = 184.1$ [55mBpy]⁺.

$\text{Fe}(\text{55mBpy})_3\text{Cl}_2 \cdot 2 \text{H}_2\text{O}$ (717.52): $\text{C}_{36}\text{H}_{42}\text{Cl}_2\text{FeO}_2\text{N}_6$ calcd. C 60.26, H 5.90, N 11.71; found C 59.16, H 6.00, N 11.55; $^1\text{H-NMR}$ (D_2O , 300 MHz) δ : 2.16 (s, 18 H), 7.20 (s, 6 H), 7.90 (d, 6 H, $J = 8.1$), 8.37 (d, 6 H, $J = 8.4$);

Synthesis of $\text{Fe}(\text{Bpp})_2\text{Cl}_2$: All steps in this synthesis were carried out using Schlenk tube techniques and argon as inert gas. 1.5 g of $\text{FeCl}_2 \cdot 4 \text{H}_2\text{O}$ ($M = 198.81 \text{ g/mol}$, $n = 7.55 \text{ mmol}$) were used as starting material and were put in a 50 mL flask. 2.1 equivalents of 2,6-di(1*H*-pyrazol-3-yl)pyridine ($M = 211.23 \text{ g/mol}$, $m = 3.35 \text{ g}$, $n = 15.86 \text{ mmol}$) were added. The mixture was subsequently dissolved in 20 mL of dry MeOH and boiled under reflux conditions for 1 h. After cooling to room temperature the MeOH was evaporated since the chloride salts of this complex don't precipitate from solution. The remaining brown-orange powder was washed with 5 x 20 mL of toluene in which ligand excess is soluble. The product was isolated via filtering on a filter drain (porosity 4) and was dried finally *in vacuo*. The resulting brown orange product was found to be associated with two water molecules. MS [DEI(+), 70 eV]: $m/z = 211.09$ [Bpp] $^+$. $\text{Fe}(\text{Bpp})_3\text{Cl}_2 \cdot 2 \text{H}_2\text{O}$ (585.23): $\text{C}_{22}\text{H}_{22}\text{Cl}_2\text{FeO}_2\text{N}_{10}$ calcd. C 56.89, H 4.77, N 13.27; found C 56.05, H 4.74, N 12.95;

Further synthesized complexes: Following complexes have been also synthesized via the precedingly described synthetic procedures. The synthesis is not described explicitly since the complexes could not be used for further experiments. $^1\text{H-NMR}$ measurements could not be conducted since all systems are partially or fully paramagnetic. They were found to have the analytical composition as follows.

Tris(6-methyl-2,2'-bipyridine)iron(II) chloride: MS [DEI(+), 70 eV]: $m/z = 170.1$ [6mBpy] $^+$. $\text{Fe}(\text{6mBpy})_3\text{Cl}_2 \cdot 3 \text{H}_2\text{O}$ (693.45): $\text{C}_{33}\text{H}_{38}\text{Cl}_2\text{FeO}_3\text{N}_6$ calcd. C 57.16, H 5.52, N 12.12; found C 56.83, H 5.09, N 12.16;

Tris(3,6'-methyl-2,2'-bipyridine)iron(II) chloride: MS [DEI(+), 70 eV]: $m/z = 184.1$ [36mBpy] $^+$. $\text{Fe}(\text{36mBpy})_3\text{Cl}_2 \cdot \text{H}_2\text{O} \cdot \text{MeOH}$ (731.54): $\text{C}_{37}\text{H}_{44}\text{Cl}_2\text{FeO}_2\text{N}_6$ calcd. C 60.75, H 6.06, N 11.49; found C 61.23, H 6.37, N 11.11;

Tris(5,6'-methyl-2,2'-bipyridine)iron(II) chloride: MS [DEI(+), 70 eV]: $m/z = 184.1$ [56mBpy]⁺. Fe(56mBpy)₃Cl₂ · H₂O · 2 MeOH (763.59): C₃₈H₄₈Cl₂FeO₆N₆ calcd. C 59.77, H 6.34, N 11.01; found C 59.31, H 6.12, N 11.34;

Bis(2,6-di(1*H*-pyrazol-1-yl)pyridine)iron(II) chloride: MS [DEI(+), 70 eV]: $m/z = 211.1$ [L]⁺. Bis(2,6-di(1*H*-pyrazol-1-yl)pyridine)iron(II) chloride (551.22): C₂₂H₂₀Cl₂FeN₁₀ calcd. C 47.94, H 3.66, N 25.41; found C 48.11, H 3.74, N 24.98;

Tris(2-(1*H*-imidazol-2-yl)pyridine)iron(II) chloride: MS [DEI(+), 70 eV]: $m/z = 145.1$ [L]⁺. Tris(2-(1*H*-imidazol-2-yl)pyridine)iron(II) chloride · 2 H₂O (600.29): C₂₄H₂₇Cl₂FeO₂N₉ calcd. C 48.02, H 4.53, N 21.00; found C 48.55, H 4.74, N 20.60;

Tris(2-(1*H*-imidazol-2-yl)pyrimidine)iron(II) chloride: MS [DEI(+), 70 eV]: $m/z = 146.1$ [L]⁺. Tris(2-(1*H*-imidazol-2-yl)pyrimidine)iron(II) chloride · 2 H₂O (603.25): C₂₁H₂₄Cl₂FeO₂N₁₂ calcd. C 41.81, H 4.01, N 27.86; found C 42.21, H 4.11, N 27.47;

Tris(2-(1-methyl-1*H*-imidazol-2-yl)pyrimidine)iron(II) chloride: MS [DEI(+), 70 eV]: $m/z = 160.1$ [L]⁺. Tris(2-(1-methyl-1*H*-imidazol-2-yl)pyrimidine)iron(II) chloride · 2 MeOH (673.39): C₂₆H₃₄Cl₂FeO₂N₁₂ calcd. C 46.38, H 5.09, N 24.96; found C 46.77, H 5.00, N 25.29;

4.2.6 Preparation of cation exchanged zeolites

Preparation of lanthanum-blocked NaY (LaNaY): A 0.1 M solution of lanthanum(III) chloride was produced by adding 3.714 g ($n = 0.01$ mmol) of the heptahydrated salt ($M = 371.37$ g/mol) to 100 mL of water. 5.0 g of NaY were suspended in it and the mixture was stirred for 24 h. Subsequent filtering and excessive washing with H₂O on air yielded a clear white powder. The complete procedure was repeated once. The powder was calcined at 450 °C for 72 h at air. Subsequently a saturated solution of NaCl was prepared by adding the

salt into water till the maximum solubility was reached and solid remained at the ground of the beaker. The supernatant fluid was decanted and poured in a separate beaker. The La-blocked zeolite was positioned on a filter drain and washed with 1.0 L of the saturated saline solution. Final washing with 1.0 L of distilled water yields a clear colorless powder with inaccessible sodalite cages that was dried on air.

Preparation of CaY, KY and NH₄Y: For every ion exchanged product 7.0 g of NaY were washed, dried and put into a flask. Saturated saline solutions were produced from CaCl₂, NH₄Cl, K₂CO₃. The zeolite was suspended in the saline solutions and stirred for 24 h. Subsequent filtering and washing yielded a white powder. The procedure was repeated four times.

4.2.7 Preparation of iron exchanged nanosized zeolites

Preparation of nanosized Fe@NaA: 400.0 mg (ambient conditions) of nanosized NaA were put into a 50 mL round bottom flask and where degassed up to ten times. Three different batches were prepared. To each of those batches 2 wt% (7.9 mg), 5 wt% (20.2 mg) and 10 wt% (40.8 mg) of FeCl₂ · 4 H₂O ($M = 198.81$ g/mol) were added a time. The flasks were again degassed and 5 mL of H₂O were carefully added via syringe. The solutions were stirred for 24 h at room temperature to reach an exchange equilibrium. Subsequent filtering over a filter drain (porosity 4) yielded a clean white powder that was washed excessively with freshly degassed H₂O and was then dried *in vacuo*. Filtering was possible due to strong agglomeration. The resulting iron contents were determined as 0.68 wt% (2 wt%), 1.06 wt% (5 wt%) and 2.67 wt% (10 wt%).

Preparation of nanosized Fe@NaX: 300.0 mg (ambient conditions) of nanosized NaX were put into a 25 mL round bottom flask and where degassed up to ten times. Three different batches were prepared. To each of those batches 2 wt% (6.1 mg), 5 wt% (15.1 mg) and 10 wt% (30.5 mg) of FeCl₂ · 4 H₂O ($M = 198.81$ g/mol) were added a time. The flasks were again degassed and 5 mL of H₂O were carefully added via syringe. The solutions were stirred for 24 h at room temperature to reach an exchange equilibrium. Subsequent filtering over a

filter drain (porosity 4) yielded a clean white powder that was washed excessively with freshly degassed H₂O and was then dried *in vacuo*. Filtering was possible due to strong particle agglomeration. The resulting iron contents were determined as 0.89 wt% (2 wt%), 1.80 wt% (5 wt%) and 3.38 wt% (10 wt%).

Preparation of nanosized Fe@NaY: 300.0 mg (ambient conditions) of nanosized NaY were put into a 25 mL round bottom flask and were degassed up to ten times. Three different batches were prepared. To each of those batches 2 wt% (6.1 mg), 5 wt% (15.1 mg) and 10 wt% (30.5 mg) of FeCl₂ · 4 H₂O (*M* = 198.81 g/mol) were added a time. The flasks were again degassed and 5 mL of H₂O were carefully added via syringe. The solutions were stirred for 24 h at room temperature to reach an exchange equilibrium. Subsequent filtering over a filter drain (porosity 4) yielded a clean white powder that was washed excessively with freshly degassed H₂O and was then dried *in vacuo*. Filtering was possible due to strong particle agglomeration. The resulting iron contents were determined as 0.76 wt% (2 wt %), 2.01 wt% (5 wt %) and 3.66 wt% (10 wt%).

4.2.8 Impregnation of zeolites with iron(II) complexes

Preparation of Fe(Bpy)₃@Y: 1.0 g of excessively washed NaY is dried on air and subsequently heated under argon and vacuum several times with a heat gun to remove water. Another flask is prepared with 0.051 g (*n* = 0.26 mmol) of iron(II)chloride tetrahydrate, 0.44 g (*n* = 2.8 mmol) of 2,2'-bipyridine and 50 mL distilled MeOH. The red solution is transferred into the flask with the zeolite and the suspension was stirred for 2 h. Subsequent filtering (pore 4) and washing with 100 mL of toluene yields 0.9 g of a pink powder which is dried *in vacuo*; The synthesis was done in a similar way for CaY, KY and NH₄Y. The resulting analysis is given in the following table; yield: *m* = 0.9 g.

Table 29. Composition of impregnated Fe(Bpy)₃@Y samples.

	Fe [wt%]	N [wt%]	C [wt%]	H [wt%]
Fe(Bpy) ₃ @NaY	0.13	0.26	12.31	3.05
Fe(Bpy) ₃ @NaY	0.14	0.23	10.45	2.50
Fe(Bpy) ₃ @CaY	0.09	0.94	12.88	2.20
Fe(Bpy) ₃ @KY	0.08	0.14	9.53	2.15
Fe(Bpy) ₃ @NH ₄ Y	0.07	3.66	10.66	3.06

Preparation of Fe(Bpp)₂@NaY: 1.0 g of excessively washed NaY is dried on air and subsequently heated under argon and vacuum several times with a heat gun to remove water. Another flask is prepared with 0.051 g ($n = 0.26$ mmol) of iron(II)chloride tetrahydrate, 0.36 g ($n = 1.7$ mmol) of 2,6-bis(1*H*-pyrazol-3-yl)pyridine and 50 mL distilled MeOH. The orange-brownish solution is transferred into the flask with the zeolite. The suspension was stirred for 4 h. Subsequent filtering (pore 4) and washing with 100 mL of toluene yields 0.9 g of a yellow powder which is dried *in vacuo*; yield: $m = 0.9$ g; 0.36 wt% Fe, 0.97 wt% N, 9.11 wt% C, 2.61 wt% H.

4.2.9 Impregnation of nanosized zeolites with iron(II) complexes

Preparation of nanosized Fe(Bpy)₃@NaX and Fe(Bpy)₃@NaY: 500.0 mg (ambient conditions) of nanosized NaX respectively nanosized NaY were put into a 25 mL round bottom flask and where degassed up to ten times to unclog the interzeolitic channels. 200.0 mg of Fe(Bpy)₃Cl₂ ($M = 524.4$ g/mol) were added and the mixture was again degassed. 8.0 mL of MeOH were poured in and the suspension was stirred at room temperature for 7 days. Thereafter, the suspension was transferred into centrifuge tubes with conical bottom and was centrifuged at 1000 g for 30 min. The overlaying solution was decanted and the solid washed with H₂O to solubilize remaining bulk complex material. The centrifuge procedure was repeated until the overlaying solution was completely clear (around five times). The remaining hybrid material was dried *in vacuo* and yielded a reddish-pink powder (yield: $m = 450$ mg). Fe(Bpy)₃@NaX: 0.59 wt% Fe, Fe(Bpy)₃@NaY: 0.48 wt% Fe;

Preparation of nanosized Fe(44mBpy)₃@NaX and Fe(44mBpy)₃@NaY: 500.0 mg (ambient conditions) of nanosized NaX respectively nanosized NaY were put into a 25 mL round bottom flask and where degassed up to ten times to unclog the interzeolitic channels. 200.0 mg of Fe(44mBpy)₃Cl₂ ($M = 679.5$ g/mol) were added and the mixture was again degassed. 8.0 mL of MeOH were poured in and the suspension was stirred at room temperature for 7 days. Thereafter, the suspension was transferred into centrifuge tubes with conical bottom and was centrifuged at 1000 g for 30 min. The overlaying solution was decanted and the solid washed with H₂O to solubilize remaining bulk complex material. The centrifuge procedure was repeated until the overlaying solution was completely clear (around seven times). The remaining zeolite hybrid material was dried *in vacuo* and yielded a reddish-pink powder (yield: $m = 450$ mg). Fe(44mBpy)₃@NaX: 0.59 wt% Fe, Fe(44mBpy)₃@NaY: 0.50 wt% Fe;

Preparation of nanosized Fe(55mBpy)₃@NaX and Fe(55mBpy)₃@NaY: 500.0 mg (ambient conditions) of nanosized NaX respectively nanosized NaY were put into a 25 mL round bottom flask and where degassed up to ten times to unclog the interzeolitic channels. 200.0 mg of Fe(55mBpy)₃Cl₂ ($M = 679.5$ g/mol) were added and the mixture was again degassed. 8.0 mL of MeOH were poured in and the suspension was stirred at room temperature for 7 days. Thereafter, the suspension was transferred into centrifuge tubes with conical bottom and was centrifuged at 1000 g for 30 min. The overlaying solution was decanted and the solid washed with H₂O to solubilize remaining bulk complex material. The centrifuge procedure was repeated until the overlaying solution was completely clear (around five times). The remaining hybrid material was dried *in vacuo* and yielded a pink powder (yield: $m = 450$ mg). Fe(55mBpy)₃@NaX: 0.47 wt% Fe, Fe(55mBpy)₃@NaY: 0.39 wt% Fe;

Remark: It was neither possible to impregnate nanosized NaX nor nanosized NaY with homoleptic iron(II) complexes from 2,6-di(1*H*-pyrazol-1-yl)pyridine, 2,6-di(1*H*-pyrazol-3-yl)pyridine, 2-(1*H*-imidazol-2-yl)pyrimidine or 6-methyl-2,2'-bipyridine with the preceding description. All hybrids oxidized rapidly during or after the procedure mainly as a result of the centrifuge procedure which cannot be done under inert conditions. Nevertheless, are these mostly the complexes which were also found not to be suitable for pH-responsive experiments in aqueous solution.

5. References

- [1] B. Weber, *Koordinationschemie – Grundlagen und aktuelle Trends*, Springer-Verlag Berlin Heidelberg, **2014**.
- [2] B. Plietker, *Iron Catalysis in Organic Chemistry: Reactions and Applications*, Wiley-VCH Verlag GmbH Weinheim, **2008**.
- [3] L. Cambi, L. Szego, *Chem. Ber. Dtsch. Ges.* **1931**, 64, 2591.
- [4] A. Werner, *Z. Anorg. Chem.* **1893**, 3, 267-330.
- [5] L. H. Gade, *Koordinationschemie*, Wiley-VCH Verlag GmbH Weinheim, **1998**.
- [6] J. S. Griffith, L.E. Orgel, *Q. Rev. Chem. Soc.* **1957**, 11, 381-383.
- [7] P. L. Gaus, F. A. Cotton, G. Wilkinson, *Basic Inorganic Chemistry, International 2nd Revised Edition*, John Wiley & Sons Ltd. United Kingdom, **1987**.
- [8] P. Gülich, H. A. Goodwin, *Spin Crossover in Transition Metal Compounds I-III*, Springer-Verlag Berlin Heidelberg, **2004**.
- [9] M. A. Halcrow, *Spin-Crossover Materials: Properties and Applications*, John Wiley & Sons Ltd. United Kingdom, **2013**.
- [10] P. Gülich, A. B. Gaspar, Y. Garcia, *Beilstein J. Org. Chem.* **2013**, 9, 342-391.
- [11] A. Hauser, *J. Chem. Phys.* **1991**, 94, 4, 2741-2748.
- [12] G. Vankó, F. Renz, G. Molnár, T. Neisius, S. Kárpáti, *Angew. Chem. Int. Ed.* **2007**, 46, 5306-5309.
- [13] P. Gülich, *Top. Curr. Chem.* **2004**, 234, 231-260.
- [14] M. Dommaschk, V. Thoms, C. Schütt, C. Näther, R. Puttreddy, K. Rissanen, R. Herges, *Inorg. Chem.* **2015**, 54, 19, 9390-9392.
- [15] M. Dommaschk, F. Gutzeit, S. Boretius, R. Haag, R. Herges, *Chem. Commun.* **2014**, 50, 12467-12478.
- [16] C. J. Ballhausen, *Introduction to Ligand Field Theory*, McGraw-Hill Book Company New York, **1962**.
- [17] H. L. Schäfer, G. Gliemann, *Basic Principles of Ligand Field Theory*, John Wiley & Sons Ltd. United Kingdom, **1969**.
- [18] H. A. Jahn, E. Teller, *Proc. R. Soc. London Ser. A* **1937**, 161, 905, 220-235.
- [19] B. Weber, F. A. Walker, K. Karaghiosoff, *Z. Anorg. Allg. Chem.* **2013**, 639, 8-9, 1498-1503.
- [20] R. Herges, *Nachr. Chem.* **2011**, 59, 817-819.
- [21] J. Hasserodt, J. L. Kolanowski, F. Touti, *Angew. Chem. Int. Ed.* **2014**, 53, 60-73.
- [22] A. S. Merbach, L. Helm. É. Tóth, *The Chemistry of Contrast Agents in Medical Magnetic Resonance Imaging*, John Wiley & Sons Ltd. United Kingdom, **2013**.

References

- [23] P. G. Morris, *Nuclear Magnetic Resonance Imaging in Medicine and Biology*, Oxford Science Publications, Oxford University Press New York, **1986**.
- [24] E. M. Haacke, R. W. Brown, M. R. Thompson, R. Venkatesan, *Magnetic Resonance Imaging: Physical Principles and Sequence Design*, John Wiley & Sons Ltd. United Kingdom, **1999**.
- [25] P. E. Watson, I. D. Watson, R. D. Batt, *Am. J. Clin. Nutr.* **1980**, 33, 1, 27-39.
- [26] G. N. La Mar, W. D. Horrocks, R. H. Holm, *NMR of Paramagnetic Molecules: Principles and Applications*, Academic Press New York, **1973**.
- [27] C. F. Geraldès, S. Laurent, *Contrast Media Mol. Imaging* **2009**, 4, 1, 1-23.
- [28] P. C. Lauterbur, M. H. M. Dias, A. M. Rudin, *Augmentation of tissue water proton spin-lattice relaxation rates by in vivo addition of paramagnetic ions*; in: P. L. Dutton, J. S. Leigh, A. Scarpa, *Frontiers in Biological Energetics*, Academic Press, New York, **1978**, 1, 752-759.
- [29] I. Solomon, *Phys. Rev.* **1955**, 99, 559-566.
- [30] C. de Haën, *Top. Magn. Reson. Imaging* **2001**, 12, 4, 221-230.
- [31] a) P. H. Kuo, E. Kanal, A. K. Abu-Alfa, S. E. Cowper, *Radiology* **2007**, 242, 3, 647-649; b) H. S. Thomsen, *Radiol. Clin. North. Am.* **2009**, 47, 5, 827-831; c) A. K. Abu-Alfa, *Adv. Chronic Kidney Dis.* **2011**, 18, 3, 188-98.
- [32] S. Viswanathan, Z. Kovacs, K. N. Green, S. J. Ratnakar, A. D. Sherry, *Chem. Rev.* **2010**, 110, 5, 2960-3018.
- [33] a) M. Mikawa, T. Yokawa, N. Miwa, M. Brautigam, T. Akaike, A. Maruyama, *Acad. Radiol.* **2002**, 9, 109-111; b) C. S. Bonnet, É. Tóth, *Chimia* **2016**, 70, 1-2, 102-108; c) C. S. Bonnet, É. Tóth, *Am. J. Neuroradiol.* **2010**, 31, 401-409.
- [34] F. Touti, P. Maurin, J. Hasserodt, *Angew. Chem. Int. Ed.* **2013**, 52, 4654-4658.
- [35] R. Jastrzab, B. Tylkowski, *New-Generation Bioinorganic Complexes*, Kindle Edition, De Gruyter Berlin Boston, **2016**.
- [36] F. Hoppe-Seyler, *Med. Chem. Unt.* **1866**, 1, 133-140.
- [37] a) J. P. Collmann, R. R. Gagne, C. A. Reed, W. T. Robinson, G. A. Rodley, *Proc. Natl. Acad. Sci. U.S.A.* **1974**, 71, 4, 1326-1329; b) G. A. Rodley, W. T. Robinson, *Nature* **1972**, 235, 438-439.
- [38] L. Pauling, C. D. Coryell, *Proc. Natl. Acad. Sci. U.S.A.* **1936**, 22, 4, 210-216.
- [39] a) S. Ogawa, T. M. Lee, A. R. Kay, D. W. Tank, *Proc. Natl. Acad. Sci. U.S.A.* **1990**, 87, 9868-9872; b) N. K. Logothetis, J. Pauls, M. Augath, Torsten Trinath, A. Oeltermann, *Nature* **2001**, 412, 150-157.
- [40] S. A. Huettel, A. W. Song, G. McCarthy, *Functional Magnetic Resonance Imaging*, Oxford University Press, Sinauer Associates Inc. Sunderland, **2014**.
- [41] C. Janiak, T. G. Scharmann, T. Bräuniger, J. Holubová, M. Nádvorník, *Z. Anorg. Allg. Chem.* **1998**, 624, 769-774.
- [42] R. N. Muller, L. V. Elst, S. Laurent, *J. Am. Chem. Soc.* **2003**, 125, 8405-8407.
- [43] V. Stavila, M. Allali, L. Canaple, Y. Stortz, C. Franc, P. Maurin, O. Beuf, O. Dufay, J. Samarut, M. Janier, J. Hasserodt, *New. J. Chem.* **2008**, 32, 428-435.
-

References

- [44] E. L. Que, E. Gianolio, S. L. Baker, A. P. Wong, S. Aime, C. J. Chang, *J. Am. Chem. Soc.* **2009**, 131, 8527-8536.
- [45] **a)** S. Venkataramani, U. Jana, M. Dommaschk, F. D. Sönnichsen, F. Tuczek, R. Herges, *Science* **2011**, 331, 445-448; **b)** M. Dommaschk, C. Schütt, S. Venkataramani, U. Jana, C. Näther, F. D. Sönnichsen, R. Herges, *Dalton Trans.* **2014**, 43, 17395; **c)** M. Dommaschk, M. Peters, F. Gutzeit, C. Schütt, C. Näther, F. D. Sönnichsen, S. Tiwari, C. Riedel, S. Boretius, R. Herges, *J. Am. Chem. Soc.* **2015**, 137, 7552-7555.
- [46] F. Touti, P. Maurin, L. Canaple, O. Beuf, J. Hasserodt, *Inorg. Chem.* **2012**, 51, 31-33.
- [47] **a)** M.-F. Penet, K. Glunde, M. A. Jacobs, A. P. Pathak, Z. M. Bhujwalla, *J. Nucl. Med.* **2008**, 49, 5, 687-690; **b)** G. Liu, Y. Liu, V. R. Sheth, M. D. Pagel, *Mol. Imaging* **2012**, 11, 1, 47-57.
- [48] R. A. Gatenby, R. J. Gillies, *Nat. Rev. Cancer* **2004**, 4, 891-899.
- [49] O. Warburg, *Naturwissenschaften* **1924**, 12, 1131-1137.
- [50] **a)** S. Y. C. Choi, C. C. Collins, P. W. Gout, Y. Wang, *J. Pathol.* **2013**, 230, 4, 350-355; **b)** J. Munoz, K. Mohd, H. Amr, M. Stoltenberg, *J. Cancer Res. Ther.* **2011**, 7, 2, 201-202.
- [51] C. Rajadurai, M. Ruben, D. Kruk, EP2072062B1, **2012**.
- [52] I.-R. Jeon, J. G. Park, C. R. Haney, T. D. Harris, *Chem. Sci.* **2014**, 5, 2461-2465.
- [53] B. Wu, G. Warnock, M. Zaiss, C. Lin, M. Chen, Z. Zhou, L. Mu, D. Nanz, R. Tuura, G. Delso, *EJNMMI Physics* **2016**, 3, 19, 1-21.
- [54] F. Touti, A. K. Singh, P. Maurin, L. Canaple, O. Beuf, J. Samarut, J. Hasserodt, *J. Med. Chem.* **2011**, 54, 4274-4278.
- [55] M. Regueiro-Figueroa, G. A. Rolla, D. Esteban-Gómez, A. De Blas, T. Rodríguez-Blas, M. Botta, C. Platas-Iglesias, *Chem. Eur. J.* **2014**, 20, 17300-17305.
- [56] E. M. Gale, I. P. Atanasova, F. Blasi, I. Ay, P. Caravan, *J. Am. Chem. Soc.* **2015**, 137, 15548-15557.
- [57] **a)** A. Takaichi, T. Okamoto, T. Matsumoto, J. Nakamura, T. Nakamura, US5174987A, Otsuka Pharmaceutical Co. Ltd., **1988**; **b)** P. N. Malcom, J. J. Brown, P. F. Hahn, A. E. Stillman, K. C. P. Li, Y. Kawamura, T. Tanaka, J. K. Noel, B. A. Molony, M. F. Johnson, C. F. Hildebolt, *J. Magn. Reson. Imaging* **2000**, 12, 702-707; **c)** S. Hirohashi, R. Hirohashi, H. Uchida, S. Kitano, M. Tanaka, N. Matsuo, H. Ohishi, *Nihon Igaku Hoshasen Gakkai Zasshi* **1994**, 54, 8, 784-788.
- [58] J. Cejka, A. Corma, S. Zones, *Zeolites and Catalysis: Synthesis, Reactions and Applications*, Wiley-VCH Verlag GmbH Weinheim, **2010**.
- [59] **a)** T. Armbruster, M. E. Gunter, *Rev. Mineral. Geochem.* **2001**, 45, 1, 1-67; **b)** L. L. Ames, *The Am. Mineralogist* **1961**, 46, 1120-1131.
- [60] A. Corma, H. Garcia, *Eur. J. Inorg. Chem.* **2004**, 1143-1164.
- [61] W. Loewenstein, M. Loewenstein, *The Am. Mineralogist* **1954**, 39, 1-2, 92-96.
- [62] K. Mori, K. Kagohara, H. Yamashita, *J. Phys. Chem. C* **2008**, 112, 2593-2600.
- [63] J. Cejka, *Zeolites and Ordered Mesoporous Materials*, The 1st FEZA school on zeolites, Prague, Czech Republic, **2005**, 2-3.
-

References

- [64] D. W. Breck, *Zeolite Molecular Sieves: Structures, Chemistry and Use*, John Wiley & Sons Ltd. United Kingdom, **1974**.
- [65] T. B. Reed, D. W. Breck, *J. Am. Chem. Soc.* **1956**, 78, 5972-5977.
- [66] a) D. Verboekend, N. Nuttens, R. Locus, J. Van Aelst, P. Verolme, J. C. Groen, J. Pérez-Ramirez, B. F. Sels, *Chem. Soc. Rev.* **2016**, 45, 3331-3352; b) W. Lutz, *Adv. Mater. Sci. Eng.* **2014**, 1-20.
- [67] H. Klein, H. Fuess, *J. Chem. Soc. Faraday Trans.* **1995**, 91, 12, 1813-1824.
- [68] X. Yuan, F. Li, L. Wang, H.A. Luo, *Lat. Am. Appl. Res.* **2007**, 37, 151-156.
- [69] N. Herron, D. R. Corbin, *Inclusion Chemistry with Zeolites: Nanoscale Materials by Design*, Springer Publishing Neatherlands, **1995**.
- [70] C. B. Khouw, M. E. Davis, *ACS Symposium Series* **1993**, 517, 14, 206-221.
- [71] Y. Yang, N. Burke, J. Zhang, S. Huang, S. Lim, Y. Zhu, *RSC Adv.* **2014**, 4, 7279.
- [72] W. H. Quayle, G. Peeters, G. L. De Roy, E. F. Vansant, J. H. Lunsford, *Inorg. Chem.* **1982**, 21, 2226-2231.
- [73] W. De Wilde, G. Peeters, J. H. Lunsford, *J. Phys. Chem.* **1980**, 84, 2306-2310.
- [74] W. H. Quayle, J. H. Lunsford, *Inorg. Chem.* **1982**, 21, 97-103.
- [75] M. Petrera, A. Gennaro, P. Gherardi, G. Gubitosa, N. Pernicone, *J. Chem. Soc. Faraday Trans. I* **1984**, 80, 709-720.
- [76] Y. Umemura, Y. Minai, T. Tominaga, *Chem. Commun.* **1993**, 1822-1823.
- [77] G. Vankó, Z. Homonnay, S. Nagy, A. Vértes, G. Pál-Borbély, H. K. Beyer, *Chem. Commun.* **1996**, 785-786.
- [78] M. Martis, K. Mori, H. Yamashita, *Dalton Trans.* **2014**, 43, 3, 1132-1138.
- [79] A. Vargas, A. Hauser, L. M. L. Daku, *J. Chem. Theory Comput.* **2009**, 5, 97-115.
- [80] K. Mizuno, J. H. Lunsford, *Inorg. Chem.* **1983**, 22, 3484-3486.
- [81] S. K. Tiwary, S. Vasuvedan, *Chem. Phys. Let.* **1997**, 277, 84-88.
- [82] S. K. Tiwary, S. Vasuvedan, *Inorg. Chem.* **1998**, 37, 5239-5246.
- [83] Y. Umemara, Y. Minai, N. Koga, T. Tominaga, *Chem. Commun.* **1994**, 893-894.
- [84] Vijayalakshmi, S. M. Yusuf, S. K. Kulshreshtha, *J. Phys. Chem. Solids* **2004**, 65, 975-979.
- [85] Z. Sojka, S. Witkowski, *Top. Catal.* **2002**, 18, 3-4, 279-182.
- [86] a) H. G. Karge, V. Dondur, *J. Phys. Chem.* **1990**, 94, 765-772; b) H. Pfeifer, D. Freude, M. Hunger, *Zeolites* **1985**, 5, 274-286.
- [87] D. Jaumain, B.-L. Su, *Catal. Today* **2002**, 73, 187-196.
- [88] K. J. Thomas, V. Ramamurthy, *Langmuir* **1998**, 14, 6687-6692.
- [89] F. Moyano, J. J. Silber, N. M. Correa, *J. Colloid. Interface Sci.* **2008**, 317, 1, 332-345.
-

References

- [90] Pharmacyclics, *Approval Letter from the Food and Drug Administration to Pharmacyclics for Gadolite® Oral Suspension*, PR Newswire, December 19, **1996**.
- [91] **a)** S. W. Young, F. Qing, K. J. Balkus, J. S. Engel, J. Lang, W. C. Dow, J. D. Mutch, R. A. Miller, *J. Magn. Reson. Imaging* **1995**, 5, 5, 499-508; **b)** D. L. Rubin, K. L. Falk, M. J. Sperling, M. Ross, S. Saini, B. Rothman, F. Shellock, E. Zerhouni, D. Stark, E. K. Outwater, U. Schmiedl, L. C. Kirby, J. Chezmar, T. Coates, M. Chang, J. M. Silverman, N. Rofsky, K. Burnett, J. Engel, S. W. Young, *J. Magn. Reson. Imaging* **1997**, 7, 5, 865-872.
- [92] S. Cotton, *Lanthanide and Actinide Chemistry – Inorganic Chemistry: A Textbook Series*, John Wiley & Sons Ltd. United Kingdom, **2006**.
- [93] I. Bresinska, K. J. Balkus, *J. Phys. Chem.* **1994**, 98, 12989-12994.
- [94] C. Platas-Iglesias, L. V. Elst, W. Zhou, R. N. Muller, C. F. G. C. Geraldes, T. Maschmeyer, J. A. Peters, *Chem. Eur. J.* **2002**, 8, 22, 5121-5131.
- [95] É. Csibók, I. Bányai, L. V. Elst, R. N. Muller, W. Zhou, J. A. Peters, *Chem. Eur. J.* **2005**, 11, 4799-4807.
- [96] M. Tsotalas, M. Busby, E. Gianolio, S. Aime, L. De Cola, *Chem. Mater.* **2008**, 20, 5888-5893.
- [97] W. Zhang, J. A. Peters, F. Mayer, L. Helm, K. Djanashvili, *J. Phys. Chem. C* **2015**, 119, 5080-5089.
- [98] **a)** H. Günther, *NMR-Spektroskopie*, Wiley-VCH Verlag GmbH Weinheim, **1992**; **b)** H. Friebolin, *Ein- und Zweidimensionale NMR-Spektroskopie: Eine Einführung*, Wiley-VCH Verlag GmbH Weinheim, **1999**.
- [99] J. P. Hornak, *The Basics of MRI*, Interactive Learning Software, Rochester Institute of Technology, 1996, <https://www.cis.rit.edu/htbooks/mri/>, May **2017**.
- [100] D. M. Grant, R. K. Harris, *Encyclopedia of Nuclear Magnetic Resonance*, John Wiley & Sons Ltd. United Kingdom, **2002**.
- [101] R. Kimmich, *NMR: Tomography, Diffusometry, Relaxometry*, Springer-Verlag Berlin Heidelberg, **1997**.
- [102] A. Abragam, *Principles of Nuclear Magnetism – International Series of Monographs on Physics*, 2nd revised edition, Oxford Science Publications, Oxford University Press New York, **1983**.
- [103] A. L. Scherzinger, W. R. Hendee, *West. J. Med.* **1985**, 143, 782-792.
- [104] R. Kimmich, *Bull. Magn. Reson.* **1980**, 1, 1, 195-218.
- [105] **a)** R. Kimmich, E. Ansaldo, *Prog. Nucl. Magn. Reson. Spectrosc.* **2004**, 44, 257-320; **b)** K. M. Gilbert, W. B. Handler, T. J. Scholl, J. W. Odgaard, B. A. Chronik, *Phys. Med. Biol.* **2006**, 51, 2825-2841; **c)** R. M. Steele, J.-P. Korb, G. Ferrante, S. Bubici, *Magn. Reson. Chem.* **2016**, 54, 502-509; **d)** http://www.stelar.it/ffc_nmr.htm, May **2017**.
- [106] Y. Gossuin, Z. Serhan, L. Sandiford, D. Henrard, T. Marquardsen, R. T. M. De Rosales, D. Sakellariou, F. Ferrage, *Appl. Magn. Reson.* **2016**, 47, 237-246.
- [107] **a)** J. Enslin, P. Gülich, *Laboratory Report*, University of Mainz, **1985**; **b)** P. Gülich, C. Schröder, Mössbauer spectroscopy, *Bunsen-Magazin* 1, 4, **2010**.
-

References

- [108] P. C. Lauterbur, P. Mansfield, *Noble Lecture* **2003**, Sal Adam, Berzeliuslaboratoriet, Karolinska Institutet.
- [109] B. W. Stewart, *World Cancer Report*, IARC Press, Lyon, **2014**.
- [110] M. Rivlin, J. Horev, I. Tsarfaty, G. Navon, *Sci. Rep.* **2013**, 3, 3045.
- [111] a) O. Warburg, K. Posener, E. Negelein, *Biochem. Z.* **1924**, 152, 309-344; b) C. Zhang, J. Liu, Y. Liang, *Nat. Commun.* **2013**, 4, 2935.
- [112] a) J. A. Helpert, J. C. Curtis, D. Hearshen, M. B. Smith, K. M. A Welch, *Magn. Reson. Med.* **1987**, 5, 302-305; b) G. Liu, J. Li, V. R. Sheth, M. D. Pagel, *Mol. Imag. Biol.* **2012**, 11, 1, 47-57; c) K. S. Kim, W. Park, J. Hu, Y. H. Bae, K. Na, *Biomaterials* **2014**, 35, 337-343.
- [113] S. J. Dorazio, P. B. Tsitovich, K. E. Sifers, J. A. Sperryak, J. R. Morrow, *J. Am. Chem. Soc.* **2011**, 133, 36, 14154-14156.
- [114] a) H. Lülfi, A. Bertucci, D. Septiadi, R. Corradini, L. De Cola, *Chem. Eur. J.* **2014**, 20, 10900-10904; b) B. Dong, S. Belkhair, M. Zaarour, L. Fisher, J. Verran, L. Tosheva, R. Retoux, J.-P. Gilson, S. Mintova, *Nanoscale* **2014**, 6, 10859-10864.
- [115] Y. Yan, E. Shao, X. Deng, J. Liu, Y. Zhang, Y. Tang, *J. Mater. Chem. B* **2014**, 2, 3041-3049.
- [116] Y.-H. Luo, L.-J. Yang, Q.-L. Liu, Y. Ling, W. Wang, B.-W. Sun, *Dalton Trans.* **2014**, 43, 16937-16942.
- [117] D. H. McCartney, *Can. J. Chem.* **1986**, 64, 1936-1942.
- [118] E. T. Ayodele, A. A. Olajire, S. O. Oladoye, *Bull. Chem. Soc. Eth.* **2000**, 14.
- [119] G. A. van Albada, I. Mutikainen, U. Turpeinen, J. Reedijk, *Acta Crystallogr. E: Struct. Rep. Online* **2005**, 61, 1411-1412.
- [120] U. P. Azad, V. Ganesan, *Chem. Electrochem.* **2014**, 1, 379-383.
- [121] P. Gütllich, E. Bill, A. X. Trautwein, *Mössbauer Spectroscopy and Transition Metal Chemistry – Fundamentals and Applications*, Springer-Verlag Berlin Heidelberg, **2011**.
- [122] S. Decurtins, F. Felix, J. Ferguson, H. U. Guedel, A. Ludi, *J. Am. Chem. Soc.* **1980**, 102, 12, 4102-4106.
- [123] a) J. H. Baxendale, P. George, *Nature* **1950**, 736-744; b) J. H. Baxendale, P. George, *Trans. Faraday Soc.* **1950**, 46, 736; c) F. Basolo, J. C. Hayes, H. M. Neumann, *J. Am. Chem. Soc.* **1954**, 76, 3807-3809; d) R. K. Murmann, E. A. Healy, *J. Am. Chem. Soc.* **1960**, 83, 2092-2098.
- [124] a) S. Raman, *J. Inorg. Nucl. Chem.* **1975**, 37, 1747-1751; b) P. Syamala, P. V. S. Rao, K. Ramakrishna, *Indian J. Chem. Sec. A* **2000**, 39, 643-645; c) C. Nakanishi, M. Senna, *J. Sol-Gel Sci. Technol.* **2005**, 35, 137-142.
- [125] S. Calogero, U. Russo, L. L. Condorelli, I. Fragal, *Transition Met. Chem.* **1979**, 4, 156-160.
- [126] J. England, C. C. Scarborough, T. Weyhermüller, S. Sproules, K. Wieghardt, *Eur. J. Inorg. Chem.* **2012**, 4605-4621.
- [127] H. Sato, T. Tominaga, *Bull. Chem. Soc. Jpn.* **1976**, 49, 697-700.
-

References

- [128] a) C. D. Johnson, I. Roberts, P. G. Taylor, *J. Chem. Soc. Perkin Trans.* **1981**, 2, 409-413; b) G. B. Ellam, C. D. Johnson, *J. Org. Chem.* **1971**, 36, 16, 2284-2288; c) P. M. Dewick, *Essentials of Organic Chemistry: For Students of Pharmacy, Medicinal, Chemistry and Biological Chemistry*, John Wiley & Sons Ltd. United Kingdom, **2006**.
- [129] G. E. Wesbey, M. D. Robert, V. Brasch, H. I. Goldberg, B. L. Engelstad, A. Moss, *Magn. Reson. Imaging* **1985**, 3, 57-64.
- [130] S. A. Barrett, C. A. Kilner, M. A. Halcrow, *Dalton Trans.* **2011**, 40, 12021-12024.
- [131] L. Pazderski, T. Pawlak, J. Sitkowski, L. Kozerski, E. Szlyk, *Magn. Reson. Chem.* **2010**, 48, 450-457.
- [132] R. Nowak, E. A. Prasetyanto, L. De Cola, B. Bojer, R. Siegel, J. Senker, E. Rössler, B. Weber, *Chem. Commun.* **2017**, 53, 971-974.
- [133] a) C. V. Krishnan, C. Creutz, H. A. Schwarz, N. Sutin, *J. Am. Chem. Soc.* **1983**, 105, 5617-5623; b) NIST Database, *Acid Dissociation Constants*, May **2017**.
- [134] a) I. Grante, A. Actins, L. Orola, *Spectrochim. Acta A* **2014**, 129, 326-332; b) X. Han, L.-Z. Wu, G. Si, J. Pan, Q.-Z. Yang, L.-P. Zhang, C.-H. Tung, *Chem. Eur. J.* **2007**, 13, 1231-1239.
- [135] E. Riedel, C. Janiak, *Anorganische Chemie*, Walter de Gruyter GmbH & Co.KG Berlin, **2004**.
- [136] J. Rebek, *Angew. Chem. Int. Ed.* **2005**, 44, 2068-2078.
- [137] E. F. T. Lee, L. V. C. Rees, *Zeolites* **1987**, 7, 143-147.
- [138] X. Hu, K. Meyer, *Inorg. Chim. Acta* **2002**, 337, 53-58.
- [139] a) J. Huang, Y. Jiang, V. R. Reddy Marthala, Y. S. Ooi, J. Weitkamp, M. Hunger, *Micropor. Mesopor. Mater.* **2007**, 104, 129-136; b) J. Huang, Y. Jiang, V. R. Reddy Marthala, B. Thomas, E. Romanov, M. Hunger, *J. Phys. Chem. C* **2008**, 112, 3811-3818; c) M. Feuerstein, M. Hunger, G. Engelhardt, J. P. Amoureux, *Solid State Nucl. Magn. Reson.* **1996**, 7, 115-120; d) S. Caldarelli, A. Buchholz, M. Hunger, *J. Am. Chem. Soc.* **2001**, 123, 7118-7123; e) J. Jiao, W. Wang, B. Sulikowski, J. Weitkamp, M. Hunger, *Micropor. Mesopor. Mater.* **2006**, 90, 246-250.
- [140] Z. Yan, D. Ma, J. Zhuan, X. Liu, X. Han, X. Bao, F. Chang, L. Xu, Z. Liu, *J. Mol. Catal. A: Chem.* **2003**, 194, 153-167.
- [141] H. E. Gottlieb, V. Kotlyar, A. Nudelman, *J. Org. Chem.* **1997**, 62, 7512-7515.
- [142] O. Laporte, W. F. Meggers, *J. Opt. Soc. Am.* **1925**, 11, 5, 459-463.
- [143] a) H. G. Karge, J. Weitkamp, *Post-Synthesis Modification I*, Springer-Verlag Berlin Heidelberg, **2002**; b) H. G. Karge, J. Weitkamp, *Characterization I*, Springer-Verlag Berlin Heidelberg, **2004**.
- [144] a) S. Mintova, J. Grand, V. Valtchev, *C. R. Chimie* **2016**, 19, 183-191; b) M. Kralj, K. Pavelic, *EMBO Reports* **2003**, 4, 11, 1008-1012.
- [145] S. Uppili, K. J. Thomas, E. M. Crompton, V. Ramamurthy, *Langmuir* **2000**, 16, 265-274.
- [146] S. Buttefey, A. Boutin, C. Mellot-Draznieks, A. H. Fuchs, *J. Phys. Chem. B* **2001**, 105, 9569-9575.
- [147] C. Beauvais, X. Guerrault, F.-X. Coudert, A. Boutin, A. H. Fuchs, *J. Phys. Chem. B* **2004**, 108, 399-404.
-

References

- [148] D. N. Stamires, *Clays Clay Miner.* **1973**, 21, 379-389.
- [149] www.cpp.edu/~psbeauchamp/pdf/spec_ir_nmr_spectra_tables.pdf, *Infrared Spectroscopy Table*, May **2017**.
- [150] G. A. Bain, J. F. Berry, *J. Chem. Educ.* **2008**, 85, 4, 532-536.
- [151] ORIGIN, OriginLab® Corporation, Northampton, MA, OriginLab **2017**.
- [152] K. Lagarec, D. G. Rancourt, *Recoil, Mössbauer spectral analysis software for Windows 1.0*, Department of Physics, University of Ottawa, Canada, **1998**.
- [153] *SpinWorks*, basic 1D NMR processing, free online software, May **2017**.
- [154] M. C. Burla, R. Caliendo, M. Camalli, B. Carrozzini, G. L. Cascarano, L. De Caro, C. Giacovazzo, G. Polidori, R. Spagna, SIR2004: an improved tool for crystal structure determination and refinement, *J. Appl. Cryst.* **2005**, 38, 381-388.
- [155] G. Sheldrick, A short history of SHELX, *Acta Cryst. A* **2008**, 64, 112-122.
- [156] L. Farrugia, ORTEP-3 for Windows - a version of ORTEP-III with a Graphical User Interface (GUI), *J. Appl. Cryst.* **1997**, 30, 565.
- [157] E. Keller, *Schakal-99*, University of Freiburg, Freiburg, Germany, **1999**.
- [158] H. G. O. Becker, *Organikum – Organisch-chemisches Grundpraktikum*, 19, bearb. und erweit. Auflage, Johann Ambrosius Barth Verlag Berlin, **1990**.
- [159] National Research Council, *Prudent Practices in the Laboratory: Handling and Disposing of Chemicals*, CRC Publishing, 1st Edition, **1995**.
- [160] B. Heyn, *Anorganische Synthesechemie: Ein integriertes Praktikum*, 2. Aufl., Springer Lehrbuch, Springer-Verlag Berlin Heidelberg, **1990**.
- [161] B. Weber, R. Betz, W. Bauer, S. Schlamp, *Z. Anorg. Allg. Chem.* **2011**, 637, 102-107.
- [162] A. P. Smith, S. A. Savage, J. C. Love, C. L. Fraser, *Org. Synth. Coll.* **2004**, 10, 517-522.
- [163] L. C. King, *J. Am. Chem. Soc.* **1944**, 66, 894-895.
- [164] J. Polin, E. Schmohel, V. Balzani, *Synthesis* **1998**, 321-324.
- [165] D. L. Jameson, K. A. Goldsby, *J. Org. Chem.* **1990**, 55, 4992-4994.
- [166] a) K. H. Sugiyarto, W.-A. McHale, D. C. Craig, A. D. Rae, M. L. Scudder, H. A. Goodwin, *Dalton Trans.* **2003**, 2443-2448; b) A.-K. Pleier, H. Glas, M. Grosche, P. Sirsch, W. R. Thiel, *Synthesis* **2001**, 1, 55-62.
- [167] M. E. Voss, C. M. Beer, S. A. Mitchell, P. A. Blomgren, P. E. Zhichkin, *Tetrahedron* **2008**, 64, 645-651.
- [168] E. V. Vlasova, V. M. Stoyanov, M. M. El'chaninov, B. S. Lukyanov, *Chem. Heterocycl. Comp.* **2010**, 46, 6, 681-683.

6. Publications and Conference Contributions

Publications

- R. Nowak, W. Bauer, T. Ossiander, B. Weber, *Eur. J. Inorg. Chem.* **2013**, 975-983.
- R. Nowak, E. A. Prasetyanto, L. De Cola, B. Bojer, R. Siegel, J. Senker, E. Rössler, B. Weber, *Chem. Comm.* **2017**, 53, 971-974.
- R. Nowak, K. Dankhoff, E. Rössler, B. Weber, *submitted 2017*.
- R. Nowak, B. Bojer, R. Siegel, J. Senker, B. Weber, *manuscript in preparation*.

Oral presentations

Institut de Science et d'Ingénierie Supramoléculaires 2013, Strasbourg, France, “Ship-in-a-bottle complexes with spin-crossover properties”.

Stipendiatentreffen des Fonds der Chemischen Industrie (VCI) 2015, Regensburg, Germany, “pH-Responsive magneto-switches for functional magnetic resonance imaging (*fMRI*)”.

Bayreuther Polymer Symposium 2015, Bayreuth, Germany, “pH-responsive nanoswitch to exploit Warburg effect for tumour detection via *fMRI*”.

International Conference on Coordination Chemistry 2016, Brest, France, “pH-Responsive magnetism of iron(II) complexes in solution and under small confinement”.

Mitteldeutsches Anorganiker-Nachwuchssymposium 2016, Halle, Germany, “Freiheit und Gefangenschaft – pH-responsiver Magnetismus von Eisen(II)-Komplexen“.

Koordinationschemie-Treffen 2017, Potsdam, Germany, “Spin-crossover without spin-crossover: proton-driven coordination-induced spin state switches”.

Poster presentations

International Conference on Multifunctional, Hybrid and Nanomaterials 2015, Sitges, Spain, “pH-responsive nanoswitch to exploit Warburg effect for tumour detection via *fMRI*”.

Bayreuther Polymer Symposium 2015, Bayreuth, Germany, “pH-responsive nanoswitch to exploit Warburg effect for tumour detection via *fMRI*”.

International Conference on Multifunctional, Hybrid and Nanomaterials 2017, Lisbon, Portugal, “pH-Responsive magnetism of iron(II) complexes in solution and under small confinement”.

7. Declaration of Independence

Eidesstattliche Versicherungen und Erklärung zu meiner Dissertation mit dem Titel:

„pH-Responsive Magnetism of Iron(II) Complexes in Solution and Under Small Confinement as Basis for Smart Contrast Agents“

(§ 5 Nr. 4 PromO)

Hiermit erkläre ich, dass keine Tatsachen vorliegen, die mich nach den gesetzlichen Bestimmungen über die Führung akademischer Grade zur Führung eines Doktorgrades unwürdig erscheinen lassen.

(§ 8 S. 2 Nr. 5 PromO)

Hiermit erkläre ich mich damit einverstanden, dass die elektronische Fassung meiner Dissertation unter Wahrung meiner Urheberrechte und des Datenschutzes einer gesonderten Überprüfung hinsichtlich der eigenständigen Anfertigung der Dissertation unterzogen werden kann.

(§ 8 S. 2 Nr. 7 PromO)

Hiermit erkläre ich eidesstattlich, dass ich die Dissertation selbständig verfasst und keine anderen als die von mir angegebenen Quellen und Hilfsmittel benutzt habe.

(§ 8 S. 2 Nr. 8 PromO)

Ich habe die Dissertation nicht bereits zur Erlangung eines akademischen Grades anderweitig eingereicht und habe auch nicht bereits diese oder eine gleichartige Doktorprüfung endgültig nicht bestanden.

(§ 8 S. 2 Nr. 9 PromO)

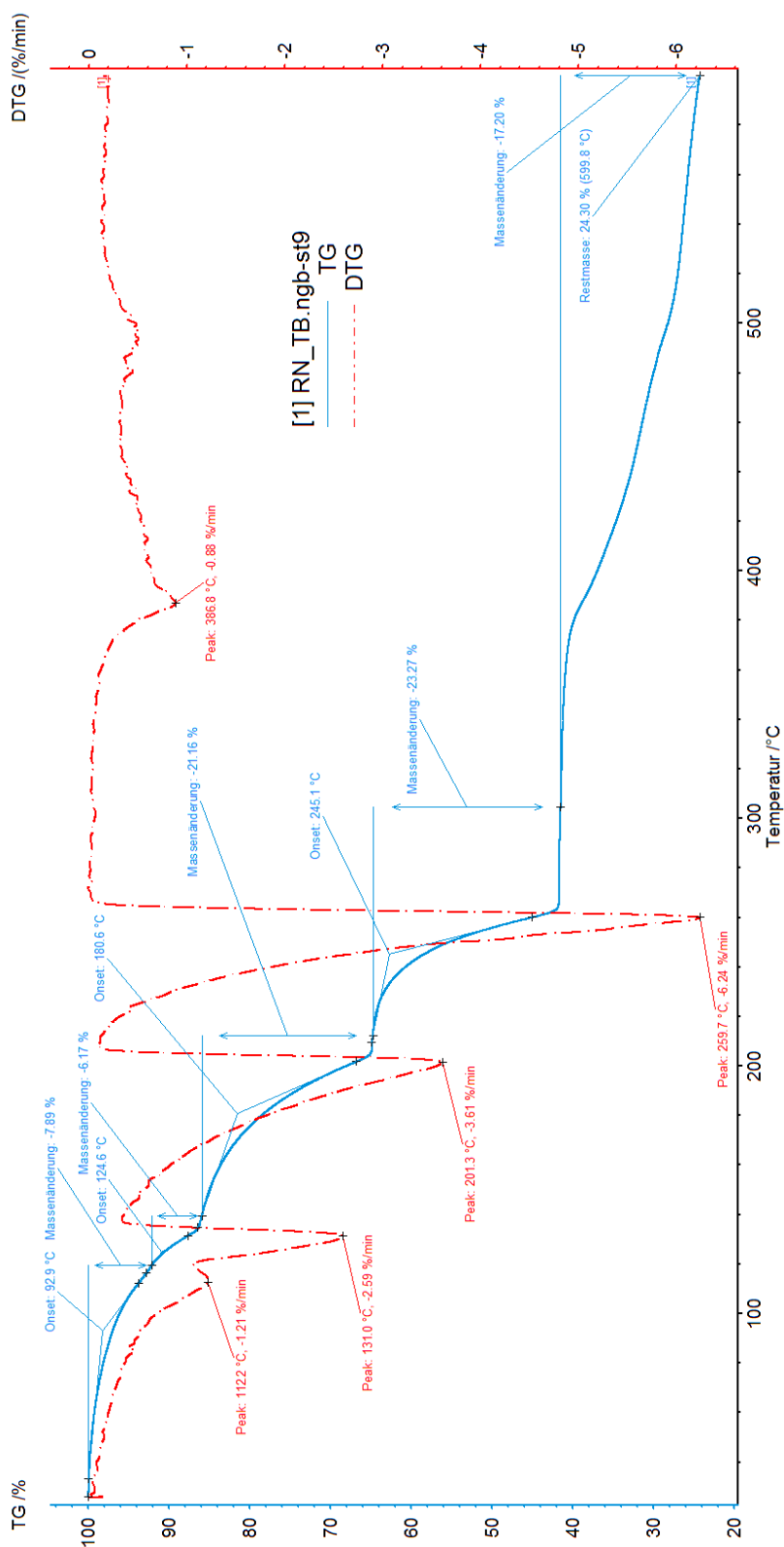
Hiermit erkläre ich, dass ich keine Hilfe von gewerblichen Promotionsberatern bzw. -vermittlern in Anspruch genommen habe und auch künftig nicht nehmen werde.

Bayreuth, 30.11.2017

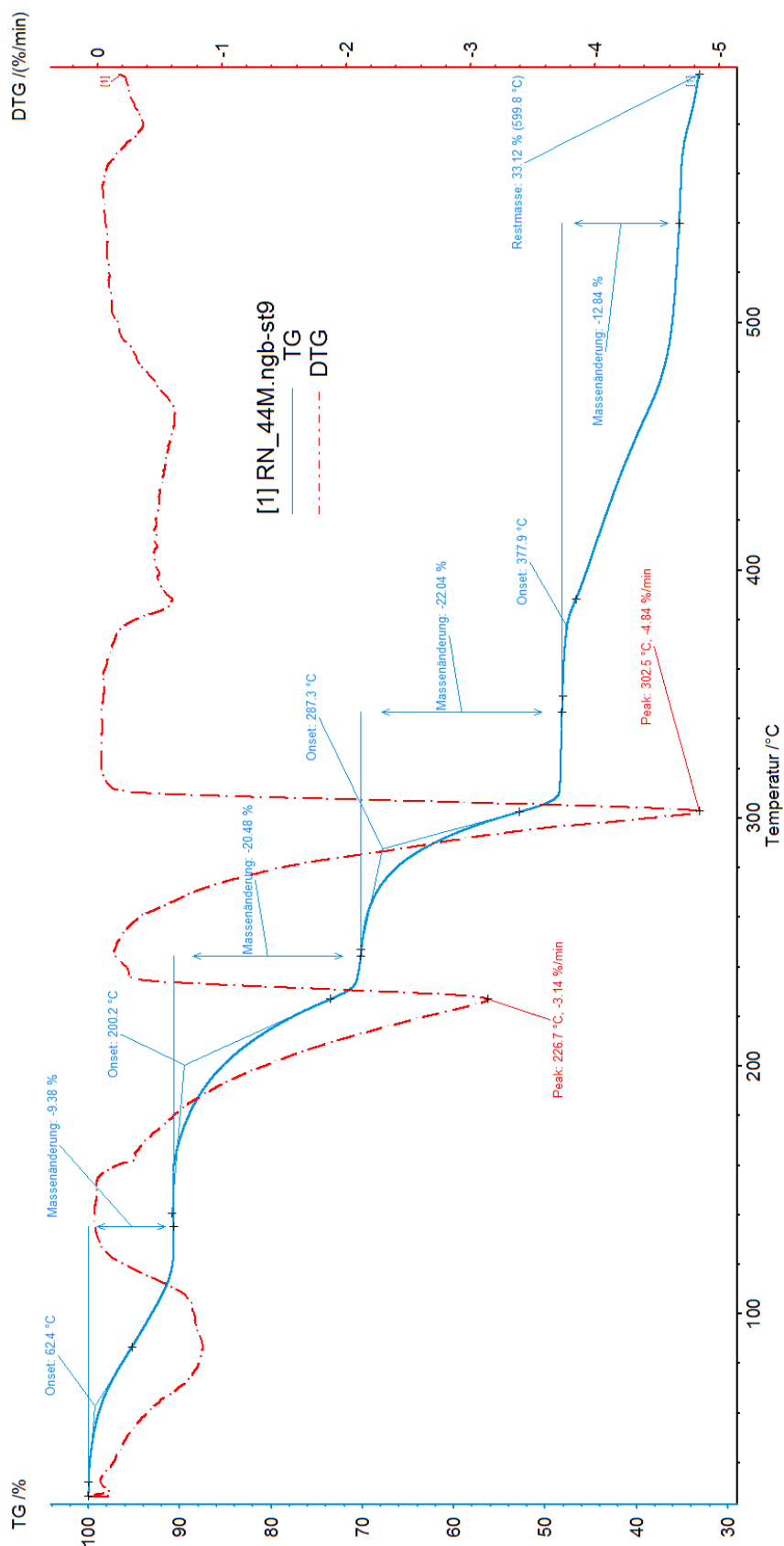
.....

Ort, Datum

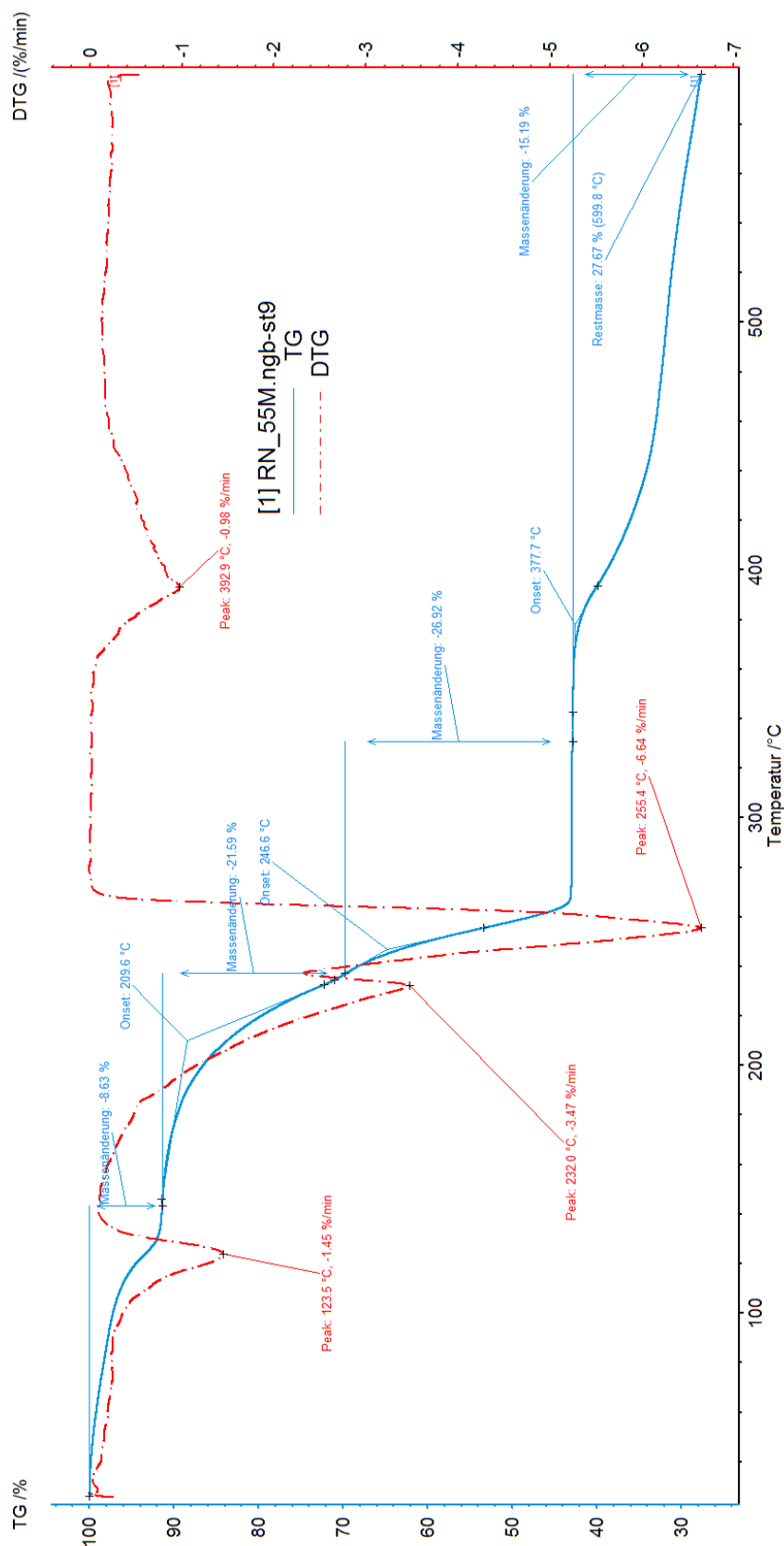
A. Appendix



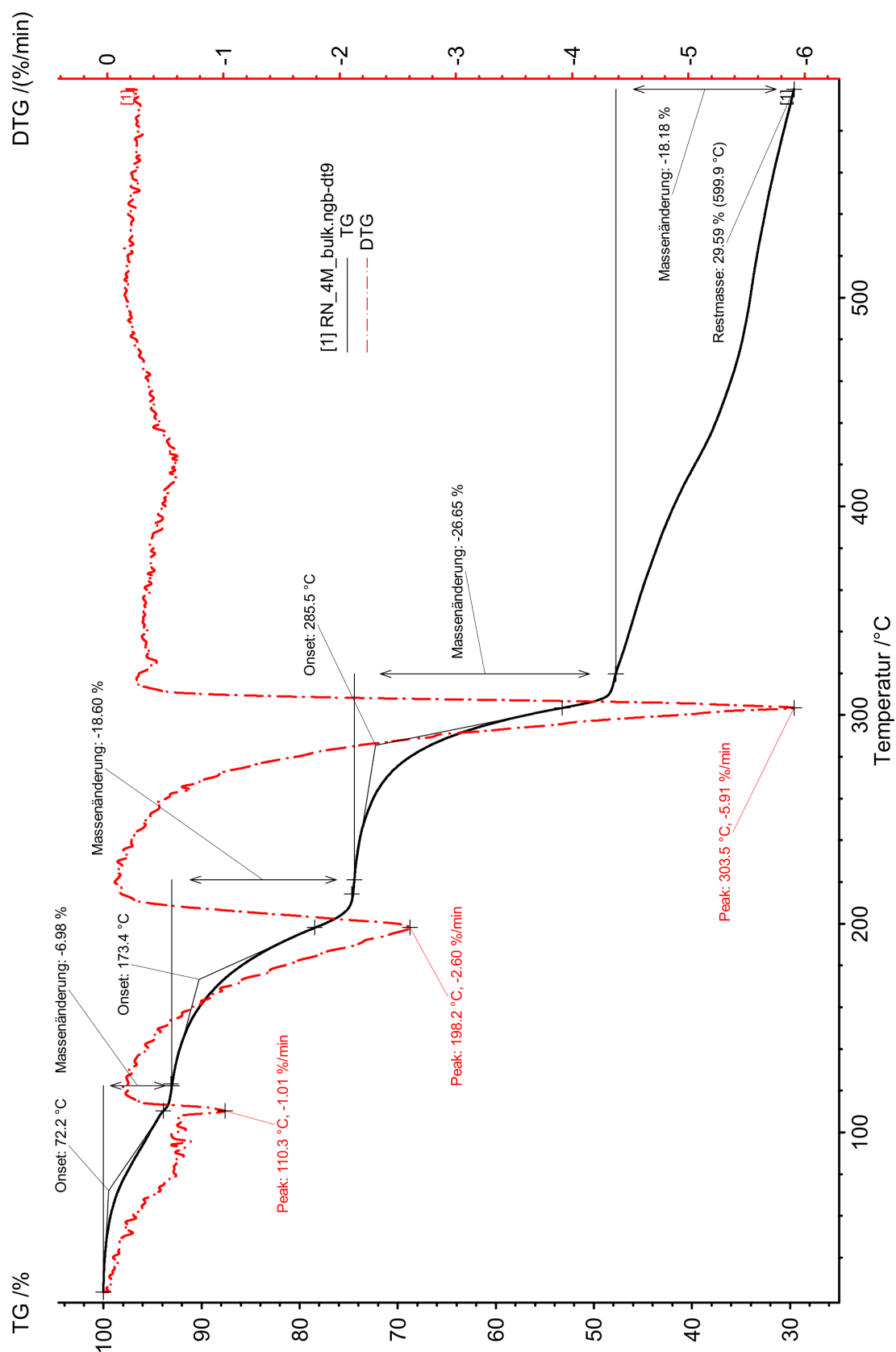
A1. Thermogravimetric analysis (TG) and differential thermogravimetric analysis (DTG) of the complex $\text{Fe}(\text{Bpy})_3\text{Cl}_2$ between 20 °C and 600 °C.



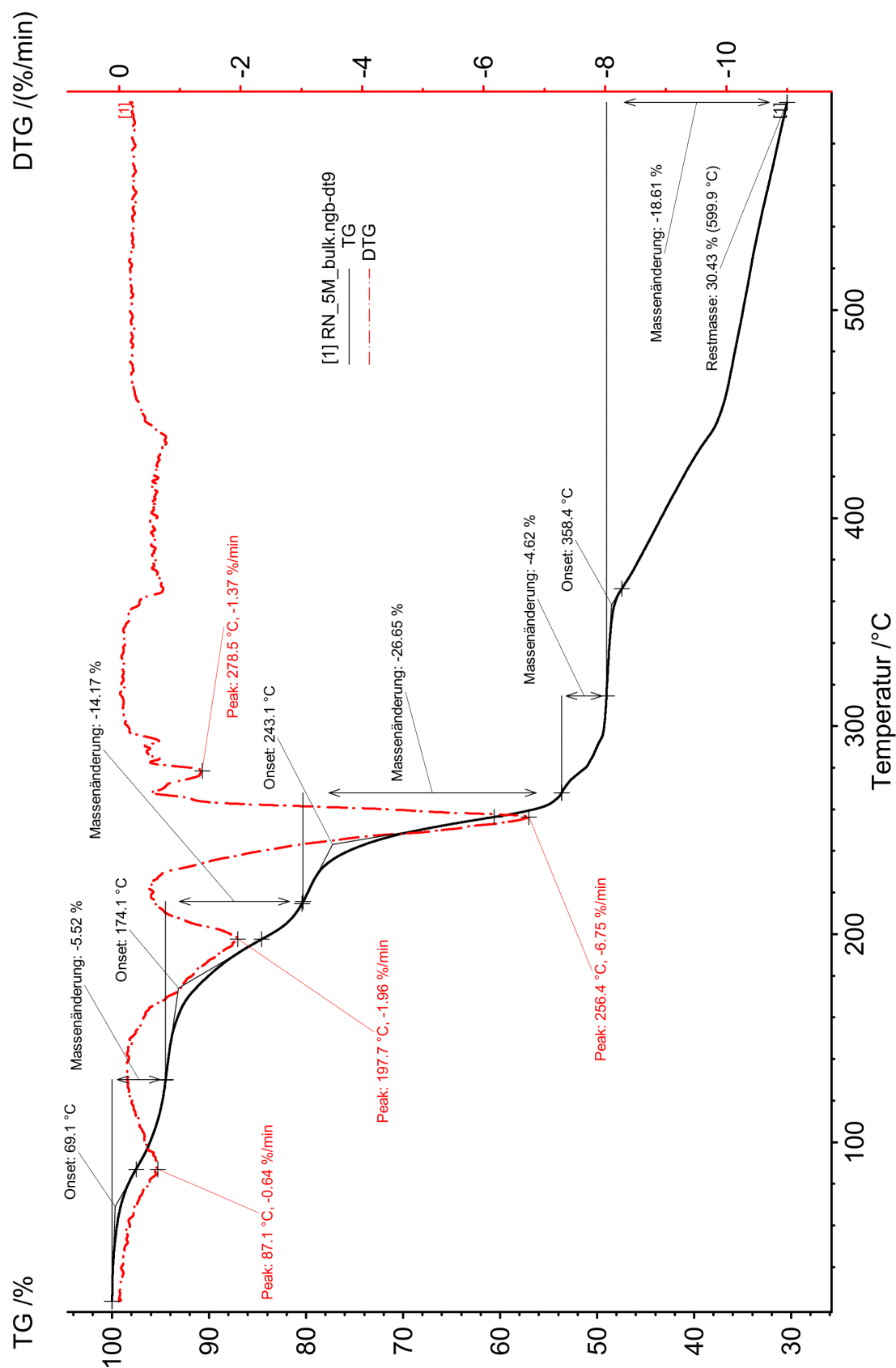
A2. Thermogravimetric analysis (TG) and differential thermogravimetric analysis (DTG) of the complex $\text{Fe}(\text{44mBpy})_3\text{Cl}_2$ between 20 °C and 600 °C.



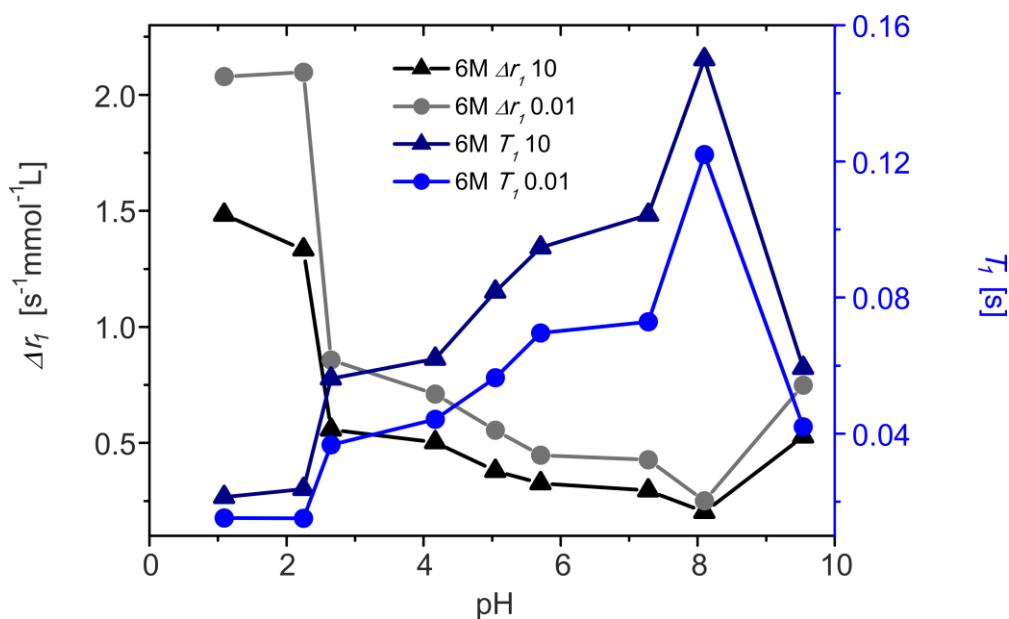
A3. Thermogravimetric analysis (TG) and differential thermogravimetric analysis (DTG) of the complex $\text{Fe}(\text{55mBpy})_3\text{Cl}_2$ between 20 °C and 600 °C.



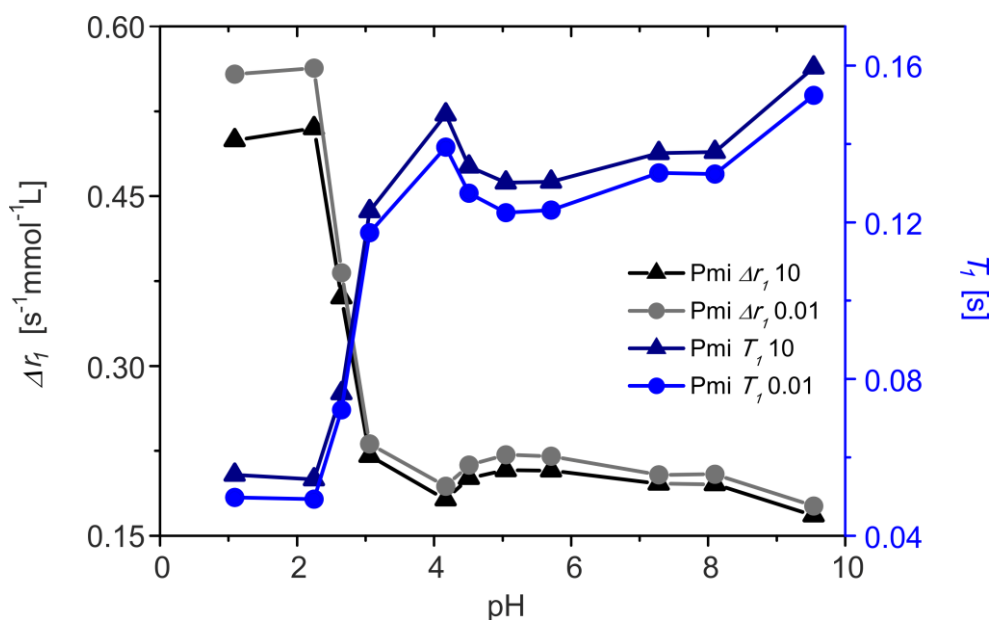
A4. Thermogravimetric analysis (TG) and differential thermogravimetric analysis (DTG) of the complex $\text{Fe}(\text{4mBpy})_3\text{Cl}_2$ between 20 °C and 600 °C.



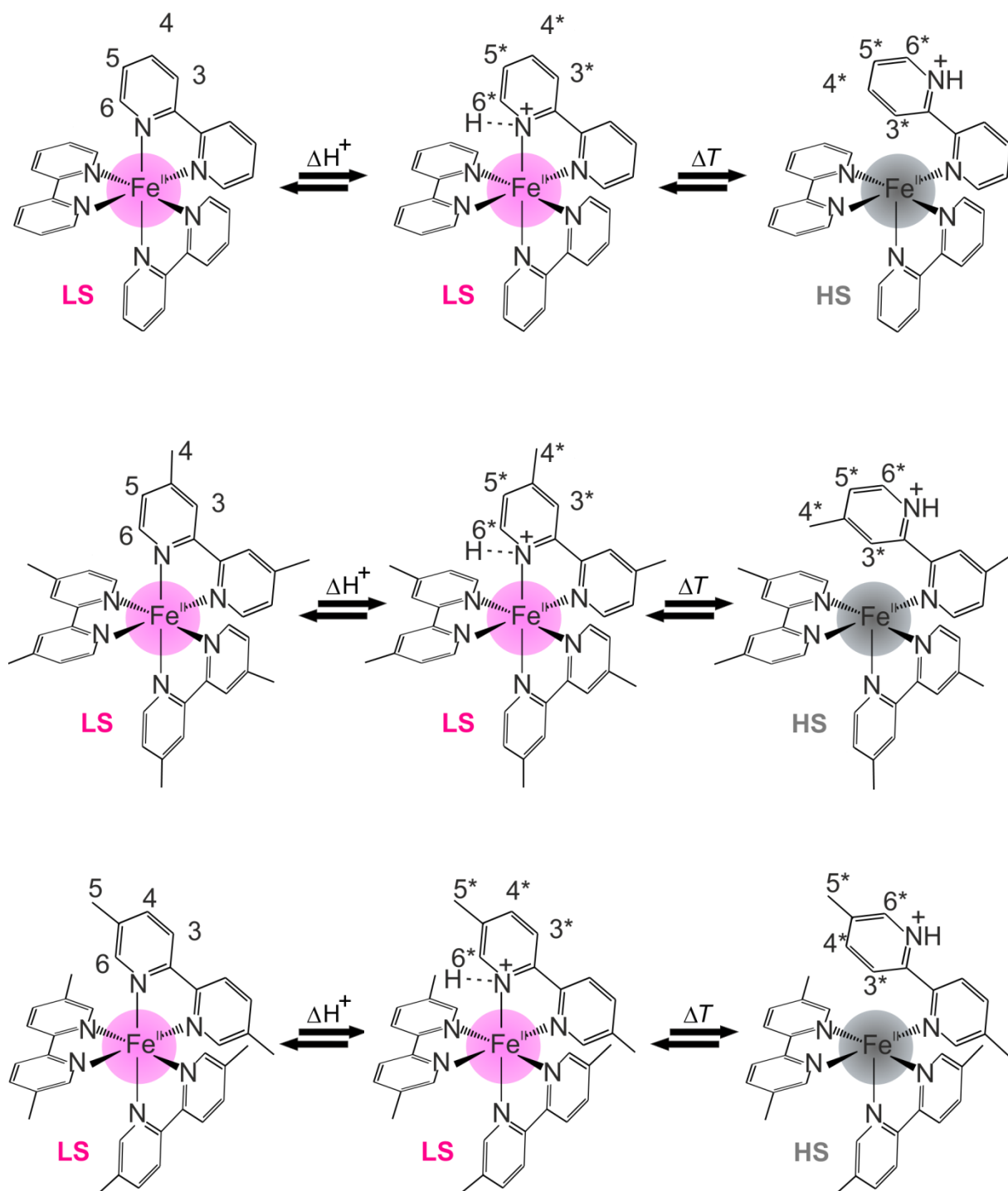
A5. Thermogravimetric analysis (TG) and differential thermogravimetric analysis (DTG) of the complex $\text{Fe}(\text{5mBpy})_3\text{Cl}_2$ between 20 °C and 600 °C.



A6. FC ^1H -NMR relaxometry of T_1 (blue) and Δr_1 (black) at an aqueous solution of $[\text{Fe}(\text{6mBpy})_3]^{2+}$ ($c = 0.16 \text{ mol/L}$) where 6mBpy = 6-methyl-2,2'-bipyridine; at a Larmor-frequency of 0.01 MHz (circle) and 10 MHz (triangle) at RT. The complex was found to decompose during acidic conditions and not to undergo a PD-CISSS.



A7. FC ^1H -NMR relaxometry of T_1 (blue) and Δr_1 (black) at an aqueous solution of $[\text{Fe}(\text{Pmi})_3]^{2+}$ ($c = 0.036 \text{ mol/L}$) where Pmi = 2-(1*H*-imidazol-2-yl)pyrimidine; at a Larmor-frequency ν of 0.01 MHz (circle) and 10 MHz (triangle) at RT. The complex was found to decompose during acidic conditions and not to undergo a PD-CISSS.



A8. $^1\text{H-NMR}$ spectroscopy atom numbering at the ligands for the complexes $[\text{Fe}(\text{Bpy})_3]^{2+}$ (top), $[\text{Fe}(44\text{mBpy})_3]^{2+}$ (middle) and $[\text{55mFe}(\text{Bpy})_3]^{2+}$ (bottom) described in this work.

Appendix

A9. Peak positions for the complex $\text{Fe}(\text{Bpy})_3^{2+}$ at pH 1.0, pH 1.9 as well as pH 2.9 and different temperatures.

$[\text{Fe}(\text{Bpy})_3]^{2+}$				
Peak positions at different temperatures and pH 1.0				
	300 K	325 K	345 K	365 K
3 (d)	8.508, 8.535	8.748, 8.775	8.927, 8.950	9.113
4 (t)	8.038, 8.065, 8.089	8.292, 8.319, 8.344	8.483, 8.504, 8.525	8.684
5 (t)	7.310, 7.332, 7.355	7.572, 7.592, 7.614	7.786, 7.803	7.972
6 (d)	7.458, 7.478	7.686, 7.704	7.869	8.065
3* (m)	8.383, 8.412, 8.432, 8.450	8.660, 8.671	8.849	9.016
4* (m)	8.383, 8.412, 8.432, 8.450	8.660, 8.671	8.849	9.016
5* (m)	7.865, 7.888, 7.908	8.116, 8.136, 8.155	8.322	8.497
6* (d)	8.820, 8.838	9.067, 9.079	9.26	9.432
$[\text{Fe}(\text{Bpy})_3]^{2+}$				
Peak positions at different temperatures and pH 1.9				
	300 K	325 K	345 K	365 K
3 (d)	8.533, 8.558	8.777, 8.802	8.964, 8.986	9.143
4 (t)	8.067, 8.089, 8.112,	8.325, 8.347, 8.369	8.516, 8.540, 8.567	8.724
5 (t)	7.354, 7.376	7.723, 7.736	7.821	8.011
6 (d)	7.493, 7.506	7.617, 7.640	7.899	8.065
3* (m)	8.457	8.701	8.883	9.056
4* (m)	8.457	8.701	8.883	9.056
5* (m)	7.887, 7.910, 7.934	8.164	8.352	8.527
6* (d)	8.849, 8.860	9.104	9.293	9.468
$[\text{Fe}(\text{Bpy})_3]^{2+}$				
Peak positions at different temperatures and pH 2.9				
	300 K	325 K	345 K	365 K
3 (d)	8.545, 8.572	8.799, 8.825	8.993, 9.013	9.176, 9.196
4 (t)	8.076, 8.101, 8.127	8.343, 8.368, 8.393	8.567, 8.589	8.759
5 (t)	7.346, 7.366, 7.389	7.623, 7.641, 7.662	7.847, 7.865	8.043
6 (d)	7.504, 7.521	7.744, 7.759	7.930, 7.941	8.105
3* (m)	8.447, 8.469	8.72	8.914	9.066
4* (m)	8.447, 8.469	8.72	8.914	9.066
5* (m)	7.904, 7.923, 7.941	8.179	8.376	8.569
6* (d)	8.857, 8.874	9.115, 9.128	9.322	9.484

Appendix

A10. Peak positions for the complex $\text{Fe}(\text{44mBpy})_3^{2+}$ at pH 1.0, pH 1.9 as well as pH 2.9 and different temperatures.

$[\text{Fe}(\text{44mBpy})_3]^{2+}$ Peak positions at different temperatures and pH 1.0				
	300 K	325 K	345 K	365 K
3 (s)	8.298	8.532	-	-
4 (CH₃)	2.464	2.708	-	-
5 (d)	7.119, 7.135	7.386	-	-
6 (d)	7.204, 7.222	7.432	-	-
3* (s)	8.197	8.428	8.606	8.787
4* (CH₃)	2.59	2.827	3.008	3.182
5* (d)	7.690, 7.708	7.926, 7.943	8.115	8.298
6* (d)	8.605, 8.623	8.845, 8.863	9.046, 9.032	9.227

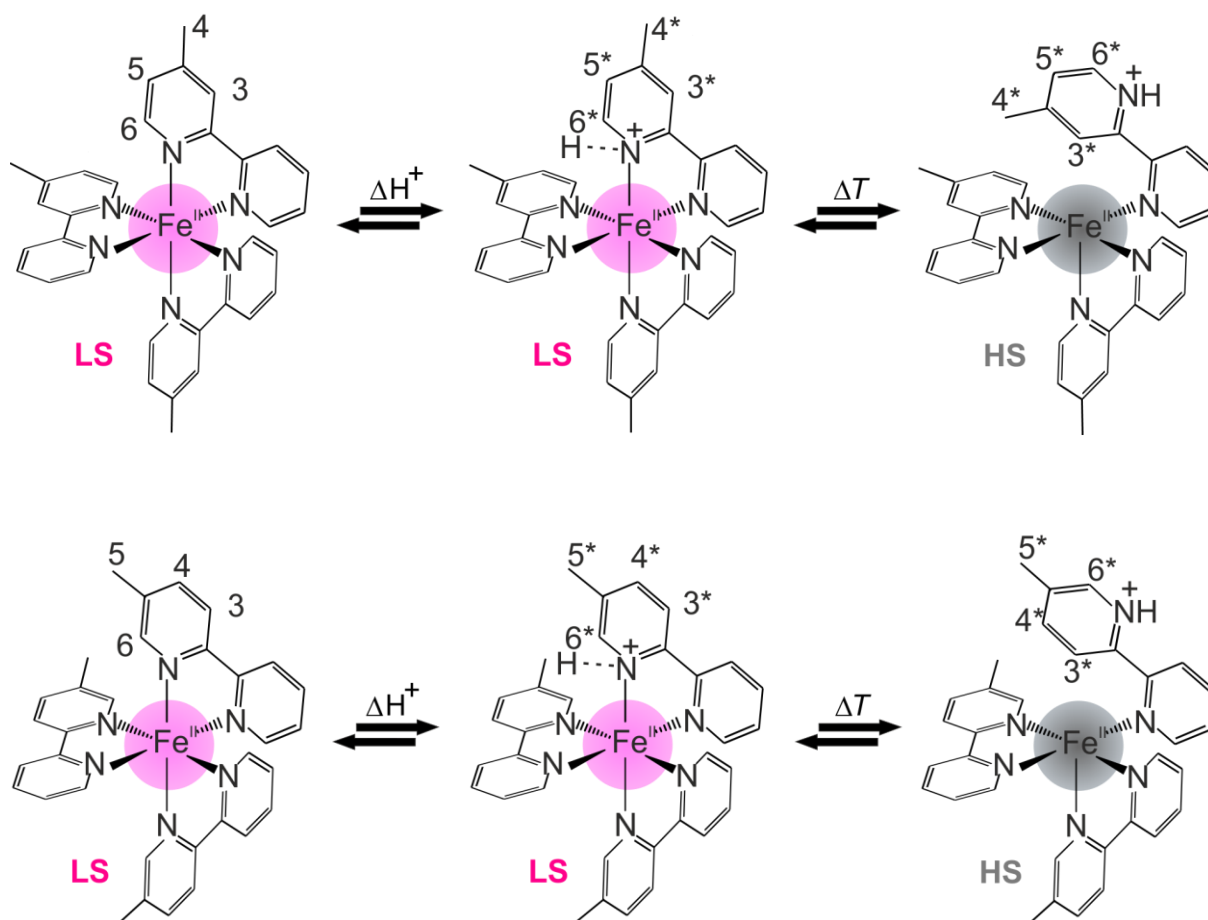
$[\text{Fe}(\text{44mBpy})_3]^{2+}$ Peak positions at different temperatures and pH 1.9				
	300 K	325 K	345 K	365 K
3 (s)	8.333	8.578	8.767	8.942
4 (CH₃)	2.506	2.77	2.969	3.151
5 (d)	7.147, 7.165	7.409	7.613	7.801
6 (d)	7.238	7.422	7.613	7.801
3* (s)	8.234	8.475	8.66	8.831
4* (CH₃)	2.618	2.866	3.057	3.232
5* (d)	7.705, 7.723	7.955, 7.972	8.147, 8.160	8.327
6* (d)	8.630, 8.649	8.883, 8.900	9.079, 9.095	9.264

$[\text{Fe}(\text{44mBpy})_3]^{2+}$ Peak positions at different temperatures and pH 2.9				
	300 K	325 K	345 K	365 K
3 (s)	8.339	8.586	8.776	8.956
4 (CH₃)	2.516	2.781	2.981	3.17
5 (d)	7.150, 7.167	7.422, 7.446	7.622	7.819
6 (d)	7.236	7.482	7.622	7.819
3* (s)	8.24	8.482	8.642	8.847
4* (CH₃)	2.624	2.871	3.066	3.249
5* (d)	7.706, 7.725	7.960, 7.974	8.165	8.34
6* (d)	8.634, 8.653	8.890, 8.905	9.087, 9.099	9.279

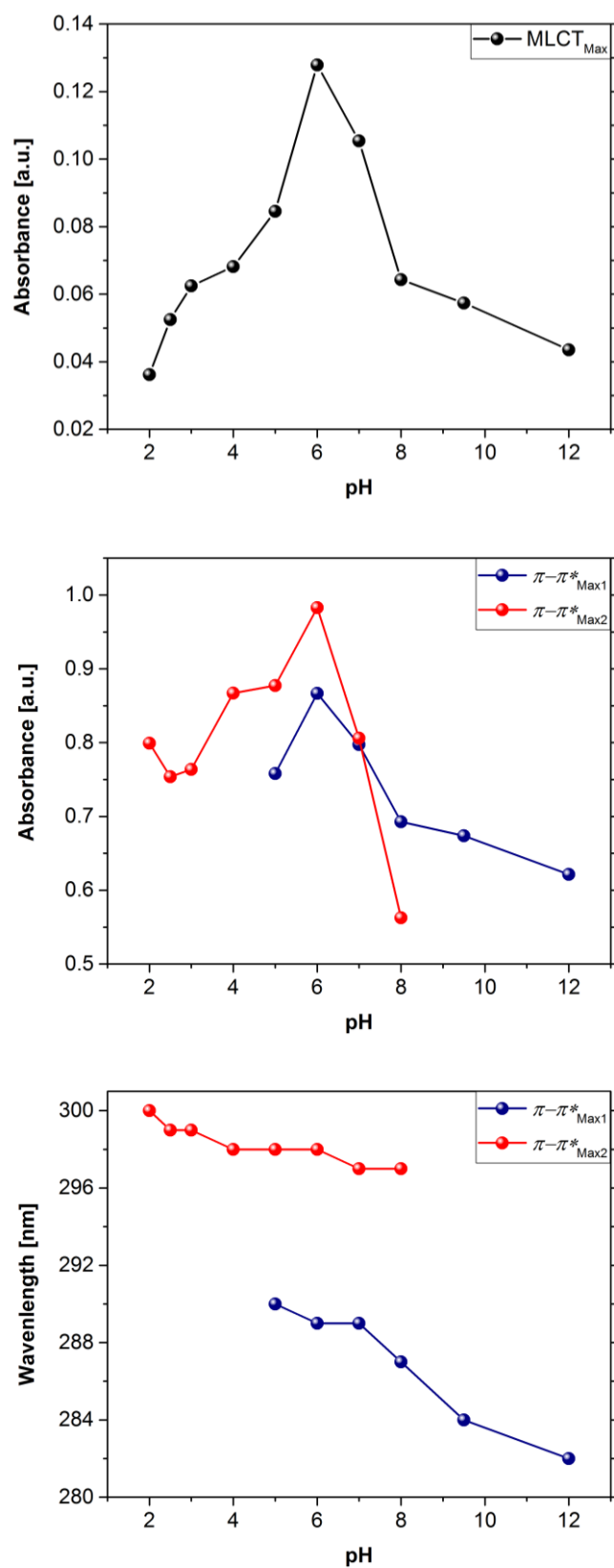
Appendix

A11. Peak positions for the complex $\text{Fe}(\text{55mBpy})_3^{2+}$ at pH 1.0, pH 1.9 as well as pH 2.9 and different temperatures.

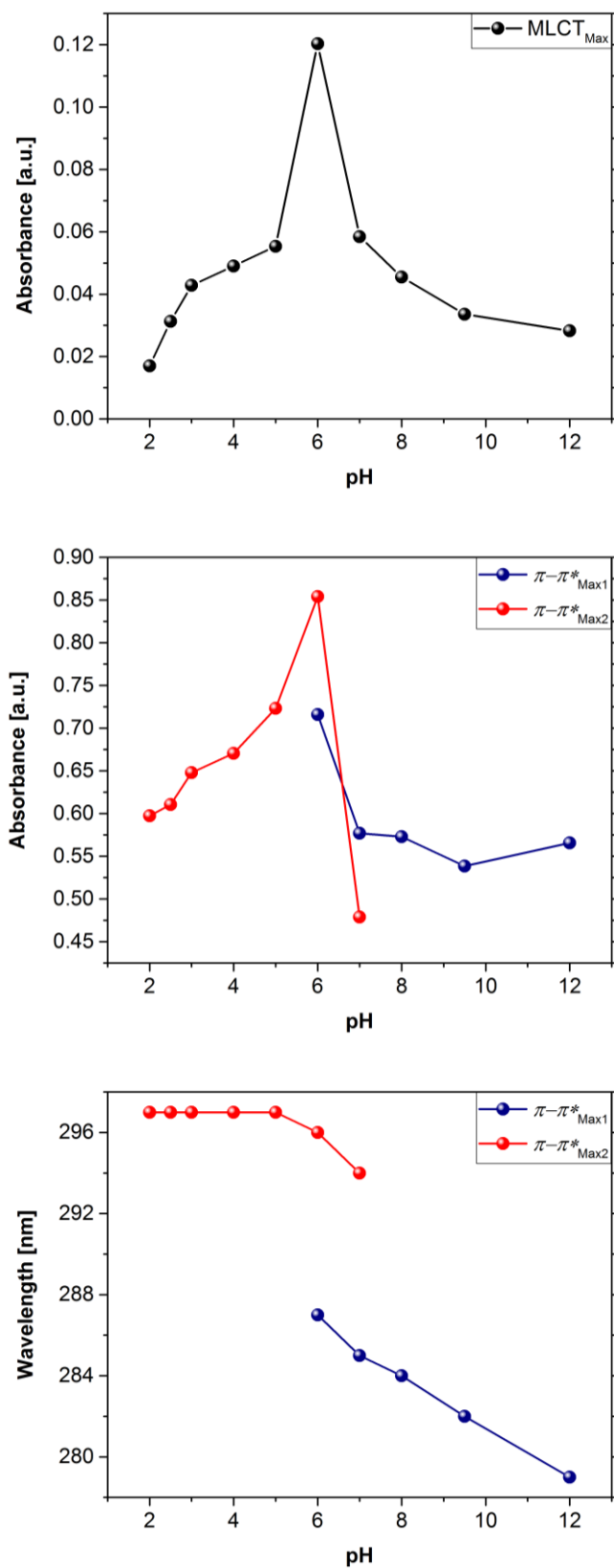
$[\text{Fe}(\text{55mBpy})_3]^{2+}$ Peak positions at different temperatures and pH 1.0				
	300 K	325 K	345 K	365 K
3 (d)	8.294, 8.323	8.534, 8.562	8.718, 8.746	-
4 (d)	7.819, 7.846	8.068, 8.096	8.254, 8.281	-
5 (CH₃)	2.088	2.324	2.51	-
6 (s)	7.122	7.346	7.513	-
3* (m)	8.171 - 8.243	8.405 - 8.475	8.621	8.784
4* (m)	8.171 - 8.243	8.405 - 8.475	8.621	8.784
5* (CH₃)	2.48	2.714	2.895	3.064
6* (s)	8.61	8.844	9.024	9.191
$[\text{Fe}(\text{55mBpy})_3]^{2+}$ Peak positions at different temperatures and pH 1.9				
	300 K	325 K	345 K	365 K
3 (d)	8.334, 8.361	8.585, 8.614	8.755, 8.784	8.952, 8.979
4 (d)	7.859, 7.887	8.124, 8.151	8.297, 8.326	8.499, 8.526
5 (CH₃)	2.126	2.377	2.544	2.743
6 (s)	7.168	7.407	7.566	7.759
3* (m)	8.205 - 8.288	8.455 - 8.534	8.622 - 8.694	8.842
4* (m)	8.205 - 8.288	8.455 - 8.534	8.622 - 8.694	8.842
5* (CH₃)	2.519	2.767	2.932	3.13
6* (s)	8.65	8.897	9.064	9.257
$[\text{Fe}(\text{55mBpy})_3]^{2+}$ Peak positions at different temperatures and pH 2.9				
	300 K	325 K	345 K	365 K
3 (d)	8.366, 8.384	8.592, 8.619	8.784, 8.813	8.964, 8.991
4 (d)	7.867, 7.893	8.130, 8.157	8.325, 8.352	8.514, 8.541
5 (CH₃)	2.131	2.385	2.576	2.755
6 (s)	7.178	7.415	7.592	7.772
3* (m)	8.213 - 8.293	8.464 - 8.540	8.697, 8.678	8.859
4* (m)	8.213 - 8.293	8.464 - 8.540	8.697, 8.678	8.859
5* (CH₃)	2.526	2.775	2.961	3.147
6* (s)	8.658	8.906	9.09	9.273



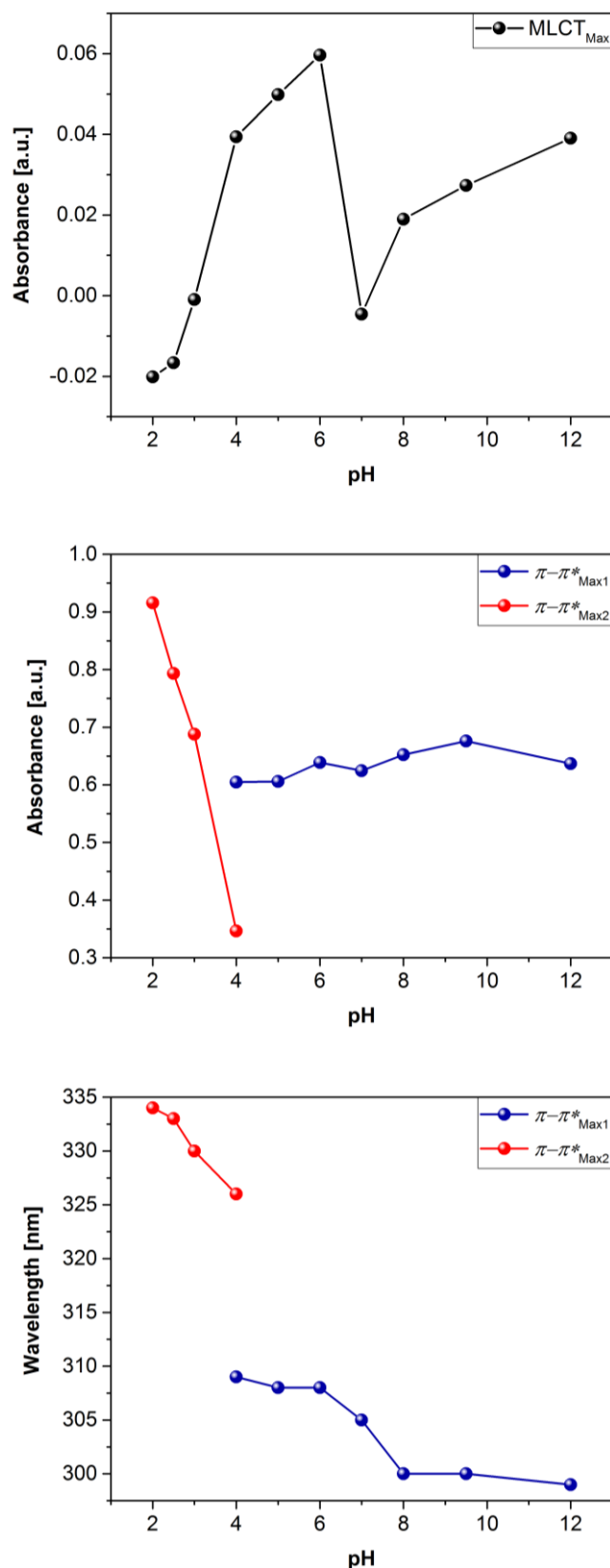
A12. ^1H -NMR spectroscopy atom numbering at the ligands for the complexes $[\text{Fe}(4\text{mBpy})_3]^{2+}$ (top) and $[\text{Fe}(5\text{mBpy})_3]^{2+}$ (bottom) described in this work.



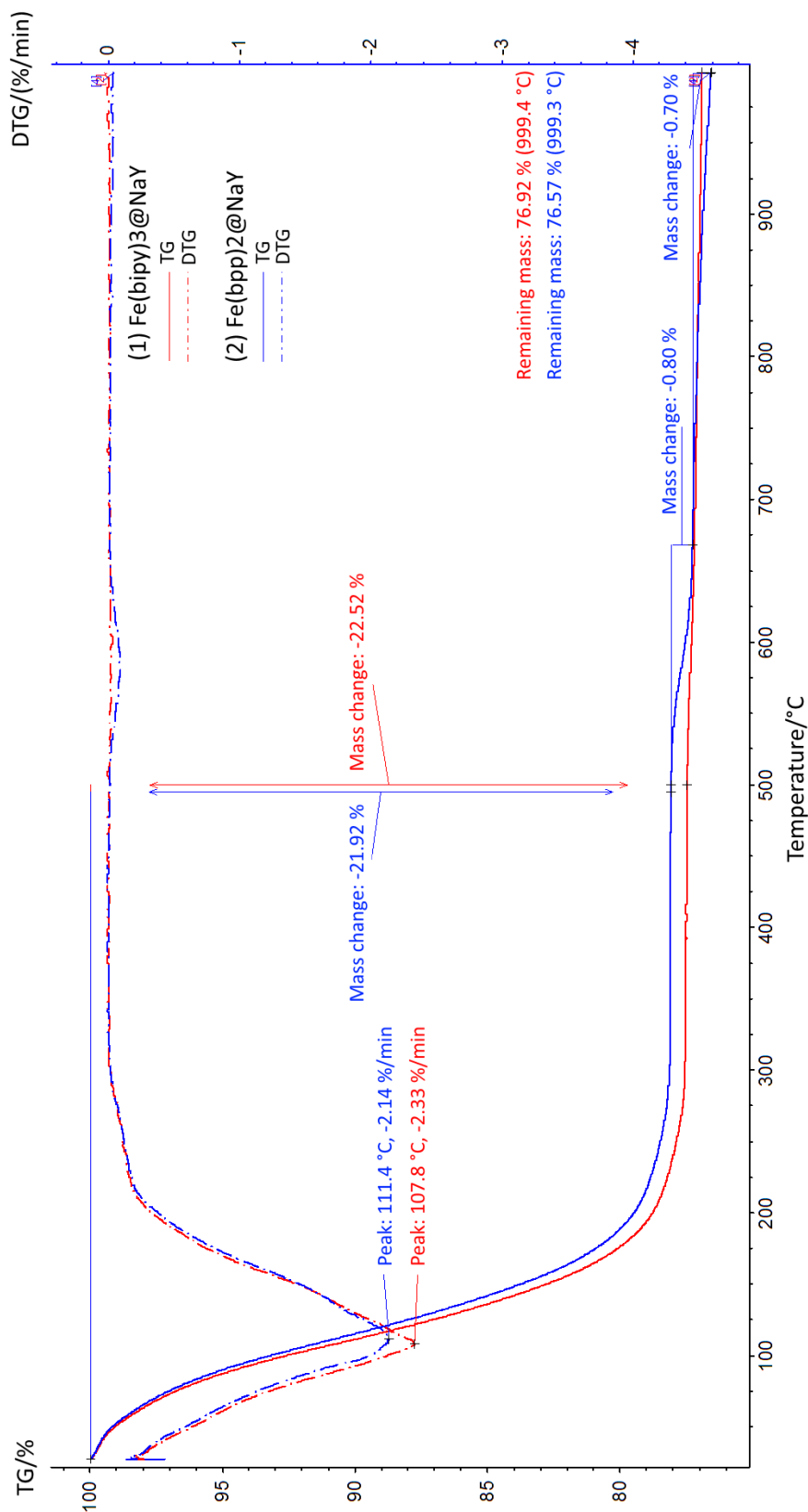
A13. pH-dependent absorbance of the MLCT-maximum (top), pH-dependent absorbance of the $\pi-\pi^*$ -maxima (middle) and pH-dependent wavenumber of the $\pi-\pi^*$ -maxima (bottom) of the complex $[\text{Fe}(\text{Bpy})_3]^{2+}$ during UV-Vis spectroscopy in aqueous solution.



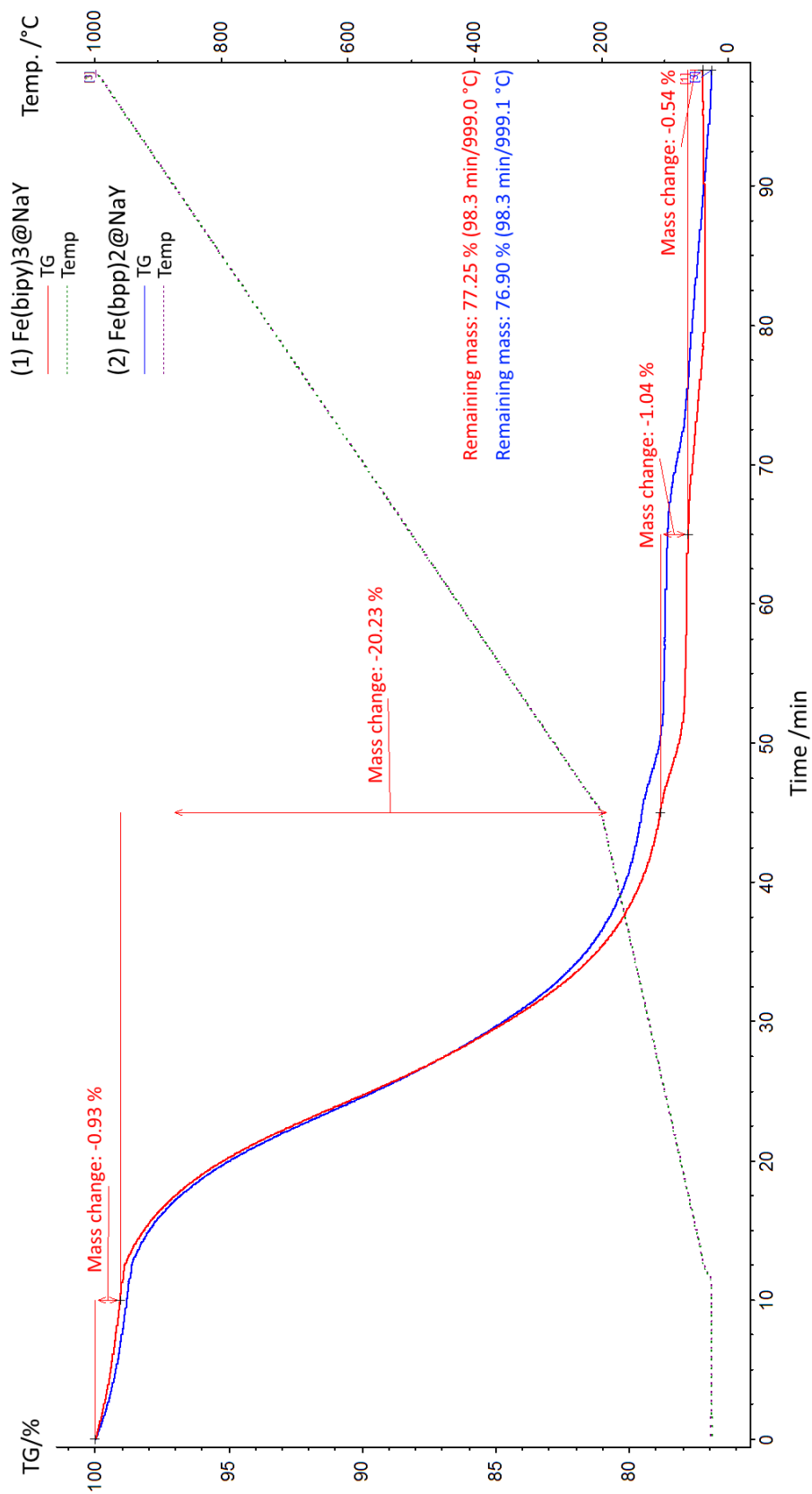
A14. pH-dependent absorbance of the MLCT-maximum (top), pH-dependent absorbance of the $\pi-\pi^*$ -maxima (middle) and pH-dependent wavelength of the $\pi-\pi^*$ -maxima (bottom) of the complex $[\text{Fe}(\text{44mBpy})_3]^{2+}$ during UV-Vis spectroscopy in aqueous solution.



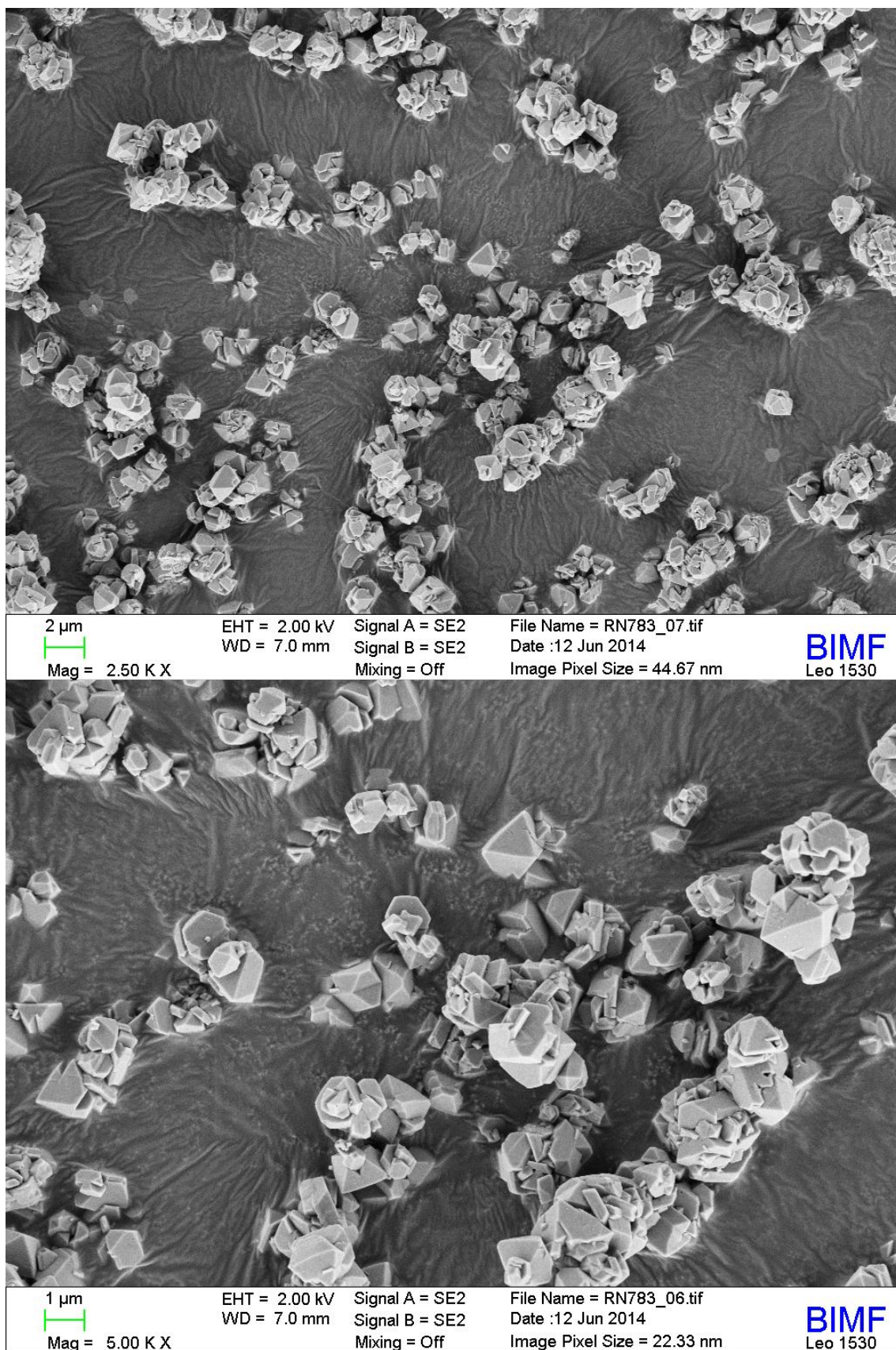
A15. pH-dependent absorbance of the MLCT-maximum (top), pH-dependent absorbance of the $\pi-\pi^*$ -maxima (middle) and pH-dependent wavelength of the $\pi-\pi^*$ -maxima (bottom) of the complex $[\text{Fe}(\text{Bpp})_2]^{2+}$ during UV-Vis spectroscopy in aqueous solution.



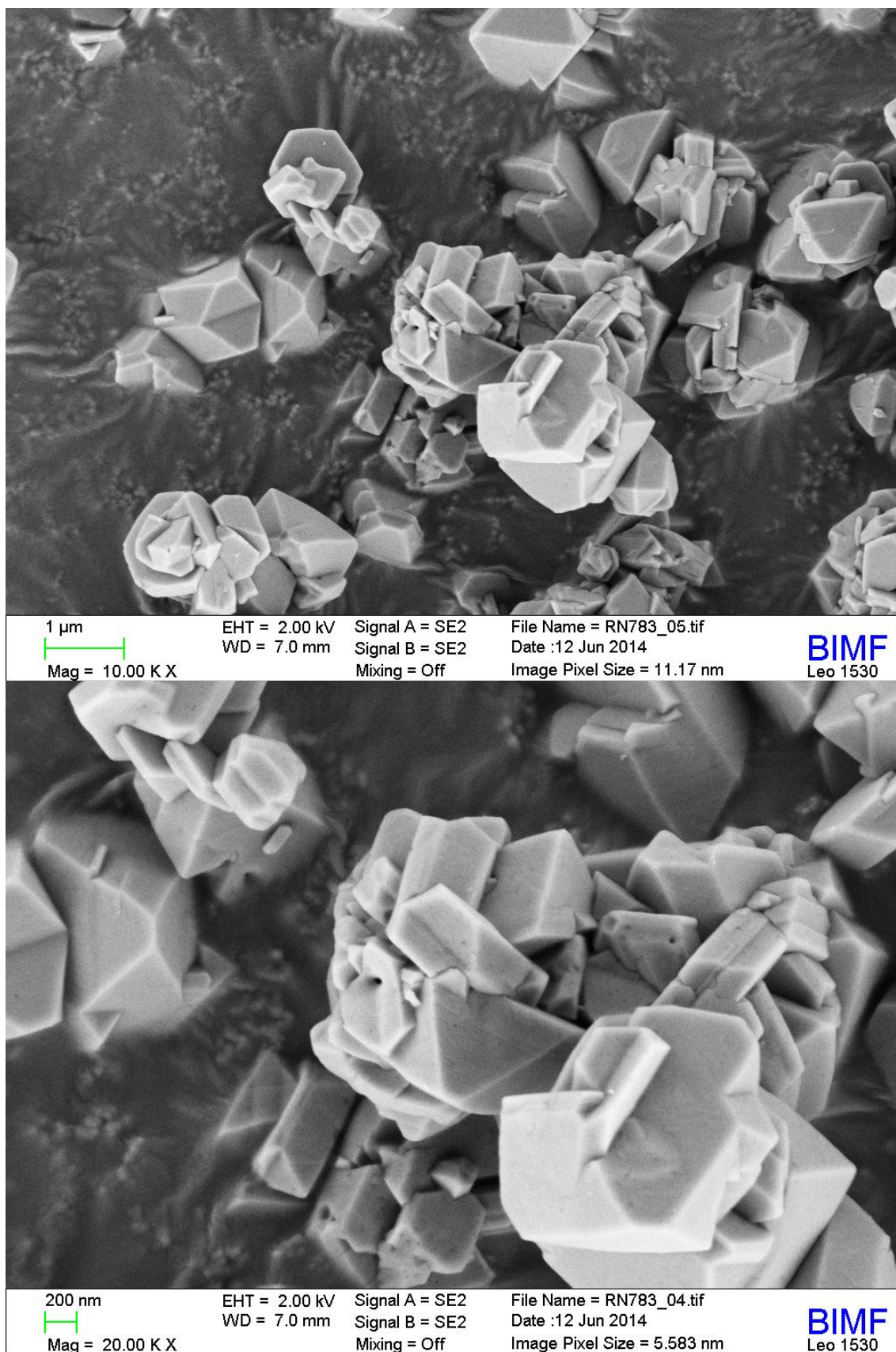
A16. Thermogravimetric analysis (TG) and differential thermogravimetric analysis (DTG) of the hybrid materials Fe(Bpy)₃@NaY (red) and Fe(Bpp)₂@NaY (blue) in the temperature domain.



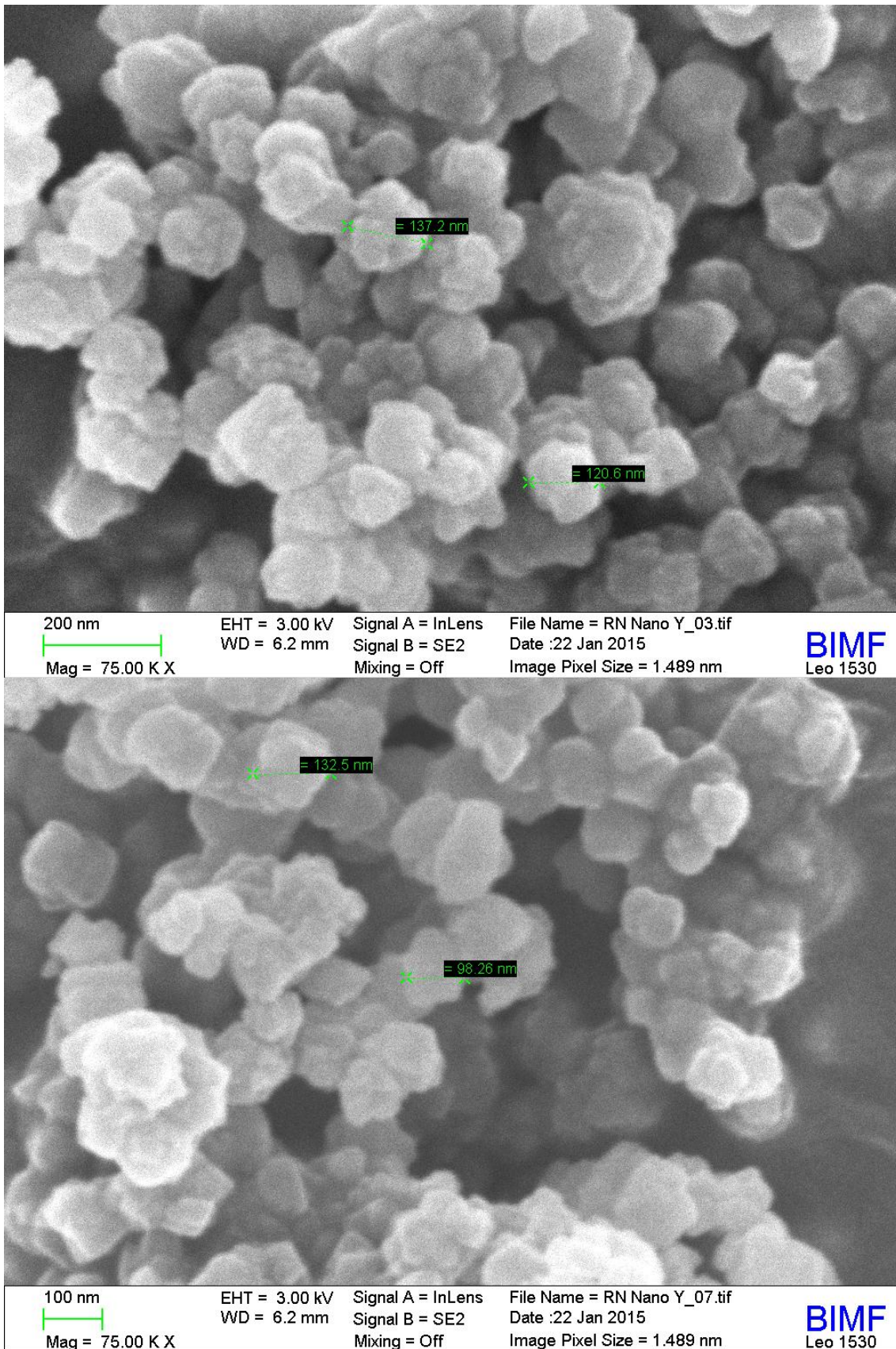
A17. Thermogravimetric analysis (TG) and differential thermogravimetric analysis (DTG) of the hybrid materials Fe(Bpy)₃@NaY (red) and Fe(Bpp)₂@NaY (blue) in the time domain.



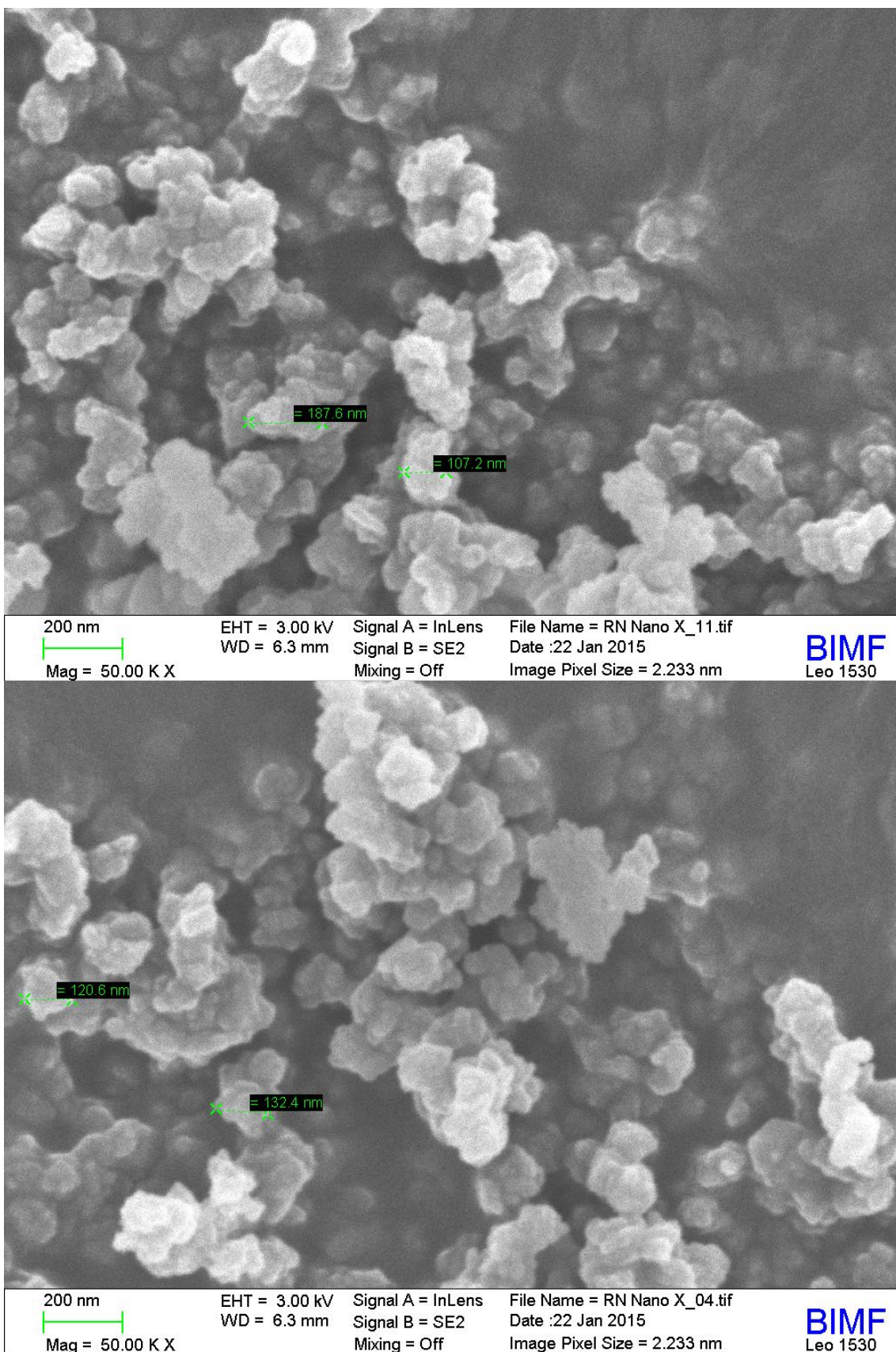
A18. Scanning electron microscopy images of microsized $\text{Fe}(\text{Bpy})_3@ \text{NaY}$ at two different magnifications and two different spots.



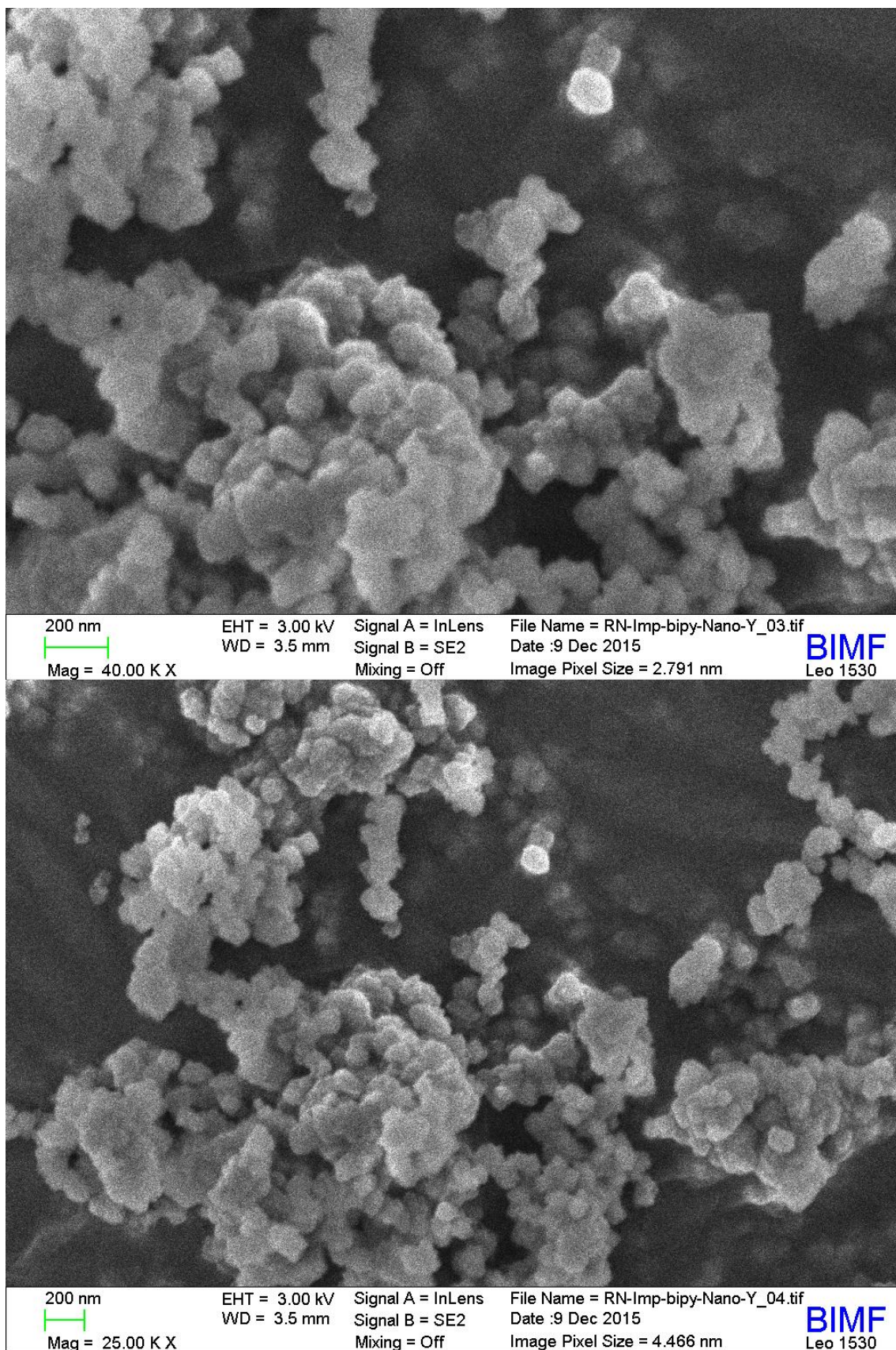
A19. Scanning electron microscopy images of microsized $\text{Fe}(\text{Bpy})_3@ \text{NaY}$ at two different magnifications and two different spots.



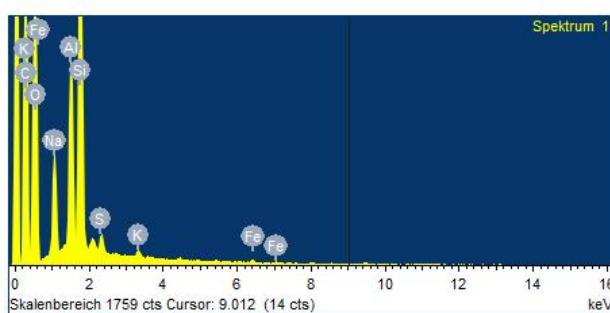
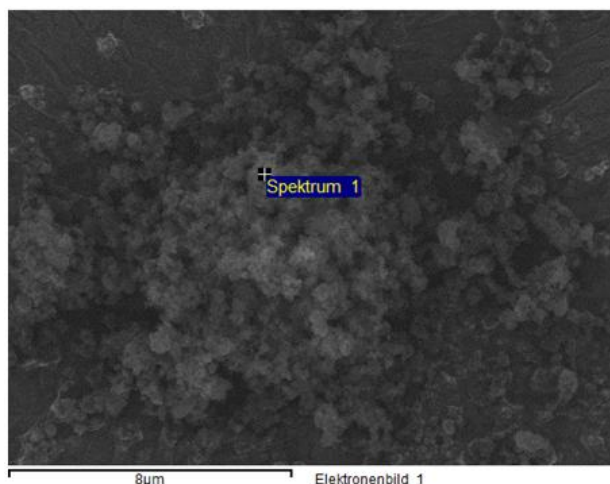
A20. Scanning electron microscopy images of nanosized zeolite NaY particles at two different magnifications and two different spots.



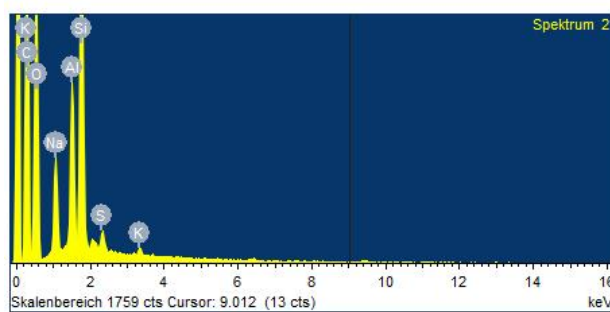
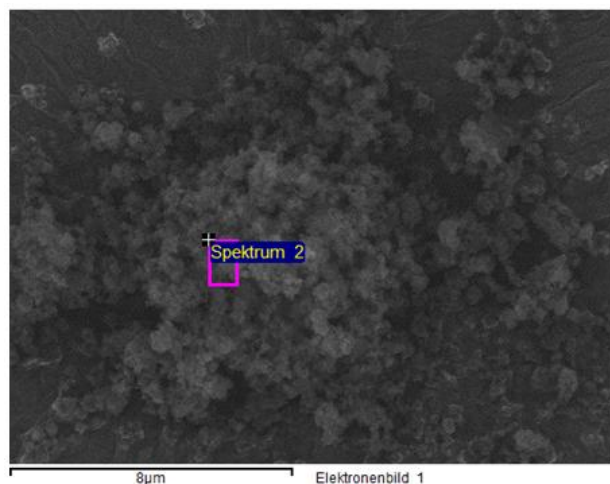
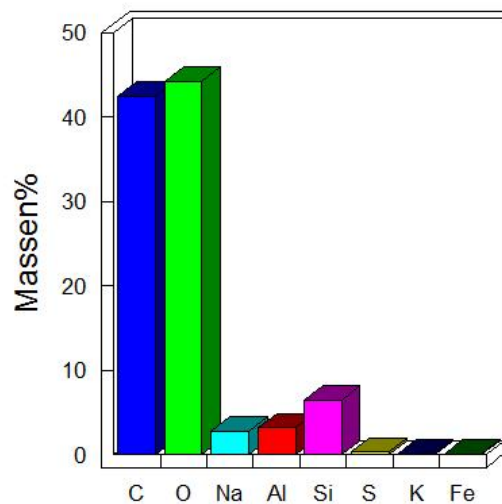
A21. Scanning electron microscopy images of nanosized zeolite NaX particles at two different magnifications and two different spots.



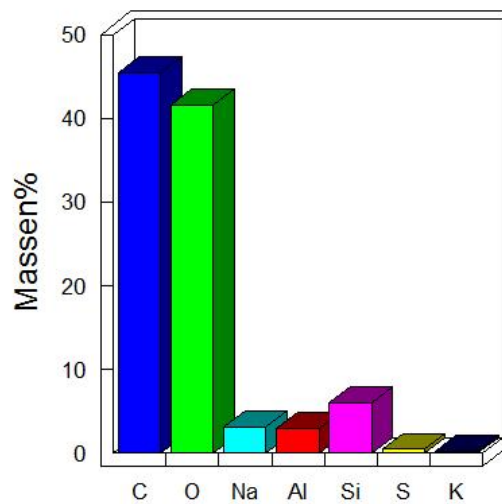
A22. Scanning electron microscopy images of nanosized $\text{Fe}(\text{Bpy})_3@ \text{NaY}$ particles at two different magnifications and two different spots.



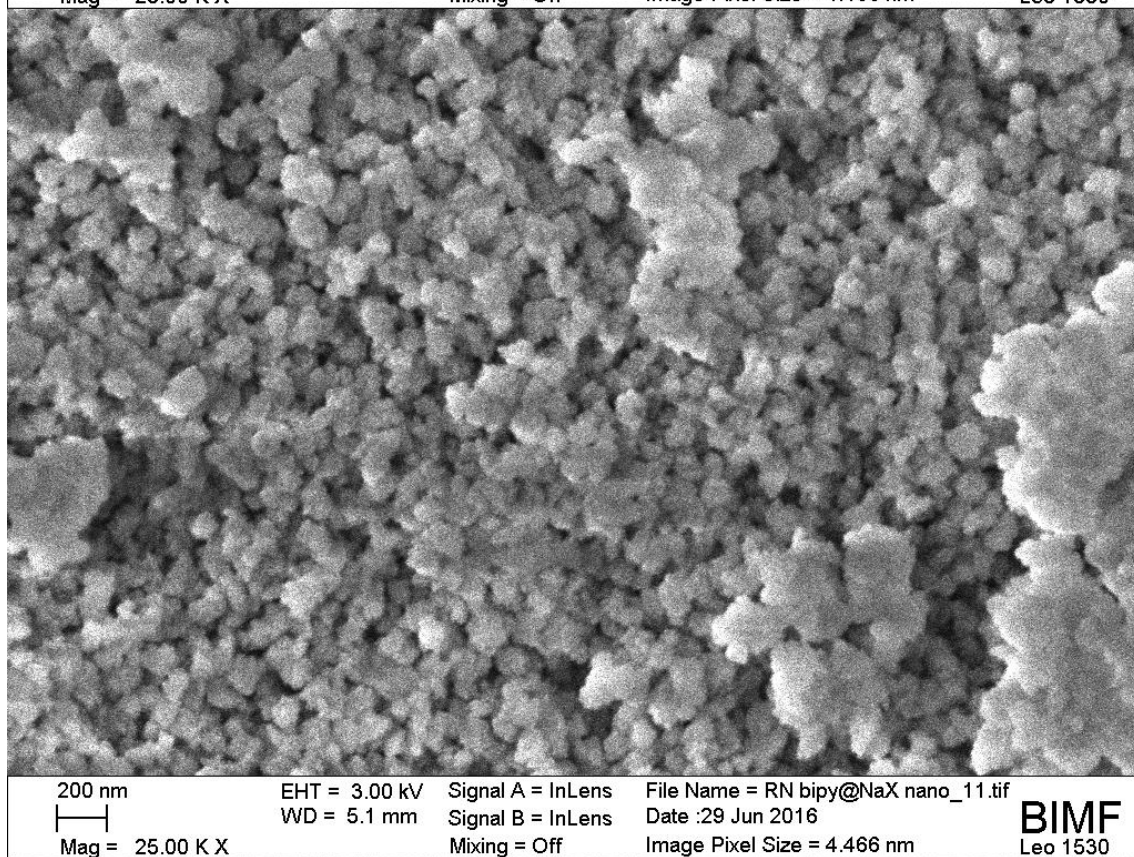
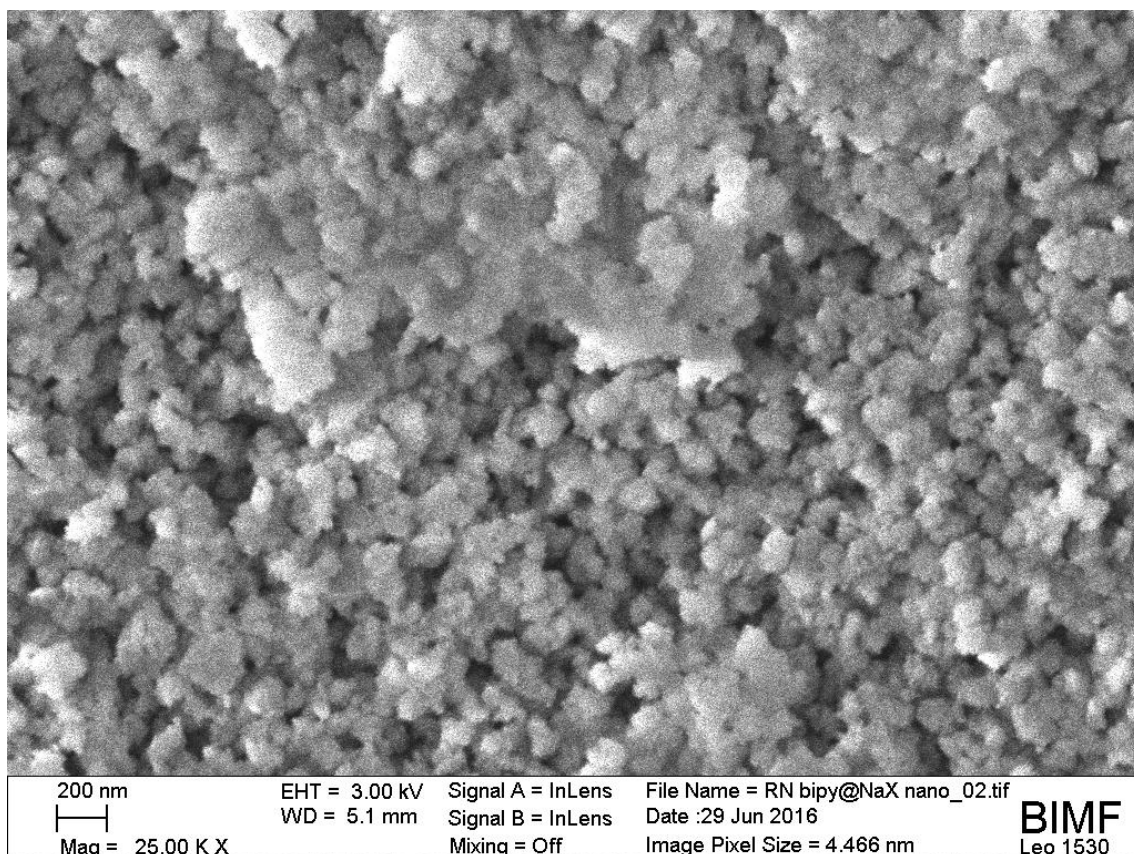
Quantitative Resultate



Quantitative Resultate

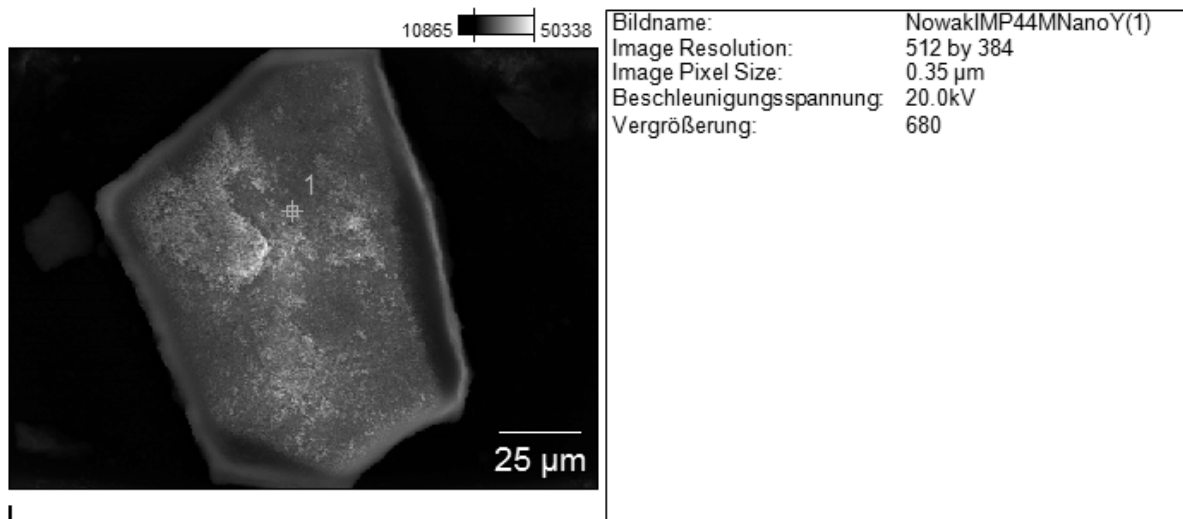


A23. EDX measurements and analysis of nanosized $\text{Fe}(\text{Bpy})_3@ \text{NaY}$ particles at two different spots.

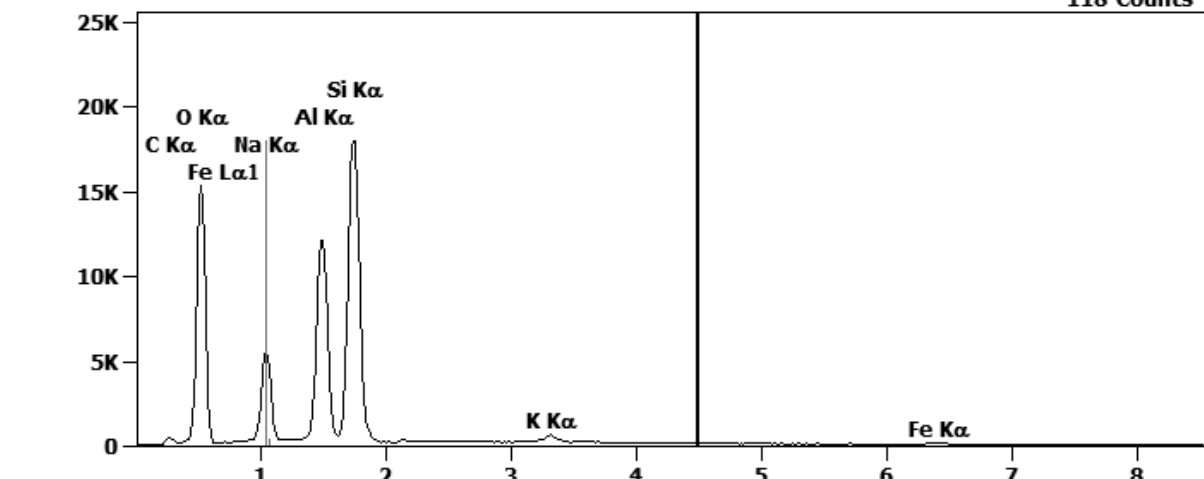


A24. Scanning electron microscopy images of nanosized $\text{Fe}(\text{Bpy})_3@NaX$ particles at two different magnifications and two different spots.

Appendix



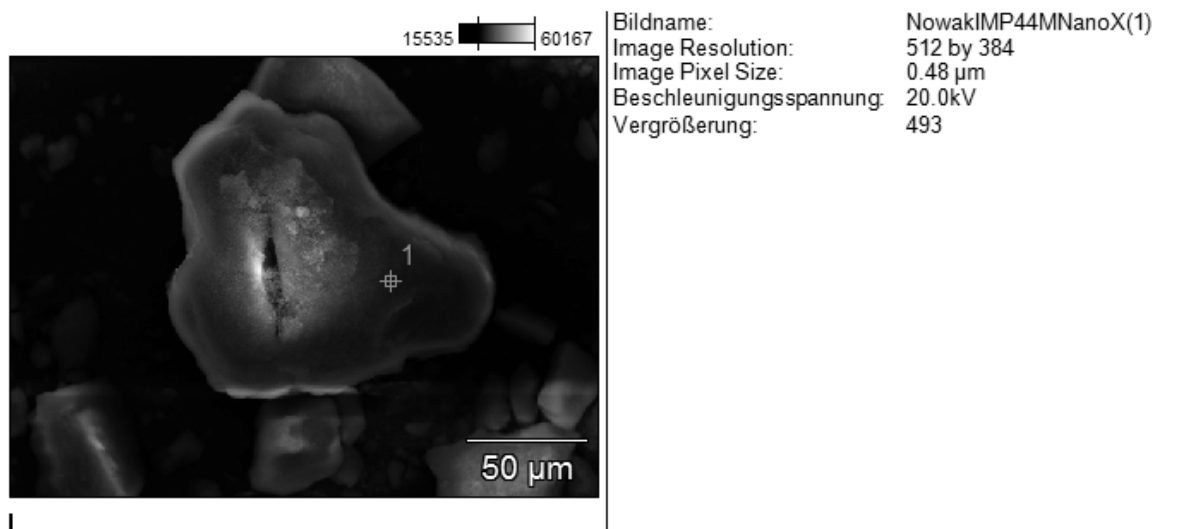
Skalierung, Counts: 19088 NowakIMP44MNanoY(1)_pt1 Cursor: 4.500 keV
 118 Counts



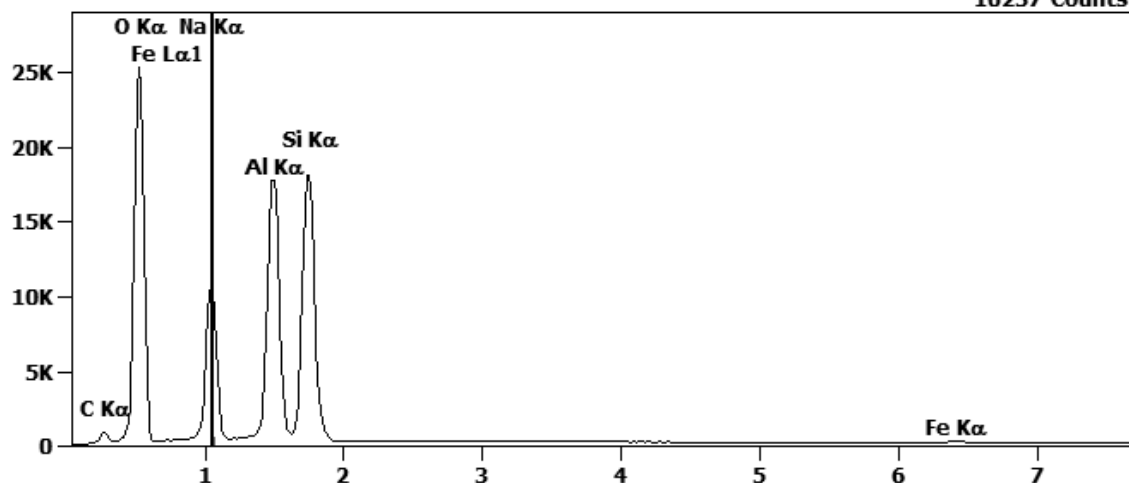
Gew.-%	C-K	O-K	Na-K	Al-K	Si-K	K-K	Fe-K
NowakIMP44MNanoY(1)_pt1	2.47	48.16	9.03	13.98	25.06	0.76	0.54
Gew.-% Fehler (+/- 1 Sigma)	C-K	O-K	Na-K	Al-K	Si-K	K-K	Fe-K
NowakIMP44MNanoY(1)_pt1	±0.06	±0.26	±0.06	±0.08	±0.11	±0.03	±0.07
Atom-%	C-K	O-K	Na-K	Al-K	Si-K	K-K	Fe-K
NowakIMP44MNanoY(1)_pt1	4.07	59.63	7.78	10.26	17.67	0.39	0.19
Atom-% Fehler (+/- 1 Sigma)	C-K	O-K	Na-K	Al-K	Si-K	K-K	Fe-K
NowakIMP44MNanoY(1)_pt1	±0.10	±0.32	±0.05	±0.06	±0.08	±0.02	±0.03

A25. EDX measurements and analysis of nanosized Fe(44mBpy)₃@NaY particles.

Appendix



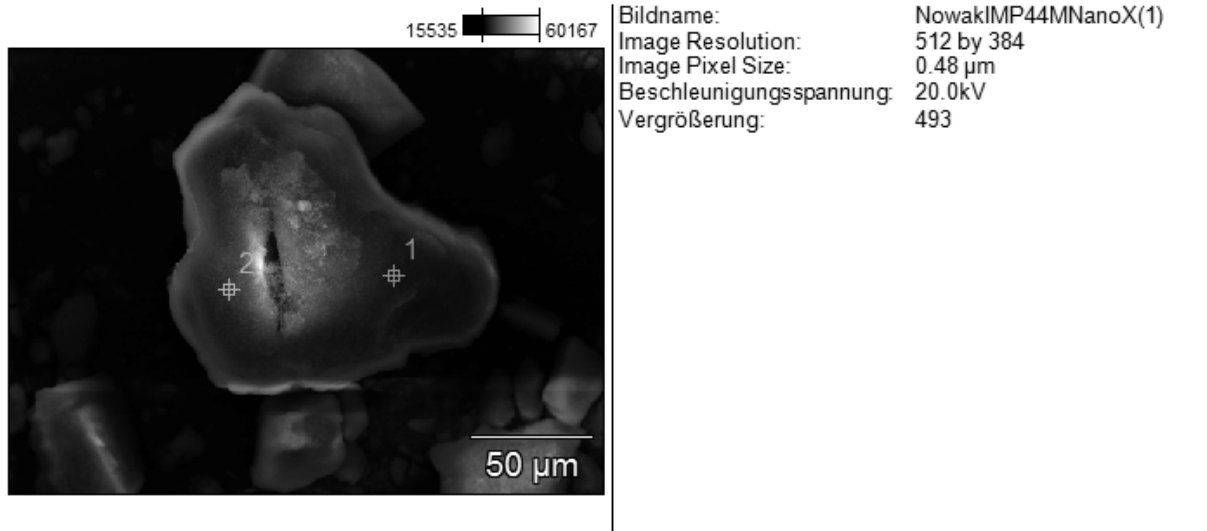
Skalierung, Counts: 25292 NowakIMP44MNanoX(1)_pt1 Cursor: 1.058 keV
 10237 Counts



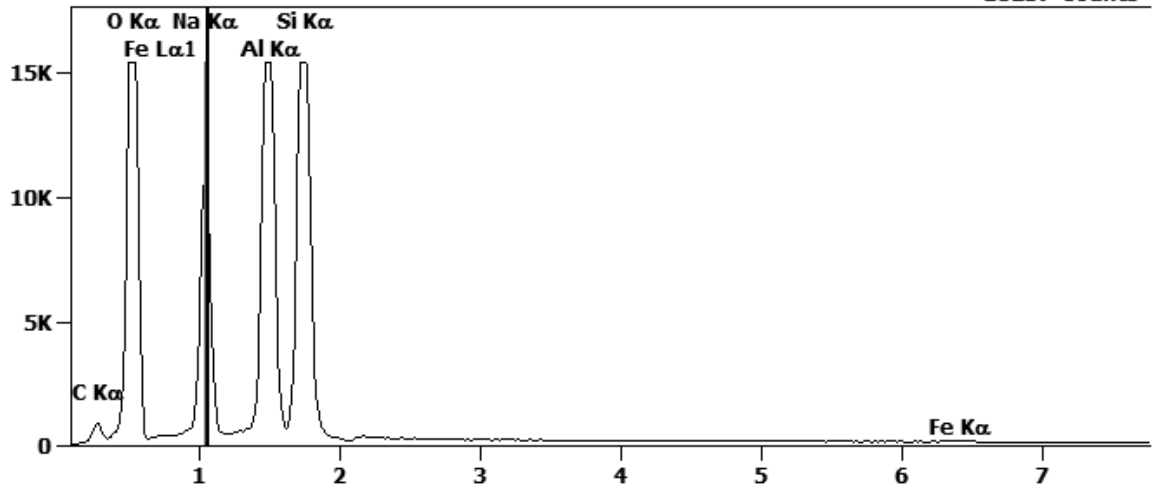
Gew.-%	C-K	O-K	Al-K	Si-K	Fe-K	Ga-K	Nb-L
NowakIMP44MNanoX(1)_pt1	3.60	59.57	15.85	19.96	0.69	0.00	0.33
Gew.-% Fehler (+/- 1 Sigma)	C-K	O-K	Al-K	Si-K	Fe-K	Ga-K	Nb-L
NowakIMP44MNanoX(1)_pt1	±0.06	±0.31	±0.08	±0.09	±0.03	±0.00	±0.05
Atom.-%	C-K	O-K	Al-K	Si-K	Fe-K	Ga-K	Nb-L
NowakIMP44MNanoX(1)_pt1	5.61	69.77	11.01	13.31	0.23	0.00	0.07
Atom.-% Fehler (+/- 1 Sigma)	C-K	O-K	Al-K	Si-K	Fe-K	Ga-K	Nb-L
NowakIMP44MNanoX(1)_pt1	±0.10	±0.36	±0.05	±0.06	±0.01	±0.00	±0.01

A26. EDX measurements and analysis of nanosized Fe(44mBpy)₃@NaX particles.

Appendix



Skalierung, Counts: 15393 **NowakIMP44MNanoX(1)_pt1** **Cursor: 1.058 keV**
10237 Counts



Gew.-%	C-K	O-K	Na-K	Al-K	Si-K	Fe-K	Ga-K	Nb-L
<i>NowakIMP44MNanoX(1)_pt1</i>	3.60	59.57		15.85	19.96	0.69	0.00	0.33
<i>NowakIMP44MNanoX(1)_pt2</i>	2.76	46.02	11.58	17.32	21.55	0.76		
Gew.-% Fehler (+/- 1 Sigma)	C-K	O-K	Na-K	Al-K	Si-K	Fe-K	Ga-K	Nb-L
<i>NowakIMP44MNanoX(1)_pt1</i>	±0.06	±0.31		±0.08	±0.09	±0.03	±0.00	±0.05
<i>NowakIMP44MNanoX(1)_pt2</i>	±0.06	±0.25	±0.07	±0.09	±0.10	±0.08		
Atom-%	C-K	O-K	Na-K	Al-K	Si-K	Fe-K	Ga-K	Nb-L
<i>NowakIMP44MNanoX(1)_pt1</i>	5.61	69.77		11.01	13.31	0.23	0.00	0.07
<i>NowakIMP44MNanoX(1)_pt2</i>	4.57	57.15	10.01	12.75	15.24	0.27		
Atom-% Fehler (+/- 1 Sigma)	C-K	O-K	Na-K	Al-K	Si-K	Fe-K	Ga-K	Nb-L
<i>NowakIMP44MNanoX(1)_pt1</i>	±0.10	±0.36		±0.05	±0.06	±0.01	±0.00	±0.01
<i>NowakIMP44MNanoX(1)_pt2</i>	±0.10	±0.31	±0.06	±0.07	±0.07	±0.03		

A27. EDX measurements and analysis of nanosized Fe(44mBpy)₃@NaX particles.